Coordination Polymer Nanofibers made of Amino Acids and Peptides and their Use as Templates to Synthesize Inorganic Nanoparticle Superstructures

Marta Rubio Martínez

A dissertation submitted to attain the degree of

Doctor of Philosophy

Supervisors

Prof. Dr. Daniel Maspoch and Dr. Inhar Imaz

Tutor

Dr. Jordi Hernando

Catalan Institute of Nanoscience and Nanotechnology

Facultat de Ciències - Química

2014

Memòria presentada per aspirar al Grau de Doctor per Marta Rubio Martínez

Marta Rubio Martínez

Prof. Dr. Daniel Maspoch

Investigador ICREA

Supramolecular Nanochemistry and Materials Group

Institut Català de Nanociència I Nanotecnologia (ICN2)

Dr. Inhar Imaz

Investigador Ramón y Cajal

Supramolecular Nanochemistry and Materials Group

Institut Català de Nanociència I Nanotecnologia (ICN2)

Dr. Jordi Hernando

Professor Agregat

Departament de Química

Universitat Autònoma de Barcelona (UAB)

Bellaterra, 10 d'abril de 2014

“The fun of chemistry is in its unexpectedness. There are times when you come to face-to-face with an unexpected phenomenon while carrying out experiments. You simply have to be sufficiently aware and open to accept the seemingly unbelievable. There are still many more valuable ideas remaining to be discovered. The question is how to find them and how to develop them into new possibilities.” (Mukaiyama, Angew. Chem. Int. Ed. 2004, 43, 5590)

The present PhD thesis has been carried out at the Supramolecular Nanochemistry and Materials Group of the Catalan Institute of Nanoscience and Nanotechnology (ICN2) following the doctoral program in Chemistry of the Autonomus University of Barcelona. According to the decision of the PhD Commission this PhD thesis is presented as a compendium of publications.

All the publications and manuscripts are listed below in order of their appearance in the thesis:

Publication 1. "Metal-biomolecule frameworks (MBioFs)." I. Imaz, M. Rubio-Martínez, J. An, I. Solé-Font, N. L. Rosi, D. Maspoch. *Chem. Commun.* **2011**, 7287-7302.

Publication 2. "Amino acid based metal-organic nanofibers." I. Imaz, M. Rubio-Martínez, W.J. Saletra, D.B. Amabilino, D. Maspoch. *J.Am.Chem. Soc.* **2009**, 131, 18222-18223.

Publication 3. "Coordination polymer nanofibers generated by microfluidics synthesis." J. Puigmartí-Luis, M. Rubio-Martínez, U. Hartfelder, I.Imaz, D. Maspoch, P.S. Dittrich. *J. Am. Chem.Soc.* **2011**, 133, 4216-4219.

Publication 4. "Localized, stepwise template growth of functional nanowires from an amino-acid supported framework in a microfluidic chip". J. Puigmartí-Luis, M. Rubio-Martínez, I.Imaz, B. Z. Cvetkovic, L. Abad, A. Perez del Pino, D. Maspoch, D. B. Amabilino. *ACS nano.* **2014**, 8, 818-826.

Publication 5. ""Dual-template" Synthesis of one-dimensional conductive nanoparticle superstructures from coordination metal-peptide polymer crystals" M. Rubio-Martinez, J. Puigmartí-Luís, I. Imaz, Petra S. Dittrich, D. Maspoch, *Small* **2013**, 24, 4160-4167.

Additional publications and manuscripts:

Publication 6. “Coordination polymer particles as potential drug delivery systems” I. Imaz, M. Rubio-Martínez, L. García-Fernández, F. García, D. Ruiz-Molina, J. Hernando, V. Puntes, D. Maspoch, *Chem. Commun.* **2010**, 133, 4737-4739.

Publication 7. “Metal-biomolecule nanostructures” M. Rubio-Martinez, I. Imaz, J. Puigmartí-Luís, D. Maspoch. *Revista de la Societat Catalana de Quimica*, **2012**, 11, 55-60.

Publication 8. “Trapping the morphological transitions of a coordination polymer by microfluidics: from needles to frames to plate like single crystals” M. Rubio-Martinez, J. Puigmartí-Luís, D. B. Amabilino, N. Domingo, I. Imaz, D. Maspoch. Submitted.

Table of Contents

Abstract

The present PhD Thesis has been dedicated to explore the coordination capabilities of amino acids and peptides to create novel nanoscale Coordination Polymers (CPs) in the form of nanofibers, and to use these nanofibers as (dual) scaffolds for the synthesis of superstructures made of inorganic nanoparticles (INPs). The use of CP nanofibers as dual scaffolds has taken advantage of the templating characteristics of CPs as well as the inherent recognition-template characteristics of the peptide that has been used to form the CP.

In the first Chapter, we show a brief introduction to CPs, focusing on those constructed from biomolecules. This Chapter includes the review entitled "*Metal–biomolecule frameworks (MBioFs)*", Chem. Commun (2011), in which an extended, detailed description of this type of materials was reported. Then, the general objectives of this Thesis are described in Chapter 2.

Chapter 3 summarizes the results reported in "*Amino acid-based metal-organic nanofibers*", J. Am. Chem. Soc.(2009). Here, we show the synthesis and characterization of CP nanofibers and gels built up from the coordination of amino acids (L- or D-aspartic acid, Asp) and metal ions (Cu(II) ions). The resulting chiral Cu(II)-Asp nanofibers have been synthesized using fast precipitation and slow diffusion techniques, from which their lenght could be extended up to 1 centimeter.

In Chapter 4, Cu(II)-Asp nanofibers have been used as the test-case-scenario to explore microfluidics technology (more precisely, laminar flow) as a new synthetic approach to achieve precise control over the assembly of metal ions and amino acids. We have demonstrated that unlike common synthetic procedures, this approach enables parallel synthesis with an unprecedented level of control over the coordination pathway and facilitates the formation of 1D CP assemblies at the nanometer length scale. In addition to Cu(II)-Asp nanofibers, the use of microfluidics has allowed the synthesis of a second type of CP nanofibers made of amino acids Ag(I)-Cysteine (Cys) nanofibers. We have also confirmed that these nanostructures can not be synthesized with more traditional methods, such as fast mixing of both components. All these results are included in the manuscript entitled "*Coordination polymer nanofibers generated by microfluidic synthesis"*, J. Am. Chem. Soc. (2011).

In a next step, Chapter 5 focuses on the use of the Ag(I)-Cys nanofibers as templates to synthesize and assemble inorganic NPs into 1D superstructures. In this Chapter, we first show the synthesis of 1-D assemblies of Ag_2S NPs by exposing the Ag(I)-Cys nanofibers to e-

beam bombardment. We then show that this template synthesis can be localized at precise positions by using microfluidic technology with micro-engineered fluidic clamps incorporated. Microfluidics allows guiding and localizing the formation of Ag(I)-Cys nanofibers, whereas the use of clamps allows immobilizing these fibers and use them as templates to synthesize 1-D Ag NP superstructures. These superstructures have been synthesized via reduction (ascorbic acid) of the Ag(I) ions inside the scaffold structure. We anticipate that the level of control achieved with microfluidics has allowed us to further use these Ag NP superstructures as second templates to synthesize conductive Ag(I)-tetracyanoquinodinmethane (TCNQ) CP crystals, allowing also the direct measurement of their conductivity properties. All these results are included in the article presented in Chapter 4 and in the article entitled "Localized template growth of functional nanofibers from an metal-amino acid-supported framework in a microfluidic chip", ACS Nano 2014.

Finally, in Chapter 6, we have increased the complexity of the Ag(I)-based CP from amino acids to peptides to exploit the inherent recognition-template characteristics of peptides. Here, we have synthesized a new class of metal-peptide scaffolds, Ag(I)-DLL belt-like crystals, that were proved to be used as dual-templates for the synthesis and assembly of two types of inorganic NPs, one on their surface (crystal face) and the other within their internal structures. In these CP scaffolds, the self-assembly and recognition capacities of peptides and the selective reduction of Ag(I) ions to Ag are simultaneously exploited to control the growth and assembly of more complex, multicompositional inorganic NP superstructures. We demonstrate that these Ag(I)-DLL belts could be applied as dual templates to create long (> 100 μm) conductive Ag@Ag NP superstructures and polymetallic, multifunctional Fe_3O_4@Ag NP composites that marry the magnetic and conductive properties of the two NP types. These results have been reported in the manuscript entitled ""Dual-template" Synthesis of one-dimensional conductive NP superstructures from coordination metal-peptide polymer crystals", Small (2013).

Resum

La present Tesi Doctoral s'ha dedicat a explorar les capacitats de coordinació d'aminoàcids i pèptids per tal de desenvolupar nous Polimers de Coordinació (PCs) en forma de nanofibres a escala nanoemetrica, i poder utilitzar-los com a (doble) plantilla per la síntesi de superestructures fetes amb nanopartícules inorgàniques (INPs). Utilitzar PC en forma de nanofibres com a doble plantilla té l'avantatge de poder aprofitar tant les propietats de plantilla com les característiques inherents de reconeixement dels pèptids per tal de formar CPs.

En el primer capítol es mostra una breu introducció als PC, centrant-se en l'ús de biomolècules. Aquest capítol inclou el treball titulat "*Metal–biomolecule frameworks (MBioFs)*", Chem. Commun (2011), on es fa una estesa i detallada descripció sobre aquests tipus de materials. A continuació, els objectius generals d'aquesta tesi es descriuen en el capítol 2.

El Capítol 3 resumeix els resultats reportats en "*Amino acid-based metal-organic nanofibers*", J. Am. Chem. Soc. (2009). Aquí, es mostra la síntesi i caracterització de nanofibres de CP i gels construïts a partir de la coordinació d'amino àcids (L-o àcid D-aspàrtic, Asp) i ions metàl · lics (Cu (II) ions). Les nanofibres quirals de Cu(II)-Asp resultants s'han sintetitzat utilitzant tècniques de precipitació ràpida i de difusió lenta, amb les quals la longitud d'aquestes pot arribar fins a 1 centímetre.

En el capítol 4, les nanofibres de Cu(II)-Asp s'han utilitzat com a cas-escenari de prova per explorar la tècnica de microfluídica (més precisament flux laminar) com a nou mètode sintètic per tal d'aconseguir un control més precís sobre l'assamblatge d'ions metàl·lics amb AA. S'ha demostrat que, a diferència dels procediments sintètics comuns, aquesta aproximació permet la síntesi en paral·lel amb un eminent nivell sobre el control de la coordinació, facilitant la formació de 1-D PC ensamblats a escala nanomètrica. A més de les nanofibres de Cu(II)-Asp, l'ús de la microfluidica ha permès la síntesis d'un segon tipus de nanofibres fetes amb aminoàcids, Ag(I)-Cisteina (Cys). S'ha confirmat que aquestes nanoestructures no es poden obtenir amb mètodes tradicionals com el de la precipitació ràpida dels dos components. Aquests resultats s'inclouen en el manuscrit "*Coordination polymer nanofibers generated by microfluidic synthesis"*, J. Am. Chem. Soc. (2011).

En un següent pas, el capítol 5 es centra en l'ús de les nanofibres de Ag (I)-Cys com a plantilles per tal de sintetitzar i acoblar NP inorgàniques en superestructures 1-D. En aquest capítol, primer es motra la síntesi de NPs de Ag_2S ensamblades en 1-D exposant les nanofibres de Ag(I)-Cys sota un bombardeig d'electrons. A continuació, es mostra que

aquestes plantilles sintetitzadades poden localitzar-se en posicions precises mitjançant la tecnologia de la microfluidica amb la incorporació de vàlvules de fluids microfabricades incorporades. La microfluídica permet orientar i localitzar la formació de les nanofibres de Ag (I)-Cys i a més, l'ús de vàlvules permet la immobilització de les fibres i poder utilitzar-les com a plantilles per a la síntesis de 1-D superestructures de NPs deAg. Aquestes superestructures s'han sintetitzat mitjançant la reducció (àcid ascòrbic) dels ions de Ag(I) que es troben dins de la plantilla. El nivell de control assolit amb la microfluídica ha permès que es puguin utilitzar més a fons aquestes superestructures de Ag NP com a segones plantilles per sintetitzar cristalls conductors de Ag (I)-tetracyanoquinodinmethane (TCNQ), permetent a més la mesura directe de les seves propietats de conductivitat. Tots aquests resultats estan inclosos en l'article presentat en el capítol 4 i en l'article titulat "Localized template growth of functional nanofibers from an metal-amino acid-supported framework in a microfluidic chip", ACS Nano 2014.

Finalment, en el capítol 6, s'ha incrementat la complexitat dels PCs de Ag(I) fets a partir d'aminoàcids amb pèptids per tal d'explotar les característiques inherents de reconeixement que tenen els pèptids. S'ha sintetitzat una nova classe de plantilles metall-pèptid, cristalls de Ag(I)-DLL similars a cintes, amb els quals s'ha demostrat que poden ser utilitzats com a doble plantilla per a la síntesi i assamblatge de dos tipus de NPs inorgàniques, unes sobre la seva superfície (cara del cristall) i les altres dins de les seves estructures internes. En aquestes plantilles, les capacitats d'auto-assamblatge i reconeixement dels pèptids, i la reducció selectiva dels ions Ag(I) a Ag s'han explotat simultàniament per tal de controlar el creixement i l'assamblatge de més complexos multicomposicionals de superestructures amb NP inorgàniques. S'ha demostrat que aquests cinturons Ag(I)-DLL poden ser utilitzats com a dobles plantilles per crear llargues (> 100 μm) i polimetàl·liques superestructures conductores de Ag@AgNP i compostos multifuncionals de NPs de Fe_3O_4@Ag combinant les propietats magnètiques i conductores dels dos tipus de NPs. Aquests resultats han estat reportats en el manuscrit titulat "“Dual-template” Synthesis of one-dimensional conductive NP superstructures from coordination metal-peptide polymer crystals", Small (2013).

Optical abstracts

1) I. Imaz, M. Rubio-Martínez, J. An, I. Solé-Font, N. L. Rosi, D. Maspoch. "Metal–biomolecule frameworks (MBioFs)." *Chem. Commun.* 2011, 47, 7287-7302. Feature Article.

Biomolecules are the building blocks of life. Nature has evolved countless biomolecules that show promise for bridging metal ions. These molecules have emerged as an excellent source of biocompatible building blocks that can be used to design Metal–Biomolecule Frameworks (MBioFs). This feature article highlights the advances in the synthesis of this class of MOFs. Special emphasis is provided on the crystal structures of these materials, their miniaturization to the submicron length scale, and their new potential storage, catalytic, and biomedical applications of life. Nature has evolved countless biomolecules that show promise for bridging metal ions. These molecules have emerged as an excellent source of biocompatible building blocks that can be used to design Metal–Biomolecule Frameworks (MBioFs). This feature article highlights the advances in the synthesis of this class of MOFs. Special emphasis is provided on the crystal structures of these materials, their miniaturization to the submicron length scale, and their new potential storage, catalytic, and biomedical applications.

2) I. Imaz, M. Rubio-Martínez, W. J. Saletra, D. Amabilino, D. Maspoch. "Amino acid-based metal-organic nanofibers." *J. Am. Chem. Soc.* 2009, 131, 18222-18223.

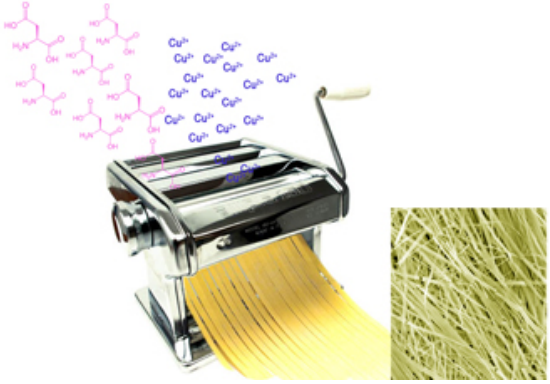

Long chiral metal–organic nanofibers can be grown using conventional coordination chemistry and biologically derived components in a diffusion controlled growth procedure.

3) J. Puigmartí-Luis, M. Rubio-Martínez, U. Hartfelder, I. Imaz, D. Maspoch, P. S. Dittrich. "Coordination polymer nanofibers generated by microfluidic synthesis." ***J. Am. Chem. Soc.*****, 2011, 133, 4216–4219.**

One-dimensional coordination polymer nanostructures are an emerging class of nanoscale materials with many potential applications. Here, we report the first case of coordination polymer nanofibers assembled using microfluidic technologies. Unlike common synthetic procedures, this approach enables parallel synthesis with an unprecedented level of control over the coordination pathway and facilitates the formation of 1D coordination polymer assemblies at the nanometer length scale. Finally, these nanostructures, which are not easily constructed with traditional methods, can be used for various applications, for example as templates to grow and organize functional inorganic nanoparticles.

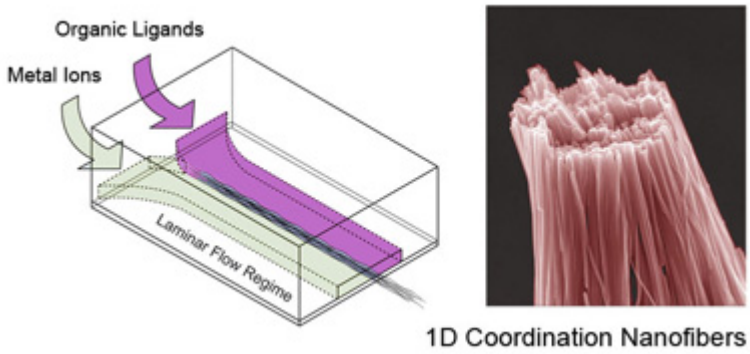

4) J. Puigmartí-Luis, M. Rubio-Martinez, I. Imaz, B. Z. Cvetkovic, L. Abad, A. Perez del Pino, D. Maspoch, D. B. Amabilino. "Localized, stepwise template growth of functional nanowires from an amino-acid-supported framework in a microfluidic chip." ***ACS nano*****, 2014, 8, 818-826.**

A spatially controlled synthesis of nanowire bundles of the functional crystalline coordination polymer (CP) Ag(I)TCNQ (tetracyanoquinodimethane) from previously fabricated and trapped monovalent silver CP (Ag(I)Cys (cysteine)) using a room-temperature microfluidic-assisted template growth method is demonstrated. The incorporation of microengineered pneumatic clamps in a two-layer polydimethylsiloxane-based (PDMS) microfluidic platform was used. Apart from guiding the formation of the Ag(I)Cys coordination polymer, this microfluidic approach enables a local trapping of the *in situ*

synthesized structures with a simple pneumatic clamp actuation. This method not only enables continuous and multiple chemical events to be conducted upon the trapped structures, but the excellent fluid handling ensures a precise chemical activation of the amino acid-supported framework in a position controlled by interface and clamp location that leads to a site-specific growth of Ag(I)TCNQ nanowire bundles. The synthesis is conducted stepwise starting with Ag(I)Cys CPs, going through silver metal, and back to a functional CP (Ag(I)TCNQ); that is a novel microfluidic controlled ligand exchange (CP → NP → CP) is presented. Additionally, the pneumatic clamps can be employed further to integrate the conductive Ag(I)TCNQ nanowire bundles onto electrode arrays located on a surface, hence facilitating the construction of the final functional interfaced systems from solution specifically with no need for post-assembly manipulation. This localized self-supported growth of functional matter from an amino acid-based CP shows how sequential localized chemistry in a fluid cell can be used to integrate molecular systems onto device platforms using a chip incorporating microengineered pneumatic tools. The control of clamp pressure and in parallel the variation of relative flow rates of source solutions permit deposition of materials at different locations on a chip that could be useful for device array preparation. The *in situ* reaction and washing procedures make this approach a powerful one for the fabrication of multicomponent complex nanomaterials using a soft bottom-up approach.

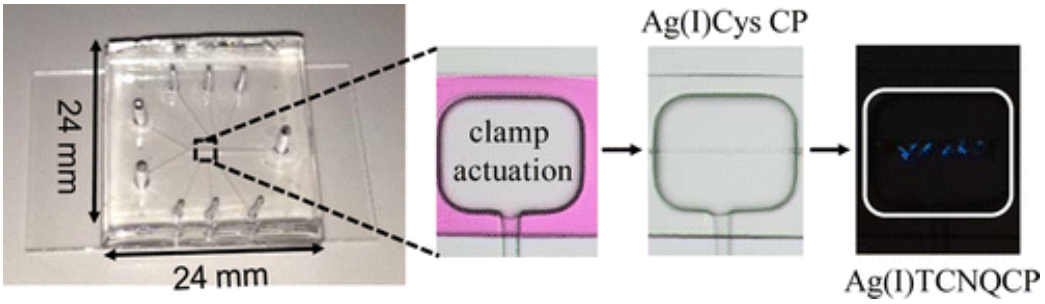

5) M. Rubio-Martinez, J. Puigmartí-Luis, I. Imaz, P. S. Dittrich, D. Maspoch. ""Dual-template" Synthesis of one-dimensional conductive nanoparticle superstructures from coordination metal-peptide polymer crystals." *Small,* 2013, 24, 4160-4167.

Bottom-up fabrication of self-assembled structures made of nanoparticles may lead to new materials, arrays and devices with great promise for myriad applications. Here a new class of metal–peptide scaffolds is reported: coordination polymer Ag(I)-DLL belt-like crystals, which enable the dual-template synthesis of more sophisticated nanoparticle

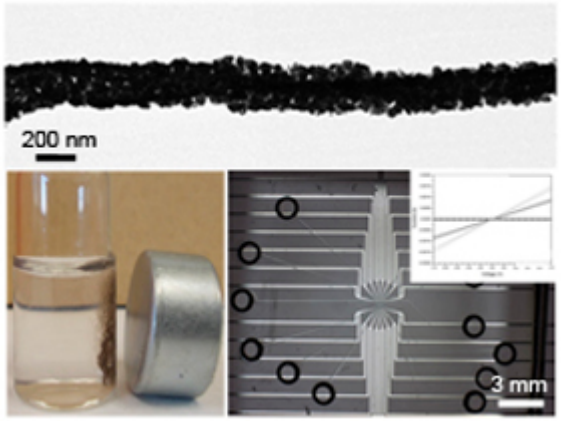

superstructures. In these bio-related scaffolds, the self-assembly and recognition capacities of peptides and the selective reduction of Ag(I) ions to Ag are simultaneously exploited to control the growth and assembly of inorganic nanoparticles: first on their surfaces, and then inside the structures themselves. The templated internal Ag nanoparticles are well confined and closely packed conditions that favour electrical conductivity in the superstructures. It is anticipated that these Ag(I)-DLL belts could be applied to create long (> 100 μ m) conductive Ag@Ag nanoparticle superstructures and polymetallic, multifunctional Fe_3O_4@Ag nanoparticle composites that marry the magnetic and conductive properties of the two nanoparticle types.

6) I. Imaz, M. Rubio-Martínez, L. García-Fernández, F. García, D. Ruiz-Molina, J. Hernando, V. Puntes, D. Maspoch. "Coordination Polymer Particles as Potential Drug Delivery Systems." ***Chem. Commun.*** **2010, 4737 - 4739.**

Micro- and nanoscale coordination polymer particles can be used for encapsulating and delivering drugs. In vitro cancer cell cytotoxicity assays showed that these capsules readily release doxorubicin, which shows anticancer efficacy. The results from this work open up new avenues for metal–organic capsules to be used as potential drug delivery systems.

7) M. Rubio-Martínez, I. Imaz, J. Puigmartí-Luis, D. Maspoch. "Metal-biomolecule nanoestructures." ***Revista de la Societat Catalana de Quimica*****, 2012, 11, 55-60.**

The miniaturization of metal-organic materials to the nanoscale is an emerging strategy for the development of new nanostructures with tailored compositions, structures and morphologies. These new nanomaterials, many of which are porous, may have a wide range of properties and consequently show promise for many practical applications, such as gas storage or separation, catalysis, sensors, drug-delivery and contrast agents. With this aim, our research group is currently developing a new approach using biomolecules to coordinate metal ions and create metal-biomolecule nanoarchitectures. These new bioinspired nanostructures will combine the properties of more conventional metal-organic nanomaterials (e. g. porosity) with the intrinsic characteristics of the biomolecules, such as biocompatibility, chirality and selective recognition capabilities. This paper presents the latest advances in the development of new synthesis methodologies and their use in producing the first metal-biomolecule nanostructures based on amino acids, such as aspartic acid (Asp) and cysteine (Cys).

Acknowledgements

És una barreja de sentiments seure i començar a escriure aquest agraïments. Per una banda estic feliç perquè ho he aconseguit, perquè he conegut a gent increïble i perquè he viscut moments únics e immillorables però d'altra banda em dona molta tristesa treure tot això del meu dia a dia. Em considero una persona molt afortunada ja que gràcies a aquesta tesis doctoral he pogut aprendre moltíssim en diferents àreas i sempre rodejada de gent molt bona i que d'alguna manera han dipositat el seu granet de sorra en aquest treball.

El primer agraïment és per l'Institut Català de Nanociència i Nanotecnologia, en especial al Prof. Jordi Pascual, per haver-me concebut la beca doctoral gràcies a la qual he pogut desenvolupar tota aquesta Tesis Doctoral.

Sens dubte l'agraïment més gran és pels meus directors de tesis, Daniel i Inhar, per donar-me la oportunitat de fer aquesta tesis, per guiar-me i ajudar-me en tot i més durant aquests anys i per haver estat uns excel·lents directors.

Un gracias especial a Inhar, por todos los buenos y no tan buenos momentos que hemos pasado juntos, por todas las horas en el laboratorio, en el servei, en el sincrotrón, en tu oficina y en los bares molones del Eixample. Has tenido más que aguante, me has guiado, me has escuchado, me has metido caña cuando tocaba y me has enseñado a hacer ciencia. Gracias por todos estos años!

També vull donar les gràcies de manera especial en Josep perquè ha estat un tercer director de tesis. Moltíssimes gràcies per totes les hores que hem estat al laboratori, per animar-me, per donar-me bons consells i per confiar en mi. Ha estat un plaer treballar amb tu!

Agrair a tots els coautors dels articles presentats en aquesta Tesis Doctoral per la seva professionalitat i ajuda, ja que sense ells aquest treball no hagués estat possible.

Gràcies també a tots els que hi van ser-hi al principi, Dani Ruiz i a tot el grup de NanosFun; en Fèlix Busqué per acollir-me al seu laboratori d'orgànica i en Jordi

Hernando per les hores que vam passar mesurant fluorescència, per ensenyar-me a quadrar els Origins i per ser el meu tutor en els inicis i en els finals d'aquesta tesis.

L'Agraïment més sentit és pel grup NanoUp, perquè han estat els millors companys que podia tenir. Hem viscut moments únics, feliços, tristos, divertits, tensos, estressants, curiosos.... tots inesborrables! Gracias a Carles, mi primer compi de laboratorio, por estar siempre ahí tanto en lo laboral como en lo personal, por ayudarme en todo y más de lo que se puede, por llevarme todo el papeleo del depósito, por sus bromas y humor matutino, por organizar súper excursiones, por sus noches musicales y por sus bailoteos en el Alfa. Gracias a las encapsuladoras, Mary, Nere, Sonia i Angels por ser la caña y llenar el laboratorio de energía, alegría y buen olor. Gràcies al MOF-inator team, Arnau, Xavi, Ivan, Abraham i Jordi per tota l'ajuda, idees, consells, ànims, per totes les birres que hem fet i per totes les hores boges que hem viscut. A big thank you al guiri Kyri of the grup for sharing your enthusiasm for science and your unique and inspiring view on things, for listening and giving advise when needed, and for helping me winning over my fears. És molt difícil escriure en aquest tros de paper tot l'apreci i amor que us tinc a cadascun de vosaltres. Gràcies per tots aquest anys i per fer-me el millor regal de despedida que podia tenir!

Gràcies al Servei de Microscòpia de la UAB, Onofre, Francesc, Pablo, Anna i Emma i al Marcos i la Belen del ICN, per totes les hores que hem passat junts i per l'ajuda constant.

Un queridísimo gracias al grupo de montañeros y escaladores, Pablo, James, Diana, Roberto, Max, Alex, Helena, Carla, Ariadna, Claudio, Arnau, Xavi, Carles, Joan y Maria, Fran y Maria, por todas las excursiones, por todos los lugares mágicos que hemos conocido, por todos los findes que hemos pasado y por todas las risas que nos hemos echado!!! Gràcies també a les noites de la uni, Eli, Anna i Noe, a Noemi por ser la mejor y más loca compañera de piso que se puede tener y a todos los que han estado siempre a mi lado, Laurita, Planes, Anna, Miguel y a mi princesita Noa.

Por último, agradecer a mi familia por todo el soporte y amor continuo que me han dado a lo largo mi vida y por estar siempre a mi lado. Y mi agradecimiento más profundo es para Cornelius, por toda la paciencia que ha tenido, especialmente estas últimas semana, por ayudarme, por soportarme, por animarme, por hacerme reír en los malos momentos y por estar siempre a mi lado. No tengo palabras para agradecerte todo lo que has hecho!

A Cornelius

Mamá, Papá,

Carlos y Anna

Chapter 1:

Introduction to Coordination Polymers made of Biomolecules

In this Chapter, the state-of-the-art of coordination polymers obtained from the association of biomolecules and metal ions is presented. We review the progress in this field providing an overview of current and future challenges for this new family of materials. Special attention is paid to the simplest biomolecules, amino acids and peptides, as they have been used extensively throughout this thesis. An overview of this type of coordination polymers (mainly focused on two- and three-dimensional frameworks) was reported in the review "*Metal-Biomolecule Frameworks (MBioFs)*", Chemical Communications 2011.

I. A brief history of coordination polymers

"Serendipity" means "happy accident" or "fortunate mistake", and that is how the first man-made coordination polymer (CP) was created in the early eighteenth century. Heinrich Diesbach, a German colormaker, discovered by accident a method for making the blue pigment known as Prussian Blue.[1] Despite being a valuable pigment used all over the world, its crystalline structure remained unknown for around 200 years.[2] Today, it is known that Prussian Blue is a CP with a 3-D cubic structure built up from the combination of heterometalic centres and cyanide organic ligands resulting in a mixed-valence polycyanide compound with a characteristic strong blue colour.

This example is the perfect illustration of the secret dream and permanent frustration of crystal engineers: that is, how to predict the final crystal structure resulting from the supramolecular assembly of metal ions and/or organic molecules. This challenge is in line with the provocative assertion of Maddox,[3] for whom "one of the continuing scandals in the physical sciences is that it remains impossible to predict the structure of even the simplest crystalline solids from knowledge of their composition". In the 80's, however, there were two crucial events that gave a real impulse to the design and prediction of new crystalline materials: on one hand, Prof. Lehn introduced the new concept of Supramolecular Chemistry;[4] and on the other hand, Prof. Etter[5] and Prof. Desiraju[6] reported several works for understanding the organisation of organic molecules through hydrogen bonds.

Since then, challenges in this field are not only the creation of new CPs, but also the understanding and prediction of their crystal structures. Prof. Wells strongly contributed to this challenge by reducing the description of crystal structures to networks formed by points with certain geometries (*e.g.* octahedral, tetrahedral, etc.) connected to other points through lines.[7] In 1989, Robson and co-workers applied Wells' approach to the design of CPs.[8] They proposed that CPs could be obtained by simply connecting centres (metal ions) having either a tetrahedral or an octahedral array of valences with rod-like connecting units (organic ligands).[9] Through this design approach, they proposed that new materials with unprecedented and interesting properties, such as porosity and catalysis, could be deliberately engineered. At that moment, nobody could imagine that this new concept would open a new world in the field of chemistry, materials science and nanotechnology. Today, twenty years later, the research in CPs continues its unstoppable growth, evidenced by the exponential increase of publications every year (Figure 1.1).

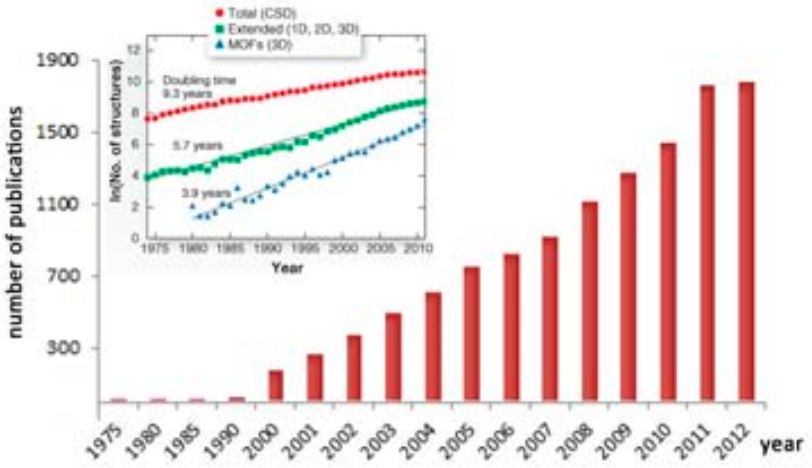

Figure 1.1. Graphic showing the increase number of published articles by year containing the words "coordination polymer" as entered, survey by SciFinder from 1975 to 2012. The inset shows the doubling time for the number of 1D, 2D and 3D structures reported in the Cambridge Structural Database.[10]

II. What is a coordination polymer?

CPs can be defined as hybrid inorganic-organic compounds extended in one-, two- or three-dimensions (1D, 2D or 3D, respectively) through coordination bonds. In other words, they are polymer structures built up from metal ions and/or inorganic clusters that are connected between them by organic ligands forming infinite arrays (Figure 1.2).[11]

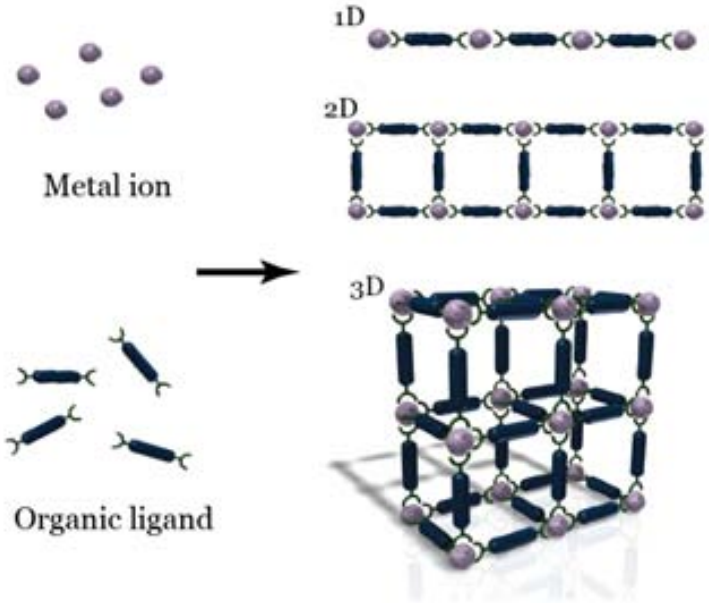

Figure 1.2. Schematic representation of the assembly of CPs showing 1D,2D and 3-D structures.

The final structure of a CP usually depends on: (i) the metal ion and its coordination geometry (Figure 1.3.a), which commonly varies from 2 to 6 in the case of transition metals or up to 10 in the case of rare earths; and (ii) the geometry and the binding modes of the organic ligand (Figure 1.3.b). Other weak interactions forces, such as hydrogen bonds, π-π stacking and van der Waals interactions, also have a strong influence in the formation of the final coordination structure.

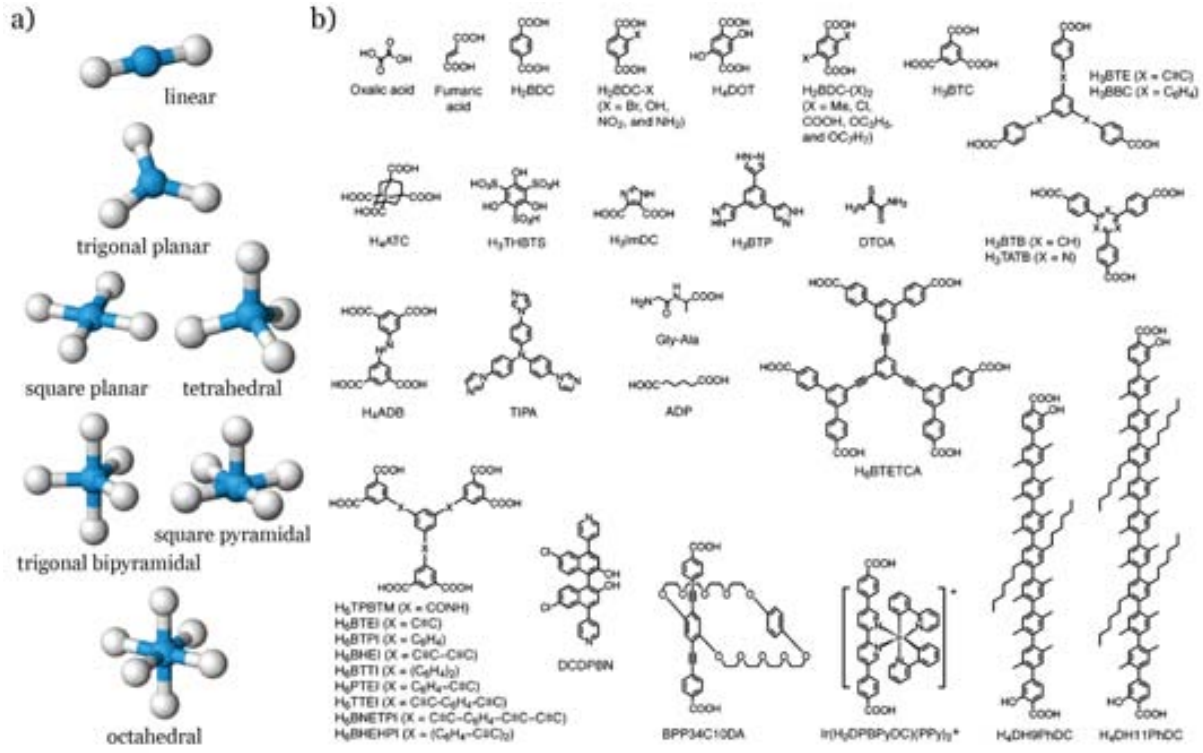

Figure 1.3. a) Common coordination geometries of transition metal ions. b) Archetypical organic molecules used as organic linkers to form CPs.

Since the publication of the first article by Prof. Robson in the 90's, thousands of new CPs are prepared every year due to their facile preparation, which generally involves diverse techniques such as hydro-/solvo-thermal, microwave, mechanochemistry and sonochemistry. This methodological variety, together with the countless available combinations of metal coordination geometries and organic ligands, gives rise to an infinite number of possible combinations with different compositions and topologies, from the simplest and most common 1D-linear, zigzag, helices, ladders and tubs geometries to the most complex 3-D architectures and planar coordination polymers. These unlimited combinations in terms of metal nodes and organic linkers together with the possibility to modify the organic ligands offer many possibilities to the synthetic chemist for the formation of new networks with novel architectures and advanced applications.[12,13] Today, this versatility makes possible the generation of crystalline structures that contain empty spaces, conferring porosity to these materials. These porous CPs are commonly known as metal-

organic frameworks (MOFs). MOFs can exhibit high BET surface areas (up to 6.500 m^2/g)[14] as well as tunable pore size and functionality, and they can host guest molecules within their cavities. Therefore, porous MOFs offer great potential for storage of hazardous gases such as CO and CO_2, fuel applications with H_2 or CH_4,[15] catalysis,[16] sensing,[17] biomedicine,[18] and gas-liquid separation (*e.g.* CO_2/CH_4,[19] xylene and alkane isomers).[20]

Table 1.1. Representative applications of CPs. (bdc, benzene-1,4-dicarboxylic acid; PF, pyridine-ferrocene; TCNQ, tetracyanoquinodimethane; azpy, phenylazopyridine; bhc, benzene hexacarboxylate; bpy, bipyridine; H_4DOBDC, dihydroxyterephtalic acid; NU-110, MOF from Northwestern University composed by copper and tcepbb ligand; tcepbb, 1,3,5-tris[(1,3-carboxylic acid-5-(4-(ethynyl)phenyl))butadiynyl]-benzene).

Applications	Compound	Property	Network	Ref.
Luminescence	[Zn(1,2-bdc)](H_2O)	Fluorescence arises from the intraligand (π-π^* transitions)	2D	21
Redox Activity	$AgPF_6(CH_3CN)_2$	Ferrocene based bridging ligands with metal ions leads the formation of redox-active CP	1D	22
Conductivity	CuTCNQ	Electric field –induced bistable switching from a high resistance to a low resistance state at a critical threshold potential	2D	23
Magnetic	$Fe_3(HCOO)_6$	Porous magnet with guest-modulated magnetic properties	3D	24
Spin crossover	$Fe_2(azpy)_4(NCS)_4$	Reversible uptake and release of guest molecules and contains electronic switching centres that are sensitive to the nature of the adsorbed guests	2D	25
Contrast Agent	$Gd_2(bhc)(H_2O)_6$	Relaxativity values one order of magnitude higher than the commercial available CA	3D	26
Catalysis	$Cd(bpy)_2(NO_3)_2$	Heterogeneous catalysis the cyanosilylation of aldehydes and ring opening of meso-carboxylic anhydrides	2D	27
Chirality	$Zn_4O(CO_2)$	Linking of organic optically active dilocular hosts inside of the MOF leading to the formation of a chiral stationary phase for carrying out the separation of enantiomers	3D	28
Ion exchange	$Zr_6O_4(OH)_4(bdc)_6$	Ion exchange of Zr(IV) by Ti(IV) increasing the CO_2 uptake by up to 81% at 273k	3D	29
Drug delivery	Fe(H_4dobdc)	Ibuprofen encapsulation by impregnation and slower release thanks to the flexibility of the structure	3D	30
Gas adsorption	NU-110	Ultrahigh porosity MOF using a supercritical CO_2 activation technique	3D	14

In addition to the inherent porous properties coming from the structures, CPs also shows the advantage of incorporating the functionalities of the metal ions as well as the organic ligands. For example, luminescent CPs can be created by using lanthanide ions

and/or organic chromophoric ligands, such as pirazine or quinoxaline, which absorb light and then pass the excitation energy to the metal ion.[31,32] Other examples are the use of paramagnetic ligands to create magnetic CPs or the incorporation of charge-transfer ligands, such as tetracyanoquinodimethane (TCNQ), to form CPs with redox activity.[33] Table 1.1. shows a brief but representative list of applications that this new class of functional materials can offer.

As a last advantage, the great versatility of CPs also opens the possibility to design them integrating more than one property, thus creating multifunctional materials. Some examples of multifunctional CPs include those that combine luminescence and conductivity properties,[34] catalysis and luminescent properties,[35] and porosity and magnetic-responsive [36] or photo[37] activity properties.

III. Our investigation: Coordination polymers made of biomolecules

As state above, the selection of the organic ligand is very important for defining the final characteristics, properties and applications of CPs. In this sense, for example, there are some potential applications (*e.g*. drug-delivery and intracellular imaging) in which it can be beneficial that MOFs are constructed from organic ligands that are biologically and environmentally compatible. A potential type of bio-friendly organic ligands can be the family of biomolecules that are present in Nature. The use of biomolecules as organic ligands offers several advantages for constructing CPs:

1. Simple biomolecules, including amino acids, nucleobases, sugars, and others, are readily and naturally available in quantities and at prices amenable to preparing bulk quantities of materials.
2. Biomolecules can lead to biologically compatible CPs.
3. Biomolecules are structurally diverse. They can be either structurally rigid or flexible; aspects that impact on the functional nature of the resulting CPs.
4. Biomolecules can have many different metal-binding sites. Consequently, they can exhibit multiple possible coordination modes, a feature that increases the potential structural diversity of CPs.
5. Many biomolecules are chiral. Therefore, they can be used to construct chiral CPs, which may have interesting recognition, separation, and catalytic properties.

6. And finally, many biomolecules have intrinsic self-assembly properties, which can be used to direct the structure and function of CPs.

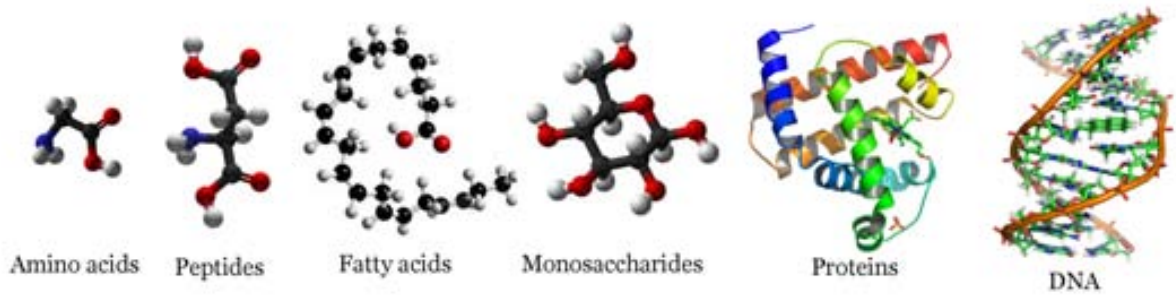

Figure 1.4. Representation of the different families of natural biomolecules present in humans, animals and plants.

In Nature, there are thousands of different types of biomolecules (Figure 1.4), which basic units can be grouped in four main families (Table 1.2): nucleic acids, saccharides, lipids and amino acids. Although the interest on using these biomolecules to construct CPs is relatively recent, a detailed study of the literature and of the structural databases done in this Thesis has been reported in the review "***Metal-Biomolecule Frameworks (MBiOFs)***". This review illustrates that a significant number of CPs using different biomolecules has already been reported. In particular, it focuses on CPs, mainly crystalline, made of biomolecules (also known as metal-biomolecule frameworks or MBiOFs) that shows 2- and 3D structures. It includes CPs made of amino acids, peptides, proteins, nucleobases, saccharides and other "small" biomolecules. In the next sections, a brief discussion of these CPs is given, focusing more attention to the use of amino acids and peptides. These two types of biomolecules have been selected in this Thesis to develop novel functional metal-biomolecule CPs at the nanometer length scale.

Table 1.2. The four major classes of biomolecules; each one have their own characteristic monomers and corresponding polymers.

Monomer	Polymer
Lipid	Diglyceride, triglyceride
Monosaccharide	Polysaccharide
Amino acid	Polypeptide (protein)
Nucleotide	Nucleic acid (DNA, RNA)

III.1. Coordination polymers made of nucleobases

Nucleic acids, nucleobases and nucleotides are among the most important biomolecules due to their role in the storage and transmission of genetic information. Nucleic acids - deoxyribonucleic acid (DNA) and ribonucleic acid (RNA)- are macromolecules formed by the union of basic units called nucleotides through phosphodiester bridges. Each nucleotide is constituted by a pentose, a molecule of phosphoric acid and nitrogenous bases. These nitrogenous bases, which are called nucleobases, show ideal characteristics to be used as bio-linkers to construct CPs because: i) they have rich H-bonding capabilities and ii) they have accessible nitrogen and oxygen electron lone pairs in their structures that are rich metal binding sites (Figure 1.5.a).

Thus far, CPs constructed from Adenine (Ade) have been the most reported.[38] The first example was presented by Prof. Davidson in 1964, who reported the use of 9-methyladenine to construct 2-D frameworks by linking Ag(I) ions using the N1, N3 and N6 coordination modes.[39] Since then, several other CPs made of Ade have been reported; some of them with remarkable CO_2 adsorption capacities.[40] An illustrative example was recently reported by Rosi and co-workers, who described the first 3-D permanently porous framework built up from infinite Zn(II)-Ade columns interconnected via multiple 2,2'-Bipyridyl-3,3'-dicarboxylate (BPDC) linkers. This framework called Bio-MOF-1 shows large 1-D channels that are stable after removal of guest solvent molecules (Figure 1.5.b). This material exhibits a high surface area (BET: 1700 $m^2 \cdot g^{-1}$) and an anionic nature, so it could be used to store cationic drug molecules. Also, its pores could be easily modified for particular applications simply via cation exchange.[41]

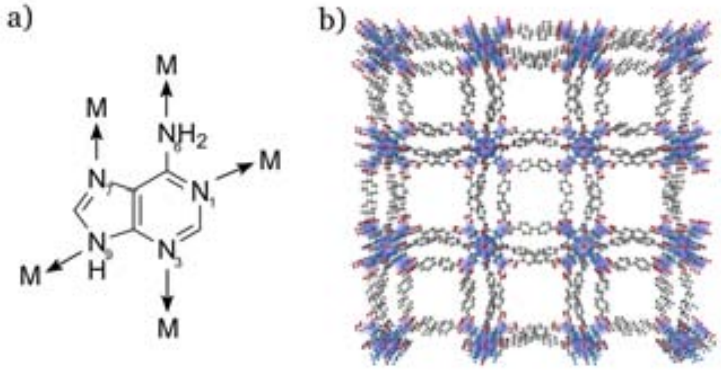

Figure 1.5. a) Potential coordination sites of Ade. b) First 3-D permanently porous frameworks structure (bio-MOF-1) made of Ade, with formula $[Zn_8(Ade)_4(bpdc)_6O \cdot 2Me_2NH_2] \cdot 8DMF \cdot 11H_2O$. (Zn, red; N, blue; C, black;).

III.2. Coordination polymers made of saccharides

Saccharides, carbohydrates, monosaccharide, oligosaccharides, polysaccharides are naturally occurring substances that have a composition according to the formula $(CH_2O)_n$. They perform numerous roles in living systems like energy storage (*e.g.* starch and glycogen) and as structural components (*e.g.* cellulose in plants). From a chemical standpoint, monosaccharides can be described as polyhydroxy aldehydes (aldose) and polyhydroxy ketones (ketose) groups that would coordinate strongly with metal ions. However, oxidation of these saccharides under acidic conditions leads to the formation of carboxylic groups. Some of these substances (*e.g.* glucaric acid and galactaric acid that results from the oxidation of sugar and lactose, respectively) were used by Robson and co-workers to produce a series of CPs.[42,43]

More recently, a very exciting study reported by Stoddart and co-workers demonstrated the possibility of using γ-cyclodextrin as a multidentate organic ligand to create functional CPs.[44] The authors reported two new metal-saccharide frameworks using 8 units γ-cyclodextrin connected into cubes through alkali metal ions, leading to porous structures with formula γ-(cyclodextrin)$(MOH)_2$ (where M is K or Rb) and with BET surface areas of 1220 $g{\cdot}cm^{-3}$.

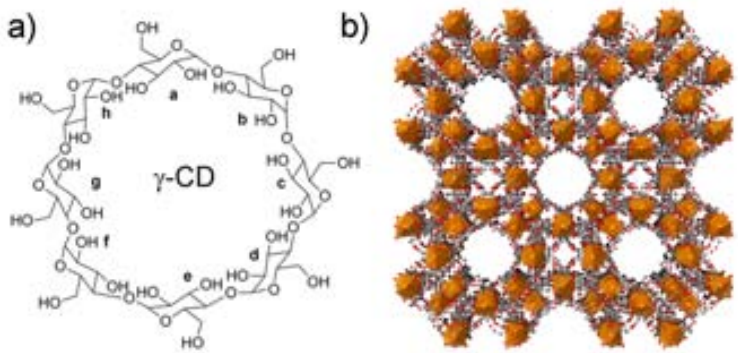

Figure 1.6. a) Representation of the γ-cyclodextrin composed by eight asymmetric D-glucopyranosyl residues. b) Porous structure of γ-(cyclodextrin)$(KOH)_2$.

IV. Our biomolecules of choice: Amino Acids and Peptides

IV.1. Amino acids: elemental molecules in life

Amino acids (AAs) are molecules with the general formula NH_2CHRCO_2H, where NH_2 and CO_2H are the amino and carboxylic acid groups, respectively, and R is the organic side chain (Figure 1.7). The first AA was discovered in the early 19th century by the French chemists Louis-Nicolas Vauquelin and Pierre Jean Robiquet, who isolated a compound found in asparagus: asparagine. Today, 20 natural AAs with their own unique size and functionality are known. Humans can synthesize 11 of them and the other 9, which are called essential AAs, are consumed in our diet. There are different ways to classify them. For example, Timberlake used a method based on the polarity of their functional group (polar and non-polar), whereas Koolman based their classification on the structure of the side of the AAs (alphatic, sulphur-containing aromatic, neutral, acidic, basic and imino acid).[45] Importantly, AAs link together via amide bonds to form peptides and proteins that serve important biological functions.

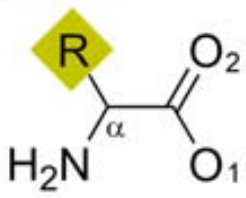

Figure 1.7. Schematic illustration of the common skeleton of a natural AA.

IV.1a. Coordination modes of Amino Acids

All natural AAs consist of a α-carbon atom onto which an amino group and a carboxylic acid group are attached. These free amino and carboxylic groups can bind metal ions, making AAs suitable building blocks for the construction of CPs. In fact, metal-AA interactions have been intensely studied because it is estimated that approximately half of all proteins contain a metal ion.[46,47] For example, a quarter part of proteins require the presence of a metal ion to carry out their functions, such as storage and transport of enzymes and signal transductions.[48,49]

In general, AAs form the typical five-membered chelate ring (also called O,N-chelating mode), leading to the formation of metal–AA chelates or discrete polynuclear clusters. However, in some cases, the α-carboxylate group can coordinate metal ions via bi- or tridentate bridging modes, thereby extending the dimensionality of the resulting metal-AA structure and forming a CP (Figure 1.8). This coordination was observed by Fleck and co-workers, who constructed a 2-D CP when combined the smallest amino acid Glycine (Gly) with Ni(II), Mn(II) and Co(II) ions in an stoichiometric ratio of 2:1.[50] In these 2-D structures, each octahedral metal ion was linked to another four metal ions by four Gly ligands, adopting the μ-O_1:O_2 coordination mode reported in Figure 1.8.

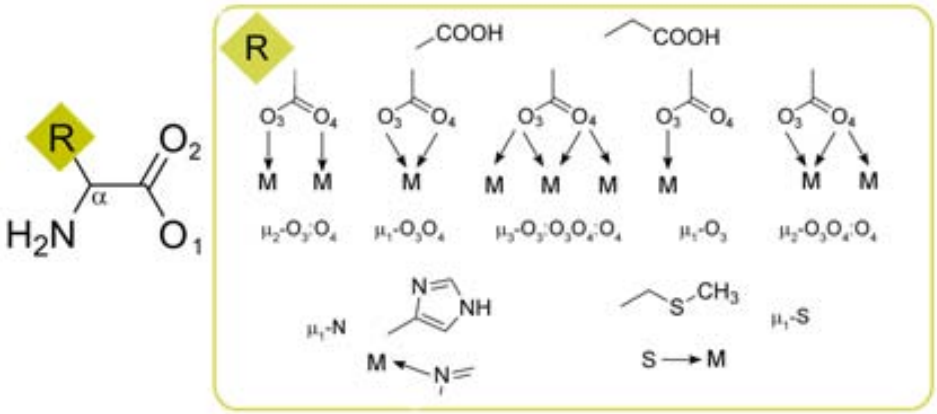

Figure 1.8. Schematic representation of AAs showing the potential coordination modes for metal ions.

In addition, the R group of the AAs can bring additional metal binding groups, such as β–carboxylate groups of aspartic (Asp) and glutamic (Glu) acids, the imidazole ring of histidine (His), the thiol or thiolether groups of cysteine (Cys) and methionine (Met), respectively, or the phenol ring of tyrosine (Tyr). These binding groups, in addition to serving as the metal binding sites in proteins, can be used for further bridging metal ions in space and thus increasing the dimensionality of metal ion-AA CPs (Figure 1.9). For instance, Lu *et al.* have used the ability of thioether groups of Met to bind to Ag(I) metal ions to prepare a homochiral heterobimetallic BioCp, $[Ag_3Cu_3(L\text{-}Met)\cdot 6(NO_3)_3(H_2O)_3]\cdot 7H_2O$.[51] In this structure, L-Met ligands bind to two different types of metal ions: (i) to Cu(II) ions through the hard amino and carboxylate sites via μ2-N1O1:O2 and simple O,N-chelating modes, and (ii) to Ag(I) ions through the soft monodentate thioether groups. The distinct coordination preference of metals to specific binding sites on the AA ligand leads to the assembly of a 3-D MBioF constructed from 1-D helical building blocks, featuring homochiral channels that host 1-D chains of water molecules.

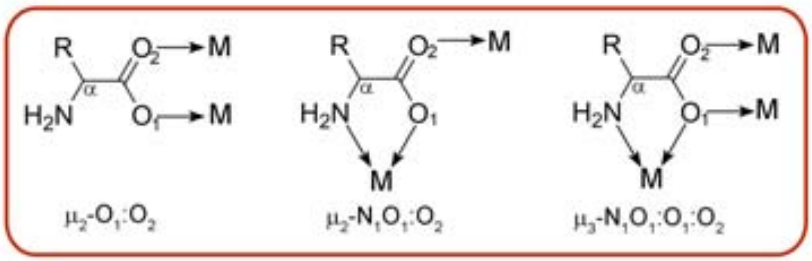

Figure 1.9. Schematic illustration of the potential coordination that the side chains can exhibit.

IV.1b. Extended Metal-AA structures

In the literature, there are essentially three major types of metal-AA CPs. These CPs can be classified according to their composition: i) metal ions and natural AAs; ii) metal ions, natural AAs, and additional bridging anions and polydentate organic ligands and iii) metal ions and chemically-modified natural AAs (e.g. AAs modified with additional metal-binding groups). In the last two classes, the presence of the organic ligands, anions, and additional metal binding groups usually serves to increase the dimensionality of the metal ion-AA framework.

1. **Metal ions/natural AAs:** As illustrated in the examples shown in the previous section, CPs can be constructed from simply linking metal ions by natural AAs. For example, Anokhina and Jacobson reported the synthesis of homochiral 1-D nickel aspartate oxide helical chains formulated as $[Ni_2O(L\text{-}Asp)(H_2O)_2]\cdot 4H_2O$.[52] In these chains, each Asp ligand coordinates five Ni(II) ions through its carboxylate and amino groups adopting the μ_2-N_1O_1:O_2 and μ_3-O_3:O_3:O_4 modes. By increasing the pH of the reaction, these helical chains were connected by additional $[NiAsp_2]^{-2}$ units to generate a 3-D porous chiral framework, $[Ni_{2.5}(OH)(L\text{-}Asp)_2]\cdot 6.55H_2O$, that exhibits 1-D channels with dimensions of 8 x 5 Å (Figure 1.10). Another example is the chiral copper aspartate nanofibers described in the article *"Amino acid-based metal-organic nanofibers"* presented in the Chapter 3 of this Thesis. In this system, the cooper is coordinated to the α- carboxylate group leading to formation of a CP. In some cases, this α-carboxylic acid can coordinate with metal ions *via* bi- (μ-O_1:O_2)[53] or tridentate (μ-N_1:O_1:O_2 or μ-N_1:O_1:O_2:O_3)[52] bridging modes and extend the frameworks to 2-D or 3-D structures as shown in Figure 1.10.

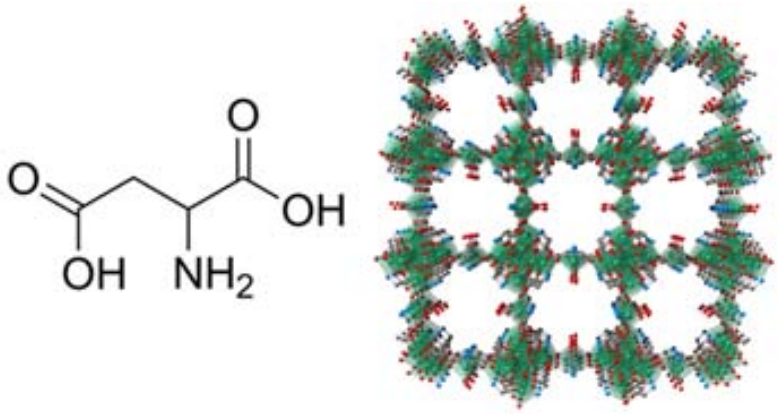

Figure 1.10. Projection of the $[Ni_2O(L\text{-}Asp)(H_2O)_2]\cdot 4H_2O$. (Ni, green; O, red; N, blue; C, gray).

2. **Metal ions/natural AAs/additional ligands:** The dimensionality of the metal-AA CPs can be increased using additional organic ligands or inorganic anions/clusters that act as linkers. Common organic ligands used to extend to 2-D or 3-D structures are the family of bipy-type ligands. For example, Rosseinsky and co-workers reported the synthesis of a 3-D pillared porous CP using the 4,4'-bipyridine as the additional ligand. In this system, Ni(II) ions are linked by Asp ligands *via* μ-O_1:O_2 and μ-O_3:O_4 coordination modes (Figure 1.8), leading to the formation of Ni(L-Asp) layers that are connected by the 4,4'-bipy linkers.[54] Another example reported by Xu and co-workers is the formation of a 3-D homochiral CP formed by connecting Cu(II) and Proline (Pro) chains through the anion polyxometalate $[BW_{12}O_4O]^{5-}$ (Keggin clusters) as the additional ligand (Figure 1.11). The resulting structure has helical channels with dimensions of 11·7 Å.[55]

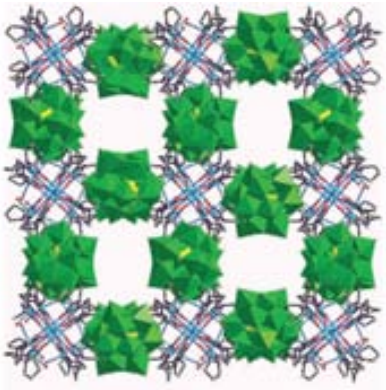

Figure 1.11. The 3D open-framework structure composed of copper-proline polymer chains covalently linked to Keggin polyoxo-anions. (B, yellow; O, red; N, dark blue; Cu, blue; W, green; C, gray) Figure adapted from reference 55.

3. **Metal ions/ AAs with chemical modification:** To increase the dimensionality of the CP, natural AAs can be also synthetically modified by introducing different functional groups to the AAs skeleton. For example, modifying the phenyl ring of phenylalanine (Phe) with a tetrazole allowed the construction of 3-D frameworks rather than the 1-D and 2-D structures that Phe tends to form (Figure 1.12). In this way, the metal ions can coordinate to the Phe-tetrazole through the carboxylate and amino groups, adopting the typical μ-N_1:O_1:O_2 mode (Figure 1.8) and through the tetrazole moiety.[56] Using a similar approach, Wang and co-workers synthesized three new 2-D chiral CPs by introducing different functionalities in the phenyl ring of Phe and tyrosine (Tyr).[57]

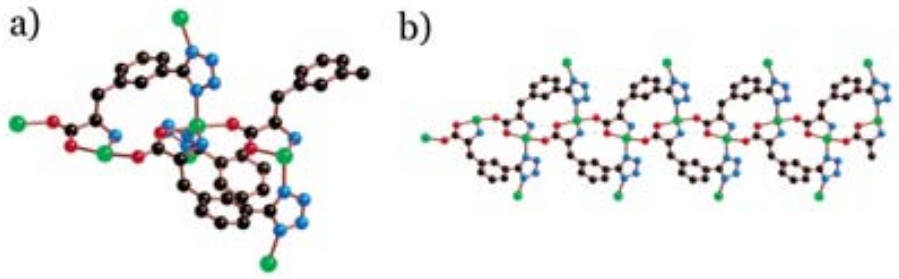

Figure 1.12. a) Part of the mono[(*S*)-5-(3-tetrazoyl)phenylalaninato]-zinc(II), [Zn(*S*))-TPA)] structure showing the 5-coordinate zinc centre bound to four (*S*)-TPA ligand, one of which is chelating (Zn, green; O, red; N, blue; C, black;). b) Projection of the zigzag chain of zinc atoms links to four equivalent parallel chains through bridging tetrazole groups. Figure adapted from ref 56.

IV.2. Peptides: a promising new class of multitopic ligands

The beginning of peptide chemistry started in 1901 with the preparation of the first dipeptide glycylglycine (GlyGly) by hydrolysis of the diketopiperazine of glycine.[58] Peptides are short oligomers composed of AAs linked by peptide bonds and therefore, constitute the rational second step of complexity to evaluate the role of biomolecules as bridging ligands. This peptide bond is formed between the carboxylic group of one AA, which reacts with the amino group of another, leading to the formation of amide group and the loss of a water molecule (Figure 1.13).

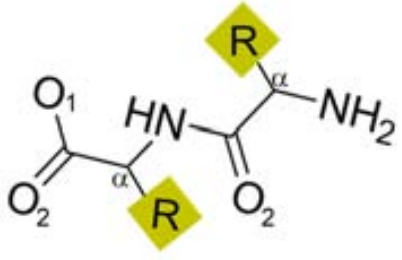

Figure 1.13. Schematic illustration of the common skeleton of peptides.

IV.2a. Coordination modes of peptides

As shown in Figure 1.14, peptides always have an amino terminus as well as a carboxylic acid terminus, both of which can coordinate metal ions. The terminal amino group usually coordinates to metal ions in a monodentate or chelating fashion, in which the oxygen atom of the neighbouring amide group also coordinates to the same metal ion, forming a five membered chelate ring (Figure 1.14). Note that peptides can also adopt a similar O,N-chelating mode to that observed for AAs. At the opposite peptide terminus, the carboxylate group can coordinate to metal ions in any of the well-known coordination modes of carboxylic acids (Figure 1.8).

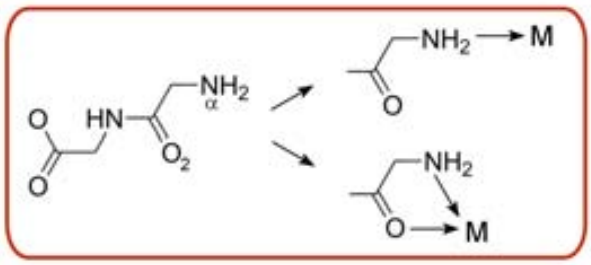

Figure 1.14. Schematic illustration showing the possible coordination modes of peptides.

It is also very important to highlight here that peptides offer endless possibilities to incorporate more metal binding groups to their structure by simply adding suitable AAs to their sequence. For example, the incorporation of more carboxylate groups can be achieved simply by synthesizing peptides made from constituents like Aspartic acid(Asp) or Glutamic acid(Glu). This versatility opens the possibility to access an unlimited number of flexible polydentate bio-related ligands that can be employed to form functional 2- and 3-D metal–peptide CPs.

IV.2b. Coordination polymers made of peptides

One of the first examples of CPs made of peptides was published by Takayama and coworkers, who synthesized a series of CPs built up from the shortest dipeptide GlyGly and Zn(II) and Cd(II) as metal ions. At pH 6, these authors obtained 2-D BioCPs formulated as $[M(GlyGly)_2]\cdot 2H_2O$ (where M is Zn(II) or Cd(II)), which are constructed by connecting each octahedral metal ion to four other metal ions through four bridging GlyGly ligands. Each GlyGly ligand bridges two metal ions through the terminal carboxylate group in a monodentate mode and the terminal amino group through the

aforementioned five-membered chelate ring. By increasing the pH to 9, a novel 2-D BioCPs with formula $[Cd(GlyGly)_2]\cdot H_2O$ was formed. In these layers, the terminal carboxylate groups of GlyGly ligands bind to two Cd(II) ions, and their amino groups coordinate to another Cd(II) ion in a monodentate mode. As a consequence, each Cd(II) ion is linked to six other Cd(II) ions by four GlyGly ligands.

Since this publication other peptide-derived BioCPs made from dipeptides have been described. Among them, the most notable example is the metal-peptide $[Zn(GlyAla)_2]$, which was reported by Rossensky and co-workers.[59] In this network, each GlyAla ligand coordinates to the tetrahedral Zn(II) ions by the terminal carboxylate group of the Ala residue and the terminal amino groups of the Gly residue, both in a monodentate mode. The layers are then aligned in an A–A fashion by hydrogen bonds to form a porous structure with square- shaped 1-D pores (solvent-accessible volume: 532.7 A^3 per unit cell at 100 K (28%)). Remarkably, this porous CP has an adaptable porosity, in which its crystal structure undergoes reversible structural changes after desorption/reabsorption of solvent molecules.

Up until today, there are not many examples of CPs constructed from peptides of more than two AA. In fact, there are only two examples using longer amino acids sequencies. One example is the 2-D CP with the formula $[Cd(GlyGlyGly)_2]\cdot 2H_2O$, which was published by Marsh group.[60] The second example was more recently reported by Yagui and co-workers, where a double ladder system based on crystalline fibers were obtained by linking the pentapetide (NH_2-Glu-pCO_2Phe-pCO_2Phe-Ala-Gly-OH) with cadmium acetate (Figure 1.15).[61]

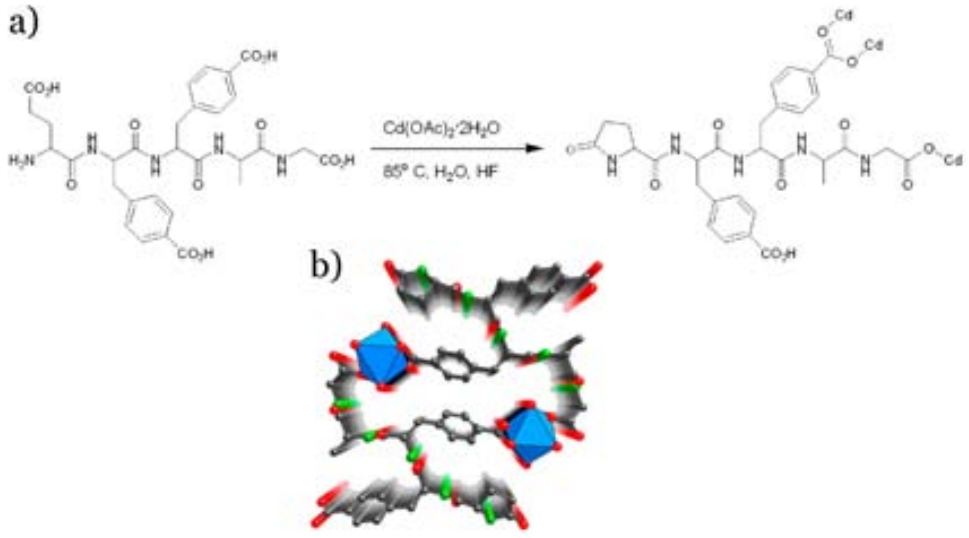

Figure 1.15. a) Reaction scheme for the formation of metal-peptide double ladders, Cd(2-pyrrolidone-pCO_2Phe-pCO_2Phe-Ala-Gly)(H_2O). b) View of the crystalline 1D framework (Cd, blue; C, gray; O, red; N, green). Figure adapted from reference 61.

IV.3. Coordination polymers made of proteins

Proteins are polymeric biomolecules composed of AAs sequences forming flexible 3-D structures that usually perform highly specialized functions in living organisms. Despite having binding modes provided by the AA constituents, there are not many examples of CPs based on them in the literature. A recent study reported by Chmielewski *et al.* proved that complex bio-related building blocks such as collagen can be used to fabricate coordination nanofibers.[62] The authors showed that collagen-based peptides (L64) can be designed and self-assembled into fibrilar scaffolds through different metal ions. On the other hand, the studies of Tezcan and co-workers, from California University, could be considered a first step towards CPs constructed with proteins.[63] In these studies they synthesized the first porous protein superstructures constructed by controlling protein-protein interactions through metal coordination. The protein framework exhibits a set of hexagonal channels between 2 and 6 nm of diameter and was created from two proteins based on the four-helix bundle hemeprotein cytochrome cb_{562} and connected through Ni (II) and Zn (II) ions (Figure 1.16).

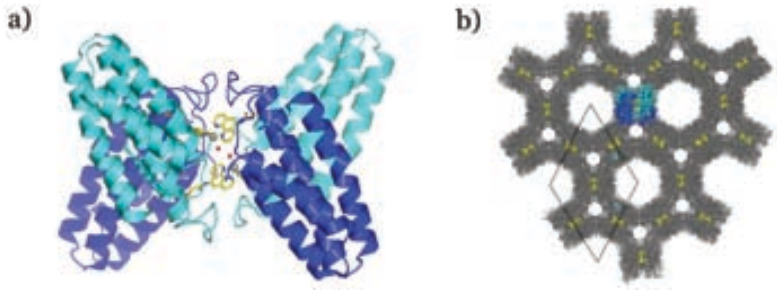

Figure 1.16. a) Representation of the hemeprotein cytrochrome cb562. b) The porous structure resulted from metal-directed protein self-assembly.

V. Properties and applications of coordination polymers made of biomolecules

A wide range of promising properties and applications can be obtained by taking advantage of the multiple inorganic and biomolecular building blocks that can be combined to prepare CPs. As a subclass of CPs, CPs made of biomolecules can incorporate their intrinsic properties (*e.g.* chirality, biocompatibility and flexibility), allowing the preparation of porous chiral structures, biocompatible materials and novel flexible storage materials.

Biomolecules can act as chiral ligands to induce the formation of homochiral CPs. This property together with the adsorption capabilities opens the possibility to design CPs for heterogeneous asymmetric catalysis and enantioselective separation.[64] For example, in 2006, Rosseinsky and co-workers showed that $[Ni_2(L\text{-}Asp)_2(4,4'\text{-}bipy)]\cdot guest$ exhibits significant enantioselective sorption capabilities of small chiral diols,[54] with levels of enantioselectivity as high as 53.7% ee (enantioselective excess) for the sorption of 2-methyl-2,4-pentane-diol. Recently, the same authors also introduced Brønsted acidic –COOH sites into the same family of chiral porous MBioCPs via post-synthetic modification for heterogeneous asymmetric catalytic methanolysis of *cis*-2,3-epoxybutane.[65] Treatment of $[Ni_2(L\text{-}Asp)_2(4,4'\text{-}bipy)]\cdot guest$ and $[Cu_2(L\text{-}Asp)_2(bpe)]\cdot guest$ (where bpe is 1,2-bis(4-pyridyl)ethane) with HCl in Et_2O affords the protonated $[Ni_2(L\text{-}Asp)_2(4,4'\text{-}bipy)\cdot(HCl)_{1.8}(MeOH)]$ and $[Cu_2(L\text{-}Asp)_2(bpe)\cdot(HCl)_2\cdot(H_2O)_2]$ frameworks. Both resulting materials are active as heterogeneous asymmetric catalysts for the methanolysis of *rac*-propylene oxide. Kim and Fedin *et al.* also studied the enantioselective separation and catalytic properties of $[Zn_2(bdc)(L\text{-}lac)(DMF)\cdot DMF]$ (where bdc is 1,4-benzendicarboxylic ligand and L-lac is L-lactic acid).[66] When this CP is stirred in the presence of racemic mixtures of sulfoxides, the resulting material shows high enantioselective adsorption capability to sulfoxides with smaller substituents. The ee values for these adsorbed sulfoxides were between 20 and 27% with excess of the *S* enantiomer in all cases.

The molecular storage-release capabilities and potential biocompatibility of CPs made of biomolecules allow these materials to be exploited as novel delivery systems for active species (e.g. drugs, vaccines, genes, etc.) as well as contrast agents in the fields of medicine, pharmaceutics and cosmetics. Thus far, however, such biomedical applications have not been fully explored, and only some examples of CPs made of biomolecules that can adsorb and release drugs have been reported. For instance, Rosi and co-workers demonstrated controlled drug release of $[Zn_8(Ade)_4(bpdc)_6O\cdot 2Me_2NH_2]\cdot 8DMF\cdot 11H_2O$.[41] This CP is modestly stable in water and biological buffers for several weeks; however, its toxicity is still unknown. Procainamide, which is a cationic drug molecule, was loaded into the pores of material via cationic exchange with the dimethylammonium cations that initially reside inside the pores (Fig. 1.17.). In addition, procainamide release was monitored in PBS buffer, and it was shown that cation exchange of drug molecules with cations within the buffer likely played a role in the drug release process. It was shown that 0.22 g of procainamide per grams of CP was loaded and that drug release was completed after ~three days. When the active specie to be released is a naturally available molecule, this molecule can also be used as an organic ligand to construct the CP. As a

consequence, the CP can release the active specie at the specific place where it degrades. This approach was developed by Serre and co-workers to fabricate a therapeutically active MBioF from the association of non-toxic Fe(III)-Fe(II) (LD_{50} = 30 $g \cdot kg^{-1}$) and nicotinic acid (pyridine-3-carboxylic acid, also called niacin or vitamin B3).[67] Since the resulting material degrades rapidly under physiological conditions, the release of nicotinic acid was achieved within few hours.

Flexibility is sometimes a hindrance to the preparation of robust porous frameworks, but it can also be an excellent characteristic for designing flexible porous frameworks, which can serve as responsive and adaptable materials.[68,69] A first example of this class of materials has been recently reported by Rosseinsky and co-workers,[59] who use a flexible GlyAla dipeptide to synthesize the adaptable porous $[Zn(GlyAla)_2]\cdot(solvent)$. Once desolvated, neighbouring peptides within the structure hydrogen bond together, which in turn occludes the pores, as confirmed by the inability of the material to adsorb N_2 and H_2 at 77 K. However, these pores gradually and cooperatively open when triggered by small molecules having polar bonds, including water, MeOH and CO_2. This behaviour is a direct consequence of the flexibility of GlyAla, because the torsional degrees of freedom of this dipeptide ligand, which strongly depend on their interaction with guest molecules, allow the methyl group to impact the accessible void volume.

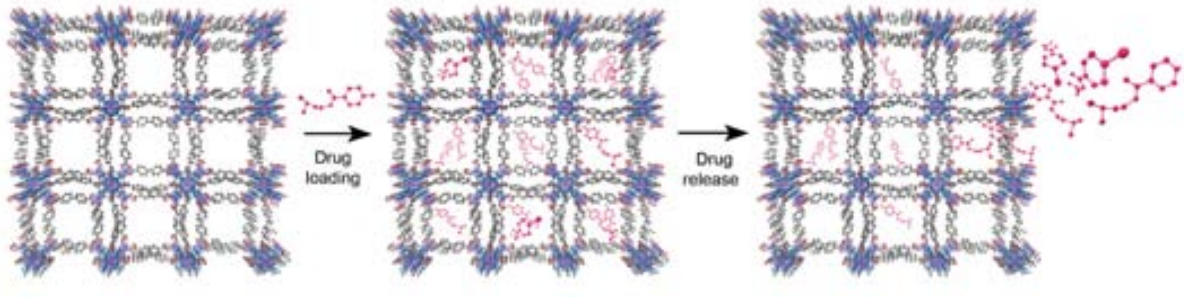

Figure 1.17. Schematics showing the use of MBioFs for encapsulating and releasing therapeutic species (illustrated by $[Zn_8(Ade)_4(bpdc)_6O\cdot 2Me_2NH_2]$). (Zn, blue; C, gray; O, red; N, green; C, grey).

VI. References

(1) Kraft, A. ON THE DISCOVERY AND HISTORY OF PRUSSIAN BLUE. *Bull Hist Chem* **2008**, *33*, 61-67.

(2) Buser, H. J.; Schwarzenbach, D.; Petter, W.; Ludi, A. The Crystal Structure of Prussian Blue: $Fe_4[Fe(CN)_6]_3xH_2O$. *Inorg. Chem.* **1977**, *16*, 2704–2710.

(3) Maddox J. Crystals from First Principles. *Nature* **1988**, *335*, 201–201.

(4) Lehn, J. M. Cryptates: Inclusion Complexes of Macropolycyclic Receptor Molecules. *Pure Appl. Chem.* **1978**, *50*, 871–892.

(5) Etter, M. C. Encoding and Decoding Hydrogen-Bond Patterns of Organic Compounds. *Acc. Chem. Res.* **1990**, *23*, 120–126.

(6) Desiraju, G. R. *Crystal Engineering: The Design of Organic Solids*; Materials science monographs; Elsevier: Amsterdam ; New York, 1989.

(7) Wells, A. F. *Three-Dimensional Nets and Polyhedra*; Wiley monographs in crystallography; Wiley: New York, 1977.

(8) Hoskins, B. F.; Robson, R. Design and Construction of a New Class of Scaffolding-like Materials Comprising Infinite Polymeric Frameworks of 3D-Linked Molecular Rods. A Reappraisal of the Zinc Cyanide and Cadmium Cyanide Structures and the Synthesis and Structure of the Diamond-Related Frameworks $[N(CH_3)_4][Cu^{I}Zn^{II}(CN)_4]$ and Cu^{I}[4,4',4",4"'-tetracyanotetraphenylmethane] $BF_4xC_6H_5NO_2$. *J. Am. Chem. Soc.* **1990**, *112*, 1546–1554.

(9) Hoskins, B. F.; Robson, R. Infinite Polymeric Frameworks Consisting of Three Dimensionally Linked Rod-like Segments. *J. Am. Chem. Soc.* **1989**, *111*, 5962–5964.

(10) Furukawa, H.; Cordova, K. E.; O'Keeffe, M.; Yaghi, O. M. The Chemistry and Applications of Metal-Organic Frameworks. *Science* **2013**, *341*, 976-984.

(11) Batten, S. R.; Champness, N. R.; Chen, X.-M.; Garcia-Martinez, J.; Kitagawa, S.; Öhrström, L.; O'Keeffe, M.; Suh, M. P.; Reedijk, J. Coordination Polymers, Metal–organic Frameworks and the Need for Terminology Guidelines. *CrystEngComm* **2012**, *14*, 3001-3004.

(12) Serre, C.; Millange, F.; Thouvenot, C.; Noguès, M.; Marsolier, G.; Louër, D.; Férey, G. Very Large Breathing Effect in the First Nanoporous Chromium(III)-Based Solids: MIL-53 or $Cr^{III}(OH)\cdot\{O_2C–C_6H_4CO_2\}\cdot\{HO_2C–C_6H_4–CO_2H_2$. *J. Am. Chem. Soc.* **2002**, *124*, 13519–13526.

(13) Tanaka, D.; Nakagawa, K.; Higuchi, M.; Horike, S.; Kubota, Y.; Kobayashi, T. C.; Takata, M.; Kitagawa, S. Kinetic Gate-Opening Process in a Flexible Porous Coordination Polymer. *Angew. Chem.* **2008**, *120*, 3978–3982.

(14) Farha, O. K.; Eryazici, I.; Jeong, N. C.; Hauser, B. G.; Wilmer, C. E.; Sarjeant, A. A.; Snurr, R. Q.; Nguyen, S. T.; Yazaydın, A. Ö.; Hupp, J. T. Metal–Organic Framework

Materials with Ultrahigh Surface Areas: Is the Sky the Limit? *J. Am. Chem. Soc.* **2012**, *134*, 15016–15021.

(15) Li, J.-R.; Kuppler, R. J.; Zhou, H.-C. Selective Gas Adsorption and Separation in Metal–organic Frameworks. *Chem. Soc. Rev.* **2009**, *38*, 1477-1504.

(16) Lee, J.; Farha, O. K.; Roberts, J.; Scheidt, K. A.; Nguyen, S. T.; Hupp, J. T. Metal–organic Framework Materials as Catalysts. *Chem. Soc. Rev.* **2009**, *38*, 1450-1459.

(17) Allendorf, M. D.; Bauer, C. A.; Bhakta, R. K.; Houk, R. J. T. Luminescent Metal–organic Frameworks. *Chem. Soc. Rev.* **2009**, *38*, 1330-1352.

(18) McKinlay, A. C.; Morris, R. E.; Horcajada, P.; Férey, G.; Gref, R.; Couvreur, P.; Serre, C. BioMOFs: Metal-Organic Frameworks for Biological and Medical Applications. *Angew. Chem. Int. Ed.* **2010**, *49*, 6260–6266.

(19) Couck, S.; Denayer, J. F. M.; Baron, G. V.; Rémy, T.; Gascon, J.; Kapteijn, F. An Amine-Functionalized MIL-53 Metal–Organic Framework with Large Separation Power for CO_2 and CH_4. *J. Am. Chem. Soc.* **2009**, *131*, 6326–6327.

(20) Alaerts, L.; Kirschhock, C. E. A.; Maes, M.; van der Veen, M. A.; Finsy, V.; Depla, A.; Martens, J. A.; Baron, G. V.; Jacobs, P. A.; Denayer, J. F. M.; *et al.* Selective Adsorption and Separation of Xylene Isomers and Ethylbenzene with the Microporous Vanadium(IV) Terephthalate MIL-47. *Angew. Chem. Int. Ed.* **2007**, *46*, 4293–4297.

(21) Wang, S.; Hou, Y.; Wang, E.; Li, Y.; Xu, L.; Peng, J.; Liu, S.; Hu, C. A Novel Organic-Inorganic Hybrid Material with Fluorescent Emission: [Cd(PT)(H_2O)]n (PT_2phthalate). *New J. Chem.* **2003**, *27*, 1144-1147.

(22) Horikoshi, R.; Mochida, T.; Moriyama, H. Synthesis and Characterization of Redox-Active Coordination Polymers Generated from Ferrocene-Containing Bridging Ligands. *Inorg. Chem.* **2002**, *41*, 3017–3024.

(23) Potember, R. S.; Poehler, T. O.; Cowan, D. O. Electrical Switching and Memory Phenomena in Cu-TCNQ Thin Films. *Appl. Phys. Lett.* **1979**, *34*, 405-407.

(24) Wang, Z.-M.; Zhang, Y.-J.; Liu, T.; Kurmoo, M.; Gao, S. [$Fe_3(HCOO)_6$]: A Permanent Porous Diamond Framework Displaying H_2/N_2 Adsorption, Guest Inclusion, and Guest-Dependent Magnetism. *Adv. Funct. Mater.* **2007**, *17*, 1523–1536.

(25) Halder, G. J. Guest-Dependent Spin Crossover in a Nanoporous Molecular Framework Material. *Science* **2002**, *298*, 1762–1765.

(26) Taylor, K. M. L.; Jin, A.; Lin, W. Surfactant-Assisted Synthesis of Nanoscale Gadolinium Metal-Organic Frameworks for Potential Multimodal Imaging. *Angew. Chem. Int. Ed.* **2008**, *47*, 7722–7725.

(27) Fujita, M.; Kwon, Y. J.; Washizu, S.; Ogura, K. Preparation, Clathration Ability, and Catalysis of a Two-Dimensional Square Network Material Composed of Cadmium(II) and 4,4'-Bipyridine. *J. Am. Chem. Soc.* **1994**, *116*, 1151–1152.

(28) Valente, C.; Choi, E.; Belowich, M. E.; Doonan, C. J.; Li, Q.; Gasa, T. B.; Botros, Y. Y.; Yaghi, O. M.; Stoddart, J. F. Metal–organic Frameworks with Designed Chiral Recognition Sites. *Chem. Commun.* **2010**, *46*, 4911-4913.

(29) Hon Lau, C.; Babarao, R.; Hill, M. R. A Route to Drastic Increase of CO_2 Uptake in Zr Metal Organic Framework UiO-66. *Chem. Commun.* **2013**, *49*, 3634-3636.

(30) Horcajada, P.; Chalati, T.; Serre, C.; Gillet, B.; Sebrie, C.; Baati, T.; Eubank, J. F.; Heurtaux, D.; Clayette, P.; Kreuz, C.; *et al.* Porous Metal–organic-Framework Nanoscale Carriers as a Potential Platform for Drug Delivery and Imaging. *Nat. Mater.* **2009**, *9*, 172–178.

(31) Bünzli, J.-C. G.; Piguet, C. Taking Advantage of Luminescent Lanthanide Ions. *Chem. Soc. Rev.* **2005**, *34*, 1048-1077.

(32) Yeh, T.-T.; Wu, J.-Y.; Wen, Y.-S.; Liu, Y.-H.; Twu, J.; Tao, Y.-T.; Lu, K.-L. Luminescent Silver Metal Chains with Unusual μ4-Bonded 2,2'-Bipyrazine. *Dalton Trans.* **2005**, 656-658.

(33) Bryce, M. R. Recent Progress on Conducting Organic Charge-Transfer Salts. *Chem. Soc. Rev.* **1991**, *20*, 355-390.

(34) Snejko, N.; Cascales, C.; Gomez-Lor, B.; Gutiérrez-Puebla, E.; Iglesias, M.; Ruiz-Valero, C.; Monge, M. A. From Rational Octahedron Design to Reticulation Serendipity. A Thermally Stable Rare Earth Polymeric Disulfonate Family with CdI2-like Structure, Bifunctional Catalysis and Optical Properties. *Chem. Commun.* **2002**, 1366–1367.

(35) Fang, Q.-R.; Zhu, G.-S.; Jin, Z.; Xue, M.; Wei, X.; Wang, D.-J.; Qiu, S.-L. A Multifunctional Metal–Organic Open Framework with a Bcu Topology Constructed from Undecanuclear Clusters. *Angew. Chem. Int. Ed.* **2006**, *45*, 6126–6130.

(36) Ohba, M.; Yoneda, K.; Agustí, G.; Muñoz, M. C.; Gaspar, A. B.; Real, J. A.; Yamasaki, M.; Ando, H.; Nakao, Y.; Sakaki, S.; *et al.* Bidirectional Chemo-Switching of Spin State in a Microporous Framework. *Angew. Chem. Int. Ed.* **2009**, *48*, 4767–4771.

(37) Lyndon, R.; Konstas, K.; Ladewig, B. P.; Southon, P. D.; Kepert, P. C. J.; Hill, M. R. Dynamic Photo-Switching in Metal-Organic Frameworks as a Route to Low-Energy Carbon Dioxide Capture and Release. *Angew. Chem. Int. Ed.* **2013**, *52*, 3695–3698.

(38) Verma, S.; Mishra, A. K.; Kumar, J. The Many Facets of Adenine: Coordination, Crystal Patterns, and Catalysis. *Acc. Chem. Res.* **2010**, *43*, 79–91.

(39) Gillen, K.; Jensen, R.; Davidson, N. Binding of Silver Ion by Adenine and Substituted Adenines. *J. Am. Chem. Soc.* **1964**, *86*, 2792–2796.

(40) An, J.; Geib, S. J.; Rosi, N. L. High and Selective CO_2 Uptake in a Cobalt Adeninate Metal–Organic Framework Exhibiting Pyrimidine- and Amino-Decorated Pores. *J. Am. Chem. Soc.* **2010**, *132*, 38–39.

(41) An, J.; Geib, S. J.; Rosi, N. L. Cation-Triggered Drug Release from a Porous Zinc–Adeninate Metal–Organic Framework. *J. Am. Chem. Soc.* **2009**, *131*, 8376–8377.

(42) Abrahams, B. F.; Moylan, M.; Orchard, S. D.; Robson, R. Channel-Containing Lanthanide Mucate Structures. *CrystEngComm* **2003**, *5*, 313-317.

(43) Abrahams, B. F.; Moylan, M.; Orchard, S. D.; Robson, R. Zinc Saccharate: A Robust, 3D Coordination Network with Two Types of Isolated, Parallel Channels, One Hydrophilic and the Other Hydrophobic. *Angew. Chem. Int. Ed.* **2003**, *42*, 1848–1851.

(44) Smaldone, R. A.; Forgan, R. S.; Furukawa, H.; Gassensmith, J. J.; Slawin, A. M. Z.; Yaghi, O. M.; Stoddart, J. F. Metal-Organic Frameworks from Edible Natural Products. *Angew. Chem. Int. Ed.* **2010**, *49*, 8630–8634.

(45) Vella, F. Color Atlas of Biochemistry. *Biochem. Educ.* **1997**, *25*, 179–180.

(46) ALBERT, A. Quantitative Studies of the Avidity of Naturally Occurring Substances for Trace Metals Amino Acids Having Only Two Ionizing Groups. *Biochem. J.* **1950**, *47*, 531–538.

(47) Yamauchi, O. Amino Acid- and Pterin-Metal Chemistry as an Approach to Biological Functions. *Pure Appl. Chem.* **1995**, *67*, 297–304.

(48) Zhou, H.; Ivanov, V. N.; Gillespie, J.; Geard, C. R.; Amundson, S. A.; Brenner, D. J.; Yu, Z.; Lieberman, H. B.; Hei, T. K. Mechanism of Radiation-Induced Bystander Effect: Role of the Cyclooxygenase-2 Signaling Pathway. *Proc. Natl. Acad. Sci.* **2005**, *102*, 14641–14646.

(49) Lu, Y.; Yeung, N.; Sieracki, N.; Marshall, N. M. Design of Functional Metalloproteins. *Nature* **2009**, *460*, 855–862.

(50) leck, M.; Bohatý, L. Two Novel Glycine Metal Halogenides: *catena* -poly[[[diaquanickel(II)]-Di-M-Glycine] Dibromide] and *catena* -poly[[[tetraaquamagnesium(II)]-M-Glycine] Dichloride]. *Acta Crystallogr. C* **2005**, *61*, m412–m416.

(51) Luo, T.-T.; Hsu, L.-Y.; Su, C.-C.; Ueng, C.-H.; Tsai, T.-C.; Lu, K.-L. Deliberate Design of a 3D Homochiral Cu^{II}-met/Ag^{I} Coordination Network Based on the Distinct Soft–Hard Recognition Principle. *Inorg. Chem.* **2007**, *46*, 1532–1534.

(52) Anokhina, E. V.; Jacobson, A. J. $[Ni_2O$ (L -Asp)$(H_2O)_2]\cdot 4H_2O$: A Homochiral 1D Helical Chain Hybrid Compound with Extended Ni–O–Ni Bonding. *J. Am. Chem. Soc.* **2004**, *126*, 3044–3045.

(53) Saunders, C. D. L.; Burford, N.; Werner-Zwanziger, U.; McDonald, R. Preparation and Comprehensive Characterization of $[Hg_6(Alanine)4(NO_3)_4]\cdot H_2O$. *Inorg. Chem.* **2008**, *47*, 3693–3699.

(54) Vaidhyanathan, R.; Bradshaw, D.; Rebilly, J.-N.; Barrio, J. P.; Gould, J. A.; Berry, N. G.; Rosseinsky, M. J. A Family of Nanoporous Materials Based on an Amino Acid Backbone. *Angew. Chem. Int. Ed.* **2006**, *45*, 6495–6499.

(55) An, H.-Y.; Wang, E.-B.; Xiao, D.-R.; Li, Y.-G.; Su, Z.-M.; Xu, L. Chiral 3D Architectures with Helical Channels Constructed from Polyoxometalate Clusters and Copper–Amino Acid Complexes. *Angew. Chem.* **2006**, *118*, 918–922.

(56) Qu, Z.-R.; Zhao, H.; Wang, X.-S.; Li, Y.-H.; Song, Y.-M.; Liu, Y.; Ye, Q.; Xiong, R.-G.; Abrahams, B. F.; Xue, Z.-L.; *et al.* Homochiral Zn and Cd Coordination Polymers Containing Amino Acid–Tetrazole Ligands. *Inorg. Chem.* **2003**, *42*, 7710–7712.

(57) Xie, Y.; Yu, Z.; Huang, X.; Wang, Z.; Niu, L.; Teng, M.; Li, J. Rational Design of MOFs Constructed from Modified Aromatic Amino Acids. *Chem. - Eur. J.* **2007**, *13*, 9399–9405.

(58) Kimmerlin, T.; Seebach, D. "100 Years of Peptide Synthesis": Ligation Methods for Peptide and Protein Synthesis with Applications to B-Peptide Assemblies: 100 Years of Peptide Synthesis. *J. Pept. Res.* **2008**, *65*, 229–260.

(59) Rabone, J.; Yue, Y.-F.; Chong, S. Y.; Stylianou, K. C.; Bacsa, J.; Bradshaw, D.; Darling, G. R.; Berry, N. G.; Khimyak, Y. Z.; Ganin, A. Y.; *et al.* An Adaptable Peptide-Based Porous Material. *Science* **2010**, *329*, 1053–1057.

(60) Lee, H.-Y.; Kampf, J. W.; Park, K. S.; Marsh, E. N. G. Covalent Metal–Peptide Framework Compounds That Extend in One and Two Dimensions. *Cryst. Growth Des.* **2008**, *8*, 296–303.

(61) Peri, D.; Ciston, J.; Gándara, F.; Zhao, Y.; Yaghi, O. M. Crystalline Fibers of Metal–Peptide Double Ladders. *Inorg. Chem.* **2013**, *52*, 13818–13820.

(62) Erdmann, R. S.; Wennemers, H. Functionalizable Collagen Model Peptides. *J. Am. Chem. Soc.* **2010**, *132*, 13957–13959.

(63) Salgado, E. N.; Radford, R. J.; Tezcan, F. A. Metal-Directed Protein Self-Assembly. *Acc. Chem. Res.* **2010**, *43*, 661–672.

(64) Liu, Y.; Xuan, W.; Cui, Y. Engineering Homochiral Metal-Organic Frameworks for Heterogeneous Asymmetric Catalysis and Enantioselective Separation. *Adv. Mater.* **2010**, *22*, 4112–4135.

(65) Ingleson, M. J.; Barrio, J. P.; Bacsa, J.; Dickinson, C.; Park, H.; Rosseinsky, M. J. Generation of a Solid Brønsted Acid Site in a Chiral Framework. *Chem. Commun.* **2008**, 1287-1289.

(66) Dybtsev, D. N.; Nuzhdin, A. L.; Chun, H.; Bryliakov, K. P.; Talsi, E. P.; Fedin, V. P.; Kim, K. A Homochiral Metal–Organic Material with Permanent Porosity, Enantioselective Sorption Properties, and Catalytic Activity. *Angew. Chem. Int. Ed.* **2006**, *45*, 916–920.

(67) Miller, S. R.; Heurtaux, D.; Baati, T.; Horcajada, P.; Grenèche, J.-M.; Serre, C. Biodegradable Therapeutic MOFs for the Delivery of Bioactive Molecules. *Chem. Commun.* **2010**, *46*, 4526-4528.

(68) Hawxwell, S. M.; Espallargas, G. M.; Bradshaw, D.; Rosseinsky, M. J.; Prior, T. J.; Florence, A. J.; Streek, J. van de; Brammer, L. Ligand Flexibility and Framework Rearrangement in a New Family of Porous Metal–organic Frameworks. *Chem. Commun.* **2007**, 1532–1534.

(69) Férey, G.; Serre, C. Large Breathing Effects in Three-Dimensional Porous Hybrid Matter: Facts, Analyses, Rules and Consequences. *Chem. Soc. Rev.* **2009**, *38*, 1380–1399.

Publication 1. "Metal-biomolecule frameworks (MBioFs)." I. Imaz, M. Rubio-Martínez, J. An, I. Solé-Font, N. L. Rosi, D. Maspoch. *Chem. Commun.* **2011**, 7287-7302.

ChemComm

Chemical Communications

www.rsc.org/chemcomm

Volume 47 | Number 26 | 14 July 2011 | Pages 7253–7528

ISSN 1359-7345

RSC Publishing

FEATURE ARTICLE
Rosi and Maspoch *et al.*
Metal–biomolecule frameworks (MBioFs)

International Year of CHEMISTRY 2011

1359-7345(2011)47:26;1-C

ChemComm

Dynamic Article Links
View Article Online

Cite this: *Chem. Commun.*, 2011, **47**, 7287–7302

www.rsc.org/chemcomm

FEATURE ARTICLE

Metal–biomolecule frameworks (MBioFs)

Inhar Imaz,[a] Marta Rubio-Martínez,[a] Jihyun An,[b] Isabel Solé-Font,[a] Nathaniel L. Rosi*[b] and Daniel Maspoch*[a]

Received 28th February 2011, Accepted 21st March 2011
DOI: 10.1039/c1cc11202c

Biomolecules are the building blocks of life. Nature has evolved countless biomolecules that show promise for bridging metal ions. These molecules have emerged as an excellent source of biocompatible building blocks that can be used to design Metal–Biomolecule Frameworks (MBioFs). This feature article highlights the advances in the synthesis of this class of MOFs. Special emphasis is provided on the crystal structures of these materials, their miniaturization to the submicron length scale, and their new potential storage, catalytic, and biomedical applications.

1. Introduction

Metal–organic frameworks (MOFs) are a class of hybrid materials comprising metal ion-based vertices and organic ligands (linkers) that serve to connect the vertices into two- or three-dimensional periodic structures.[1–3] The structures and properties of MOFs can be carefully tailored by judicious selection of metal ion and organic linker building blocks. A hallmark property of MOFs is their intrinsic porosity, which renders them potentially useful for gas storage, separations, catalysis, and a variety of additional applications that rely on highly specific host–guest interactions. Their promising properties coupled with the ease by which their structures can be modified make MOFs one of the most exciting, diverse, and rapidly growing areas of modern chemistry research.

Many potential applications of MOFs may require them to be constructed from benign building blocks that are biologically and environmentally compatible. For example, most biological applications, including drug delivery or intracellular imaging, would clearly require non-toxic MOF materials. In addition, many proposed applications will require bulk quantities of MOFs. To reduce their environmental impact, bulk MOF materials should be either environmentally compatible or

[a] *CIN-2 (ICN-CSIC), Catalan Institute of Nanotechnology, Campus UAB, Bellaterra, Spain. E-mail: daniel.maspoch.icn@uab.es; Fax: +34-93-581-4747; Tel: +34-93-581-3304*
[b] *Department of Chemistry, University of Pittsburgh, 219 Parkman Ave., Pittsburgh, PA 15260, USA. E-mail: nrosi@pitt.edu; Fax: +1 412-624-8611; Tel: +1 412-624-3987*

Inhar Imaz

Inhar Imaz was born in Hendaia, Basque Country, France, in 1978. He received his PhD in Materials Science from the Université Bordeaux I in 2005, where he studied the formation of heterometallic metal–organic architectures from tetrahedral building blocks. He joined the CIN-2 (ICN-CSIC) centre in 2005 as a Postdoctoral fellow. At the present, he is a researcher under the "Ramón y Cajal" program at the Catalan Institute of Nanotechnology. His research is focused on the design, the synthesis and the study of novel nanostructured metal–organic materials. He is exploring new synthetic methodologies, properties and applications of supramolecular nanomaterials.

Marta Rubio-Martínez

Marta Rubio-Martínez was born in Barcelona, Catalonia, Spain, in 1982. She received her BSc degree in Chemistry and her MSc in Nanotechnology at the Universitat Autònoma de Barcelona (UAB). She is currently pursuing a PhD in Chemistry at the CIN2 (ICN-CSIC) in the Supramolecular Nanochemistry & Materials Group under the supervision of Dr Daniel Maspoch and Dr Inhar Imaz. Her research interests include the design, synthesis and study of a new family of biocompatible materials constructed from metal ions and biomolecules.

Fig. 1 Schematic representation illustrating the biomolecules (*e.g.* amino acids, peptides, nucleotides, *etc.*) that scientists can take from nature to synthesize MBioFs.

easily recyclable. New generations of MOFs should be designed according to specific composition criteria that address their environmental and biological compatibility.

Recently, biomolecules have emerged as building blocks for constructing Metal–Biomolecule Frameworks (MBioFs, Fig. 1). MBioFs are defined as MOFs constructed from at least one biomolecule which serves as an organic linker. Biomolecules offer several advantages as building blocks, which are highlighted here:

- Simple biomolecules, including amino acids, nucleobases, sugars, and others, are readily and naturally available in quantities and at prices amenable to preparing bulk quantities of materials.
- Biomolecules can lead to biologically-compatible MOFs.
- Biomolecules are structurally diverse. They can be either structurally rigid or flexible, aspects that impact the functional nature of the resulting MBioF.
- Biomolecules can have many different metal-binding sites. Consequently, they can exhibit multiple possible coordination modes, a feature that increases the potential structural diversity of MBioFs.
- Many biomolecules have intrinsic self-assembly properties which can be used to direct the structure and function of MBioFs.
- Finally, many biomolecules are chiral. Therefore, they can be used to construct chiral MBioFs, which may have interesting recognition, separation, and catalytic properties.

Jihyun An

Jihyun An was born in Daegu, Korea. She received a BS degree in Chemistry Education from Seoul National University in 2004, and MS and PhD degrees in Chemistry under the supervision of Prof. Nathaniel L. Rosi from University of Pittsburgh in 2008 and 2010, respectively. Her PhD work was focused on the design, synthesis and characterization of adenine-based metal–organic frameworks. She joined the group of Prof. Chad A. Mirkin at Northwestern University as a post-doctoral researcher in 2010.

Isabel Solé-Font

Isabel Solé was born in La Gornal, Catalonia, Spain, in 1981. She received her BSc degree in Chemistry from Universitat de Barcelona (UB), and she earned her PhD in Chemical Engineering at the UB and at the Institut de Química Avançada de Catalunya. After postdoctoral work in Prof. Alexander Couzis group at City College of New York, she moved to the Catalan Institute of Nanotechnology (ICN). She is working on controlling the supramolecular assembly of (bio)molecules, metal ions and nanoscale building blocks at the nanometre scale.

Nathaniel L. Rosi

Nathaniel L. Rosi was born in Grayling, Michigan, in 1976. He earned a BA in chemistry from Grinnell College in 1999 and a PhD in chemistry from the University of Michigan in 2003. After post-doctoral research at Northwestern University (2003–2006), he began his independent career at the University of Pittsburgh. His group focuses on developing synthetic methods for directing the assembly of biomolecules, metal clusters, and nanoparticles into hierarchical materials. In particular, he is interested in precisely controlling and tailoring the architecture and properties of these materials for environmental and biomedical applications.

Daniel Maspoch

Daniel Maspoch was born in L'Escala, Catalonia, Spain, in 1976. He received his BSc degree in chemistry from Universitat de Girona in 1999, and he earned his PhD in materials science at the UAB and at the Institut de Ciencia de Materials de Barcelona in 2004. After post-doctoral work in Prof. Chad A. Mirkin's group at Northwestern University, he moved to the Catalan Institute of Nanotechnology, thanks to the "Ramón y Cajal" Program financial support. His group is working on controlling the supramolecular assembly of (bio)molecules, metal ions and nanoscale building blocks at the nanometre scale.

This suite of characteristics renders biomolecules particularly attractive building blocks for constructing MOFs with new properties and applications that cannot be accessed using the simple organic linkers traditionally used in MOF construction. In this review, we highlight some of the most significant advances in the preparation and characterization of MBioFs and offer insight into the current and future challenges and opportunities in this sub-discipline of MOF research.

2. Synthesis and structure of metal–biomolecule frameworks

2.1 Amino acids

α-Amino acids (AAs) are molecules with the general formula NH_2CHRCO_2H (where NH_2 and CO_2H are the amino and carboxylic acid groups, respectively, and R is the organic side chain). AAs link together *via* amide bonds to form peptides and proteins that serve important biological functions. They are also excellent organic ligands and may coordinate metal ions through both their carboxylate and amino groups. In most cases, AAs form metal–AA chelates or discrete polynuclear clusters that have important biological functions in nature such as transporting metal ions in blood.[4] However, AAs can exhibit a wide variety of coordination modes, and therefore, they represent promising biomolecules for interlinking metal ions into MBioFs.

There are essentially three major types of MBioFs made from AAs. They are either constructed from (i) metal ions and natural AAs; (ii) metal ions, natural AAs, and additional bridging anions and polydentate organic ligands; or (iii) metal ions and chemically-modified natural AAs (*e.g.* AAs modified with additional metal-binding groups). In the last two classes, the presence of the organic ligands, anions, and additional metal binding groups serves to increase the dimensionality of the metal ion–AA framework.

As stated above, all natural AAs consist of an α-carbon atom onto which an amino group and an α-carboxylic acid group are attached. Through these metal binding groups, it is well-known that AAs tend to form discrete complexes *via* formation of the typical five-membered glycinate chelate ring (also called O,N-chelating mode, see Fig. 2). In some cases, the α-carboxylate group can coordinate metal ions *via* bi- or tridentate bridging modes (Fig. 2). When this occurs, extended metal ion–AA frameworks can be created. To date, 1-D coordination networks[5] based on pure AAs are more common than 2-D or 3-D extended structures.[6–14] 2-D metal ion–AA frameworks have been obtained, for example, when glycine (Gly) coordinates to metal ions (*e.g.* Ni(II),[6] Mn(II),[7] and Co(II))[8] in a 2 : 1 fashion. In these 2-D structures, each octahedral metal ion is linked to another four metal ions by four Gly ligands adopting a μ_2-O_1:O_2 coordination mode (Fig. 2). Another typical connectivity pattern that leads to the formation of 2-D frameworks is when two AA ligands coordinate to an octahedral metal ion in the typical O,N-chelating mode. However, each AA also bridges neighbouring metal ions using the second oxygen atom of its carboxylate (μ_2-N_1O_1:O_2 coordination mode, see Fig. 2). Examples of these 2-D structures have been obtained by combining

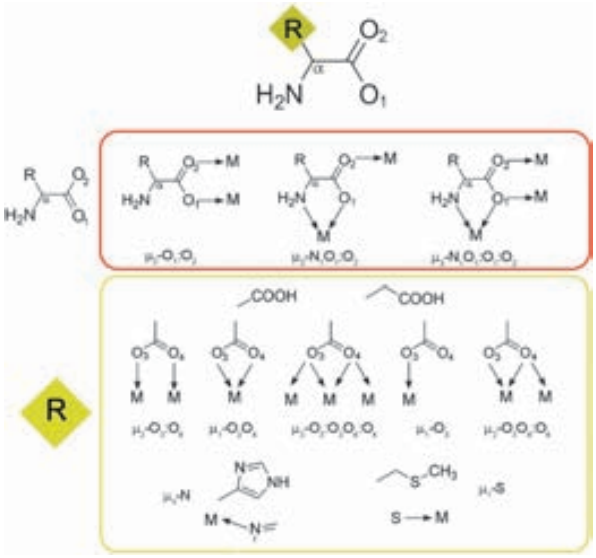

Fig. 2 Schematic illustration of the common skeleton of a natural AA (top), and the potential coordination modes that this skeleton (middle) and the side chains (bottom) can exhibit. Note that the top side chains correspond to Asp and Glu, and the bottom ones to His and Met.

L-phenylalanine (Phe) with Mn(II)[9] and Cu(II),[10] L-tryptophan (Trp) with Mn(II)[11] and Ni(II),[12] and L-glutamine (Gln) with Cu(II).[13]

3-D metal ion–AA frameworks are scarce. However, there are some AAs bearing R side chains with metal binding groups, such as the β-carboxylate groups of aspartic (Asp) and glutamic (Glu) acids, the imidazole group of histidine (His), the thiol or thioether groups of cysteine (Cys) and methionine (Met), respectively, or the phenol ring of tyrosine (Tyr). These binding groups, in addition to serving as metal binding sites in proteins, can be used to bridge metal ions together and further increase the dimensionality of metal ion–AA networks (Fig. 2).

Chemists have produced some interesting MBioFs by interlinking metal ions [*e.g.* Pb(II),[15] Cd(II),[16,17] Ni(II),[18] Zn(II),[19,20] Cu(II)[21,22] and Co(II)][23] using Asp and Glu. For example, Anokhina and Jacobson reported the synthesis of homochiral 1-D nickel aspartate oxide helical chains formulated as $[Ni_2O(L\text{-}Asp)(H_2O)_2]\cdot 4H_2O$.[24] In these chains, each Asp ligand coordinates five Ni(II) ions through its carboxylate and amino groups adopting the μ_2-N_1O_1:O_2 and μ_3-O_3:O_3:O_4 modes. By increasing the pH of the reaction, these helical chains were connected by additional $[NiAsp_2]^{2-}$ units to generate a 3-D porous chiral framework, $[Ni_{2.5}(OH)(L\text{-}Asp)_2]\cdot 6.55H_2O$, that exhibits 1-D channels with dimensions of 8 × 5 Å (Fig. 3a).[18] Rosseinsky *et al.* described a homochiral AA-derived MBioF, $[Zn(Asp)]\cdot H_2O$.[19] The connection of 4-, 5-, and 6-coordinated Zn(II) ions through Asp ligands *via* μ_2-N_1O_1:O_2 and μ_2-O_3:O_4 modes leads to the formation of this 3-D framework with cavities having a volume of 33 $Å^3$. Water molecules encapsulated in the cavities can be removed upon heating to 350 °C. A third interesting MBioF with formula $[Cu(L\text{-}Asp)(Im)]\cdot 2H_2O$ (where Im is imidazole) has been described by Pellacani *et al.*[22] This framework is constructed from Cu(II) ions bridged

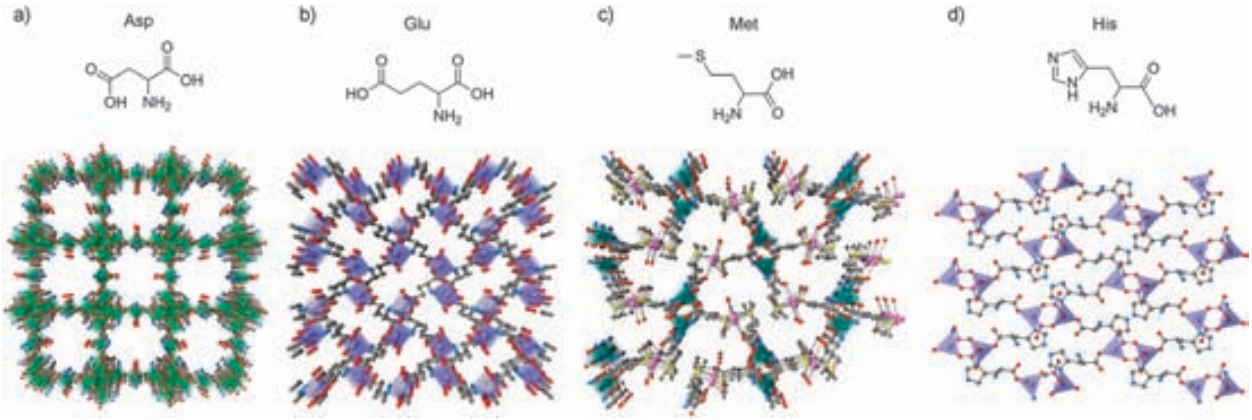

Fig. 3 Projection of the metal–AA frameworks along with their AA components of (a) $[Ni_{2.5}(OH)(L\text{-}Asp)_2]\cdot 6.55H_2O$, (b) $Zn(L\text{-}Glu)(H_2O)]\cdot H_2O$, (c) $[Ag_3Cu_3(L\text{-}Met)\cdot 6(NO_3)_3(H_2O)_3]\cdot 7H_2O$ and (d) $Zn(HPO_3)(His)(H_2O)_{1/2}$.

by Asp ligands. Each Asp moiety is linked to three Cu(II) ions *via* the μ_2-N_1O_1:O_2 and μ_1-O_3 modes. Glu also has been used to create a series of nearly isostructural 3-D MBioFs formulated as $[M(L\text{- or }D\text{-}Glu)(H_2O)]\cdot H_2O$ (where M is Cd(II),[17] Zn(II),[20] Cu(II),[21] or Co(II)).[23] In these structures, the Glu ligands serve as multidentate ligands to coordinate to three different metal ions *via* the μ_2-N_1O_1:O_2, μ_1-O_3:O_4 and μ_2-O_3:O_4 modes; each octahedral metal ion is coordinated with three Glu ligands. Fig. 3b shows the resulting 3-D structure with large chiral 7 × 9 Å 1-D channels.

Lanthanide ions commonly form coordinate bonds with carboxylic groups, and therefore, they also can be used as the metal ion component of AA-based MBioFs. To date, 2-D coordination layers constructed from trivalent Dy(III), Ho(III) and Pr(III) ions and Glu ligands as well as from Sm(III) ions and Asp ligands have been described.[25] In addition, Gao *et al.* spatially linked the well-known cubane-like $[Dy_4(\mu_3\text{-}OH)_4]$ lanthanide cluster using Asp ligands to form a 3-D framework formulated as $[Dy_4(\mu_3\text{-}OH)_4(Asp)_3(H_2O)_8]\cdot 2(ClO_4)\cdot 10H_2O$.[26] This structure has 1-D parallelogram-shaped channels with dimensions of 4 × 9 Å. Recently, analogous Er(III) and Eu(III)-based MBioFs have been prepared.[27]

There are other AAs that feature metal binding groups in their side chains, yet their utility as building blocks in MBioFs is still relatively unexplored. For instance, Lu *et al.* have used the ability of thioether groups of Met to bind to Ag(I) metal ions to prepare a homochiral heterobimetallic MBioF, $[Ag_3Cu_3(L\text{-}Met)\cdot 6(NO_3)_3(H_2O)_3]\cdot 7H_2O$ (Fig 3c).[28] In this structure, L-Met ligands bind to two different types of metal ions: (i) to Cu(II) ions through the hard amino and carboxylate sites *via* μ_2-N_1O_1:O_2 and simple O,N-chelating modes, and (ii) to Ag(I) ions through the soft monodentate thioether groups. The distinct coordination preference of metals to specific binding sites on the AA ligand leads to the assembly of a 3-D MBioF constructed from 1-D helical building blocks, featuring homochiral channels that host 1-D chains of water molecules. His has also been employed by Chen and Bu to form a 2-D layered framework.[29] Fig. 3d shows a representation of the layers, which are composed of inorganic Zn(II)/HPO_3^{2-} clusters that are further connected to each other by zwitterionic His ligands. The use of His as a linker is unusual because it prefers to form 5 or 6 membered rings between metal ions and its amino, carboxylate, or imidazole groups. In this example, Bu *et al.* overcame this tendency by carefully adjusting the pH to obtain the zwitterionic form of His. In this form, the protonated amine group does not coordinate with metal ions, which therefore enables both the imidazole and carboxylate groups to coordinate different metal ions. This discovery will certainly lead to the more prevalent use of His as a bridging AA ligand to obtain 3-D MBioFs in the near future.

The second class of AA-derived MBioFs are constructed by using additional organic ligands or inorganic anions/clusters that act as linkers within the metal ion–AA frameworks to increase their dimensionality. To date, some examples of these MBioFs have been described.[30–36] An illustrative example was reported by Xu *et al.*, who synthesized a 3-D homochiral MBioF by connecting Cu(II)–L- or D-Pro chains through polyoxometalate $[BW_{12}O_{40}]^{5-}$ clusters.[30] The resulting structure has helical channels with dimensions of 11 × 7 Å. More recently, two non-chiral 3-D MBioFs obtained by bridging Cu(II)–Gly and Cu(II)/Gd(III)–L-Ala chains using azide and 1,3-benzene dicarboxylate ligands, respectively, have also been described.[31,32]

In addition to the linkage of AA-derived chains, some 3-D pillared MBioFs resulting from the connection of metal ion–Asp layers through bipy-type ligands have been reported. Rosseinsky *et al.* synthesized an enantiopure crystalline nanoporous MOF, $[Ni_2(L\text{-}Asp)_2(4,4'\text{-bipy})]\cdot guest$ (Fig. 4a), by mixing $Ni(Asp)\cdot 3H_2O$ salt and 4,4′-bipyridine (4,4′-bipy) in a mixture of water and methanol at 150 °C.[33] In this framework, neutral chiral Ni(L-Asp) layers are connected by 4,4′-bipy linkers to afford a pillared structure with 1-D sinusoidal channels (3.8 × 4.7 Å) defined by the length of the 4,4′-bipy ligands and the separation between the Ni(II) centers in the Ni(L-Asp) layers. The Ni(L-Asp) layers are formed by octahedrally-coordinated Ni(II) ions linked by Asp ligands, which each bind to one Ni(II) center *via* μ_2-N_1O_1:O_2 and μ_2-O_3:O_4 modes. Isostructural homochiral MBioFs containing Co(II) ions have also been reported.[34] Interestingly, these MBioFs are stable after removal of the guest solvent, and the pore characteristics (*e.g.* shape, cross-section, chemical functionality, and volume) can be controlled

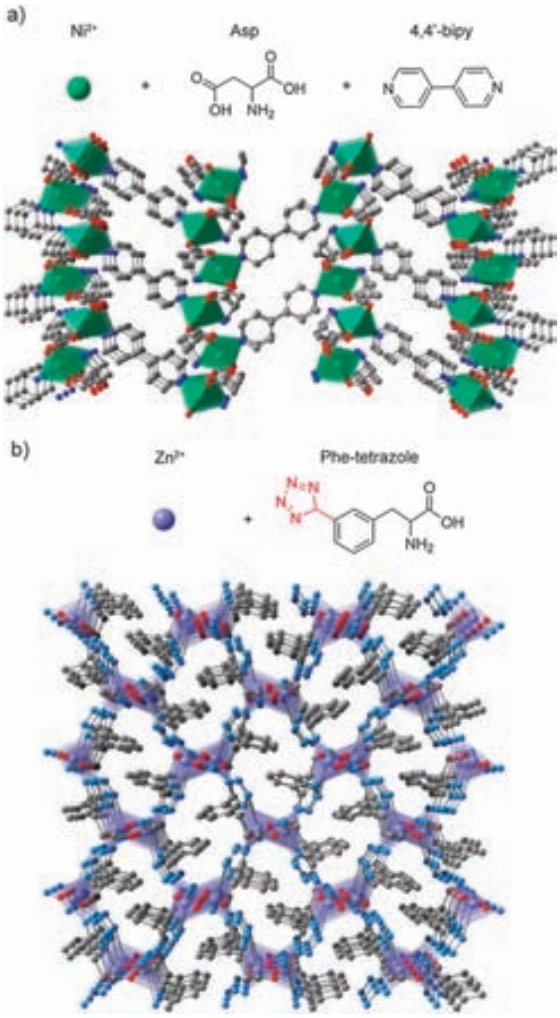

Fig. 4 (a) Representation of the metal–Asp framework $[Ni_2(L\text{-Asp})_2(4,4'\text{-bipy})]$ resulting from linking Ni–Asp layers by 4,4-bipy ligands (Type #2). (b) Representation of the structure [Zn(Phe-tetrazole)] generated by using Phe functionalized with a tetrazole moiety (Type #3).

by substituting the pillaring 4,4′-bipy ligand with extended bipy-type ligands, such as 4,4′-azopyridine (azpy), 3,5-bis-(4-pyridyl)pyridine (35bpp), among others.[35] For example, the pillaring of Ni(L-Asp) layers through azpy ligands leads to an analogous structure having nearly linear channels with variable dimensions of 4.1 × 3.8 Å (windows) and 7.8 × 3.7 Å (pores), whereas the use of 35bpp ligands yields a pillared structure with channels whose dimensions range between 6.7 × 4.9 Å and 10.3 × 5.4 Å.

Natural AAs are sometimes modified to extend the dimensionality and potential topologies of homochiral metal ion–AA frameworks. For example, while Phe tends to form 1-D and 2-D metal ion–AA structures, modifying its phenyl ring with a tetrazole allows construction of 3-D frameworks. Xiong *et al.* described the synthesis of two isostructural homochiral networks with noninterpenetrated $SrAl_2$ topologies constructed by linking Zn(II) or Cd(II) ions with this Phe-tetrazole ligand (Fig. 4b).[37] In this porous structure, each metal ion is coordinated to four of these ligands and each ligand bridges four metal centers through the carboxylate and amino groups adopting the typical μ_2-N_1O_1:O_2 coordination mode and through the tetrazole moiety. Using a similar approach, Wang *et al.* further proved that one can control the size and the shape of the grids of 2-D Zn(II) and Cd(II) chiral frameworks by introducing different functionalities to the phenyl ring of Phe.[38] Chiral coordination networks also have been obtained using cysteic acid obtained from Cys.[39] This ligand is able to coordinate Cu(II) and Cd(II) ions through the carboxylate and amino groups adopting the typical μ_2-N_1O_1:O_2 coordination mode and through the SO_3 moiety in a monodentate mode, thus leading to the formation of 3-D frameworks.

2.2 Peptides

Peptides are short polymeric biomolecules composed of AAs linked by peptide bonds. Each peptide has a distinctive sequence depending on the conformation and stereochemical configuration of their constituent AAs. As a consequence, they have specific recognition properties and intrinsic chirality that may be useful for a wide range of applications, including asymmetric catalysis and enantioselective separation.[40] If one analyzes the simplest peptide, the dipeptide glycylglycine (GlyGly, Fig. 5), it can be concluded that peptides also have the ability to act as bridging bio-related ligands. First, peptides always have an amino terminus and a carboxylic acid terminus, both of which can coordinate metal ions *via* different coordination modes. The terminal amino group usually coordinates to metal ions in a monodentate or chelating fashion, in which the oxygen atom of the neighbouring amide group also coordinates to the same metal ion forming a five-membered chelate ring. Note here that peptides can also adopt a similar O,N-chelating mode to that observed for AAs. At the opposite peptide terminus, the carboxylate group can coordinate to metal ions in any one of the well-known coordination

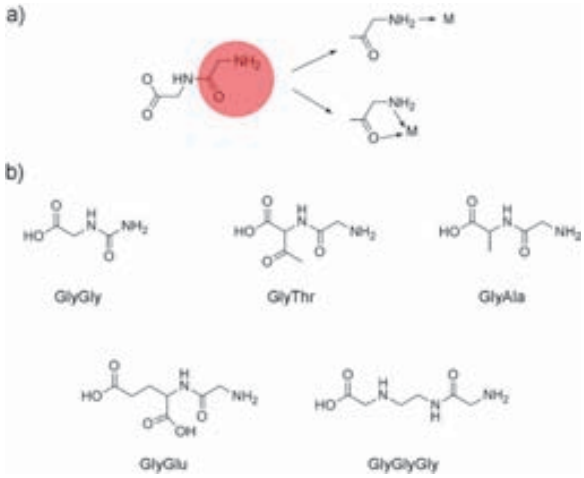

Fig. 5 (a) Potential coordination modes of the terminal amino group of peptides: monodentate and five-membered chelate mode. Note here that the terminal carboxylate group can exhibit the same coordination modes than those shown in Fig. 2. (b) Representation of all di- and tripeptides used for synthesizing MBioFs.

modes of carboxylic acids (Fig. 2). Second, and more importantly, there are endless possibilities to design peptides that incorporate more metal binding groups to their structure by simply adding suitable AAs to their sequence. For example, the incorporation of more carboxylate groups can be achieved simply by synthesizing peptides made from constituent Asp or Glu. This versatility affords the possibility to access an unlimited number of flexible polydentate bio-related ligands that will certainly be employed by chemists to form functional 2- and 3-D metal–peptide frameworks in the near future.

As stated above, the simplest and shortest peptide is GlyGly (Fig. 5b). Using this peptide, Takayama *et al.* first synthesized three metal–peptide frameworks by adjusting the pH values of aqueous solutions containing Zn(II) or Cd(II) metal salts and GlyGly peptide.[41] At pH 6, these authors obtained 2-D MBioFs formulated as $[M(GlyGly)_2]\cdot 2H_2O$ (where M is Zn(II) or Cd(II)), which are constructed by connecting each octahedral metal ion to four other metal ions through four bridging GlyGly ligands. Each GlyGly ligand bridges two metal ions through the terminal carboxylate group in a monodentate mode and the terminal amino group through the aforementioned five-membered chelate ring (*vide supra*). By increasing the pH to 9, a novel 2-D MBioF with formula $[Cd(GlyGly)_2]\cdot H_2O$ was formed. In these layers, the terminal carboxylate groups of GlyGly ligands bind to two Cd(II) ions, and their amino groups coordinate to another Cd(II) ion in a monodentate mode. As a consequence, each Cd(II) ion is linked to six other Cd(II) ions by four GlyGly ligands.

Since the publication of the first peptide-derived MBioFs, other metal–peptide networks made from dipeptides have been reported.[42–45] $[Zn(GlyThr)_2]\cdot 2H_2O$,[42] $[Cd(AlaThr)_2]\cdot 4H_2O$,[43] $[Cd(AlaAla)_2]$[43] and $[Zn(GlyAla)_2]\cdot$solvent[44] consist of metal–peptide sheets connected through strong hydrogen bonds. Interestingly, these MBioFs exhibit a metal–peptide connectivity similar to that observed for $[M(GlyGly)_2]\cdot 2H_2O$,[41] in which each metal ion is connected to four other metal ions through four dipeptide ligands. However, their structures are not identical because of the different coordination spheres (number and configuration) of the metal ions and/or the different metal–peptide coordination modes. While $[Zn(GlyThr)_2]\cdot 2H_2O$ and $[Cd(AlaThr)_2]\cdot 4H_2O$ have porous structures with 1-D channels resulting from the assembly of square-like 2-D layers through H-bonds, $[Cd(AlaAla)_2]$ forms a non-porous structure built-up from H-bonded distorted square lattices. Among them, however, the most notable MBioF is probably $[Zn(GlyAla)_2]\cdot$solvent, which was recently reported by Rosseinsky *et al.*[44] As shown in Fig. 6a, each GlyAla ligand coordinates to the tetrahedral Zn(II) ions by the terminal carboxylate group of the Ala residue and the terminal amino groups of the Gly residue, both in a monodentate mode. The layers are then aligned in an A–A fashion by hydrogen bonds to form a porous structure with square-shaped 1-D pores (solvent-accessible volume: 532.7 $Å^3$ per unit cell at 100 K (28%)). Remarkably, this porous MBioF has an adaptable porosity, in which its crystal structure undergoes reversible structural changes after desorption/reabsorption of solvent molecules.

With this family, one can clearly see that the substitution of one of the two constituent AAs of the dipeptides is sufficient to obtain different metal–peptide structures. Gasque *et al.* synthesized two MBioFs made from the connection of Pb(II) or Cd(II) ions through GlyGlu ligands.[46] The first material has a 2-D metal–peptide framework, in which both carboxylate groups of each Glu residue coordinate to four Pb(II) ions in a tridentate mode. The second is a 3-D porous MBioF, $[Cd(GlyGlu)_2]\cdot 3H_2O$, that has 1-D channels (Fig. 6b). In this structure, each octahedral Cd(II) ion is linked in three dimensions to four other Cd(II) ions by four GlyGlu ligands. The amino groups do not participate in the coordination of Cd(II) ions, and only the carboxylate groups of the Glu residue bind to Cd(II) ions in a bidentate mode. Interestingly, the simple addition of a metal-binding site to the peptides allows the formation of 3-D metal–peptide frameworks.

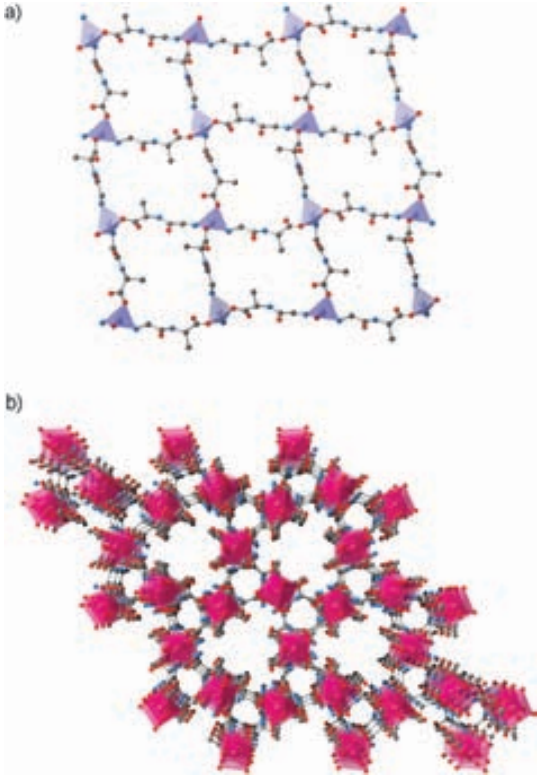

Fig. 6 Representation of (a) one layer of $[Zn(GlyAla)_2]$ and (b) the porous structure of $[Cd(GlyGlu)_2]$.

To date, there are not many examples of MBioFs constructed from peptides of more than two AAs. In fact, to our knowledge, there is only one report on the use of tripeptides as organic linkers to form 2-D metal–peptide frameworks. This example was published by Marsh *et al.*, who used the tripeptide GlyGlyGly to synthesize a 2-D MBioF with formula $[Cd(GlyGlyGly)_2]\cdot 2H_2O$.[43] From a structural point of view, this structure is similar to that of $[Cd(GlyGly)_2]\cdot H_2O$ (pH = 9) reported by Takayama *et al.*[41]

2.3 Proteins

Proteins, including antibodies, enzymes and structural proteins, are long AA sequences with complex and flexible 3-D structures that usually perform highly specialized functions

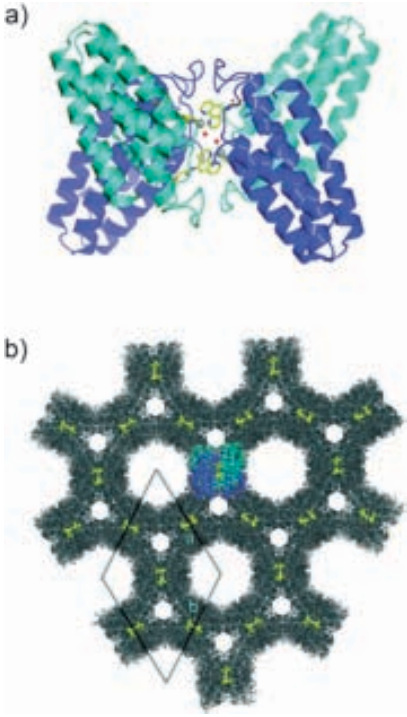

Fig. 7 Representation of (a) an engineered protein based on the four-helix bundle hemeprotein cytochrome cb_{562}, and (b) the porous structure resulted from its metal-directed assembly. (© The Royal Society of Chemistry, reprinted with permission.)

in cells (*e.g.* cellular dynamics, communication, *etc.*). Because of their AA constituents, proteins clearly also have the ability to coordinate metal ions. In fact, many metal ions are required in some proteins for proper folding, and many natural protein complexes are currently known.[47] However, there are no examples of extended coordination frameworks constructed from the association of metal ions and proteins in the literature. This may be partially attributable to the complexity and flexibility of protein structures and the difficulty to control the coordination of metal ions at the interfaces of proteins. It is our opinion, however, that several fascinating studies recently reported by Tezcan *et al.* serve as the starting point for considering the use of proteins to construct MBioFs.[48] In these studies, well-defined protein superstructures were constructed by controlling protein–protein interactions through metal coordination.[49] Using this strategy (called metal-directed protein self-assembly), they synthesized the first porous protein-derived framework which consists of two engineered proteins based on the four-helix bundle hemeprotein cytochrome cb_{562} connected through Ni(II) and Zn(II) ions.[50] This material, which exhibits a set of hexagonal channels with dimensions of 6 and 2 nm (Fig. 7), illustrates the promising future of this field.

2.4 Nucleobases

Nucleobases are key constituents of nucleic acids that are involved in base-pairing; that is, adenine (Ade) binds to thymine or uracil with the help of two H-bonds, whereas guanine specifically recognizes cytosine through three H-bonds. In addition, nucleobases also have accessible nitrogen and oxygen electron lone pairs, which allows these molecules to act as multidentate organic ligands.[51] Their rich metal binding and H-bonding capabilities, together with the rigidity of their molecular structures, make them ideal bio-linkers for constructing topologically diverse families of MBioFs.

Thus far, MBioFs constructed from Ade have been the most reported.[52] Ade offers five potential metal-binding sites, the N6 amino group and the N1, N3, N7 and N9 imino nitrogens (Fig. 8a), and a rich range of different metal-ion binding patterns.[53] To our knowledge, the first suspicion that Ade could be used to obtain extended metal–nucleobase frameworks with dimensionalities higher than 0[54] or 1-D[55] was published by Davidson in 1964.[56] They proposed the formation of 2-D frameworks constructed by linking Ag(I) ions *via* the N1, N3 and N6 coordination of 9-methyladenine.

However, it was not until recently that chemists started to discover novel Ade-derived MBioFs, many of which exhibit interesting adsorption properties. Rosi *et al.* have largely contributed to their fabrication. The first 3-D permanently porous framework described by these authors was $[Zn_8(Ade)_4(bpdc)_6O{\cdot}2Me_2NH_2]{\cdot}8DMF{\cdot}11H_2O$ (also called bio-MOF-1, where bpdc is biphenyldicarboxylate).[57] This MBioF consists of infinite Zn(II)–Ade columns composed of apex-sharing Zn(II)–Ade octahedral cages. Each cage consists of eight Zn^{2+} cations connected through four Ade ligands

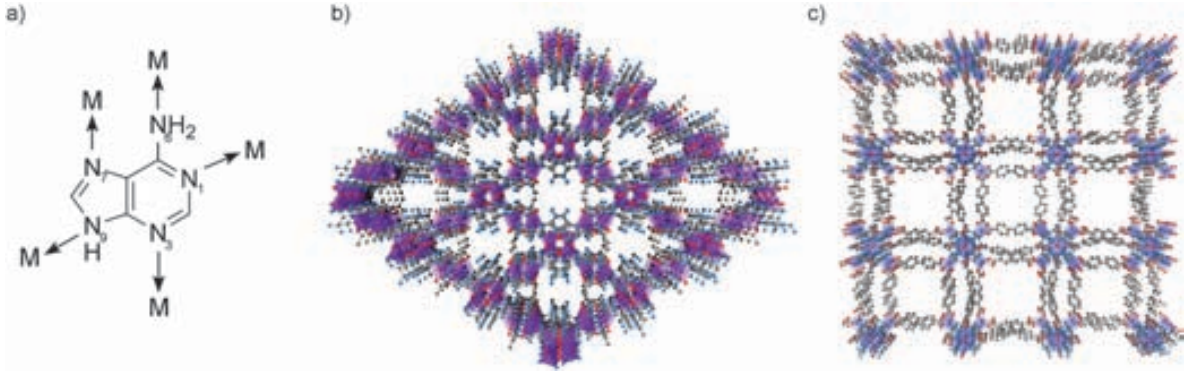

Fig. 8 (a) Potential coordination sites of Ade. (b) Porous structure of $[Co_2(Ade)_2(CO_2CH_3)_2]{\cdot}2DMF{\cdot}0.5H_2O$. (c) Porous structure of $[Zn_8(Ade)_4(bpdc)_6O{\cdot}2Me_2NH_2]{\cdot}8DMF{\cdot}11H_2O$.

via N1, N3, N7, and N9 coordination. As shown in Fig. 8c, the Zn(II)–Ade columns are then interconnected *via* multiple BPDC linkers, resulting in large 1-D channels that are stable after removal of guest solvent molecules. Interestingly, the nitrogen adsorption studies of this material revealed a BET surface area of 1700 $m^2\ g^{-1}$. The authors have exploited the anionic nature of this MBioF, showing that it can be used to store cationic drug molecules and that its pores can be easily modified for particular applications simply *via* cation exchange.

The same authors recently reported a second porous Ade-derived MBioF with formula $[Co_2(Ade)_2(CO_2CH_3)_2]\cdot 2DMF\cdot 0.5H_2O$ (also called bio-MOF-11), consisting of Co(II)–Ade–acetate "paddle wheel" clusters.[58] Each cluster is formed by two Co(II) ions that are bridged by two Ade (*via* N3 and N9 coordination) and two acetate ligands. These clusters are further linked together by Ade ligands (*via* the N7 coordination) to build a 3-D structure with periodically distributed cavities (Fig. 8b). These cavities, which are aligned into a 2-D channel-like network, are large enough to accommodate a 5.8 Å diameter sphere. Again, it is interesting to note that this framework is stable after removing the solvent and has a BET surface area of 1040 $m^2\ g^{-1}$. The presence of exposed Lewis-basic nitrogens within the channels makes this material particularly useful for selective capture of carbon dioxide.

Another porous Ade-derived 3-D MBioF was described by Lezama *et al.*[59] This framework, with formula $[Cu_2(Ade)_4(H_2O)_2]\cdot[Cu(ox)(H_2O)]_2\cdot\sim 14H_2O$ (where ox is oxalate), is formed by paddle-wheel clusters consisting of two Cu(II) ions bridged by four Ade ligands *via* N3 and N9 coordination. N7 nitrogen atom of the each Ade ligand is further connected to another Cu(II)–ox unit, which in turn connects to another cluster to afford a 3-D structure. The resulting structure contains 1-D tubular channels with a diameter of about 13 Å. The water guest molecules within the channels can be removed at 95 °C without disrupting the crystal structure. The collection of metal–Ade frameworks has been expanded with the 2-D structure $[Cd_3(Ade)_2(ap)_2(H_2O)_2]\cdot 1.5H_2O$ (where ap is adipic acid)[60] and a family of extended metal–Ade frameworks has been synthesized using 9-substituted Ade ligands.[61] Interestingly, in the first structure, the repeating unit is a trinuclear Cd(II) cluster created from three lineal Cd(II) ions bridged by two bridging Ade ligands (*via* N3 and N9 coordination) and two bridging adipate ligands. These clusters are further connected through Ade ligands (*via* N3 and N7 coordination) to form a 2-D sheet structure.

2.5 Saccharides (carbohydrates)

Saccharides (carbohydrates) are organic compounds that are divided into monosaccharides and disaccharides (sugars), oligosaccharides, and polysaccharides. They perform numerous roles in living systems, ranging from energy storage (*e.g.* starch and glycogen) to providing structure (*e.g.* cellulose in plants and chitin in arthropods). To date, saccharides have not been extensively used as bio-related ligands to generate MBioFs. However, Stoddart *et al.* have recently reported a very exciting study that exploits their use as multidentate organic ligands to form functional MBioFs.

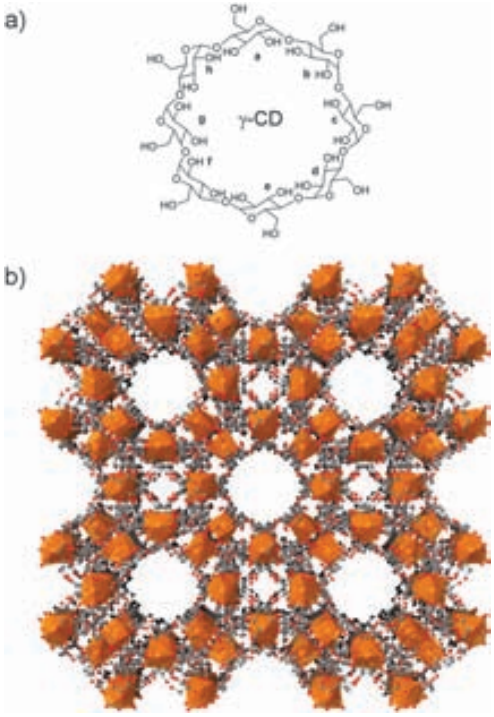

Fig. 9 Representation of (a) γ-cyclodextrin (γ-CD), a symmetrical cyclic oligosaccharide composed of eight asymmetric α-1,4-linked D-glucopyranosyl residues, and (b) the porous structure of $(\gamma\text{-CD})(KOH)_2$.

These authors reported two metal–saccharide frameworks synthesized from γ-cyclodextrin (γ-CD), a symmetrical cyclic oligosaccharide that is mass-produced enzymatically from starch and comprises eight asymmetric α-1,4-linked D-glucopyranosyl residues (Fig. 9a).[62] Both frameworks, which have the empirical formula $[(\gamma\text{-CD})(MOH)_2]$ (where M is K or Rb), are constructed from six γ-CD units connected into $(\gamma\text{-CD})_6$ cubes through the metal ions. These cubes are further linked by the alkali metal K^+ or Rb^+, leading to a porous framework in which apertures of 0.78 nm provide access to larger spherical voids of 1.7 nm at the center of each γ-CD (Fig. 9b). Remarkably, both structures are permanently porous after heating to nearly 200 °C and exhibit BET surface areas of 1220 g cm^{-3} (K^+) and 1030 g cm^{-3} (Rb^+).

Although metal–saccharide frameworks are still very rare, MBioFs made from derivatives obtained from the oxidation of these biomolecules are more present in the literature. For example, saccharic or glucaric acid, a substance produced naturally in small amounts by mammals, including humans, is the result of glucose oxidation. Glucaric acid is also found in many fruits and vegetables, with the highest concentrations found in oranges, apples, grapefruit, and cruciferous vegetables. Robson *et al.* associated glucaric acid with Zn(II) ions to form a 3-D network, $[Zn(C_6H_8O_8)]\cdot 2H_2O$.[63] In this structure, Zn(II) ions are chelated at both ends of the glucarate ligand by a carboxylate oxygen donor and an adjacent hydroxyl group. The resulting open-framework shows two types of channels, one hydrophilic and the other hydrophobic, depending on the positioning of hydroxyl groups in the walls of the channel.

The square channel has dimensions of approximately 5.8 × 5.8 Å and accommodates water molecules. The same authors also synthesized a family of frameworks using galactaric acid:[64] (i) $[M_2(C_6H_4O_8)_3]\cdot 8H_2O$ (M is La(III), Ce(III) or Pr(III)) shows isostructural 3-D structures with 1-D channels, and (ii) $[M_2(C_6H_4O_8)_3(H_2O)_4]\cdot 10H_2O$ (M is Nd(III) or Eu(III)) forms 2-D layers with the (6,3) topology that stack through H-bonds in an ABAB fashion, resulting in 1-D channels.

2.6 Other "small" biomolecules

Besides the common molecules (*e.g.* AAs, peptides, proteins, *etc.*) that one typically recognizes as biomolecules, there are also many acids and bases naturally present in humans, animals or plants as either the free acid or carboxylate salt. Some of these molecules have more than one carboxylate group, which make them perfect candidates as MBioF linkers (Fig. 10a). These carboxylic acids include formic and oxalic acids and fumaric, glutaric, malic and succinic acids that play key roles as intermediates in the Krebs cycle, which is of central importance in all living cells. All of these linkers have been extensively used to obtain a wide diversity of metal–organic frameworks. For this reason, a number of excellent reviews have been recently published detailing this area. Rather than focusing on all the different frameworks obtained with these particular types of biomolecules,[65] this section of the review will outline some basic concepts and focus only on a few recent examples that illustrate their important role as bridging ligands.

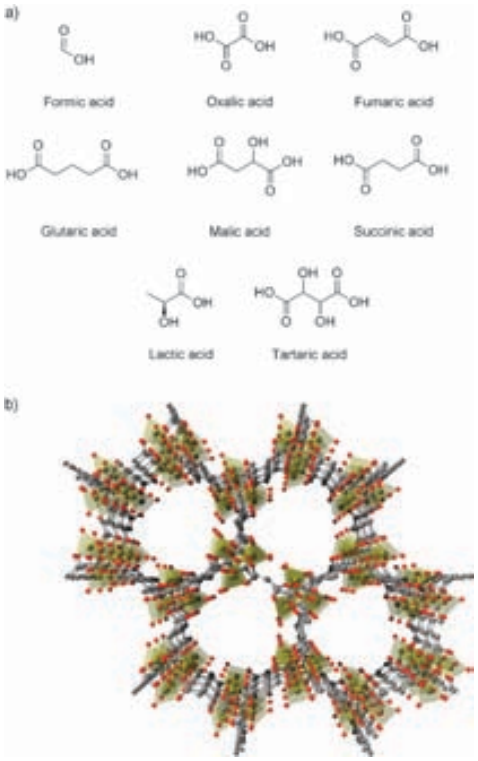

Fig. 10 (a) Representation of some dicarboxylate ligands that are naturally present in humans, animals or plants. (b) Representation of the porous structure $[Fe_3O(MeOH)_3(fum)_3(CO_2CH_3)]\cdot 4.5MeOH$.

Formic acid is the simplest carboxylic acid. Although it has a very simple structure, formate leads to a large variety of coordination modes, and consequently, it can be used to form topologically different metal–organic architectures when it is associated to divalent or trivalent metal ions. An illustrative example is the porous 3-D Mn(II) formate with formula $[Mn(HCOO)_2]\cdot 1/3(C_4H_8O_2)$ reported by Kim *et al.*[66] In this structure, each Mn(II) ion is coordinated by six formate ligands and each formate ligand is bound to three Mn(II) ions to form a porous material with 1-D zigzag channels having windows of approximately 4.5 Å in diameter. The BET surface of this material after guest removal is 240 $m^2\ g^{-1}$. In addition, Cheetham *et al.* recently described $[M(HCOO)_3]\cdot[(CH_3)_2NH_2]$ (where M is Zn(II) or Mn(II)), a 3-D multiferroic framework.[67]

Similar to formic acid, other common natural diacids, such as oxalic, succinic (suc) and fumaric (fum) acids, also exhibit a rich coordination chemistry that can be used to create functional frameworks.[68] For example, as shown in Fig. 10b, Férey *et al.* reported a 3-D Fe(III) fumarate open-framework with formula $[Fe_3O(MeOH)_3(fum)_3(CO_2CH_3)]\cdot 4.5MeOH$.[69] This framework has trimeric clusters connected to each other through fumarate ligands. Each cluster is formed by three octahedral Fe(III) ions bridged by six fumarate dianions. The resulting structure has a 1-D pore channel system that is filled with solvent and cages that are filled with acetate groups. Interestingly, this structure exhibits unique swelling behaviour upon adsorption of water and various alcohols.[70]

Another molecule that is naturally available in plants and also as one of the main acids in wine is tartaric acid. Using tartaric acid, Williams *et al.* prepared several tartrate-derived chiral porous frameworks.[71] Also, lactic acid or milk acid, which plays a role in biochemical processes, has been used to synthesize metal–organic frameworks. For example, Kim *et al.* reported the synthesis and properties of a 3-D permanently porous framework having 1-D channels with dimensions of 5 Å.[72]

3. Metal–biomolecule submicron structures

Miniaturization of MBioFs to the submicron scale regime is a very important strategy for the development of new materials with novel and often enhanced properties compared to the aforementioned MBioFs, opening up novel avenues for their use, for example, in biomedical applications.[73] In nature, the self-assembly of biomolecules provides a large number of submicron structures that have a rich range of shapes, sizes and essential functionalities. It is expected, then, that the association of biomolecules with metal ions under specific conditions could also yield novel "artificial" functional metal–biomolecule submicron structures.

There are two types of potential metal–biomolecule submicron structures: (i) crystalline particles, and (ii) amorphous particles. The first class can be prepared by using synthetic methodologies in which the crystallization process is controlled at this length scale. This control can be achieved, for example, by increasing the nucleation rate through the use of solvothermal conditions, microwave, ultrasound, rapid precipitation, *etc.*, or by confining the crystallization using an emulsion or a template. To date, both solvothermal and microwave conditions have been used by Férey *et al.* to miniaturize the above-mentioned

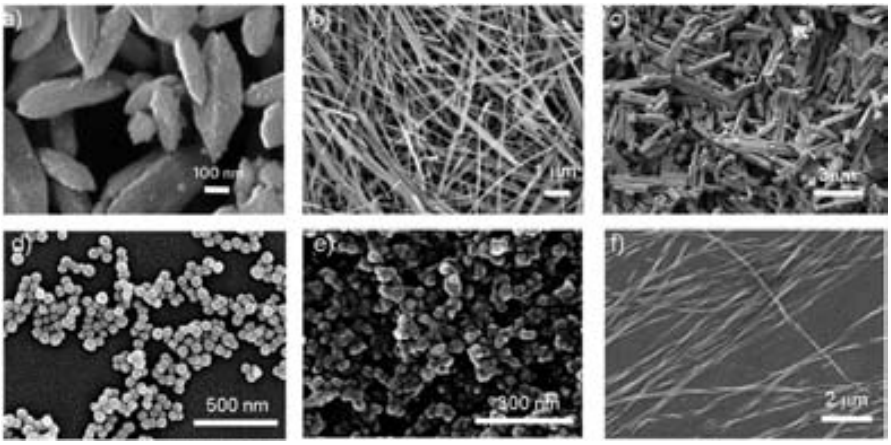

Fig. 11 Representative SEM images of metal–biomolecule submicron structures showing the wide diversity of morphologies obtained so far: (a) submicron $[Fe_3O(MeOH)_3(fum)_3(CO_2CH_3)]\cdot 4.5MeOH$ seed-like crystals, (b) crystalline Cu(II)–Asp fibers, (c) Cu(II)–ValValGlu rod-like crystals, (d) amorphous Tb(III)-*c*,*c*,*t*-(diamminedichlorodisuccinato)Pt(IV) spheres, (e) amorphous Gd(III)-5′-AMP particles, and (f) Ag(I)–Cys nanobelts. (© The Nature Publishing Group and The American Chemical Society, reprinted with permission.)

$[Fe_3O(MeOH)_3(fum)_3(CO_2CH_3)]\cdot 4.5MeOH$ MBioF (Fig. 11).[74] By controlling the hydrothermal synthetic conditions (temperature and time), the authors controlled its nucleation, and consequently, the resulting crystalline particle size (up to 150 nm in diameter). Submicron crystalline metal–AA fibers have also been prepared by Maspoch *et al.* using the coordination of Cu(II) ions and Asp ligands followed by a fast precipitation.[75] Here, the length of the fibers was controlled by adjusting the addition rate of Asp solution, which was inversely related to the length of the fibers produced. For example, mixing both solutions by using a very slow diffusion rate led to very long (up to one centimetre) fibers, whereas a fast mixing decreased this length up to tens of micrometres. Similarly, Mantion and Taubert *et al.* have reported the formation of a series of metal–peptide rod-like submicron crystals.[76] These crystals were obtained by combining Cu(II) or Ca(II) ions with a protected ValValGlu at room temperature and at 80 °C.

Clearly, biomolecules are usually flexible molecules that are difficult to crystallize. For this reason, it is not surprising that most of the metal–biomolecule submicron structures generated to date are amorphous particles. Even though their amorphous character precludes precise characterization of the metal ion–biomolecule connectivity and dimensionality, it is clear that the formation of these amorphous particles is principally due to bridging interactions between metal ions and biomolecules. For example, Lin *et al.* used fast precipitation methods to obtain sub-50 nm metal–organic spherical particles constructed from Tb(III) ions and *c*,*c*,*t*-(diamminedichlorodisuccinato)Pt(IV).[77] Similar spherical colloidal particles have also been obtained using nucleobases and nucleotides.[78,79] Indeed, Dong, Wang *et al.* synthesized particles by mixing $HAuCl_4$ and adenine at room temperature,[78] whereas Kimizuka *et al.* prepared fluorescent 40 nm spheres by combining lanthanide ions (*e.g.* Gd(III), Tb(III), *etc.*) and the nucleotide 5′-AMP.[79]

Amorphous fibers have also been prepared using mixing methods. With this simple methodology, Chmielewski *et al.* synthesized metal–collagen fibers that assembled upon addition of transition metals (*e.g.* Zn(II), Cu(II), Ni(II) and Co(II)) to a peptide composed of repeating Pro-Hyp-Gly sequences modified with metal coordination nodes, such as nitrilotriacetic acid, histidine and bipyridil.[80] Similarly, Tang *et al.* and Abramchuk *et al.* bridged Ag(I) ions by Cys ligands to create metal–AA nanobelts and nanofibers,[81] whereas Kimizuka *et al.* obtained metal–nucleotide fibers when mixing Tb(III) ions and the nucleotide dG_2MP in molar ratios from 1 : 1 to 1 : 3.[82]

Another excellent strategy that allows the fabrication of fibers and wires is their controlled assembly on solid surfaces. Zamora, Gómez-Herrero *et al.* enormously contributed to develop this approach.[83] These authors used different deposition methods, including sonication, drop casting and sublimation, to generate, for example, single Cd(II)–mercaptopurine chains on mica.

4. Properties and applications

A wide range of promising properties can be obtained by taking advantage of the multiple inorganic and biomolecular building blocks that can be combined to prepare MBioFs. As a subclass of MOFs, MBioFs can exhibit porous structures with high internal surface areas, high porosities, and tailorable pore sizes. Also, the ability of metal ions to interact with phonons and electrons allows for the preparation of MBioFs with interesting magnetic, luminescence, ferroelectric and electronic properties. A number of excellent reviews have recently been published detailing the field of magnetic, electronic and optical MOFs,[84,85] including some examples of MBioFs. So, rather than focusing on these properties which are expected to be similar to those exhibited by MOFs, this section of the review will outline some examples in which the use of biomolecules improves upon current MOF capabilities or introduces new potential applications.

4.1 Storage

Table 1 summarizes the storage capacity of some remarkable permanently porous MBioFs. It is well known that the

Table 1 Representative permanently porous MBioFs

Compound	T^a/°C	N_2/BET surface ($m^2\ g^{-1}$)	Gas and molecular storage	Ref.
AAs				
$[Ni_2O(L\text{-}Asp)H_2O]\cdot 4H_2O$	80 (vacuum)	157	1,3-Butanediol sorption	24
$[Ni_2(L\text{-}Asp)_2(4,4'\text{-bipy})]\cdot 2H_2O$	200		CO_2 (247 $m^2\ g^{-1}$) sorption	33
$[Co_2(L\text{-}Asp)_2(4,4'\text{-bipy})]\cdot 2H_2O$	150 (vacuum)		H_2 sorption	34
Peptides				
$[Zn(GlyAla)_2]\cdot$(solvent)			Reversible flexible structure; CO_2, MeOH and H_2O sorption	44
Nucleobases				
$[Co_2(Ade)_2(CO_2CH_3)_2]\cdot 2DMF\cdot 0.5H_2O$	100 (vacuum)	1040	Selective CO_2 (6.0 mmol g^{-1} at 1 bar and 0 °C) sorption	58
$[Zn_8(Ade)_4(bpdc)_6O\cdot 2Me_2NH_2\cdot 8DMF\cdot 11H_2O]$	100 (vacuum)	1700	Cation exchange capabilities, including cationic drugs and lanthanide ions	57
Saccharides				
$[(\gamma\text{-CD})(KOH)_2]$	175	1220		62
$[(\gamma\text{-CD})(RbOH)_2]$	200	1030	Inclusion of several molecules (*e.g.* Rhodamine B, 4-phenylazoplenol, *etc.*)	62
Other "small" biomolecules				
$[Ni_7(suc)_6(OH)_2(H_2O)_2]\cdot 2H_2O$	200–240		Reversible H_2O sorption/desorption	90
$[Ni_7(suc)_4(OH)_6(H_2O)_3]\cdot 7H_2O$	170 (vacuum)	135		91
[Cu(*trans*-fum)]			Ar (416 $m^2\ g^{-1}$) and CH_4 (82 $cm^3\ g^{-1}$) sorption	92
$[Mn_3(HCOO)_6]\cdot(CH_3OH)\cdot(H_2O)$	110 (vacuum)		Sorption of more than 30 kinds of guests (*e.g.* DMF, benzene, *etc.*); structural changes	93
$Mn(HCOO)_2\cdot 1/3(C_4H_8O_2)$	150	240	Selective CO_2 (297 $m^2\ g^{-1}$), and H_2 (240 $m^2\ g^{-1}$) sorption	66

[a] Activation temperature.

sorption and storage capabilities of metal–organic materials are directly related to their structural characteristics.[86] For this reason, an important factor to be considered here is that most biomolecules are flexible molecules. Flexibility is sometimes a hindrance to the preparation of robust porous frameworks, but it can also be an excellent characteristic for designing flexible porous frameworks which can serve as responsive and adaptable materials.[87,88] A first example of this class of materials has been recently reported by Rosseinsky *et al.*,[44] who synthesized the adaptable porous $[Zn(GlyAla)_2]\cdot$(solvent) (Fig. 6). Once desolvated, neighbouring peptides within the structure hydrogen bond together, which in turn occludes the pores, as confirmed by the inability of the material to adsorb N_2 and H_2 at 77 K. However, these pores gradually and cooperatively open when triggered by small molecules having polar bonds, including water, MeOH and CO_2. This behaviour is a direct consequence of the flexibility of GlyAla (Fig. 5), because the torsional degrees of freedom of these dipeptide ligands, which strongly depend on their interaction with guest molecules, allow the methyl group to impact the accessible void volume. For example, when CO_2 molecules penetrate the pores, the hydrogen bonds between neighbouring peptides break because of the repulsion between the methyl group and CO_2.

In contrast, there are not many biomolecules that can act as rigid ligands. One of these biomolecules, Ade, has been used by An and Rosi to prepare two porous MBioFs. $[Zn_8(Ade)_4(bpdc)_6\cdot O\cdot 2Me_2NH_2]$ is an anionic porous material with a measured BET surface area of 1700 $m^2\ g^{-1}$. The dimethylammonium cations that reside in its pores can be exchanged with tetramethylammonium, tetraethylammonium and tetrabutylammonium cations when it is soaked in DMF solutions containing these cations.[89] This cation-exchange process systematically decreases the pore volume and surface area of the resulting material and allows one to tune its N_2 and CO_2 adsorption capacities. In addition, a second framework, $[Co_2(Ade)_2(CO_2CH_3)_2]\cdot 2DMF\cdot 0.5H_2O$, exhibits interesting adsorption properties: it has a high CO_2 capacity, with an impressive selectivity for CO_2 over N_2.[58] As suggested by the authors, the presence of the Lewis basic amino and pyrimidine groups of Ade as well as the narrow pore dimensions of this material improve the CO_2 adsorption properties.

4.2 Catalysis and separation

An important property of biomolecules is that they can act as chiral ligands to induce the formation of homochiral MBioFs. This property together with the above-mentioned adsorption capabilities opens the possibility to use MBioFs for heterogeneous asymmetric catalysis and enantioselective separation.[40]

In 2006, Rosseinsky *et al.* showed that the $[Ni_2(L\text{-}Asp)_2(4,4'\text{-bipy})]\cdot$guest (Fig. 4a) exhibits significant enantioselective sorption capabilities of small chiral diols,[33] with levels of enantioselectivity as high as 53.7% ee (enantioselective excess) for the sorption of 2-methyl-2,4-pentane-diol. Recently, the same authors also introduced Brønsted acidic –COOH sites into the same family of chiral porous MBioFs *via* post-synthetic modification for heterogeneous asymmetric catalytic methanolysis of *cis*-2,3-epoxybutane.[94] Treatment of the $[Ni_2(L\text{-}Asp)_2(4,4'\text{-bipy})]\cdot$guest and $[Cu_2(L\text{-}Asp)_2(bpe)]\cdot$guest (where bpe is 1,2-bis(4-pyridyl)ethane) with HCl in Et_2O affords the protonated $[Ni_2(L\text{-}Asp)_2(4,4'\text{-bipy})\cdot(HCl)_{1.8}(MeOH)]$ and $[Cu_2(L\text{-}Asp)_2(bpe)\cdot(HCl)_2\cdot(H_2O)_2]$ frameworks. Both resulting materials are active as heterogeneous asymmetric catalysts for the methanolysis of *rac*-propylene oxide. Fig. 12 illustrates that the porous Cu(II)-based MBioF also shows good catalytic

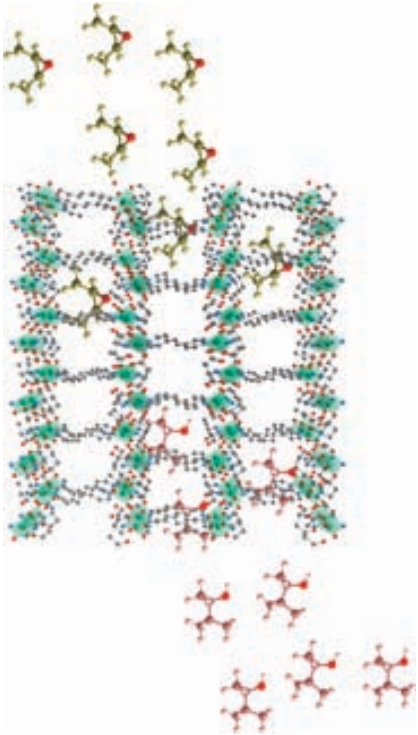

Fig. 12 Schematic illustration of the methanolysis of epoxides (*cis*-2,3-epoxybutane) using $[Cu_2(L\text{-}Asp)_2(bpe)\cdot(HCl)_2\cdot(H_2O)_2]$ as an heterogeneous asymmetric catalyst.

activity for the methanolysis of other epoxides. Its chiral induction ability, however, is modest, and the best results were observed for the methanolysis of the *cis*-2,3-epoxybutane that afforded 3-methoxybutan-2-ol with a modest 17% ee.

Kim and Fedin *et al.* also have studied the enantioselective separation and catalytic properties of $[Zn_2(bdc)(L\text{-}lac)(DMF)\cdot DMF]$ (where bdc is 1,4-benzendicarboxylic acid and L-lac is L-lactic acid).[72] When this MBioF is stirred in the presence of racemic mixtures of sulfoxides, the resulting material shows high enantioselective adsorption capability to sulfoxides with smaller substituents. The ee values for these adsorbed sulfoxides were between 20 and 27% with excess of the *S* enantiomer in all cases. In addition, the same MBioF shows excellent size- and chemoselective catalytic oxidation of thiothers to sulfoxides by urea hydroperoxide or hydrogen peroxide. These interesting results inspired Fedin and Bryliakov *et al.* to fabricate the first chiral chromatographic column for the separation of racemic mixtures of chiral alkyl aryl sulfoxides using this enantiopure MBioF as the stationary phase.[95] Also, by combining its chromatographic and catalytic properties, the authors developed a one-pot process for the synthesis of enantiomerically pure sulfoxides.

4.3 Biomedical applications

The molecular storage-release capabilities and potential biocompatibility of MBioFs together with the possibility to miniaturize them to the submicron length scale are excellent characteristics that allow these materials to be exploited as novel delivery systems for active species (*e.g.* drugs, vaccines, genes, *etc.*) in the fields of medicine, pharmaceutics and cosmetics. Thus far, however, such biomedical applications have not been fully explored, and only some examples of MBioFs that can adsorb and release drugs have been reported. A possible explanation is that many examples of MBioFs stable in aqueous and buffer conditions are not yet known. For instance, Rosi *et al.* demonstrated controlled drug release of $[Zn_8(Ade)_4(bpdc)_6O\cdot 2Me_2NH_2]\cdot 8DMF\cdot 11H_2O$.[57] This MBioF is modestly stable in water and biological buffers for several weeks; however, its toxicity is still unknown. Procainamide, which is a cationic drug molecule, was loaded into the pores of material *via* cationic exchange with the dimethylammonium cations that initially reside inside the pores (Fig. 13a). In addition, procainamide release was monitored in PBS buffer, and it was shown that cation exchange of drug molecules with cations within the buffer likely played a role in the drug release process. It was shown that 0.22 g of procainamide per gram of MBioF was loaded and that drug release was completed after $\sim$3 days.

Similarly, Horcajada *et al.* have recently reported an excellent study that proves the promising use of submicron crystals of MBioFs as platforms for drug delivery and imaging.[74] They showed that two MBioFs, such as $[Fe_3O(MeOH)_3(fumarate)_3\text{-}(CO_2CH_3)]\cdot 4.5MeOH$ and $[Fe_3O(MeOH)(C_6H_4O_8)_3Cl]\cdot 6MeOH$ (where $C_6H_4O_8$ is galactarate), could adsorb appreciable amounts of several drugs (*e.g.* busulfan, azidothymidine triphosphate and cidofovir). The loading was achieved by soaking both MBioFs in saturated drug solutions. Interestingly, in both cases, the successful design of the drug delivery system was confirmed by proving the controlled and progressive release of the encapsulated drug as well as their *in vitro* anticancer efficacies. Finally, and very importantly, these authors also proved that the degradation of these MBioFs produces endogenous substances, thus minimizing their toxicity. For example, the fumarate-derived MBioF degrades after seven days of incubation at 37 °C, releasing large quantities of their ligands (72% of fumaric acid) and Fe(III) ions. These major degradation products are endogenous, and consequently, the toxicity values are low [LD_{50}(Fe(III)) = 30 g kg^{-1} and LD_{50}(fumaric acid) = 10.7 g kg^{-1}]. The low toxic effects of these MBioFs were further demonstrated by *in vivo* subacute toxicity assays done by injecting up to 150 mg of sub-micron crystals during four consecutive days.

Fig. 13b shows another excellent strategy for using MBioFs in therapeutic applications. When the active species to be released is a naturally available molecule, this molecule can be used as an organic ligand to construct the framework. As a consequence, the MBioF releases the active species at the specific place where it degrades. This approach has been used by Serre *et al.* to fabricate a therapeutically active MBioF from the association of non-toxic Fe(III)–Fe(II) (LD_{50} = 30 g kg^{-1}) and nicotinic acid (pyridine-3-carboxylic acid, also called niacin or vitamin B3).[96] Since the resulting material degrades rapidly under physiological conditions, the release of nicotinic acid was achieved within few hours.

Alternatively, the active ingredient of the MBioF can be the inorganic component and a naturally available molecule can be used as a bridging ligand to create a therapeutically active metal–organic network. This approach was first used by Lin *et al.*, who demonstrated the formation of sub-50 nm spherical

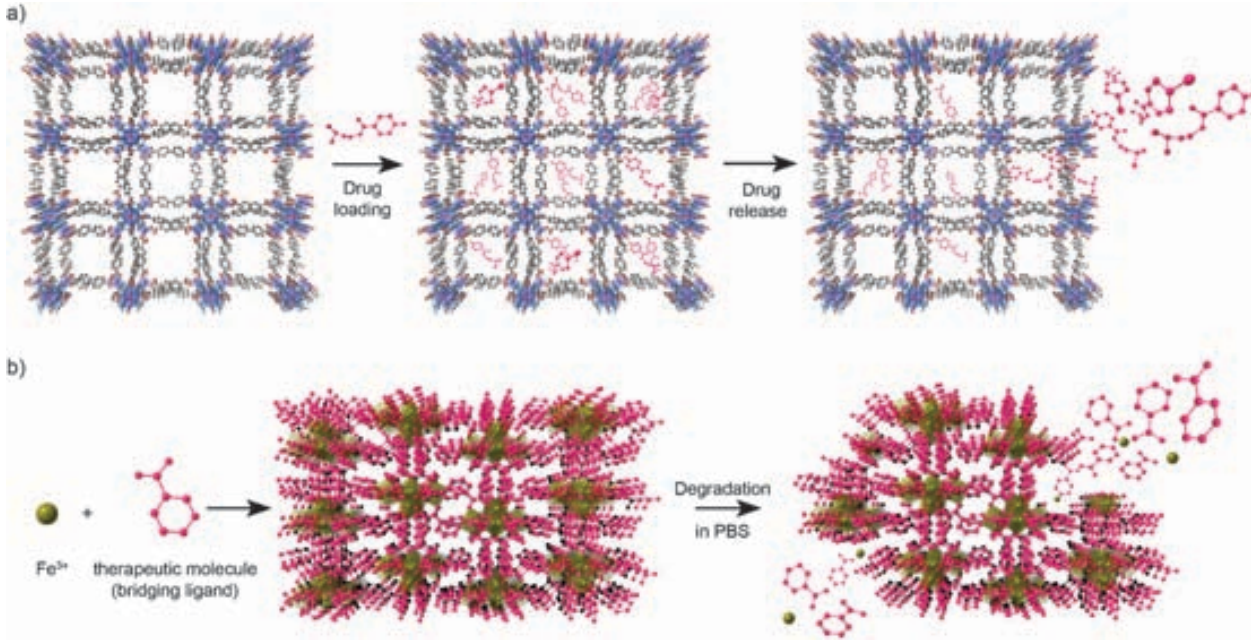

Fig. 13 Schematic illustration showing two potential approaches to use MBioFs as therapeutic carriers. (a) The use of MBioFs (illustrated by $[Zn_8(Ade)_4(bpdc)_6O{\cdot}2Me_2NH_2]$) for encapsulating and further releasing therapeutic species. (b) The use of therapeutic species as bridging organic ligands to build up the MBioF; the therapeutic species are released as the MBioF degrades.

particles constructed from the linkage of the cisplatin antitumoral drug by succinic acid.[77] These Pt-containing spheres were further coated with an amorphous silica-shell to control the degradation, and therefore, the antitumoral complex release.

MBioFs are also excellent candidates for serving as contrast agents because they can be composed of biocompatible organic ligands and highly paramagnetic metal ions (*e.g.* Gd(III), Mn(II), *etc.*). For instance, Horcajada and Gref *et al.* contributed to this field by synthesizing a NMOF comprising Fe(III) metal ions connected through fumarate ligands that show a R1 relaxivity of 50 s^{-1} mM^{-1} of Fe(III), which can be considered sufficient for *in vivo* use (Fig. 14).[74]

4.4 Sensors

MBioFs have two major advantages that render them useful as novel sensors. First, they can be permanently porous structures and can exhibit high surface areas. Second, interactions between guest molecules and the pores of metal–organic structures can induce changes in their physical properties. Third, some biomolecules (*e.g.* peptides, antibodies) have the ability to recognize specific analytes. Thus far, however, few sensors based on MBioFs have been reported, and only the porous anionic $[Zn_8(Ade)_4(bpdc)_6{\cdot}O{\cdot}2Me_2NH_2]$ framework loaded with lanthanide cations has shown promise for serving as a photostable O_2 sensor (Fig. 15).[97] This MBioF is able to incorporate lanthanide ions (*e.g.* Tb(III), Sm(III), Eu(III) and Yb(III)) simply by soaking it in DMF solutions of nitrate salts of these ions. Importantly, the resulting materials are luminescent, even in water, a property that can be used to detect O_2 and that points toward their potential applicability as intracellular O_2 sensors. Indeed, when a sample of Yb(III)-loaded MBioF was exposed to O_2 gas, an approximate 40% decrease in

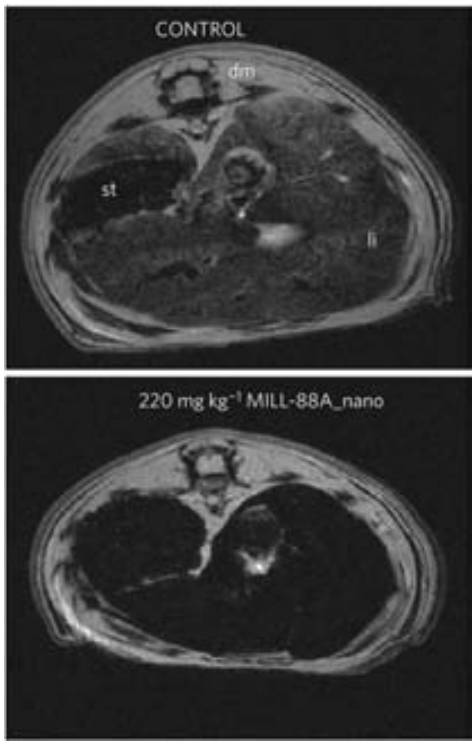

Fig. 14 Magnetic resonance images acquired with gradient echo of control rats (top) and rats injected with 220 mg kg^{-1} of $[Fe_3O(MeOH)_3(fum)_3(CO_2CH_3)]{\cdot}4.5MeOH$ (bottom) in liver. (© The Nature Publishing Group, reprinted with permission.)

Yb(III) luminescence was observed within the first 5 minutes. Interestingly, the total signal intensity was recovered after exposing this material to N_2. Importantly, this experiment

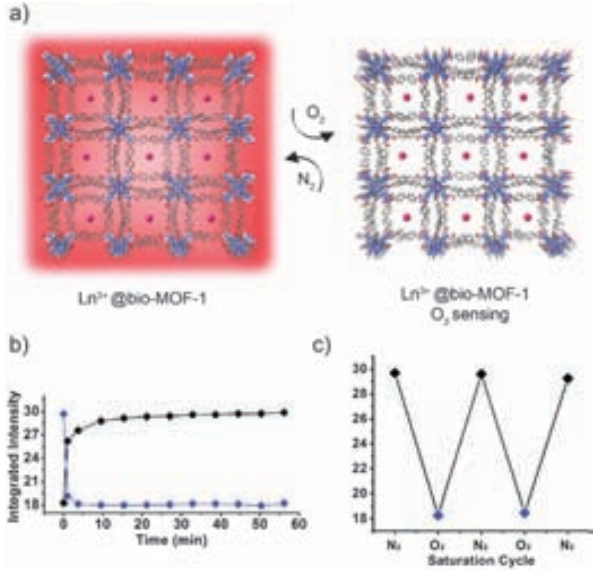

Fig. 15 (a) Schematic illustration showing the potential use of $[Zn_8(Ade)_4(bpdc)_6{\cdot}O{\cdot}2Me_2NH_2]$ as a O_2 sensor. (b) Decrease in the Yb(III) luminescence signal over time upon exposure to O_2 (blue) and revival of the Yb(III) signal over time exposure to N_2 (black). (c) Integrated intensities of Yb(III) emission over multiple cycles of exposure to N_2 (black) and O_2 (blue). (© The American Chemical Society, reprinted with permission.)

was reversible after several cycles of exposure to O_2 and N_2. We also note that the near-infrared luminescence of Yb(III) is ideal for biological samples, which are virtually transparent to NIR radiation.

5. Conclusions and outlook

MOFs are increasingly finding applications as drug-delivery agents, contrast agents, catalysts, sensors, and storage and separation systems. Many of these applications require biologically and environmentally compatible MOFs. We expect that many of these potential applications may become a reality if the MOFs are constructed from biomolecules. Biomolecules provide the ideal characteristics to construct more biologically compatible and easily recyclable MOFs, endow MOFs with outstanding functionalities, such as chirality and specific recognition/self-assembly capabilities, and serve as building blocks for bioinspired structures with dimensions down to the micrometre length scale. Compared to the synthesis of MOFs with conventional organic linkers, the field of MBioFs is in its nascent stage. The application of MBioFs to biomedicine, for example, will strongly benefit from a better understanding of and better control over the coordination chemistry of biomolecules and the development of new synthetic and crystallization methodologies. This future research, which will involve scientists of many different fields, will certainly expand the variety of biomolecules (*e.g.* long peptides, proteins, DNA, *etc.*) that can be used for constructing MBioFs, which in turn will broaden the scope of structures, properties and practical applications of this exciting class of MOFs.

Acknowledgements

This work was supported by projects VALTEC08-2-003 and MAT2009-13977-C03. D. M. and I. I. thank the Ministerio de Ciencia e Innovación for RyC contracts. M. R.-F. thank the Catalan Institute of Nanotechnology for a research fellowship. N.R. acknowledges support from the University of Pittsburgh and the American Chemical Society Petroleum Research Fund (PRF 47601-G10).

Notes and references

1 Special issue on metal–organic framework materials. *Chem. Soc. Rev.* 2009, **38**, 1201.
2 (*a*) O. M. Yaghi, M. O'Keeffe, N. W. Ockwig, H. K. Chae, M. Eddaoudi and J. Kim, *Nature*, 2003, **423**, 705–714; (*b*) C. Janiak, *Dalton Trans.*, 2003, 2781–2804; (*c*) J. L. James, *Chem. Soc. Rev.*, 2003, **32**, 276–288; (*d*) U. Mueller, M. Schubert, F. Teich, H. Puetter, K. Schierle-Arnd and J. Pastre, *J. Mater. Chem.*, 2006, **16**, 626–636.
3 G. Férey, *Chem. Soc. Rev.*, 2008, **37**, 191–214.
4 O. Yamauchi, A. Odani and M. Takani, *J. Chem. Soc., Dalton Trans.*, 2002, 3411–3421.
5 C. D. L. Saunders, N. Burford, U. Werner-Zwanziger and R. McDonald, *Inorg. Chem.*, 2008, **47**, 3693–3699.
6 (*a*) C. D. Ch'ng, S. G. Teoh, S. Chantrapromma, H. K. Fun and S. M. Goh, *Acta Crystallogr., Sect. E: Struct. Rep. Online*, 2008, **64**, M865–M866; (*b*) M. Fleck and L. Bohaty, *Acta Crystallogr., Sect. C: Cryst. Struct. Commun.*, 2005, **61**, M412–M416.
7 (*a*) R. Mrozek, Z. Rzaczynska, M. Sikorska-Iwan and T. Glowiak, *J. Chem. Crystallogr.*, 1999, **29**, 803–808; (*b*) T. Glowiak and Z. Ciunik, *Acta Crystallogr., Sect. B: Struct. Crystallogr. Cryst. Chem.*, 1978, **34**, 1980–1983.
8 K. Stenzel and M. Fleck, *Acta Crystallogr., Sect. E: Struct. Rep. Online*, 2004, **60**, M1470–M1472.
9 J. B. Weng, M. C. Hong, R. Cao, Q. Shi and A. S. C. Chan, *Chin. J. Struct. Chem.*, 2003, **22**, 195–199.
10 D. Vanderhe, M. B. Lawson and E. L. Enwall, *Acta Crystallogr., Sect. B: Struct. Crystallogr. Cryst. Chem.*, 1971, **B27**, 2411–2418.
11 Y. Xie, H. H. Wu, G. P. Yong and Z. Y. Wang, *Acta Crystallogr., Sect. E: Struct. Rep. Online*, 2006, **62**, M2089–M2090.
12 J. Wang, X. Xu, W. Ma, L. Lu and X. Yang, *Acta Crystallogr., Sect. E: Struct. Rep. Online*, 2007, **63**, M2867–M2868.
13 J. M. Schveigkardt, A. C. Rizzi, O. E. Piro, E. E. Castellano, R. C. de Santana, R. Calvo and C. D. Brondino, *Eur. J. Inorg. Chem.*, 2002, 2913–2919.
14 H. Strasdeit, I. Busching, S. Behrends, W. Saak and W. Barklage, *Chem.–Eur. J.*, 2001, **7**, 1133–1142.
15 L. Gasque, S. Bernes, R. Ferrari, C. R. de Barbarin, M. D. Gutierrez and G. Mendoza-Diaz, *Polyhedron*, 2000, **19**, 649–653.
16 L. Gasque, S. Bernes, R. Ferrari and G. Mendoza-Diaz, *Polyhedron*, 2002, **21**, 935–941.
17 (*a*) R. J. Flook, H. C. Freeman and M. L. Scudder, *Acta Crystallogr., Sect. B: Struct. Crystallogr. Cryst. Chem.*, 1977, **33**, 801–809; (*b*) M. X. Li, H. J. Zhao, M. Shao, Z. X. Miao and S. W. Liang, *J. Coord. Chem.*, 2007, **60**, 2549–2557.
18 E. V. Anokhina, Y. B. Go, Y. Lee, T. Vogt and A. J. Jacobson, *J. Am. Chem. Soc.*, 2006, **128**, 9957–9962.
19 J. A. Gould, J. T. A. Jones, J. Bacsa, Y. Z. Khimyak and M. J. Rosseinsky, *Chem. Commun.*, 2010, **46**, 2793–2795.
20 C. M. Gramaccioli, *Acta Crystallogr.*, 1966, **21**, 600–605.
21 (*a*) M. Mizutani, N. Maejima, K. Jitsukawa, H. Masuda and H. Einaga, *Inorg. Chim. Acta*, 1998, **283**, 105–110; (*b*) C. M. Gramaccioli and R. E. Marsh, *Acta Crystallogr.*, 1966, **21**, 594–600.
22 L. Antolini, G. Marcotrigiano, L. Menabue, G. C. Pellacani and M. Saladini, *Inorg. Chem.*, 1982, **21**, 2263–2267.
23 Y. G. Zhang, M. K. Saha and I. Bernal, *CrystEngComm*, 2003, **5**, 34–37.
24 E. V. Anokhina and A. J. Jacobson, *J. Am. Chem. Soc.*, 2004, **126**, 3044–3045.

25 (*a*) I. Csoregh, M. Czugler, P. Kierkegaard, J. Legendziewicz and E. Huskowska, *Acta Chem. Scand.*, 1989, **43**, 735–747; (*b*) I. Csoregh, P. Kierkegaard, J. Legendziewicz and E. Huskowska, *Acta Chem. Scand., Ser. A*, 1987, **41**, 453–460; (*c*) J. Torres, C. Kremer, E. Kremer, H. Pardo, L. Suescun, A. Mobru, S. Dominguez, A. Mederos, R. Herbst-Irmer and J. M. Arrieta, *J. Chem. Soc., Dalton Trans.*, 2002, 4035–4041.
26 B. Q. Ma, D. S. Zhang, S. Gao, T. Z. Jin, C. H. Yan and G. X. Xu, *Angew. Chem., Int. Ed.*, 2000, **39**, 3644–3646.
27 (*a*) R. Y. Wang, H. Liu, M. D. Carducci, T. Z. Jin, C. Zheng and Z. P. Zheng, *Inorg. Chem.*, 2001, **40**, 2743–2750; (*b*) H. Y. Zhang, H. J. Yu, H. X. Xu, J. S. Ren and X. G. Qu, *Polyhedron*, 2007, **26**, 5250–5256.
28 T. T. Luo, L. Y. Hsu, C. C. Su, C. H. Ueng, T. C. Tsai and K. L. Lu, *Inorg. Chem.*, 2007, **46**, 1532–1534.
29 L. Chen and X. H. Bu, *Chem. Mater.*, 2006, **18**, 1857–1860.
30 H. Y. An, E. B. Wang, D. R. Xiao, Y. G. Li, Z. M. Su and L. Xu, *Angew. Chem., Int. Ed.*, 2006, **45**, 904–908.
31 Z. L. Chen, C. F. Jiang, W. H. Yan, F. P. Liang and S. R. Batten, *Inorg. Chem.*, 2009, **48**, 4674–4684.
32 F. Luo, Y. T. Yang, Y. X. Che and J. M. Zheng, *CrystEngComm*, 2008, **10**, 1613–1616.
33 R. Vaidhyanathan, D. Bradshaw, J. N. Rebilly, J. P. Barrio, J. A. Gould, N. G. Berry and M. J. Rosseinsky, *Angew. Chem., Int. Ed.*, 2006, **45**, 6495–6499.
34 P. Zhu, W. Gu, F. Y. Cheng, X. Liu, J. Chen, S. P. Yan and D. Z. Liao, *CrystEngComm*, 2008, **10**, 963–967.
35 J. P. Barrio, J. N. Rebilly, B. Carter, D. Bradshaw, J. Bacsa, A. Y. Ganin, H. Park, A. Trewin, R. Vaidhyanathan, A. I. Cooper, J. E. Warren and M. J. Rosseinsky, *Chem.–Eur. J.*, 2008, **14**, 4521–4532.
36 (*a*) J. N. Rebilly, J. Bacsa and M. J. Rosseinsky, *Chem.–Asian J.*, 2009, **4**, 892–903; (*b*) M. J. Ingleson, J. Bacsa and M. J. Rosseinsky, *Chem. Commun.*, 2007, 3036–3038; (*c*) B. Wisser, Y. Lu and C. Janiak, *Z. Anorg. Allg. Chem.*, 2007, **633**, 1189–1192; (*d*) M. Dan, *J. Mol. Struct.*, 2004, **706**, 127–131; (*e*) G. Aromi, J. J. Novoa, J. Ribas-Arino, S. Igarashi and Y. Yukawa, *Inorg. Chim. Acta*, 2008, **361**, 3919–3925; (*f*) A. Ghosh and R. A. Sanguramath, *J. Chem. Sci.*, 2008, **120**, 217–222.
37 Z. R. Qu, H. Zhao, X. S. Wang, Y. H. Li, Y. M. Song, Y. J. Liu, Q. Ye, R. G. Xiong, B. F. Abrahams, Z. L. Xue and X. Z. You, *Inorg. Chem.*, 2003, **42**, 7710–7712.
38 Y. Xie, Z. Yu, X. Huang, Z. Wang, L. Niu, M. Teng and J. Li, *Chem.–Eur. J.*, 2007, **13**, 9399–9405.
39 H.-Y. Li, F.-P. Huang, Y.-M. Jiang and X.-J. Meng, *Inorg. Chim. Acta*, 2009, **362**, 1867–1871.
40 Y. Liu, W. Xuan and Y. Cui, *Adv. Mater.*, 2010, **22**, 4112–4135.
41 T. Takayama, S. Ohuchida, Y. Koike, M. Watanabe, D. Hashizume and Y. Ohashi, *Bull. Chem. Soc. Jpn.*, 1996, **69**, 1579–1586.
42 E. Ueda, Y. Yoshikawa, N. Kisshimoto, M. Tadokoro, H. Sakurai, N. Kajiwara and Y. Kojima, *Bull. Chem. Soc. Jpn.*, 2004, **77**, 981–986.
43 H. Y. Lee, J. W. Kampf, K. S. Park and N. G. Marsh, *Cryst. Growth Des.*, 2008, **8**, 296–303.
44 J. Rabone, Y. F. Yue, S. Y. Chong, K. C. Stylianou, J. Bacsa, D. Bradshaw, G. R. Darling, N. G. Berry, Y. Z. Khimyak, A. Y. Ganin, P. Wiper, J. B. Claridge and M. J. Rosseinsky, *Science*, 2010, **329**, 1053–1057.
45 (*a*) M. Tiliakos, E. Katsoulakou, A. Terzis, C. Raptopoulou, P. Cordopatis and E. Manessi-Zoupa, *Inorg. Chem. Commun.*, 2005, **8**, 1085–1089; (*b*) M. Tiliakos, D. Raptis, A. Terzis, C. P. Raptopoulou, P. Cordopatis and E. Manessi-Zoupa, *Polyhedron*, 2002, **29**, 229–238; (*c*) M. Tiliakos, E. Katsoulakou, V. Nastopoulos, A. Terzis, C. Raptopoulou, P. Cordopatis and E. Manessi-Zoupa, *J. Inorg. Biochem.*, 2003, **93**, 109–118.
46 R. Ferrari, S. Bernés, C. R. de Barbarín, G. Mendoza-Díaz and L. Gasque, *Inorg. Chim. Acta*, 2002, **339**, 193–201.
47 (*a*) T. Zhou, D. H. Hamer, W. A. Hendrickson, Q. J. Sattentau and P. D. Kwong, *Proc. Natl. Acad. Sci. U. S. A.*, 2005, **11**, 14575–14580; (*b*) I. Bertini, H. B. Gray, E. I. Stiefel, and J. S. Valentine, *Biological Inorganic Chemistry: Structure and Reactivity,* University Science Books, Sausalito, 2007; (*c*) J. Emsley, C. G. Knight, R. W. Farndale, M. J. Barnes and R. C. Liddington, *Cell*, 2000, **101**, 47–56.
48 E. N. Salgado, R. J. Radford and F. A. Tezcan, *Acc. Chem. Res.*, 2010, **43**, 661–672.
49 (*a*) J. D. Brodin, A. Medina-Morales, T. Ni, E. N. Salgado, X. I. Ambroggio and F. A. Tezcan, *J. Am. Chem. Soc.*, 2010, **132**, 8610–8617; (*b*) R. J. Radford, P. C. Nguyen, T. B. Ditri, J. S. Figueroa and F. A. Tezcan, *Inorg. Chem.*, 2010, **49**, 4362–4369; (*c*) R. J. Radford and F. A. Tezcan, *J. Am. Chem. Soc.*, 2009, **131**, 9136–9137; (*d*) E. N. Salgado, R. A. Lewis, J. Faraone-Mennella and F. A. Tezcan, *J. Am. Chem. Soc.*, 2008, **130**, 6082–6084; (*e*) E. N. Salgado, R. A. Lewis, S. Mossin, A. L. Rheingold and F. A. Tezcan, *Inorg. Chem.*, 2009, **48**, 2726–2728; (*f*) E. N. Salgado, J. Faraone-Mennella and F. A. Tezcan, *J. Am. Chem. Soc.*, 2007, **129**, 13374–13375.
50 R. J. Radford, M. Lawrenz, P. C. Nguyen, J. A. McCammon and F. A. Tezcan, *Chem. Commun.*, 2011, **47**, 313–315.
51 (*a*) N. Hadjiliadis and E. Sletten, *Metal-complexes–DNA interactions*, Blackwell Publishing Ltd, John Wiley & Sons Ltd., 2009; (*b*) S. Sivakova and S. J. Rowan, *Chem. Soc. Rev.*, 2005, **34**, 9–21.
52 S. Verma, A. K. Mishra and A. Kumar, *Acc. Chem. Res.*, 2010, **43**, 79–91.
53 M. A. Salam and K. Aoki, *Inorg. Chim. Acta*, 2000, **311**, 15–24.
54 (*a*) J. Y. An, R. P. Fiorella, S. J. Geib and N. L. Rosi, *J. Am. Chem. Soc.*, 2009, **131**, 8401–8403; (*b*) E. Sletten, *Acta Crystallogr., Sect. B: Struct. Crystallogr. Cryst. Chem.*, 1969, **B25**, 1480–1491; (*c*) P. X. Rojas-González, A. Castiñeiras, J. M. González-Pérez, D. Choquesillo-Lazarte and J. Niclós-Gutiérrez, *Inorg. Chem.*, 2002, **41**, 6190–6192.
55 (*a*) C. S. Purohit and S. Verma, *J. Am. Chem. Soc.*, 2006, **128**, 400–401; (*b*) C. S. Purohit and S. Verma, *J. Am. Chem. Soc.*, 2007, **129**, 3488–3489; (*c*) P. I. Vestues and E. Sletten, *Inorg. Chem.*, 1981, **52**, 269–274.
56 K. Gillen, R. Jensen and N. Davidson, *J. Am. Chem. Soc.*, 1964, **86**, 2792–2796.
57 J. An, S. J. Geib and N. L. Rosi, *J. Am. Chem. Soc.*, 2009, **131**, 8376–8377.
58 J. An, S. J. Geib and N. L. Rosi, *J. Am. Chem. Soc.*, 2010, **132**, 38–39.
59 J. P. Garcia-Teran, O. Castillo, A. Luque, U. Garcia-Couceiro, P. Roman and L. Lezama, *Inorg. Chem.*, 2004, **43**, 4549–4551.
60 E. C. Yang, H. K. Zhao, B. Ding, X. G. Wang and X. J. Zhao, *New J. Chem.*, 2007, **31**, 1887–1890.
61 C. S. Purohit, A. K. Mishra and S. Verma, *Inorg. Chem.*, 2007, **46**, 8493–8495.
62 R. A. Smaldone, R. S. Forgan, H. Furukawa, J. J. Gassensmith, A. M. Z. Slawin, O. M. Yaghi and J. F. Stoddart, *Angew. Chem., Int. Ed.*, 2010, **49**, 8630–8634.
63 B. F. Abrahams, M. Moylan, S. D. Orchard and R. Robson, *Angew. Chem., Int. Ed.*, 2003, **42**, 1848–1851.
64 B. F. Abrahams, M. Moylan, S. D. Orchard and R. Robson, *CrystEngComm*, 2003, **5**, 313–317.
65 C. N. R. Rao, S. Natarajan and R. Vaidhyanathan, *Angew. Chem., Int. Ed.*, 2004, **43**, 1466–1496.
66 D. N. Dybtsev, H. Chun, S. H. Yoon, D. Kim and K. Kim, *J. Am. Chem. Soc.*, 2004, **126**, 32–33.
67 P. Jain, V. Ramachandran, R. J. Clark, H. D. Zhou, B. H. Toby, N. S. Dalal, H. W. Kroto and A. K. Cheetham, *J. Am. Chem. Soc.*, 2009, **131**, 13625–13627.
68 P. M. Forster and A. K. Cheetham, *Angew. Chem., Int. Ed.*, 2002, **41**, 457–459.
69 C. Serre, F. Millange, S. Surble and G. Férey, *Angew. Chem., Int. Ed.*, 2004, **43**, 6286–6289.
70 C. Serre, C. Mellot-Draznieks, S. Surble, N. Audebrand, Y. Filinchuk and G. Férey, *Science*, 2007, **315**, 1828–1831.
71 S. Thushari, J. A. K. Cha, H. H. Y. Sung, S. S. Y. Chui, A. L. F. Leung, Y. F. Yen and I. D. Williams, *Chem. Commun.*, 2005, 5515–5517.
72 D. N. Dybtsev, A. L. Nuzhdin, H. Chun, K. P. Bryliakov, E. P. Talsi, V. P. Fedin and K. Kim, *Angew. Chem., Int. Ed.*, 2006, **45**, 916–920.
73 A. Carné, C. Carbonell, I. Imaz and D. Maspoch, *Chem. Soc. Rev.*, 2011, **40**, 291–305.
74 P. Horcajada, T. Chalati, C. Serre, B. Gillet, C. Sebrie, T. Baati, J. F. Eubank, D. Heurtaux, P. Clayette, C. Kreuz, J. S. Chang, Y. K. Hwang, V. Marsaud, P. N. Bories, L. Cynober, S. Gil, G. Férey, P. Couvreur and R. Gref, *Nat. Mater.*, 2010, **9**, 172–178.

75 I. Imaz, M. Rubio-Martínez, W. J. Saletra, D. B. Amabilino and D. Maspoch, *J. Am. Chem. Soc.*, 2009, **131**, 18222–18223.
76 A. Mantion, L. Massuger, P. Rabu, C. Palivan, L. B. McCusker and A. Taubert, *J. Am. Chem. Soc.*, 2008, **130**, 2517–2526.
77 W. J. Rieter, K. M. Pott, K. M. L. Taylor and W. B. Lin, *J. Am. Chem. Soc.*, 2008, **130**, 11584–11585.
78 H. Wei, B. Li, Y. Du, S. Dong and E. Wang, *Chem. Mater.*, 2007, **19**, 2987–2993.
79 (*a*) R. Nishiyabu, N. Hashimoto, T. Cho, K. Watanabe, T. Yasunaga, A. Endo, K. Kaneko, T. Niidome, M. Murata, C. Adachi, Y. Katayama, M. Hashizume and N. Kimizuka, *J. Am. Chem. Soc.*, 2009, **131**, 2151–2158; (*b*) R. Nishiyabu, C. Aime, R. Gondo, T. Noguchi and N. Kimizuka, *Angew. Chem., Int. Ed.*, 2009, **48**, 9465–9468; (*c*) C. Aim, R. Nishiyabu, R. Gondo and N. Kimizuka, *Chem.–Eur. J.*, 2010, **16**, 3604–3607.
80 M. M. Pires, D. E. Przybyla and J. Chmielewski, *Angew. Chem., Int. Ed.*, 2009, **48**, 7813–7817.
81 (*a*) C. Li, K. Deng, Z. Y. Tang and L. Jiang, *J. Am. Chem. Soc.*, 2010, **132**, 8202–8209; (*b*) P. M. Pakhomov, S. S. Abramchuk, S. D. Khizhnyak, M. M. Ovchinnikov and V. M. Spiridonova, *Nanotechnol. Russ.*, 2010, **5**, 209–213.
82 C. Aime, R. Nishiyabu, R. Gondo, K. Kaneko and N. Kimizuka, *Chem. Commun.*, 2008, 6534–6536.
83 (*a*) R. Mas-Ballesté, J. Gómez-Herrero and F. Zamora, *Chem. Soc. Rev.*, 2010, **39**, 4220–4233; (*b*) F. Zamora, *Inorg. Chim. Acta*, 2009, **362**, 691–706.
84 (*a*) D. Maspoch, D. Ruiz-Molina and J. Veciana, *Chem. Soc. Rev.*, 2007, **36**, 770–818; (*b*) M. Kurmoo, *Chem. Soc. Rev.*, 2009, **38**, 1353–1379; (*c*) D. Maspoch, D. Ruiz-Molina and J. Veciana, *J. Mater. Chem.*, 2004, **14**, 2713–2723.
85 M. D. Allendorf, C. A. Bauer and R. K. Bhakta, *Chem. Soc. Rev.*, 2009, **38**, 1330–1352.
86 J. R. Li, R. J. Kuppler and H. C. Zhou, *Chem. Soc. Rev.*, 2009, **38**, 1477–1504.
87 S. M. Hawxwell, G. Mínguez Espallargas, D. Bradshaw, M. J. Rosseinsky, T. J. Prior, A. J. Florence, J. van de Streek and L. Brammer, *Chem. Commun.*, 2007, 1532–1534.
88 G. Férey and C. Serre, *Chem. Soc. Rev.*, 2009, **38**, 1380–1399.
89 J. An and N. L. Rosi, *J. Am. Chem. Soc.*, 2010, **132**, 5578–5579.
90 P. M. Forster and A. K. Cheetham, *Angew. Chem., Int. Ed.*, 2002, **41**, 457–459.
91 N. Guillou, C. Livage, W. van Beek, M. Nogues and G. Férey, *Angew. Chem., Int. Ed.*, 2003, **42**, 644–647.
92 K. Seki, S. Takamizawa and W. Mori, *Chem. Lett.*, 2001, 122–123.
93 Z. M. Wang, B. Zhang, H. Fujiwara, H. Kobayashi and M. Kurmoo, *Chem. Commun.*, 2004, 416–417.
94 M. J. Ingleson, J. Perez Barrio, J. Bacsa, C. Dickinson, H. Park and M. J. Rosseinsky, *Chem. Commun.*, 2008, 1287–1289.
95 A. L. Nuzhdin, D. N. Dybtsev, K. P. Bryliakov, E. P. Talsi and V. P. Fedin, *J. Am. Chem. Soc.*, 2007, **129**, 12958–12959.
96 S. R. Miller, D. Hertaux, T. Baati, P. Horcajada, J. M. Grenèche and C. Serre, *Chem. Commun.*, 2010, **46**, 4526–4528.
97 J. An, C. M. Shade, D. A. Chengelis-Czegan, S. Petoud and N. L. Rosi, *J. Am. Chem. Soc.*, 2011, **133**, 1220–1223.

Chapter 2:

Objectives

Objectives

The main objective of the present PhD Thesis is i) to exploit the coordination capabilities of amino acids and peptides to develop novel nanoscale CPs in the form of nanofibers; and ii) use these nanofibers as (dual) scaffolds for the synthesis of superstructures made of inorganic nanoparticles taking advantage of the templating characteristics of CPs as well as the inherent recognition-template characteristics of peptides. To achieve this objective, a series of partial objectives have been defined. They are focused on increasing the complexity of i) the composition of the nanofibers, from amino acids to peptides; ii) the synthetic methodologies; and iii) the use of these nanofibers as scaffolds, from single to dual-scaffolds. These objectives are summarized in the following points:

- Design, synthesis and full characterization of 1-D nanofibers built up from the assembly of amino acids (AAs) and metal ions. Here, we aim to control the length of the resulting nanofibers by tuning the synthetic conditions.

- Introduce microfluidics technology (in particular microfluidic laminar flow) as a new synthetic approach to achieve precise control over the assembly process of metal ions and AAs to form nanofibers. In this way, we pretend to precisely control the location in which these nanofibers are synthesized.

- Study the use of metal-AA nanofibers made of amino acids (in particular, those made of Ag(I) ions and Cysteine) as single scaffolds to produce superstructures made of inorganic nanoparticles. Here, we aim to template the growth and assembly of inorganic nanoparticles along the nanofibers structure via reaction or reduction (*e.g.* thermal or photo) of the metal ions inside the scaffold structure. Taking advantage of microfluidics, we aim to control the precise location of the templated synthesis of the superstructures made of Ag nanoparticles, thereby allowing the direct measurement of their conductivity properties as well as their re-use as a template to grow conductive Ag(I)-tetracianoquinidimethane (TCNQ) CP crystals.

- Design, synthesis and full characterization of 1-D nanofibers assembled from using metal ions and peptides. Show that these metal-peptide nanostructures can be used as dual-templates for the synthesis and assembly of two types of inorganic nanoparticles, one on their surface (crystal face) and the other within their internal structures. For this, we aim to study the capability of these peptides to direct the nucleation, growth and/or assembly of inorganic nanoparticles on the surfaces of the nanofibers. Furthermore, we

aim to combine this capability with the use of the metal ions inside the nanofibers to grow and assembly other type of inorganic nanoparticles. As a result, we want to demonstrate the use of metal-peptide nanofibers as dual templates to develop core-shell, multifunctional superstructures that marry the properties (e.g. magnetism and conductivity) of the two-nanoparticle types.

Chapter 3:

Nanoscale Coordination Polymers made of Amino Acids

In this Chapter, we show the synthesis of chiral coordination polymer nanofibers that are formed from the association of Cu(II) ions and the amino acid Aspartic Acid. We anticipate that the length of these Cu(II)-Asp nanofibers could be controlled by using a diffusion controlled growth method. This method allowed the synthesis of nanofibers with lengths up to 1 centimeter. All these results are included in the manuscript "*Amino acid based metal-organic nanofibers*", Journal of the American Chemical Society 2009.

I. Assembling biomolecules in nanostructures

An important aspect of biomolecules is that they present encoded structural and functional information. Biomolecules have many functional groups (*e.g.* carbonyl, carboxyl, amino, sulfhydryl and phosphate groups) that can establish different types of weak interactions (that is, van der Waals, hydrophobic, electrostatic and hydrogen bonding) between them, thereby inducing their self-organization. Today, it is known that the self-assembly of biomolecules into more complex nanostructures is essential for the existence of life: biomolecules such as amino acids, proteins, DNA, virus particles and cells spontaneously self-assemble and auto-organize to form a myriad of complex nanostructures with essential functionalities in Nature.[1]

Figure 3.1 illustrates some examples of these nanostructures made of biomolecules. One of these examples is collagen, which is a structural protein made of repetitious amino acid sequences forming a triple helix shape, where each chain is hydrogen bonded to each other. Figure 3.1.a shows a transmission electron microscope (TEM) image of a thin section cut through an area of mammalian lung tissue, in which a connective tissue of fibers of Collagen Type I is seen. A second example is the nucleosome that consists of a segment of DNA wound in sequence around eight histone protein cores. Many nucleosome core particles are connected by stretches of linker DNA, creating a nucleosomal thread (also referred to as "beads-on-a-string"; Figure 3.1.b). Other well-known examples are DNA fibers and amyloids. DNA molecules are double-stranded helices formed by nucleobases, which are self-assembled through hydrogen-bond and π-π stacking interactions (Figure 3.1.c).[2,3] In the second case, amyloids are highly ordered filamentous structures formed by the self-assembly of polypeptide molecules stabilized by a network of hydrogen bonds and hydrophobic interactions (Figure 3.1.d). Two other examples found in Nature are the nanotubular Tobacco Mosaic Virus (TMV) and the Streptococcus pyogenes bacteria. The helical architecture of the TMV (Figure 3.1.e) is formed by the self-assembly of 2000 copies of the same protein wrap around a single strand of RNA[4], whereas Streptococcus pneumonia is a Gram-positive bacteria composed of multiple subunits of a single major backbone (pilin) that are covalently attached to each other leading to the formation of chains (Figure 3.1.e).

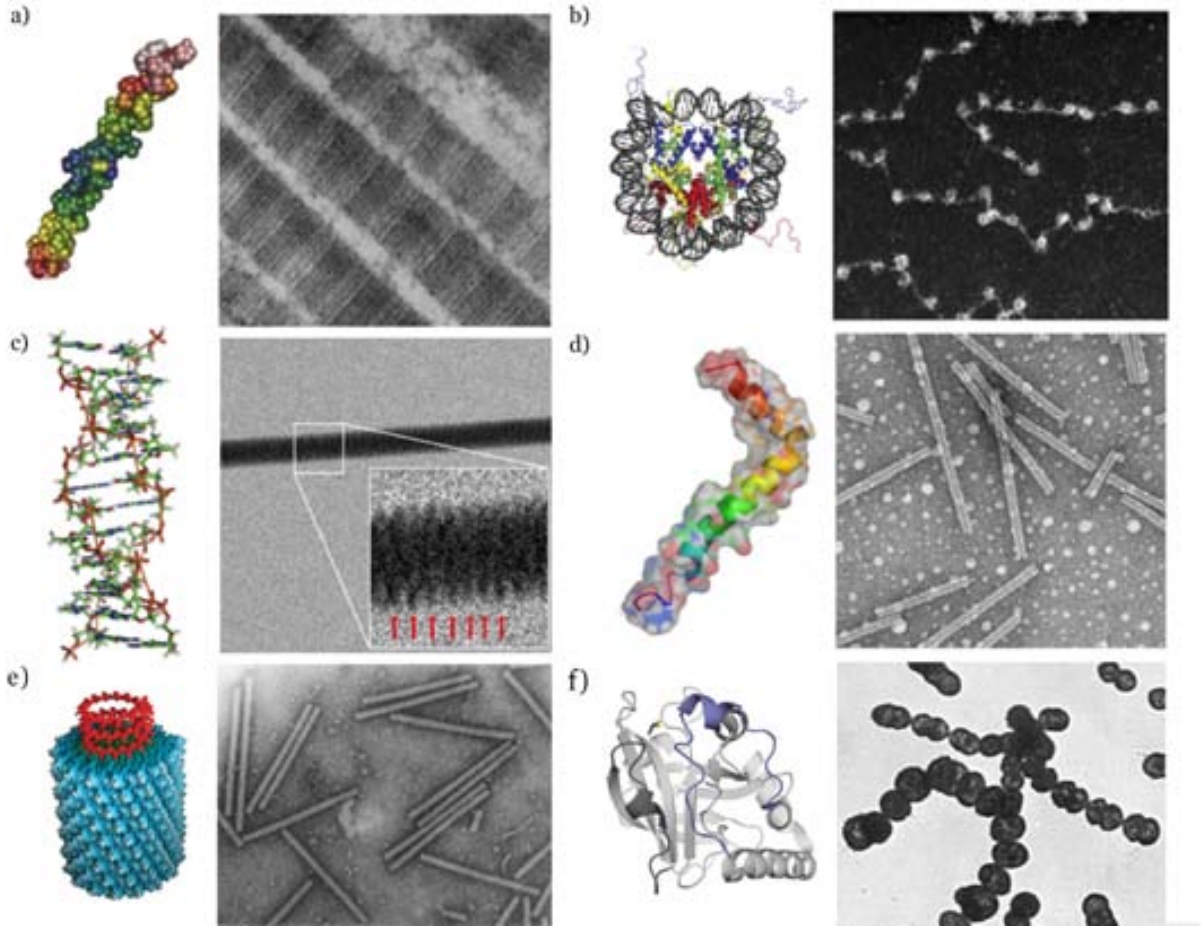

Figure 3.1. Examples of nanostructures made of the self-assembly of biomolecules: a) triple coiled-coil (collagen); b) wrapped (nucleosome); c) double-strand (DNA); d) fibrils (amyloids); e) nanotubes (Tobacco Mosaic Virus); f) chains (streptococcus). Structure imaged adapted from ref 10.

Inspired by what Nature can do, many research groups have shown high interest for understanding and controlling the self-assembly of natural, synthetic and chemically modified biomolecules as a new approach for developing functional artificial, mesoscopic architectures and nanostructured materials. An example that illustrates the potentiality of this approach was reported by Stupp and co-workers, who demonstrated that hydrophilic peptides modified with long alkyl chains become amphiphilic (see Figure 3.2.a).[5] Because of their amphiphilic character, these peptides self-assemble into 1D-nanostructures, mainly nanofibers with cylindrical geometry, through intermolecular hydrogen bonding under physiological conditions. Also, Zhang's group from Massachusetts Institute of Technology designed an eight-residue KFE8 (Phe-Lys-Phe-Glu-Phe-Lys-Phe-Glu) peptide and used the right-handed twits of its backbone in β-strand conformation to form left-handed helical ribbons of regular pitch at the nanometer scale (Figure 3.2.c).[6] Willner and co-workers reported the self-assembly of a DNA scaffold made of DNA strips that include 'hinges' to which biomolecules can be tethered (Figure 3.2.d).[7] They attached two enzymes or a

cofactor-enzyme pair to the DNA scaffold, and demonstrated that the enzyme cascades or the cofactor-mediated biocatalysts can proceed effectively. The reader is also referred to selected excellent reviews that highlight this approach by describing other artificial nanostructures built up from the self-assembly of biomolecules.[8,9]

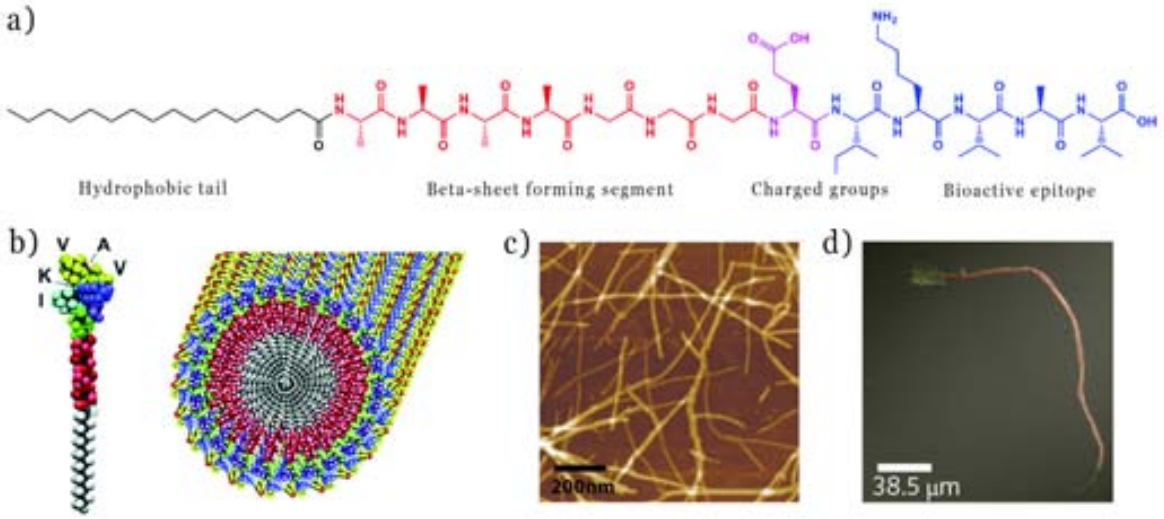

Figure 3.2. a) Molecular structure of a representative peptide amphiphile (Ile-Lys-Val-Ala-Val (IKVAV)) with four rationally designed chemical entities. b) Molecular graphics illustration of an IKVAV-containing peptide amphiphile molecule and its self-assembly into nanofibers.[5] c) Atomic force microscopy image of the peptide KFE8 (with the sequence Phe-Lys-Phe-Glu-Phe-Lys-Phe-Glu) self-assembly in aqueous solution into left-handed helical ribbons over mica, 4 days after preparation.[6] d) Confocal microscopy images of the FAM–HRP/TAMRA–GOx enzymes assembled on the two-hexagon DNA scaffold. Enzymes: glucose oxidase (GOx) and horseradish peroxidase (HRP). Dyes: 5-carboxyfluorescein N-succinimidyl ester (FAM) and 5-carboxy-tetramethylrhodamine N-succinimidyl ester (TAMRA).[7]

II. Our investigation: Nanoscale Coordination Polymers made of Amino Acids

Analogously to the use of weak interactions (*e.g.* hydrogen bonds, electrostatic interactions, etc.), coordination-driven self-assembly of biomolecules can be an alternative to create functional "artificial" nanostructures. In Chapter 1, we have seen that biomolecules can effectively coordinate with metal ions, and that they both can form extended metal-biomolecule networks. So, by controlling this self-assembly at the sub-micrometre regime (100-1000 nm) or even further down to the nanoscale (1-100 nm), one can in principle access to a whole new family of nanostructures in which biomolecules are connected by

metal ions.[11] To date, however, not many examples of metal-biomolecule nanostructures have been reported. A summary of existing nanostructures synthesized using this approach is given below, classified as 0D- crystalline or amorphous particles and 1-D nanofibers and rods.

II.1. 0-D particles

II.1a Crystalline particles

In general, metal-biomolecule 0-D nanocrystals are the nanosized version of well-known bulk CPs. This first class of particles is usually prepared by using synthetic methodologies in which the crystallization process is controlled at this length scale. This control can be achieved, for example, by increasing the nucleation rate through the use of solvothermal conditions, microwave, ultrasound, rapid precipitation, etc., or by confining the crystallization using an emulsion or a template. In most of these methods, it is essential to tune one or more reaction conditions, such as the type of solvents, precursor concentrations, pH, temperature and time.

For example, Serre and co-workers synthesized small crystals (below 200 nm) of nanoMIL-88A ($[Fe_3O(MeOH)_3(fum)_3(CO_2CH_3)]\cdot 4.5MeOH$; where fum is fumaric acid) by mixing Fe(III) ions with fumaric acid and by screening different solvents (DMF, absolute ethanol, methanol, or distilled water) as well as solvothermal, hydrothermal conditions and reaction times (2, 6 and 24h).[12] Two years later, the same group also demonstrated that other ways can be used to control the nucleation and crystal growth and consequently, the size of the final nanoMIL-88A.[13] The most effective method was the microwave (MW) synthesis. They showed that MW-assisted hydrothermal synthesis at 100°C using distilled water as solvent is a very fast and easy route to obtain high yields of small nanoparticles of MIL-88A (<100 nm).

Once miniaturized, these authors took advantage of their high porosity (to absorb and store guest molecules, such as drugs, inside the channels) and of the size of particles, which is below 200 nm (considered by many researchers as a critical barrier for a potential use in biomedical applications),[14] to show that this nanoMIL-88A could be used in biomedicine for drug delivery and imaging. First, they demonstrated the adsorption of several antitumor or

antiviral drugs (cidofovir, busulfan and doxorubicin) onto the nanoMIL-88A (Figure 3.3). The efficiency of the drug delivery system was confirmed by the controlled and progressive release of the encapsulated drugs as well as their *in vitro* anticancer efficacies. In addition, the presence of Fe(III) paramagnetic ions makes this nanoscale CP very interesting for contrast agents properties. The efficiency of this iron-based CP is directly related to its relaxivity; in other words, to its capacity to modify the relaxation times of the water protons in the surrounding medium when a magnetic field is applied. The higher the quantity and the mobility of the metal coordinated water in the first and second coordination spheres, the higher the relaxivity will be. In this sense, these nanoparticles show not only paramagnetic iron atoms in their matrix, but also an interconnected porous network filled with metal coordinated and/or free water molecules. The relaxivity r_2 of this iron fumarate nanoparticles under a 9.4 T magnetic field was in the order of 50 $s^{-1} \cdot mM^{-1}$, which can be considered as sufficient for *in vivo* use. However, what makes these nanoparticles very attractive for these biomedical applications is the fact that the degradation of nanoMIL-88A produces endogenous substances, thus minimizing their toxicity. This fumarate-derived nanoparticles degrades after seven days of incubation at 37 °C, releasing large quantities of their ligands: 72% of fumaric acid and Fe(III) ions. The majority of these degradation products are endogenous and consequently, the toxicity values are low [LD_{50}(Fe(III)) = 30 g kg^{-1} and LD_{50} (fumaric acid) = 10.7 g kg^{-1}].

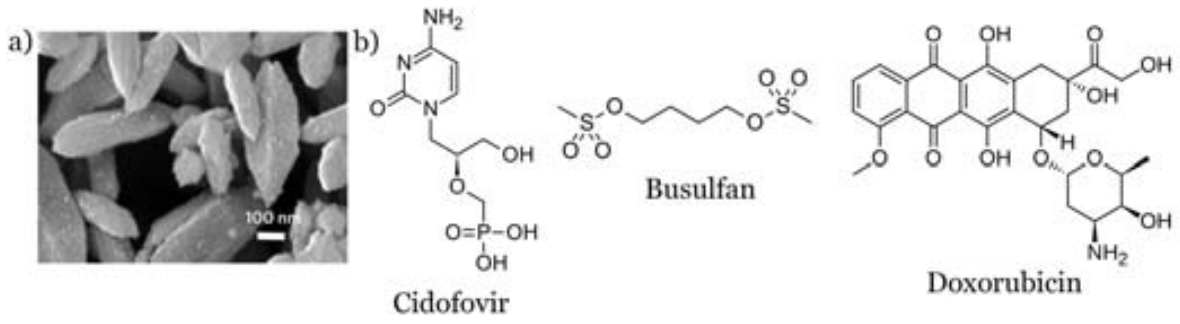

Figure 3.3. a) SEM image of the of the biodegradable porous iron carboxylate nanoMIL-88A. b) Representation of the four antitumoral and retroviral drugs used to study the efficacy of these nanocarriers. Figure adapted from ref 12.

II.1b Amorphous particles

Biomolecules are usually very flexible molecules, which difficult their crystallization. For this reason, it is not surprising that most of the metal–biomolecule submicron structures generated up until today are amorphous particles. Even though their amorphous character precludes precise characterization of the connectivity between the biomolecules and metal

ions, it is clear that the formation of these amorphous particles is principally due to bridging interactions between metal ions and biomolecules. For example, Lin and co-workers used fast precipitation methods to obtain sub-50 nm metal–organic spherical particles constructed from Tb(III) ions, cisplatin antitumoral drug c,c,t-(diamminedichlorodisuccinato)Pt(IV) and succinic acid.[15] These Pt-containing spheres were further coated with an amorphous silica-shell to control the degradation and therefore, the antitumoral complex release. Similar spherical colloidal particles were obtained using nucleobases and nucleotides. Dong, Wang and co-workers synthesized spherical particles with an average diameter of 300 nm by mixing $HAuCl_4$ and adenine at room temperature (Figure 3.4.a),[16] whereas Kimizuka and co-workers prepared fluorescent 40 nm-in-diameter spheres by combining lanthanide ions (*e.g.* Gd(III), Tb(III), etc.) with the nucleotide 50-AMP in a HEPES buffer (Figure 3.4.b). Here, the lanthanide ions are proposed to coordinate to both, the nucleobase and the phosphate group present in the nucleotide. These amorphous nanoparticles show intrinsic functions such as energy transfer from nucleobase to lanthanide ions and excellent performance as contrast enhancing agents for magnetic resonance imaging (MRI).[17] Furthermore, these nanoscale CPs were shown to be effective materials for the encapsulation of guest species. For example, water-soluble anionic dyes such as fluorescein and perylene were encapsulated into this lanthanide-nucleotide system by adding the dye during the synthesis.[18]

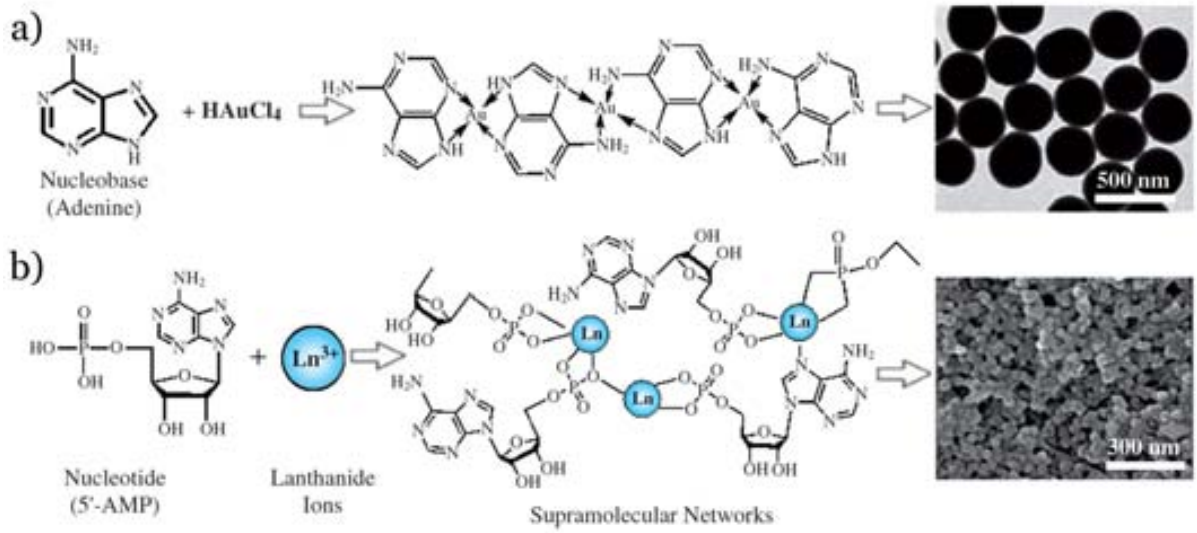

Figure 3.4. a) Scheme and TEM image of the Au(III)-Adenine colloidal particles obtained by simply mixing the precursor aqueous solutions of adenine and $HAuCl_4$. b) Scheme and SEM image of nanoparticles formed by self-assembly of 5'-AMP and lanthanide ions. Figure adapted from ref 17.

II.2. 1-D nanofibers and nanorods

As mentioned in Section I of this Chapter 3, a common shape of many of the nanostructures formed by the self-assembly of biomolecules is fibers. However, not many examples of these fibers driven by coordination with metal ions have been described. In fact, the article "Amino acid based metal-organic nanofibers" presented in this Chapter describes one of the first examples of 1-D nanofibers. These fibers will be outlined in the next section. Also, during the course of this PhD Thesis, several other groups have expanded the variety of CP nanofibers and nanorods made of biomolecules.

For example, Chmielewski and co-workers showed that collagen could also be used to fabricate CP nanofibers. Collagen is a group of naturally occurring proteins that are present in the form of elongated fibrils in fibrous tissues. They synthesized metal–collagen fibers (as we can see in Figure 3.5.) that assembled upon addition of transition metal ions (*e.g.* Zn(II), Cu(II), Ni(II) and Co(II)) to a peptide composed of repeating poly(prolyl-hydroxyprolyl-glycyl (Pro-Hyp-Gly) sequences modified with metal coordination nodes, such as nitrilotriacetic acid, histidine and bipyridil.[19]

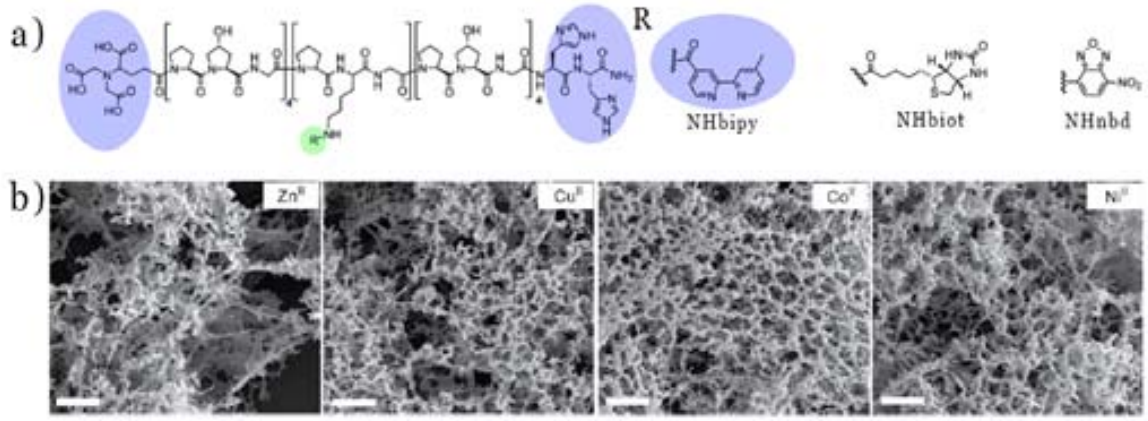

Figure 3.5. a) General structure of peptides NHbipy (bipyridyl), NHbiot (biotin) and NHnbd (nitrobenzoxadiazole). Metal ligands are shaded in blue. b) SEM images of metal-collagen fibers made of the coordination of NHbipy peptide with several metals ions. Scale bar: 5 μm. Figure adapted from ref 19.

Using a similar synthetic approach, Jiang and co-workers synthesized chiral coordination nanofibers based on the association of Ag(I) ions and D-cysteine and L-cysteine ligands.[20] They showed that the self-assembly of Ag(II) ions and L-Cys leads to the production of pure right-handed helical nanobelts with diameters below of 100 nm, whereas the use of D-Cys gives rise pure left-handed helical nanobelts. They showed also that racemic Ag(I)/DL-Cyswas assembled into a totally different product, two-dimensional achiral

nanosheets. Abramchuk and co-workers used the same ingredients, Ag(I) ions and Cysteine, to form nanostructured gels with fibrilar architectures.[21] Working with peptides, Mantion and Taubert could also synthesized CP nanorods. They used precipitation induced by poor solvents for the formation of a series of metal–peptide rod-like submicron crystals (Figure 3.6).[25] These crystals were obtained by combining Cu(II) or Ca(II) ions with a protected ValValGlu peptide at 80ºC using a water/ethanol mixture and adjusting the pH of the tripeptide using diluted aqueous ammonia. It was found that the formation of these long nanorods (with lenghts ranging up to several micrometers and widths of 200 nm) was due to the self-assembling properties of the peptide and specific metal–peptide and metal–ammonia interactions. In general this synthetic strategy provides further control over the size of the nanostructures through modifications of the reaction conditions (the polarity of the solvents, the rate of addition of the poor solvent, and the concentration of the reactants).

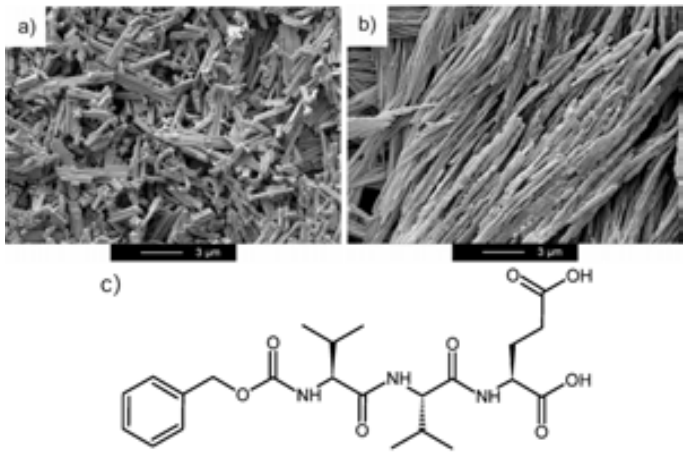

Figure 3.6. SEM images of metal-peptide frameworks (MPFs) a) The calcium complex MPF-2 b) The copper complex MPF-3 c) Peptide ligand used for the construction of the MPFs. Figure adapted from ref. 25.

Nucleotides can be also adequate building blocks to create 1D nanostructures. Kimizuka and co-workers obtained metal–nucleotide fibers when Tb(III) ions were mixed with the dimer guanine nucleotide (dG2MP) in molar ratios from 1 : 1 to 1 : 3.[22]

Finally, beyond the classical batch synthesis, another excellent strategy that allows the fabrication of fibers and wires is the controlled assembly on solid surfaces. Zamora, Gómez-Herrero and co-workers contributed enormously to the development of this approach. These authors used different deposition methods, including sonication, drop casting and sublimation to generate by *in-situ* reaction single Cd(II)–mercaptopurine (MP) chains on mica surfaces (Figure 3.7).[23]

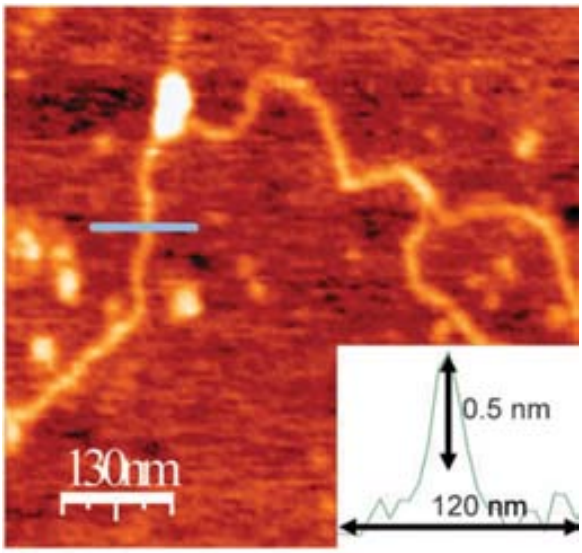

Figure 3.7. AFM topographic image of a 1D single chain of polyanion $[Cd(6\text{-}MP)2]_n^{n-}$ formed on mica surfaces. Figure adapted from ref 24.

III. Our results: Amino acid based metal-organic nanofibers

The article presented in this Chapter, "Amino acid based metal-organic nanofibers", describes one of the first examples of nanoscale crystalline metal–AA fibers. These nanofibers were initially synthesized by using a fast precipitation approach. We demonstrated that the simple addition of an aqueous solution of Cu(II) ions to an aqueous/ethanol mixture solution of L- or D- Asp leads to the immediate precipitation of a blue solid composed of Cu(II)-Asp nanofibers with a diameter around 100 nm. The immediate coordination is further promoted by the addition of NaOH that deprotonates the carboxylic acids of the AA, creating an easy access point for the metal ions. The obtained nanofibers were characterized by: electron microscopy (SEM and TEM), which allowed us to study their shape and size (Figure 2.a-c from the Article); EDX microanalysis, which confirmed the presence of copper on the fibers (Figure S.6. of S.I.); infrared spectroscopy,

which showed the formation of a CP between the Cu(II) ions and the Asp (Figure S.2. of S.I.); and X-ray powder diffraction, which proved the crystallinity of fibers (Figure S.5. of S.I.).

We observed also that when the concentrations of both reactants are increased, a homogeneous aqueous gelation occurs (Figure 3.8.a.). This opaque blue gel is stable for months at room temperature. SEM and TEM images (Figure 3.8.b-c) of this gel revealed that it is formed by the interlacement of Cu(II)-Asp nanofibers.

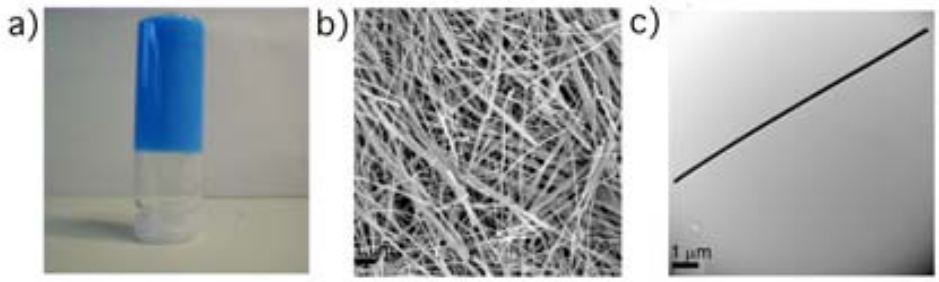

Figure 3.8. a) Image of the Cu(II)-Asp gel. b-c) SEM and TEM images of the Cu(II)-Asp nanofibers forming this gel.

Moreover, the length of the fibers could be controlled by adjusting the addition rate of the Asp solution: faster rates give shorter fibers. This result made us to try for the first time the interfacial polymerization methodology. This approach allows a very slow mixture of both Cu(II) ions and Asp and it is based on the creation of an interface between the two-reactant solutions in a test tube (Figure 3.9). The ethanolic layer slowly diffuses into the aqueous phase. This slow diffusion allows to slow down the self-assembly of both components and to homogenize its growth along the diffusion direction. As a result, dark blue fibers with lengths up to one-centimeter can be formed. On the contrary, identical nanofibers synthesized by the fast mixing methodology have lengths down to tens of micrometers.

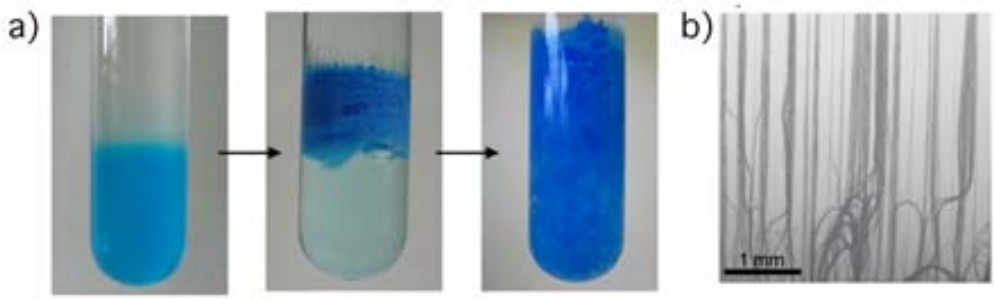

Figure 3.9. a) Sequential images showing the diffusion process and formation of the Cu(II)-Asp nanofibers. b) Optical images of the resulting nanofibers, showing that they can be homogeneously synthesized with lengths up to 1 centimeter.

Finally, the chirality of Cu(II)-Asp nanofibers synthesized using the L- and D-Asp enantiomers was studied by Circular Dichroism (CD) spectroscopy in the solid state in collaboration with Prof. David Amabilino from ICMAB (Barcelona, Spain). The enantiomeric nanofibers showed a CD spectrum with a strong Cotton effect with the crossing wavelength at 637 nm near the absorption of the Cu(II) complexes (Figure 3.10). The shape and magnitude of these Cotton effects clearly showed the chiral coordination sphere of the metal ion in the nanofibers, confirming that the intrinsic property of the AAs is propagated to the CP structure.

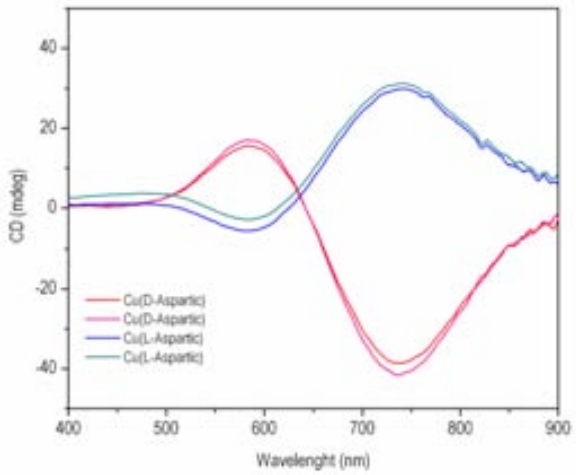

Figure 3.10. Solid state CD spectra of L- (blue and green) and D- (pink and red) Cu(II)-Asp nanofibers.

To conclude, in this Chapter, we have demonstrated a new synthetic route to fabricate novel long, chiral 1-D CP nanostructures built up from the assembly of AAs and metal ions. Very long (up to 1 cm) nanofibers can be grown using conventional coordination chemistry in a diffusion controlled growth procedure. Furthermore, simple changes in the reaction strategy can induce a decrease of the fiber length or the formation of a metal-organic gel.

IV. References

(1) Ma, N.; Sargent, E. H.; Kelley, S. O. Biotemplated Nanostructures: Directed Assembly of Electronic and Optical Materials Using Nanoscale Complementarity. *J. Mater. Chem.* **2008**, *18*, 954-964.

(2) Alivisatos, A. P.; Johnsson, K. P.; Peng, X.; Wilson, T. E.; Loweth, C. J.; Bruchez, M. P.; Schultz, P. G. Organization of "Nanocrystal Molecules" Using DNA. *Nature* **1996**, *382*, 609–611.

(3) Wilner, O. I.; Orbach, R.; Henning, A.; Teller, C.; Yehezkeli, O.; Mertig, M.; Harries, D.; Willner, I. Self-Assembly of DNA Nanotubes with Controllable Diameters. *Nat. Commun.* **2011**, *2*, 540–548.

(4) Sachse, C.; Chen, J. Z.; Coureux, P.-D.; Stroupe, M. E.; Fändrich, M.; Grigorieff, N. High-Resolution Electron Microscopy of Helical Specimens: A Fresh Look at Tobacco Mosaic Virus. *J. Mol. Biol.* **2007**, *371*, 812–835.

(5) Cui, H.; Webber, M. J.; Stupp, S. I. Self-Assembly of Peptide Amphiphiles: From Molecules to Nanostructures to Biomaterials. *Biopolymers* **2010**, *94*, 1–18.

(6) Zhang, S.; Marini, D. M.; Hwang, W.; Santoso, S. Design of Nanostructured Biological Materials through Self-Assembly of Peptides and Proteins. *Curr. Opin. Chem. Biol.* **2002**, *6*, 865–871.

(7) Wilner, O. I.; Weizmann, Y.; Gill, R.; Lioubashevski, O.; Freeman, R.; Willner, I. Enzyme Cascades Activated on Topologically Programmed DNA Scaffolds. *Nat. Nanotechnol.* **2009**, *4*, 249–254.

(8) Yin, P.; Choi, H. M. T.; Calvert, C. R.; Pierce, N. A. Programming Biomolecular Self-Assembly Pathways. *Nature* **2008**, *451*, 318–322.

(9) Chiu, C.-Y.; Ruan, L.; Huang, Y. Biomolecular Specificity Controlled Nanomaterial Synthesis. *Chem. Soc. Rev.* **2013**, *42*, 2512–2527.

(10) Wikipedia Creative Commons.

(11) Carné, A.; Carbonell, C.; Imaz, I.; Maspoch, D. Nanoscale Metal–organic Materials. *Chem. Soc. Rev.* **2011**, *40*, 291–305.

(12) Horcajada, P.; Chalati, T.; Serre, C.; Gillet, B.; Sebrie, C.; Baati, T.; Eubank, J. F.; Heurtaux, D.; Clayette, P.; Kreuz, C.; *et al.* Porous Metal–organic-Framework Nanoscale Carriers as a Potential Platform for Drug Delivery and Imaging. *Nat. Mater.* **2009**, *9*, 172–178.

(13) Chalati, T.; Horcajada, P.; Gref, R.; Couvreur, P.; Serre, C. Optimisation of the Synthesis of MOF Nanoparticles Made of Flexible Porous Iron Fumarate MIL-88A. *J. Mater. Chem.* **2011**, *21*, 2220–2227.

(14) Gupta, A. K.; Gupta, M. Synthesis and Surface Engineering of Iron Oxide Nanoparticles for Biomedical Applications. *Biomaterials* **2005**, *26*, 3995–4021.

(15) Rieter, W. J.; Pott, K. M.; Taylor, K. M. L.; Lin, W. Nanoscale Coordination Polymers for Platinum-Based Anticancer Drug Delivery. *J. Am. Chem. Soc.* **2008**, *130*, 11584–11585.

(16) Wei, H.; Li, B.; Du, Y.; Dong, S.; Wang, E. Nucleobase–Metal Hybrid Materials: Preparation of Submicrometer-Scale, Spherical Colloidal Particles of Adenine–Gold(III) via a Supramolecular Hierarchical Self-Assembly Approach. *Chem. Mater.* **2007**, *19*, 2987–2993.

(17) Aimé, C.; Nishiyabu, R.; Gondo, R.; Kimizuka, N. Switching On Luminescence in Nucleotide/Lanthanide Coordination Nanoparticles via Synergistic Interactions with a Cofactor Ligand. *Chem. - Eur. J.* **2010**, *16*, 3604–3607.

(18) Nishiyabu, R.; Hashimoto, N.; Cho, T.; Watanabe, K.; Yasunaga, T.; Endo, A.; Kaneko, K.; Niidome, T.; Murata, M.; Adachi, C.; *et al.* Nanoparticles of Adaptive Supramolecular Networks Self-Assembled from Nucleotides and Lanthanide Ions. *J. Am. Chem. Soc.* **2009**, *131*, 2151–2158.

(19) Pires, M. M.; Przybyla, D. E.; Chmielewski, J. A Metal-Collagen Peptide Framework for Three-Dimensional Cell Culture. *Angew. Chem. Int. Ed.* **2009**, *48*, 7813–7817.

(20) Li, C.; Deng, K.; Tang, Z.; Jiang, L. Twisted Metal–Amino Acid Nanobelts: Chirality Transcription from Molecules to Frameworks. *J. Am. Chem. Soc.* **2010**, *132*, 8202–8209.

(21) Pakhomov, P. M.; Abramchuk, S. S.; Khizhnyak, S. D.; Ovchinnikov, M. M.; Spiridonova, V. M. Formation of Nanostructured Hydrogels in L-Cysteine and Silver Nitrate Solutions. *Nanotechnologies Russ.* **2010**, *5*, 209–213.

(22) Aimé, C.; Nishiyabu, R.; Gondo, R.; Kaneko, K.; Kimizuka, N. Controlled Self-Assembly of Nucleotide–lanthanide Complexes: Specific Formation of Nanofibers from Dimeric Guanine Nucleotides. *Chem. Commun.* **2008**, 6534–6536.

(23) Amo-Ochoa, P.; Rodríguez-Tapiador, M. I.; Castillo, O.; Olea, D.; Guijarro, A.; Alexandre, S. S.; Gómez-Herrero, J.; Zamora, F. Assembling of Dimeric Entities of Cd(II) with 6-Mercaptopurine to Afford One-Dimensional Coordination Polymers: Synthesis and Scanning Probe Microscopy Characterization. *Inorg. Chem.* **2006**, *45*, 7642–7650.

(24) Mas-Ballesté, R.; Gómez-Herrero, J.; Zamora, F. One-Dimensional Coordination Polymers on Surfaces: Towards Single Molecule Devices. *Chem. Soc. Rev.* **2010**, *39*, 4220–4223.

(25) Mantion, A.; Massüger, L.; Rabu, P.; Palivan, C.; McCusker, L. B.; Taubert, A. Metal–Peptide Frameworks (MPFs): "Bioinspired" Metal Organic Frameworks. *J. Am. Chem. Soc.* **2008**, *130*, 2517–2526.

Publication 2. "Amino acid based metal-organic nanofibers." I. Imaz, M. Rubio-Martínez, W.J. Saletra, D.B. Amabilino, D. Maspoch. *J.Am.Chem. Soc.* **2009**, 131, 18222-18223.

J|A|C|S COMMUNICATIONS

Published on Web 12/07/2009

Amino Acid Based Metal−Organic Nanofibers

Inhar Imaz,[†] Marta Rubio-Martínez,[†] Wojciech J. Saletra,[‡] David B. Amabilino,[‡] and Daniel Maspoch*[,†]

Centre d'Investigació en Nanociència i Nanotecnologia (CIN2, ICN-CSIC), Esfera UAB, Campus UAB, 08193 Bellaterra, Spain, and Institut de Ciència de Materials de Barcelona (CSIC), Campus UAB, 08193 Bellaterra, Spain

Received October 13, 2009; E-mail: daniel.maspoch.icn@uab.es

Self-assembly of small molecules and/or metal ions into nanostructures, such as spheres, tubes, rods, tapes, fibers, and crystalline particles, has evolved as an attractive strategy for fabricating materials with tunable physical and chemical properties via control of their composition, size, and shape. This versatility has opened up a broad range of potential applications in catalysis, electronics, sensing, medical diagnostics, tissue engineering, data storage, and drug delivery.[1] Recently, conventional coordination chemistry has also started to attract a great amount of interest for synthesizing these nanoscale structures. In particular, several recent studies have demonstrated that an infinite coordination polymerization of metal ions through organic ligands followed by a precipitation can generate infinite coordination polymer particles (ICPs).[2,3] Thus far, these ICPs have shown not only promising functionalities, such as magnetism,[4] porosity,[5] ion exchange[6] or optical properties,[6] but also a capacity for use as novel encapsulating matrices.[7]

Even though the latter approach, in principle, can provide interesting ICPs, nanoscale one-dimensional (1-D) coordination polymers, including rods, tubes, and fibers, are still scarce. In 2004, Martin et al. synthesized the first discrete metal−organic nanotubes by using templated layer-by-layer growth.[8] Soon after, Lin et al. prepared Gd(III)-based nanorods able to act as contrast agents through a water-in-oil microemulsion-based technique,[9] whereas Oh et al. used hydrothermal synthesis to obtain porous In(III)-based hexagonal nanorods.[10] More recently, coordination polymer-based gels and nanofibers have been described by You and Loh's groups, respectively.[11,12] These nanofibers are efficient in light harvesting, because fluorescence resonance energy transfer is favored in the 1-D structure.[12] Therefore, designing novel synthetic routes to fabricate 1-D coordination polymer nanostructures will certainly open up exciting opportunities for developing a new class of electronically, optically, and biologically active materials.

Here we report a facile template-free strategy to very long (up to one centimeter) discrete chiral coordination polymer nanofibers under ambient conditions using aqueous/organic interfacial coordinative polymerization (Figure 1). The nanofibers have diameters between 100 and 200 nm. The synthesis is based on the well-known capacity of the L- or D-aspartic acids (Asp) to generate biorelated coordination polymers when they are reacted with transition metal ions.[13] The dicarboxylate form of the Asp and Cu(II) metal ions are separated by the interface between an organic solvent containing the sodium aspartate and an aqueous phase containing the transition metal ions. The Cu(II)-Asp product, which starts to polymerize at the interface, contains exclusively long nanofibers that grow oriented along the diffusion direction. Nanofibers with shorter lengths on the order of micrometers are also produced when the phases are mixed under stirring. This observation indicates that the formation of nanofibers is not determined by the interface but more likely by

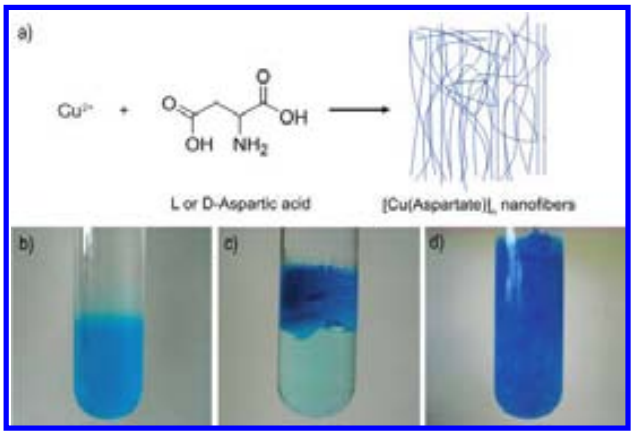

Figure 1. (a) Schematic illustration of the synthesis of Cu-Asp-based nanofibers. (b−d) Pictures taken at 0 (b), 24 (c), and 120 h (d) illustrating the aqueous/organic interfacial coordinative polymerization method used to fabricate nanofibers with lengths on the order of centimeters.

the nature of the coordination polymerization of the Cu-Asp system. However, it is clear that the length of the resulting nanofibers is highly dependent on the method used for their synthesis.

In a typical experiment, L- or D-aspartic acid and NaOH were dissolved in an ethanol/water mixture (5/1), whereas $Cu(NO_3)_2 \cdot 6H_2O$ was dissolved in water. The solutions were then transferred carefully to a test tube, generating an interface between the two layers (Figure 1b). After 3 days, dark blue fibers start to form at the liquid−liquid interface (Figure 1c). Then, as the ethanolic layer slowly diffused into the aqueous phase, these fibers gradually grew oriented along with the diffusion direction. After 2 weeks, the entire aqueous phase was filled homogeneously with dark-blue metal−organic nanofibers (Figure 1d).

Figure 2a shows a photomicrograph of bundles of these fibers, illustrating their ∼1 cm length and high orientation. Transmission electron microscopy (TEM) images of these fibers show a very homogeneous sample of fibers with diameters of 100−200 nm (Figure 2c). The sample uniformity and narrow diameter distribution were also confirmed by field-emission scanning electron microscopy (FESEM). Figure 2b shows a typical FESEM image of a nanofiber thin film cast on an aluminum substrate from a colloidal suspension. The sample appears to be exclusively nanofibers, consistent with TEM images.

X-ray powder diffraction performed on the Cu-Asp nanofibers confirmed their crystalline character, but their single crystal structure determination, and therefore a detailed analysis of the structural connectivity, was not feasible due to their sub-200 nm diameter. However, some additional characterization appears to indicate that Cu(II) ions and Asp ligands are arranged in 1-D chains with the general formula $[Cu(Asp)(H_2O)_x]_n$.[14] The chemical composition of these fibers was first determined by energy dispersive X-ray (EDX) spectroscopy, which confirmed the presence of copper, oxygen,

[†] Centre d'Investigació en Nanociència i Nanotecnologia.
[‡] Institut de Ciència de Materials de Barcelona.

10.1021/ja908721t

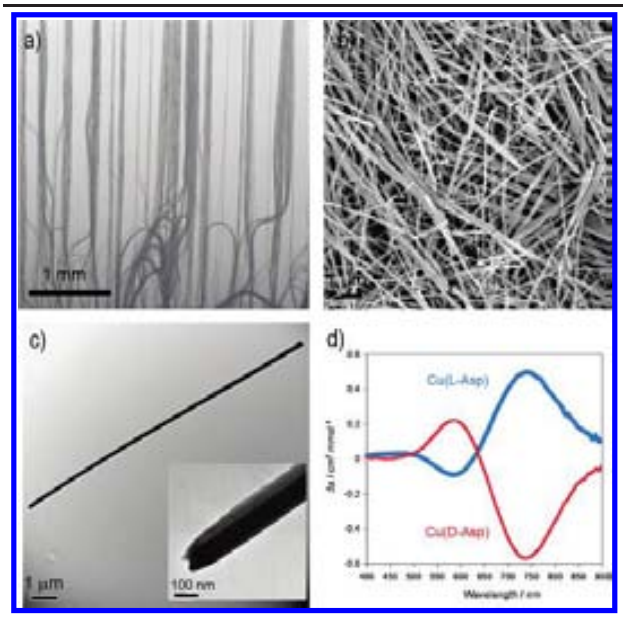

Figure 2. (a) Optical microscope, (b) FESEM, and (c) TEM images of Cu-Asp-based nanofibers. (d) Solid state CD spectra of L- (blue) and D- (red) Cu-Asp-based nanofibers.

nitrogen, and carbon. The infrared spectra show that both carboxylate groups of the Asp moieties are coordinating to the Cu(II) ions, as evidenced by the multiple characteristic asymmetric and symmetric COO^- bands centered at 1622/1586 cm^{-1} and 1403/1368 cm^{-1}, respectively.[14] A broad band in the region 2600−3600 cm^{-1} indicates the presence of water molecules and extensive hydrogen bonding. These facts, enhanced by the elemental analysis, which confirms that the ratio between Cu(II) ions and Asp is 1:1, enable us to suggest tentatively the formation of $[Cu(Asp)(H_2O)_x]$ polymeric chains.

The chirality of Cu-Asp fibers constructed from L- and D- aspartic acid was studied by Circular Dichroism (CD) spectroscopy in the solid state, using a procedure developed previously.[15] The enantiomeric nanofibers show an opposite Cotton effect (Figure 2d). The CD spectra of Cu-(D-Asp) fibers exhibit a strong Cotton effect with the crossing wavelength at 637 nm near the absorption of the Cu(II) complex. The shape and magnitude of these Cotton effects shows clearly the chiral coordination sphere of the metal ion in the nanofibers. It is noteworthy that this signal arising from d−d transitions is much clearer than those of other Cu(II) complexes.[16] The sign of the CD signal is determined by the enantiomeric form, L- or D-, of the component aspartic acid.

Cu-Asp-based nanofibers with shorter lengths on the order of micrometers were also synthesized by fast addition of an aqueous solution of $Cu(NO_3)_2 \cdot 6H_2O$ to an aqueous solution of L- or D-sodium aspartate under stirring. Interestingly, as the concentrations of both reactants were increased up to 0.07 M, homogeneous aqueous gelation was observed (Figure 3a). This opaque blue gel is stable for months at room temperature. Figure 3b shows an FESEM image of this gel, showing the characteristic interlacement of Cu-Asp-based nanofibers.

In conclusion, long chiral nanofibers can be grown using conventional coordination chemistry and biologically derived components in a diffusion controlled growth procedure. Furthermore, simple changes in the reaction strategy can induce a decrease of the fiber length or the formation of a metal−organic gel. Owing to the high flexibility of coordination polymer composition, the present strategy will certainly expand the synthesis of novel nanoscale 1D coordination polymers for future electronic, optical, drug delivery, and sensing applications.

Figure 3. (a) Photograph and (b) FESEM image of the Cu-Asp-based gel.

Acknowledgment. This work was supported by Projects VALTEC08-2-0003 and MAT2006-13765-C02. I.I. and D.M. thank the MICINN for JdC and RyC contracts, respectively. M.R. and W.J.S. thank the ICN and CSIC, respectively, for research contracts.

Supporting Information Available: Detailed synthetic procedure, IR, XRPD, TEM, EDX and FE SEM images. This material is available free of charge via the Internet at http://pubs.acs.org.

References

(1) (a) Bell, A. T. *Science* **2003**, *299*, 1688. (b) Bruchez, M. J.; Moronne, M.; Gin, P.; Weiss, S.; Alivisatos, A. P. *Science* **1998**, *281*, 2031. (c) Wu, M.-H.; Whitesides, G. M. *Appl. Phys. Lett.* **2001**, *78*, 2273.
(2) (a) Spokoyny, A. M.; Kim, D.; Sumrein, A.; Mirkin, C. A. *Chem. Soc. Rev.* **2009**, *38*, 1218. (b) Lin, W.; Rieter, W. J.; Taylor, K. M. L. *Angew. Chem., Int. Ed.* **2009**, *48*, 650.
(3) (a) Oh, M.; Mirkin, C. A. *Nature* **2005**, *438*, 651. (b) Sun, X.; Dong, S.; Wang, E. *J. Am. Chem. Soc.* **2005**, *127*, 13102.
(4) (a) Coronado, E.; Galán-Mascarós, J. R.; Monrabal-Capilla, M.; García-Martínez, J.; Pardo-Ibáñez, P. *Adv. Mater.* **2007**, *19*, 1359. (b) Imaz, I.; Maspoch, D.; Rodríguez-Blanco, C.; Pérez-Falcón, J. M.; Campo, J.; Ruiz-Molina, D. *Angew. Chem., Int. Ed.* **2008**, *47*, 1857. (c) Guari, Y.; Larionova, J. *Chem. Commun.* **2006**, 2613.
(5) Jeon, Y.-M.; Armatas, G. S.; Heo, J.; Kanatzidis, M. G.; Mirkin, C. A. *Adv. Mater.* **2008**, *20*, 2105.
(6) Oh, M.; Mirkin, C. A. *Angew. Chem., Int. Ed.* **2006**, *45*, 5492.
(7) Imaz, I.; Hernando, J.; Ruiz-Molina, D.; Maspoch, D. *Angew. Chem., Int. Ed.* **2009**, *48*, 2325.
(8) Hou, S.; Harrell, C.; Trofin, L.; Kohli, P.; Martin, C. R. *J. Am. Chem. Soc.* **2004**, *126*, 5674.
(9) Rieter, W. J.; Taylor, K. M. L.; An, H.; Lin, W.; Lin, W. *J. Am. Chem. Soc.* **2006**, *128*, 9024.
(10) Cho, W.; Lee, H. J.; Oh, M. *J. Am. Chem. Soc.* **2008**, *130*, 16945.
(11) Zhang, S.; Yang, S.; Lan, J.; Tang, Y.; Xue, Y.; You, J. *J. Am. Chem. Soc.* **2009**, *131*, 1689.
(12) Zhang, X.; Chen, Z.-K.; Loh, K. P. *J. Am. Chem. Soc.* **2009**, *131*, 7210.
(13) (a) Anokhina, E. V.; Go, Y. B.; Lee, Y.; Vogt, T.; Jacobson, A. J. *J. Am. Chem. Soc.* **2006**, *128*, 9957. (b) Vaidhyanathan, R.; Bradshaw, D.; Rebilly, J.-N.; Barrio, J. P.; Gould, J. A.; Berry, N. G.; Rosseinsky, M. J. *Angew. Chem., Int. Ed.* **2006**, *45*, 6495. (c) An, J.-Y.; Geib, S. J.; Rosi, N. L. *J. Am. Chem. Soc.* **2009**, *131*, 8376.
(14) Antolini, L.; Marcotrigiano, G.; Menabue, L.; Pellacani, G. C.; Saladini, M. *Inorg. Chem.* **1982**, *21*, 2263.
(15) Minguet, M.; Amabilino, D. B.; Wurst, K.; Veciana, J. *J. Chem. Soc., Perkin Trans. 2* **2001**, 670.
(16) (a) Downing, D. S.; Urbach, F. L. *J. Am. Chem. Soc.* **1969**, *91*, 5977. (b) Nishida, Y.; Kida, S. *Bull. Chem. Soc. Jpn.* **1970**, *43*, 3814. (c) Szlyk, E.; Surdykowski, A.; Barwiolek, M.; Lasen, E. *Polyhedron* **2002**, *21*, 2711.

JA908721T

SUPPORTING INFORMATION

Amino Acid-based Metal-Organic Nanofibers

Inhar Imaz,[†] Marta Rubio,[†] Wojciech J. Saletra,[‡] David B. Amabilino,[‡] Daniel Maspoch*,[†]

[†]*Centre d'Investigació en Nanociència i Nanotecnologia (CIN2, ICN-CSIC), Campus UAB, 08193 Bellaterra, Spain.*

[‡]*Institut de Ciència de Materials de Barcelona (CSIC), Campus UAB, 08193 Bellaterra, Spain.*

SI1. Synthetic details of Cu-(D-Asp) and Cu-(L-Asp) nanofibers preparation

- ***Synthesis by interfacial polymerization of very long nanofibers***

$Cu(NO_3)_2 \cdot 6H_2O$ (1.5 mmol, 300 mg) was dissolved in water (2ml). In parallel, a solution of L- or D-aspartic acid (1 mmol, 133 mg) in an ethanol/water mixture (5ml/1ml) was prepared. The aspartic acid was then deprotonated by addition of NaOH (2 mmol, 80 mg). Both solutions were carefully transferred to a test tube, generating an interface between the two layers. After 3 days, the first fibers started to appear at the interface.
Anal.: Calc. for $Cu(C4H5NO4) \cdot 4H2O$: Cu : 23.82; C: 18.01; H: 5.24; N: 4.91; O: 47.99 Found Cu : 22.78; C: 17.76; H: 5.4; N: 5.06.

- ***Synthesis of nanofibers by fast addition***

The nanofibers were prepared by the addition of an aqueous solution (2 mL) of $Cu(NO_3)_2 \cdot 6H_2O$ (1.5 mmol, 300 mg) in an aqueous solution (10 mL) of aspartic acid (1 mmol, 133 mg) and NaOH (2 mmol, 80 mg). The solution turned immediately to a deep blue colour. Immediately, a dendritic growth of blue nanofibers was observed.

- ***Synthesis of the Cu(aspartate) gel***

The gel preparation was similar to that used to prepare the nanofibers by direct mixing. In this case, $Cu(NO_3)_2$ (6 mmol, 1.2 g) was diluted in 2 mL of H_2O and added to a water solution (10 mL) of aspartic acid (4 mmol, 532 mg) and NaOH (8 mmol, 320 mg) under stirring. Immediately, the solution turned to dark blue. After few seconds, the gel was formed, and the solution was totally fixed.

SI2. Infrared spectra of Cu-(D-Asp) and Cu-(L-Asp) nanofibers

Methods for FT-IR: FT-IR spectra were collected on a Perkin Elmer spectrometer in the range of 400-4000 cm^{-1}on ATR.

- *Cu-(D-Asp) fibers:*

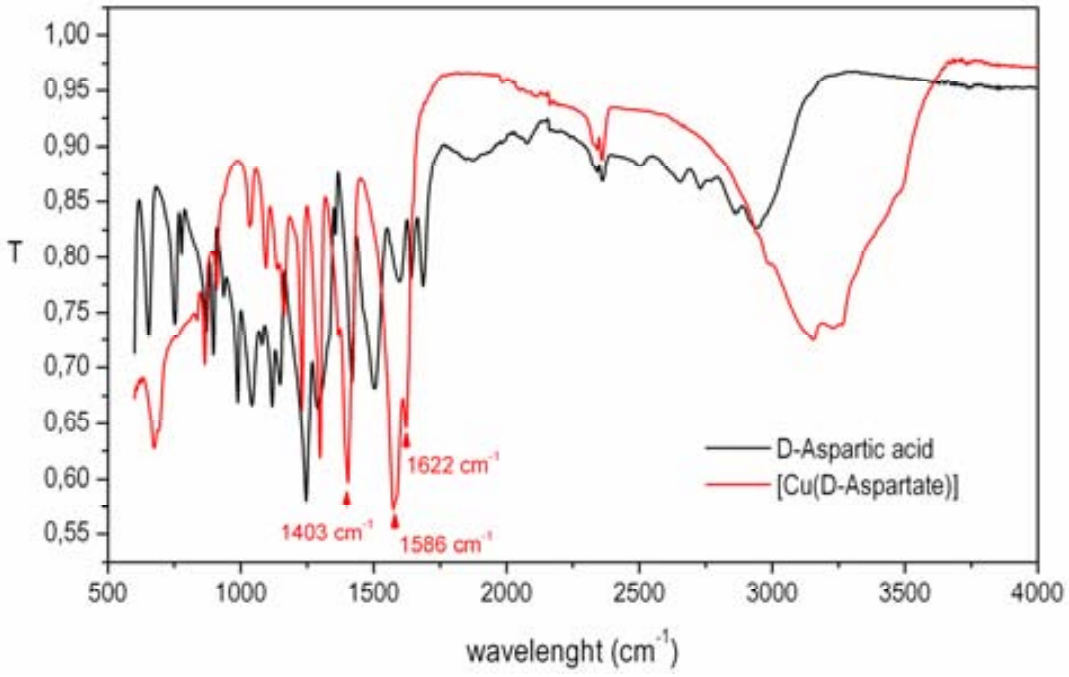

- *Cu-(L-Asp) fibers:*

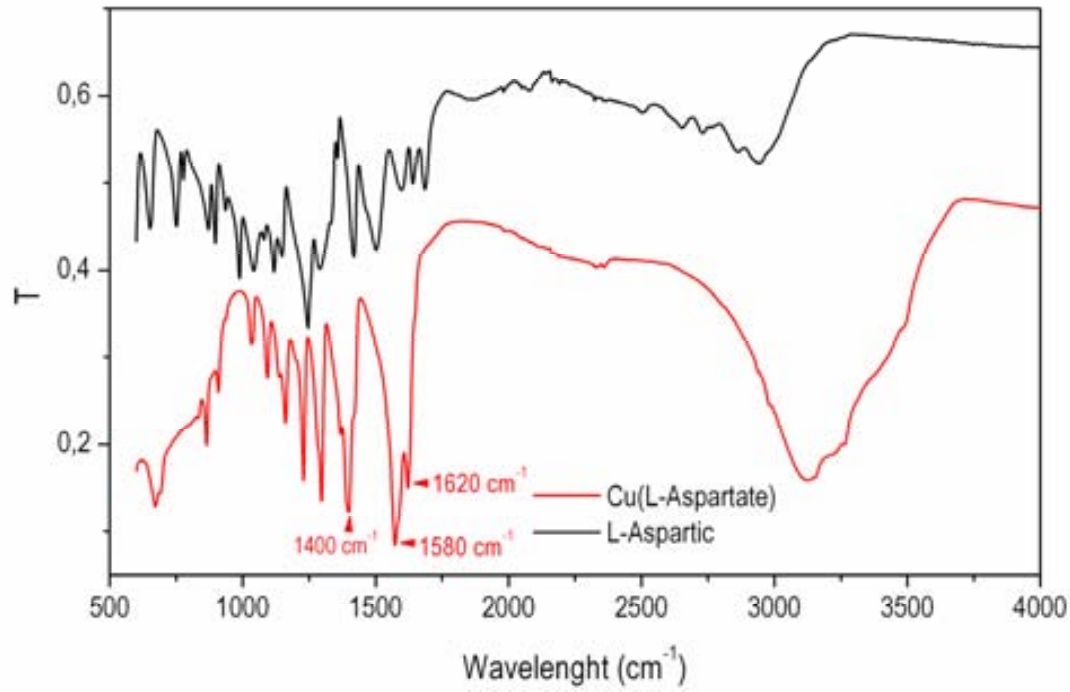

SI3.Optical microscopy images of Cu-(D-Asp) nanofibers grown by interfacial polymerization

SI4.Optical microscopy images of Cu-(D-Asp) nanofibers obtained with polarized light

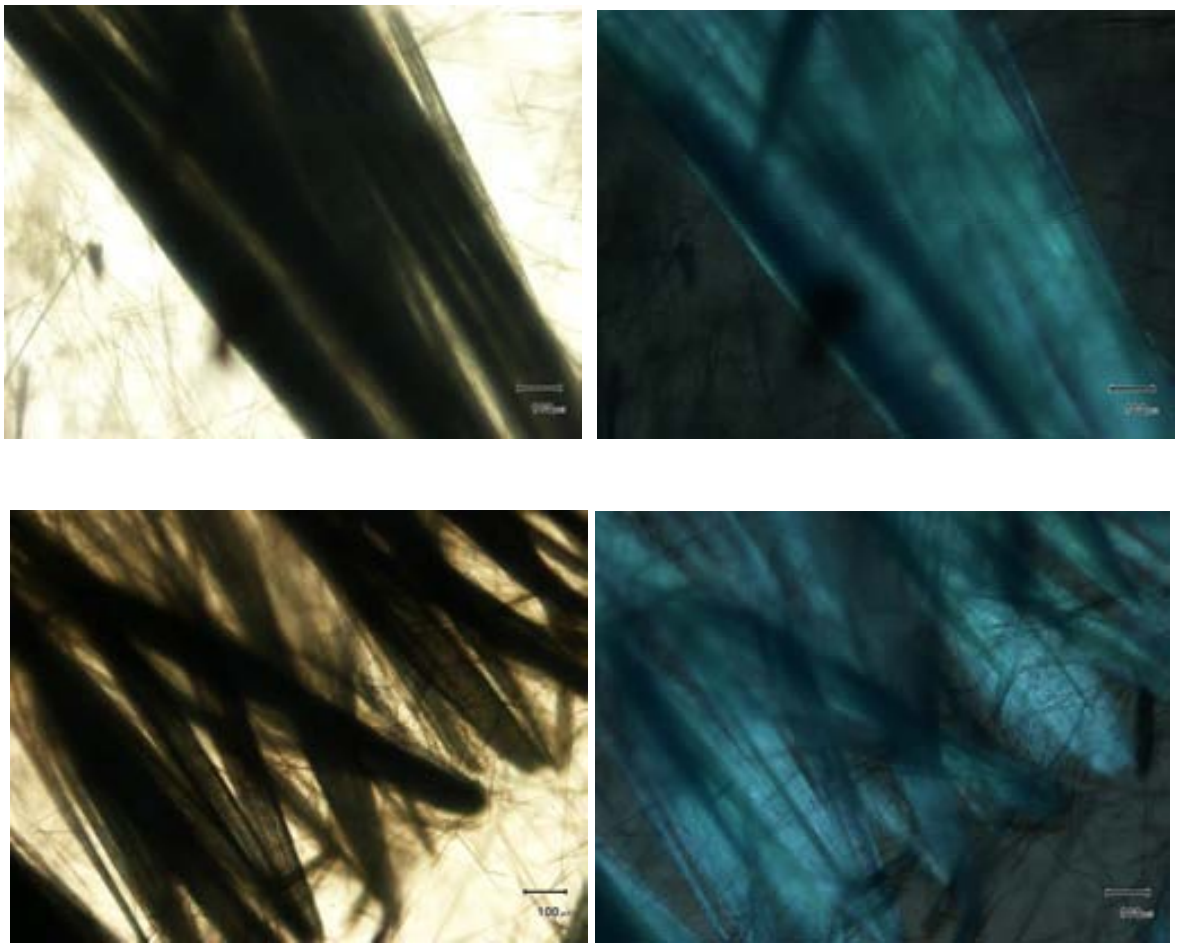

Optical (left) and polarizing optical photomicrographs of the fibers. The weak polarization is only seen in the clusters of fibers, while smaller bundles of fibers have extremely weak or null polarization.

SI5. X-Ray Powder diffraction patterns of Cu-(D-Asp) and Cu-(L-Asp) nanofibers

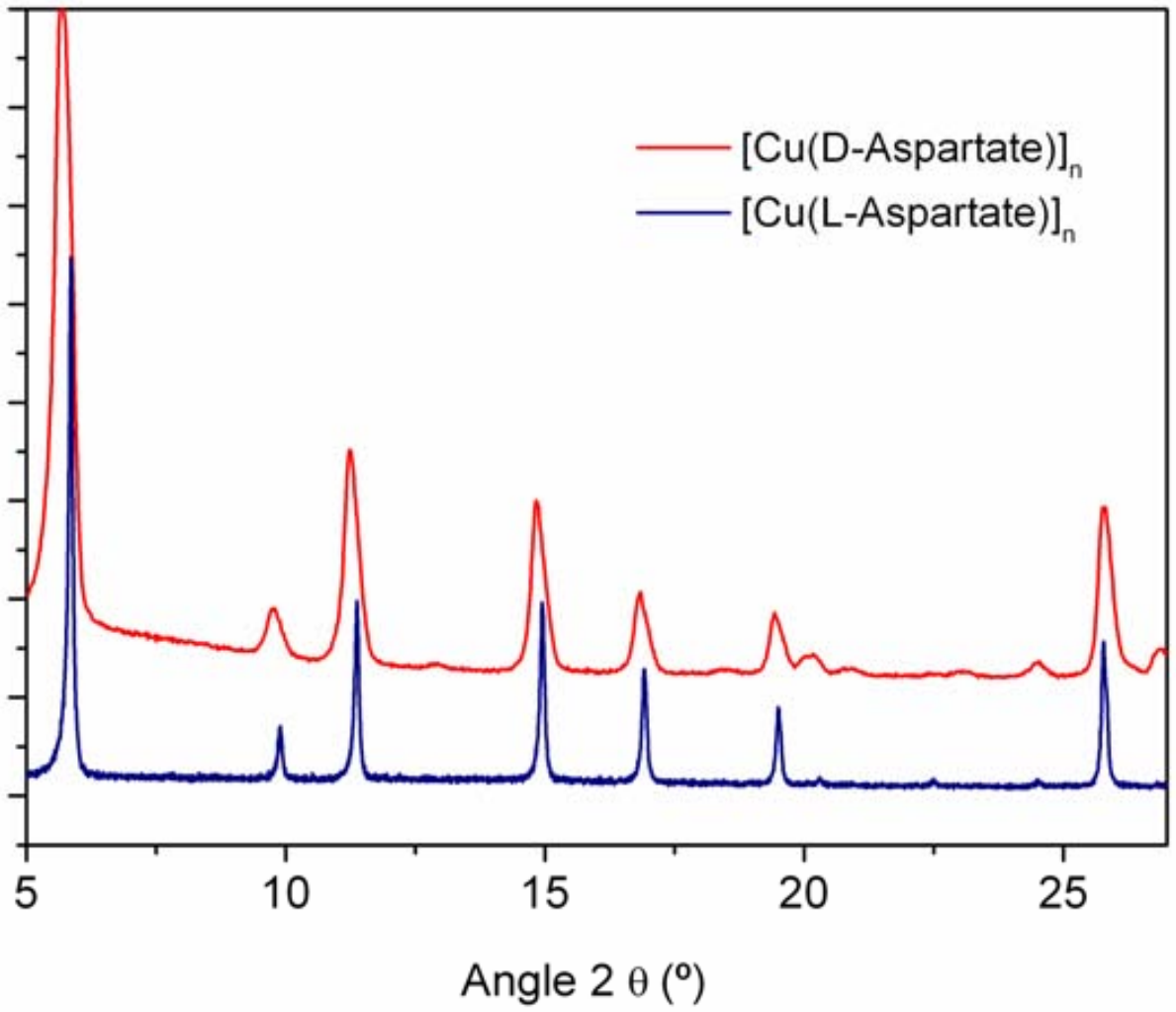

SI6.Scanning Electron microscopy images of Cu-(D-Asp) nanofibers grown by interfacial polymerization

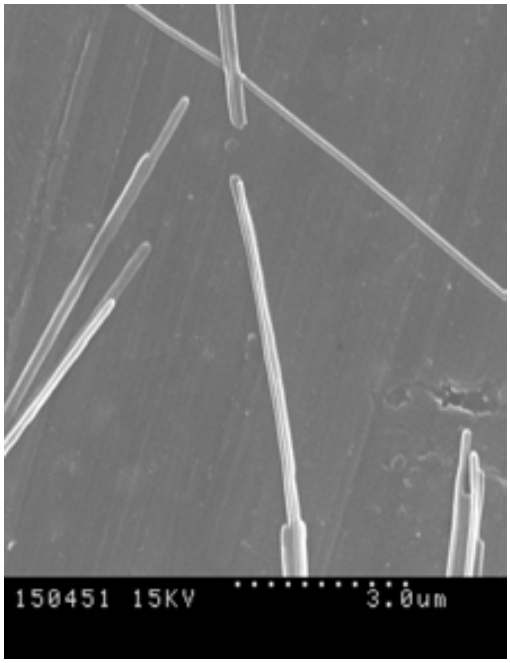

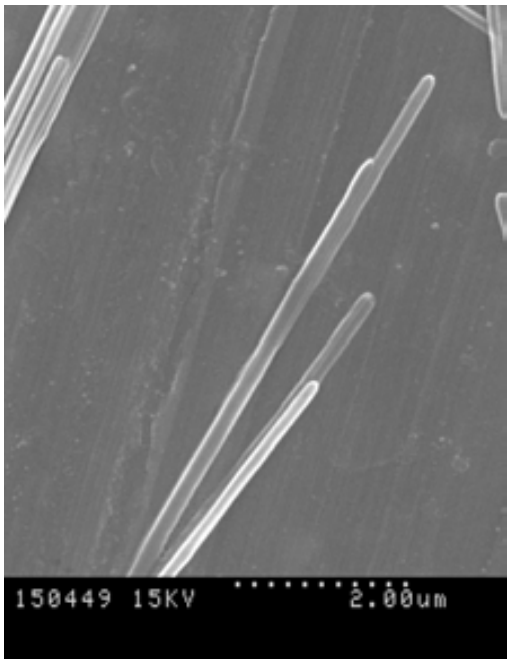

SI7.Transmission Electron microscopy images of Cu-(D-Asp) nanofibers grown by interfacial polymerization

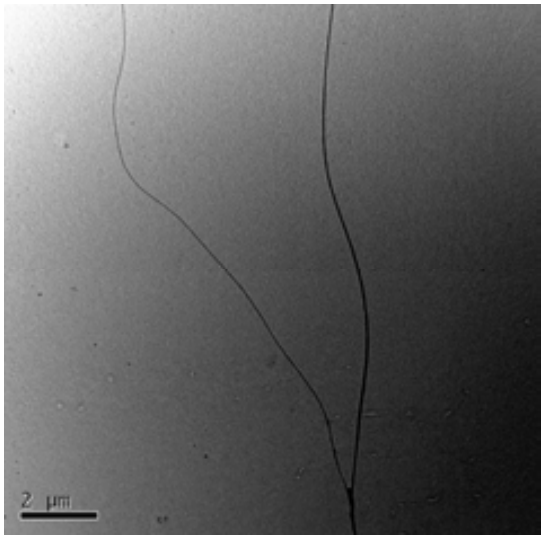

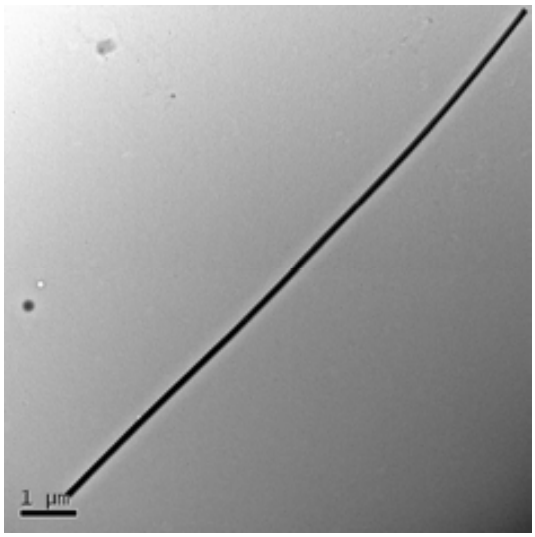

Chapter 4:

Microfluidics: A New Route to 1D Nanoscale Coordination Polymers made of Amino Acids

In this Chapter, we show the first case of coordination polymer nanofibers (made of amino acids) assembled using microfluidic technologies. Unlike common synthetic procedures, this approach enables parallel synthesis with an unprecedented level of control over the coordination pathway and facilitates the formation of 1D coordination polymer assemblies at the nanometer length scale compared to more traditional methods. All these results are included in the manuscript "*Coordination polymer nanofibers generated by microfluidic synthesis*", Journal of American Chemical Society 2011.

I. Microfluidics: Controlling small volumes in very large scale

Microfluidics was defined by Prof. G. M. Whitesides, one of the pioneers in the field, as "*the science and technology of systems that process or manipulate small (10^{-9} to 10^{-18} litres) amounts of fluids, using channels with dimensions of tens of hundreds of micrometres*".[1] Since then, this type of technology has experienced a tremendous evolution, having today real applications in numerous fields ranging from basic research to diagnostic tools that are commonly used in hospitals.[2]

As shown in Figure 4.1, the beginnings of microfluidics is related to the first research projects that focused on the need of several techniques, such as gas chromatography,[3] high-pressure liquid chromatography,[4] and capillary electrophoresis, for manipulating liquids at a very high precision.[5] Microfluidics revolutionized these techniques (and also the chemical analysis field) by allowing the analysis of tiny quantities of samples with high sensitivity. At the same time, the beginnings of microfluidics are also intertwined with the arrival of the continuous inkjet technology in the 1950s and the first commercial inkjet printers developed by Siemens.[6] In fact, these inkjet printers can be considered as the first microfluidic devices. Other companies such as IBM, who started a large development program for computer printers in the 1970s, drove technological advances in this field. In the 1980s, Canon and Hewlett Packard independently developed on-demand inkjets and released low cost, mass-market inkjet printers. Hewlett Packard resolved clogging and reliability problem by being the first to sell disposable inkjet print heads. In this period, advances in micropumps and valves also led to the emergence of microfluidics as invaluable tools for analytical applications in chemistry and pharmaceutical research.[7–9] A high control over materials, interfaces, flow control and dimensionality gave the opportunity to achieve well performing devices. In 1979, Terry and co-workers presented one of the first examples of these devices. They fabricated a gas chromatograph based on micrometre-sized etched channels on a silicon wafer.[10] The next development step was the concept of miniaturized total chemical analysis systems (known as μTAS technology), pioneered by Manz in 1990, which resulted in the development of microfluidic high-pressure liquid chromatography systems as well as microfluidic capillary electrophoresis in 1992.[11]

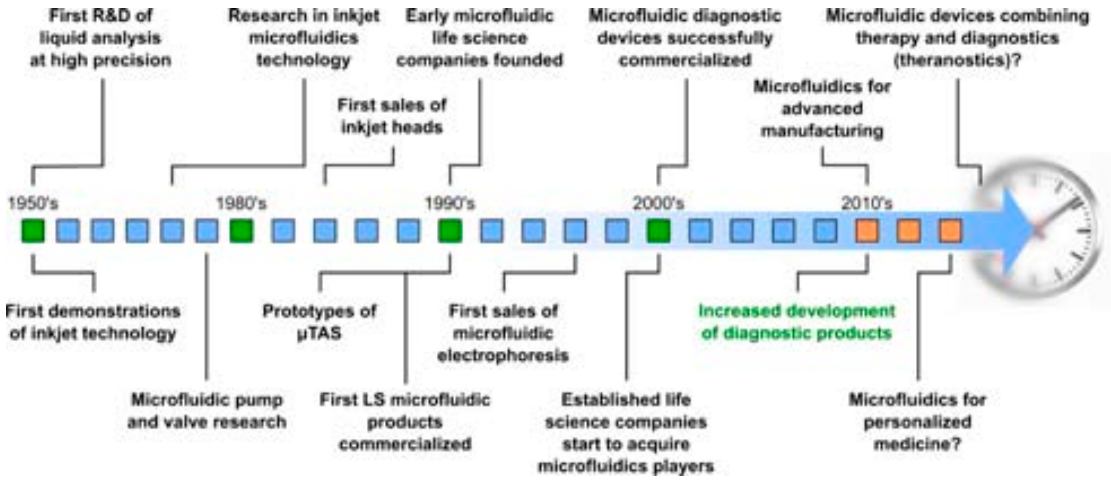

Figure 4.1. Timeline of the evolution of microfluidic technology. Image from IBM.

Over the course of the 90s, the exploration on microfluidics crossed the frontier between basic and applied research, and many companies started to produce new instruments based on microfluidic devices. This breakthrough was made possible by the introduction of soft lithography by Whitesides and co-workers,[12] which allowed a microstructure to be replicated repeatedly using a poly(dimethysiloxane) (PDMS) polymer. As a result, microfluidic devices could be replicated cheaply from a master form in any laboratory, ultimately leading to a wide spread use of this technology.

This discovery allowed Hewlett Packard to start producing microfluidic devices for laboratories and miniaturizing analytical equipment.[13] At the same time, the first portable diagnostic systems started to appear in the market. For example, the Biosite Triage system provides an effective implementation of microfluidics as an alternative to nitrocellulose membranes found in pregnancy tests.[14,15] Nowadays, many successful microfluidic diagnostic products are found on the market, and microfluidics cover most, if not all, of the diagnostic segments with devices (also known as lab-on-a-chip) for pathogen detection[16], critical care, haematology, blood typing, electrophoretic separation,[17] and cytometers.[18]

II. Microfluidic platforms: a mainstream technology for the preparation of materials

Beyond the exponential growth of microfluidic platforms in rapid diagnostics and analytical techniques, microfluidics has also shown a high potential as a novel synthetic tool. The down sizing of the reaction vessels to microfluidic dimensions leads to different, novel effects that dominate the dynamics of fluid. These effects are (i) a faster thermal diffusion; (ii) the laminar flow; (iii) the surface forces; and (iv) the capillarity. All these "novel" phenomena makes possible to make reactions under unique conditions when compared to conventional batch processes (Table 4.1). For example, microfluidics allow conducting reactions in turbulence-free environments, in the absence of gravity effects, in large surface to volume ratios, with superior manipulation of small liquid volumes and with an excellent control of mass and heat transport. Furthermore, microfluidics permit for a high control in the localisation of the reactions, thereby allowing the *in situ* manipulation and characterization of the synthesized materials using spectroscopic (*e.g.* Raman spectroscopy) and diffraction techniques. [19]

Table 4.1. Comparison between the characteristic of batch methods and microfluidics

Bulk Methods	**Microfluidic Methods**
• Gravity	• No gravity or negligible effect
• Turbulent conditions	• Turbulence-free conditions
• Low surface area to volume ratios	• Large surface to volume ratios • Possibility of designing kinetic routes due to the excellent control of mass and heat transfer
• Limited control on the manipulation of small fluid volumes	• Excellent manipulation of reagents
• Possibilities for *in situ* characterization	• Limited *in situ* characterization (spectroscopic techniques or diffraction studies)
• A wide variety of liquids can be used	• The solvents must be chosen according to the chip material
• Limited screening possibilities with automated expensive equipment	• Large scale integration and possibilities for simultaneous screening analysis
• Difficult to control concentration and temperature gradients	• Well controlled concentration and temperature gradients
• Large scale preparation feasible	• Maximum scale of the order of mg
• Facile separation (filtration)	• Potential issues with clogging or removal of material from the chip

To date, the five major microfluidic approaches that are used for the preparation of micro- and nanomaterials are: a) Droplet-based methods, which rely on the formation of droplet microreactors generated by reagent flows towards a junction where an immiscible carrier fluid causes the spontaneous formation of a succession of discrete "slugs" or droplets. This type of system is particularly attractive for crystallisation and high-throughput screening studies (Figure 4.2.a). For instance, the multi-step synthesis of CdS and CdS–CdSe core–shell nanoparticles reported by Ismagilov and co-workers;[20] b) Valve-based platforms, which are devices that use microelectromechanical (MEMS) valves and pumps for controlling intermixing of nanoliter quantities of reagents on a single wafer. Parallel operation permits to perform hundreds of reactions at once (Figure 4.2.b). For example, high-throughput screening of different protein crystallisation conditions was reported by employing this method.[21,22] The high degree of valve integration enabled by this approach permits a large scale integration of crystallisation trials, and hence, a rapid screening of different crystallisation conditions; c) Well-based approaches that use micro-fabricated wells on wafers, and do not require pumps or valves, as the reagents are mixed by sliding two wafers horizontally against each other. By creating many wells on a single wafer it becomes possible to study thousands of trials within a single day (Figure 4.2.c). Zheng and co-workers, for example, screened the crystallisation conditions of four known proteins and one protein whose crystals were not known previously by employing this well-based method. The authors proved that this methodology permitted the formation of diffraction-quality crystals;[23] d) Digital microfluidics picoliter, in which microliter-sized droplets are independently addressed on an open array of electrodes coated with a hydrophobic insulator. Through the application of a series of potentials to these electrodes, droplets can be individually made to merge, mix, split, and dispense from reservoirs (Figure 4.2.d). These programmable digital microfluidic platforms have been employed recently to accurately deposit single crystals of metal–organic frameworks (MOF) on a surface. In this work, the authors demonstrated a high-throughput fabrication of single MOF crystal arrays on a planar surface upon controlled evaporation of femtoliter droplets of MOF building block solutions:[24] and e) Continuous flow platforms, which are based on continuous laminar flows of the reactants in microchannels. This flow condition leads to well-defined reaction interfaces within the platforms, intermixing the reactants solely by diffusion and allowing precise control over the reaction time (Figure 4.2.e).

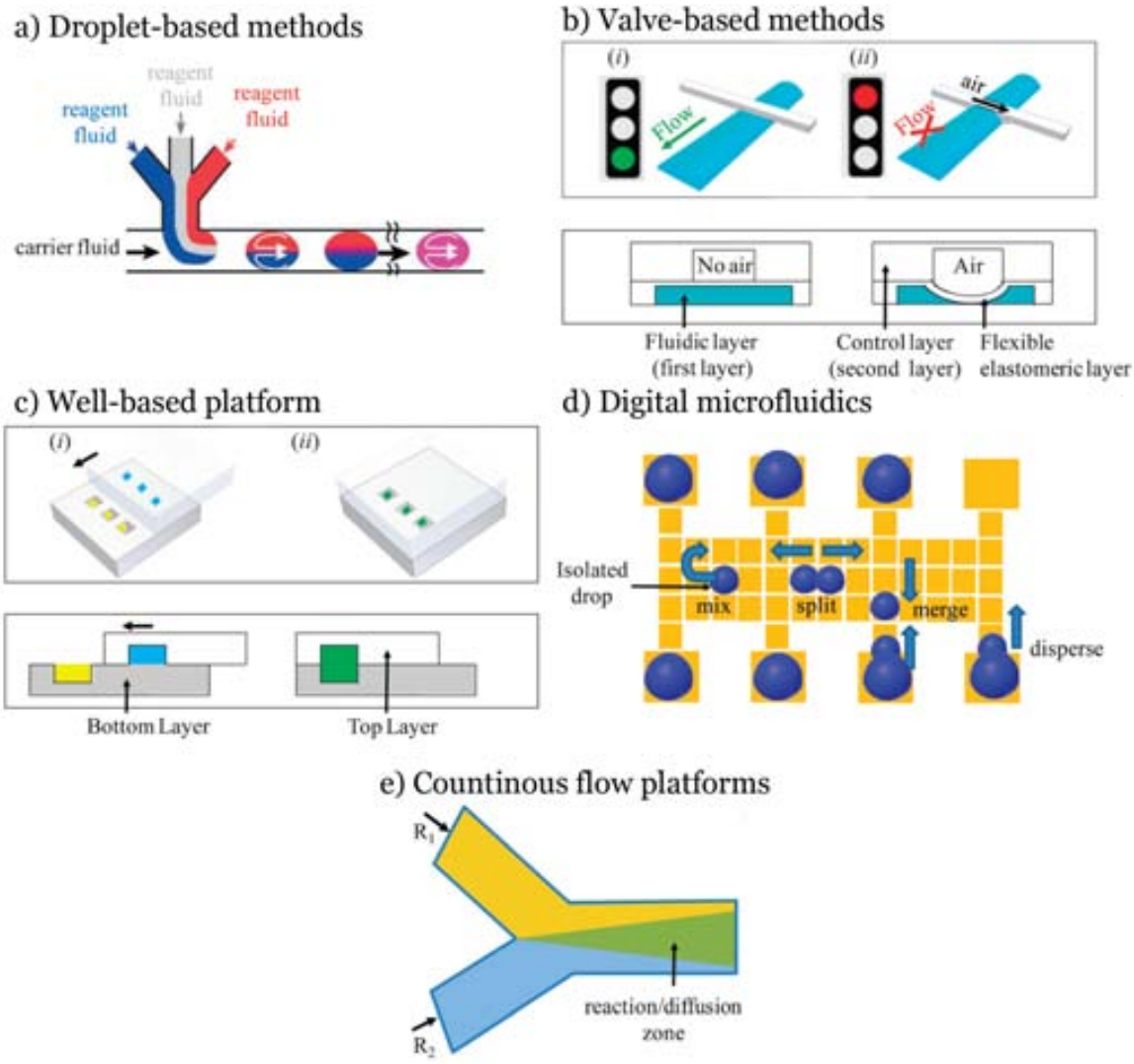

Figure 4.2. Scheme showing five distinct microfluidic approaches employed for crystallisation studies. a) Schematic illustrations of a microfluidic droplet generator. b) Valve-based platforms. Top and side view illustrations showing (i) a valve-based platform where the flexible membrane is not actuated and (ii) when it is actuated. c) Well- based approach. Top and side view illustrations showing from (i) to (ii) how the SlipChip operates. d) Digital microfluidics showing all fluidic elementary operations allowed. e) Schematic illustration of the laminar flow regime operating in a continuous flow platform where R1 and R1 are reagent streams. The green areas represent the reaction/diffusion zone. Figure adapted from ref. 19.

III. Our investigation: Microfluidics as a new tool for synthesizing nanoscale coordination polymers

III.1. Examples of nanoscale coordination polymers synthesized by microfluidics

Analogously to the other types of nanomaterials, the advantages of microfluidics must be very beneficial not only for optimizing the synthesis of nanoscale coordination polymers with a better control on their size and shape but also for discovering new ones. Thus far, however, not many examples of this type of nanomaterials synthesized by microfluidics can be found in the literature; and all of them were reported during the period of this Thesis.

In 2011, De Vos *et al.* were the first to show that microfluidics could be used for the synthesis of metal-organic materials.[25] In particular, they synthesized metal-organic crystals in a micro-scale reactor, in which the reagents phases were injected in an immiscible carrier fluid, causing the spontaneous formation of droplets where the reaction occurs (Figure 4.3.) In this particular case, the immiscibility of the water and oil phases was exploited as a template for the controlled formation of hollow metal–organic $Cu_3(btc)_2$ (where btc is trimesic acid; also known as HKUST-1) microcapsules made of the self-assembly of small crystals. The authors described the crystallisation process as a dynamic on-going process of nucleation and crystal growth that resulted in the formation of crystalline $Cu_3(btc)_2$ membranes with a uniform wall thickness.

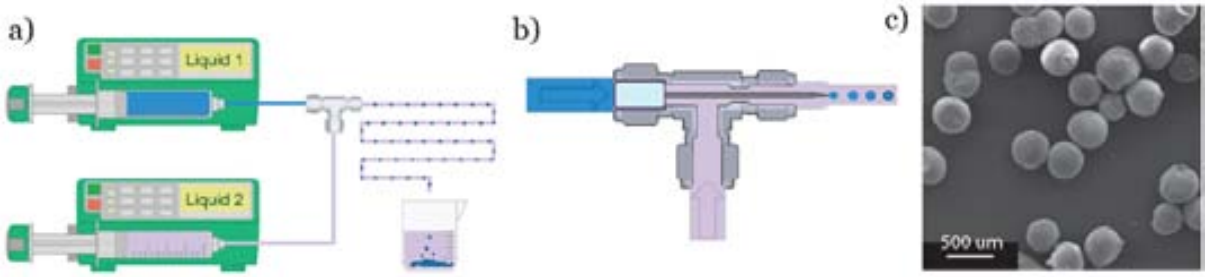

Figure 4.3. a) Schematic illustration of the preparation of hollow MOF capsules using the syringe pumps set-up. b) Cut-away view of the T-junction showing details of the emulsification step. The metal-ion-containing aqueous solution (blue) flows through a tapered capillary centred in the tubing, and the ligand-containing organic solution (purple) flows around it. Growing droplets detach when the force due to interfacial tension is exceeded by the drag force of the surrounding organic phase. c) SEM image of several hollow $Cu_3(btc)_2$ capsules. Figure adapted from ref. 25.

More recently, Moon *et al.* reported a microfluidic-based technology that enables the solvothermal and hydrothermal synthesis of MOFs and MOF-composite superstructures using oil microdroplets as a reactors.[26] Four representative MOF structures, copper trimesate HKUST-1, zinc terephtalate MOF-5, zinc aminoterephtalate IRMOF-3 and zirconium terephtalate UiO-66 were synthesized using the droplet-based microfluidic approach yielding substantially faster kinetics in comparison to the convectional batch processes. In addition they reported the possibility to create MOF heterostructures using imidazolate frameworks (ZIFs) in a two-step process: Firstly, the iron oxide precursor solution and the oil phase were injected and reacted in a microreactor at 80 ºC for 2 minutes. Then, the resulting iron oxide particles were transported downstream to a second microreactor, where they merged and reacted with a mixture of ZIF-8 precursor (zinc nitrate and 2-methylimidazolate in methanol, and polystyrenesulphonate). This leads to the creation of core-shell Fe_3O_4@ZIF-8 composite superstructures (dimensions: 700 ± 50 nm).

The latest study found in literature was reported by Coronas and co-workers, who demonstrated the feasibility of the droplet-based microfluidic approach for the crystallization of the iron fumarate MIL-88B MOF.[27] In this study, they confirmed that the size of the resulting crystals was dependent of the temperature and residence time. They observed a continuous increase in particle size from average sizes ranging from 90 to 900 nm with higher residence times or higher temperatures.

III.2. Our technique: Microfluidic Laminar Flow

In this Thesis, microfluidic laminar flow platforms have been selected among the above-mentioned classes of microfluidics for the synthesis of novel nanoscale coordination polymers made of AAs. Continuous flow platforms use streams of reagents that flow through microfabricated channels (Figure 4.2.e). The small dimensions of these devices lead to a laminar flow regime. Laminar flow is a phenomenon that occurs when two fluids flow together in parallel layers without any disruption or turbulences. Under these conditions, the motion of the reactant molecules is orderly and occurs in straight lines parallel to the pipe walls.

The parameter that defines if a flow is laminar is the Reynolds number (Re). Re is a dimensionless number that is used to quantify the relative importance of inertial forces (density, ρ [kg/m^3]; mean velocity, ν [m/s]; diameter, d [m]) and the viscous forces (the

dynamic viscosity, μ [Pa·s]) within a flowing fluid.[28] For a flow in a tube, *i.e.* the microchannels, *Re* has the form:

$$Re = \frac{\rho v d}{\mu} = \frac{inertial\ forces}{viscous\ forces}$$

When viscous forces are stronger than inertial forces, the Reynolds number is low (generally below 2000) and the flow is laminar.[8] The transition between laminar and turbulent flows lies between 2000 and 3000. In this range, the internal forces start to dominate over the viscous forces leading to a turbulent flow in the microsystems. In this thesis, all reactions were performed using a microfluidic chip with a length scale of d $\approx 10^{-6}$ m; that is, the Reynolds number is usually lower than 10, which indicates a laminar flow regime.

As state above, in this laminar flow regime, the reagent streams co-flow along the entire channel length and intermix only through diffusion at their interface. This type of intermixing allows a precise control over the local concentrations of reactants, making this system interesting for chemical reactions and crystallisation processes. In addition, by changing the flow rate of the reagent streams, it is also possible to control the reaction/diffusion zone created at the interface of two streams and the total residence time.

Therefore, there are several physical phenomena that dominate at the microliter scale and that must be considered when one makes a chemical reaction in a microfluidic laminar flow platform. The most important parameters will be discussed in the following:

III.2a. Diffusion

In a simple one-dimensional model, the diffusion of reagents in microfluidic reactors can be described using the equation:

$$d^2 = 2\,D\,t$$

where *d* is the distance that a molecule moves in a time *t*, and *D* is the diffusion coefficient of the molecule. At the micrometre length scale, diffusion becomes very important because if one simply reduces the distance by a factor of 2, the diffusion time becomes 4 times shorter. Thus, the diffusion and intermixing of a reactant occurs very fast within the microchannel, allowing to precisely control the mixing process by selecting the appropriate flow rate.[29] In this Chapter, all nanostructures were synthesized in a laminar flow, in absence of any turbulence, so the intermixing of the reactants is governed only by diffusion due to the micrometre size of the channels.

III.2b. Flow rate and residence time

The flow rate is the volume of the reaction mixture that passes through the device per unit time. A reaction parameter directly related to the flow rate is the residence time, which can be defined as the amount of time that the fluid is running through the microchannels, and hence able to react. The residence time (τ) is calculated based on the reactor volume (V) and the flow rate (q):

$$\tau = V/q$$

The reactor volume can therefore be calculated as V= high · length · width since the microchannels have a rectangular shape, whereas the flow rate is the sum of all four flows used. Thus, a precise control over the residence time can be achieved by changing the total volume and the flow rate. For example, either a decrease in the flow rate or the use of a larger volume reactor results in a longer residence time inside the device, thereby allows more time for the crystallization process to occur.

III.2c. Pressure inside a channel

The pressure inside the microfluidic channel is an important parameter to be considered in microfluidic systems because it can cause fails and/or ruptures in the devices. In standard fluid dynamics, the pressure drop (Δp) over a round tube is given by the Hagen-Poiseuille's law:

$$\Delta p = \frac{8\mu l Q}{\pi r^4} = RQ$$

where r is the radius [m], Q the volumetric flow rate [m^3/s], μ the viscosity of the liquid [$N{\cdot}s/m^2$], l the length of the channel, and R the fluid resistance [$N{\cdot}s/m^5$], which indicates the shear forces between the walls of the channels and the liquid that is flowing through them.

However, in most microfluidic applications, including those described in this Chapter, the channels have a rectangular shape that makes the expression for the fluid resistant (R) more complicated. For a laminar flow regime (Re < 2000) and a rectangular aspect ratio of the channels (w/h < 1), the fluid resistance (R [$N{\cdot}s/m^5$]) can be simplified to:[30,31]

$$\Delta p = R\,Q = \frac{a\,\mu\,Q\,l}{w h^3}\,, a = \left[12[1 - \frac{192}{w\pi^5}]\tanh\frac{\pi w}{2h}\right]^{-1}$$

Thus, Δp is dependent on several factors, including the length (l), the width (w), the etch depth (h) of the channel and the velocity of the fluid (v). All these parameters can be

modulated in the fabrication of the device, and they must be chosen appropriately to limit the pressure inside the microfluidic reactor.

III.3. Design, fabrication and manipulation of the microfluidic laminar flow platform

It is known that one of the common problems associated with working at these small dimensions is the obstruction of the microchannels. For example, the reaction/diffusion zone in a system with only two inlets can reach the side of the channels. This is due to the parabolic speed profile present in the channels, which can lead to a precipitation of solid products on the channel walls where the fluid speed is zero (Figure 4.4b).

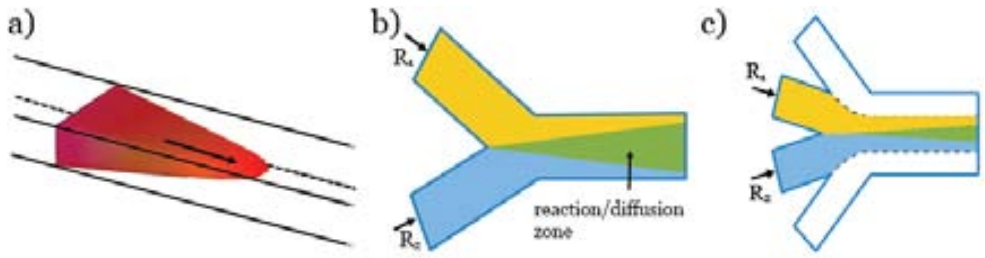

Figure 4.4. a) Illustration of the parabolic flow profile inside a microfluidic channel. b) Schematic illustration of the laminar flow platform using only the reagents flows. c) Illustration of a hydrodynamic flow-focussing platform containing two focussing flows. Figure adapted from ref. 19.

A way to solve this problem is to add multiple coaxially focused flows (generally with the corresponding solvents), which make it possible to further control the flow speed profile as well as the intermixing of the reactants. As shown in Figure 4.4c, adding auxiliary flows to the main channel shifts the reaction/diffusion zone further down the channel, hereby reducing the total reaction zone length and inhibiting contact with channels walls. Accordingly, in this Thesis, two additional flow channels were added to the two main channels of continuous flow platform (Figure 4.4c). Both, the design and fabrication of these devices were done by Dr. Josep Puigmartí at the ETH (Zurich; Switzerland) and in the cleanroom facilities at the CNM (Barcelona; Spain). A step-by-step explanation of this soft-lithography fabrication of the polydimethylsiloxane (PDMS) microchips as well as how it was used is explained below.[32,30]

III.3a. Wafer fabrication

The first step in the fabrication of the microchip is the design of the system. As state above, we designed a system with four input channels where the reactants and solvent solutions could be injected and a main channel where the solutions of reactants intermix and react. Using computer-aided design (CAD) software, we created a detailed drawing of the setup, which then was transferred to a quartz glass photomask (Figure 4.5).

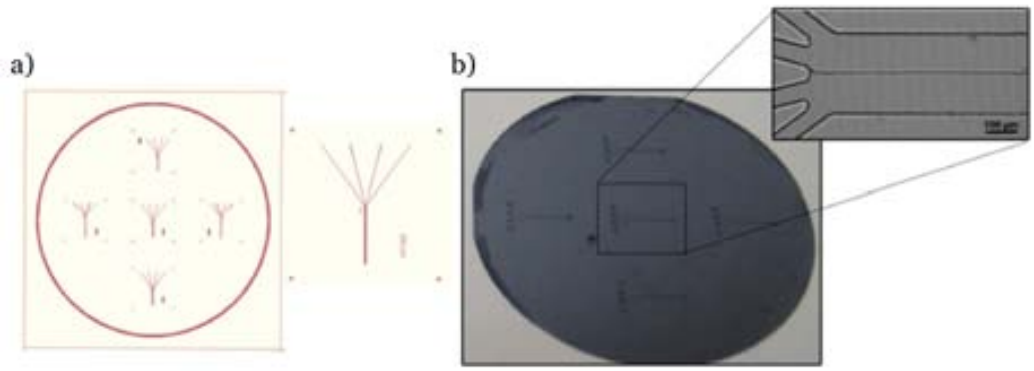

Figure 4.5. a) Design made by CAD of our microreactor. b) Photograph of the designed mask and optical image of the microreactor used in the fabrication of metal-organic nanomaterials formed by four inlet channels for the reactants solutions.

As a substrate, we used a 4-inch silicon wafer, which was previously cleaned and dehydrated for 5 min at 180°C. A negative epoxy-based photoresist, SU-8 (from MicroChem Corp.), was spun on the silicon wafer by spin coating and subsequently heated on a hotplate to remove most of the solvent. The transmission of our design to the substrate was achieved by photolithography process exposing the wafer to 365 nm UV-light using a mask aligner (MA-6 mask aligner, Karl Suess). Next, a post exposure bake (PEB) was done on a hotplate in order to obtain a uniform density of the photoresist (15 min at 100°C). In a final step the film was develop by placing the wafer in a SU-8 developer bath (ethylene glycol monomethyl ether acetate) for a few minutes (1 to 6 min) and then, rinsed with isopropanol and blow dried (Figure 4.6). All the wafers were inspected under a microscope and hard baked at 180°C for 2 hours to remove any residual solvent and to fix the SU-8 features. Finally, the silicon master mold was silanized using 1H,1H,2H,2H-perfluorodecyldimethyl-clorosilane (ABCR) to avoid PDMS adhesion during chip fabrication.

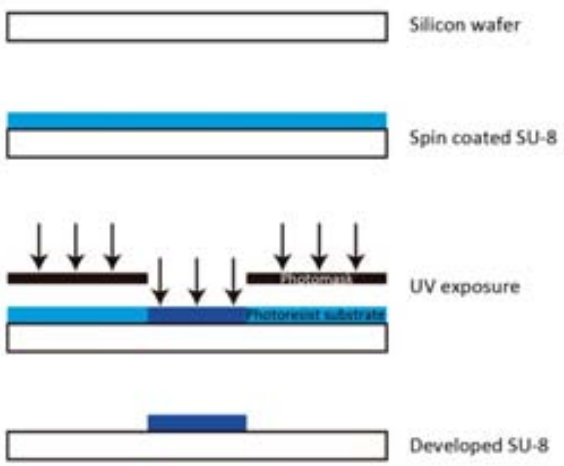

Figure 4.6. Illustration of the microfabrication steps involved in the production of SU-8 master mold by soft-lithography.

III.3b. Device fabrication

As shown in Figure 4.7, the microfluidic device was made from polydimethylsiloxane (PDMS, SYLGARD® 184 Silicone Elastomer Kit) using the master mold. PDMS belongs to a group of polymeric organosilicon compounds comprised of repeated units of silicon and oxygen, with methyl groups attached to the silicon atoms. For the manufacture of our microfluidic devices, the PDMS was supplied in two components to remain in liquid form: a base and a curing agent in a 1 to 10 (v/v) ratio. The mixture was degassed to remove gas bubbles in a desiccator and poured over the master mold taped onto the bottom of a petri dish. In the next step, the mixture was cured at 80 ºC for 3 h, and then the PDMS slab was peeled off. Each single chip was cut to size, and inlet and outlet holes were punched with a Biopsy puncher to connect the channels with external tubing. To seal the top of the device, the PDMS slab was plasma-bonded to a glass cover slip using a plasma cleaner. Our microfluidic device had four 50 μm × 50 μm input microchannels, and a 250μm × 50 μm main reactor channel. The total length of the main reactor channel was 9 mm.

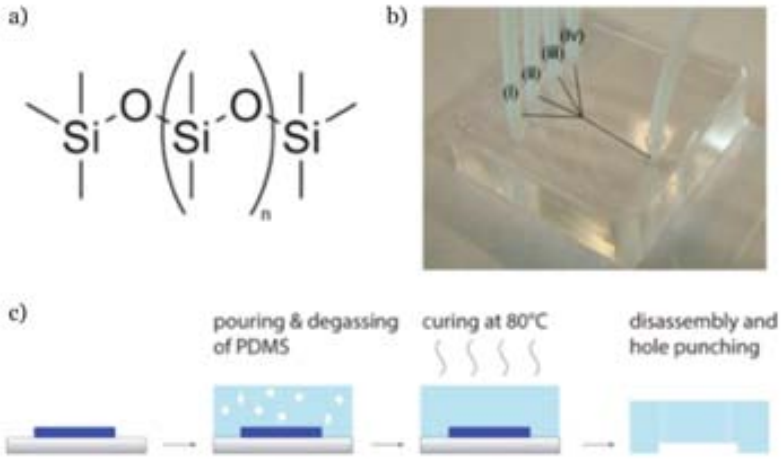

Figure 4.7. a) Repeated structure of PDMS, b) Photograph of the finished microreactor with four inlet and one outlet channels. c) Schematic illustration showing the fabrication of the microfluidic device from the master mold and PDMS.

III.3c. Microfluidic device operation

The microfluidic devices used to synthesize the metal-organic nanostructures presented in this thesis are based on 4 neMESYS pumps from Cetoni (Figure 4.8). The advantage of this system was that many syringes can be used in parallel, and the laminar flow of each syringe was easily accomplished and controlled. The reactant solutions were carried in the syringes trying to not enclose any bubbles in the syringe or in the tubing leading to the microfluidic device.

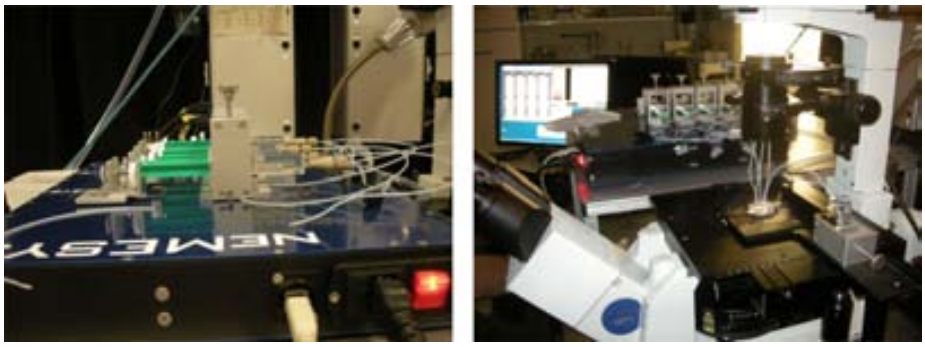

Figure 4.8. Photographs of the microfluidic chip operation.

III.4. Examples of nanomaterials generated by microfluidic laminar flow

The first example of the preparation of nanomaterials using laminar flow regimes was reported by Whitesides and co-workers, who synthesized inorganic microcrystal arrays of

calcium carbonate (calcite) and calcium phosphates (apatites).[34] The crystallization phenomena occurs as a result of the transport of the reactive species to the interfaces within the capillary by diffusion, leading to a self-assembled layer of ~5 μm crystals. Since this pioneer publication, numerous syntheses have been performed under laminar flow. One example is the synthesis of quantum dot nanoparticles carried out by De Mello and co-workers.[35] Quantum dots were obtained by controlling the mixing conditions of $Cd(NO_3)_2{\cdot}4H_2O$ and Na_2S aqueous solutions inside a planar glass–silicon–glass sandwich microfluidic platform. In this study, these authors demonstrated that the use of microfluidics to synthesize nanomaterials offers distinct advantages over bulk fabrication procedures due to the small size of the microreactor. Miniaturisation improves thermal and chemical homogeneity across the reaction area, thus decreasing the polydispersity of the crystallites and lessening the likelihood of nanoparticle coalescence.

A key advantage of using microfluidics as a synthetic methodology is the fast heat and mass transfer that can be achieved due to the high surface to volume ratio of the microchannels. Consequently, phenomena like nucleation take place in very short time and no further nucleation and aggregation processes occur during the growth of crystals, permitting systematic studies of growth processes.[36] Based on this principle, Jensen *et al.* designed a continuous microfluidic system (Figure 4.9) for seeded crystallization with integrated detection tools monitoring the growth kinetics as well as screening the effects of process parameters in order to gain insight into the fundamentals of the crystallization process.[37] To perform and test the effectiveness of there microfluidic setup, the authors chose Gly as a model system due to it being a common pharmaceutical excipient with three well known polymorphic forms (α-, β- and γ-).

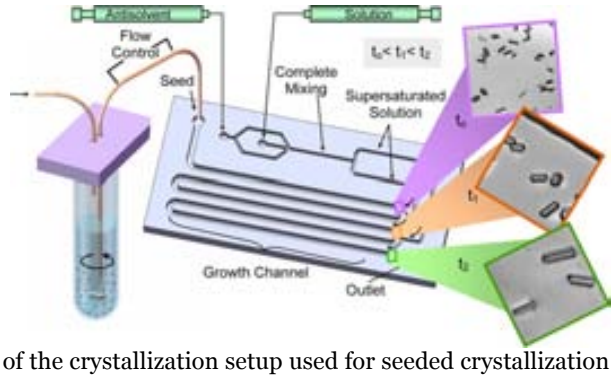

Figure 4.9. Schematic of the crystallization setup used for seeded crystallization of small organic molecules with in situ detection tools for determining the size and shape of the crystals.

IV. Our results: Synthesis of 1D nanoscale coordination polymers made of amino acids under microfluidics laminar flow

The article presented in this chapter, "Coordination polymer nanofibers generated by microfluidic synthesis", describes for the first time the use of microfluidic laminar flow to control the formation of coordination polymer nanofibers based on the assembly of Cu(II) and Ag(I) ions with aspartic acid (Asp) and cysteine (Cys) amino acids, respectively. As described in Section III.3. the synthesis of these nanofibers was performed in a microfluidic platform with four input channels using syringe pump systems. With this device, Cu(II)-Asp nanofibers identical to those synthesized in Chapter 3 were prepared by co-injecting two aqueous solutions of copper nitrate and Asp through the two internal channels and pure water through the two auxiliary channels. The Cu(II)-Asp nanofibers appeared at the interface between the two central flows (Figure 4.10.a), where the two reagents were brought into contact. The resulting material were bundles of well-aligned Cu(II)-Asp nanofibers with diameters ranging from 50 to 200 nm (Figure 4.10.b). It is interesting to note here that those Cu(II)-Asp were perfectly aligned to the direction of the flows.

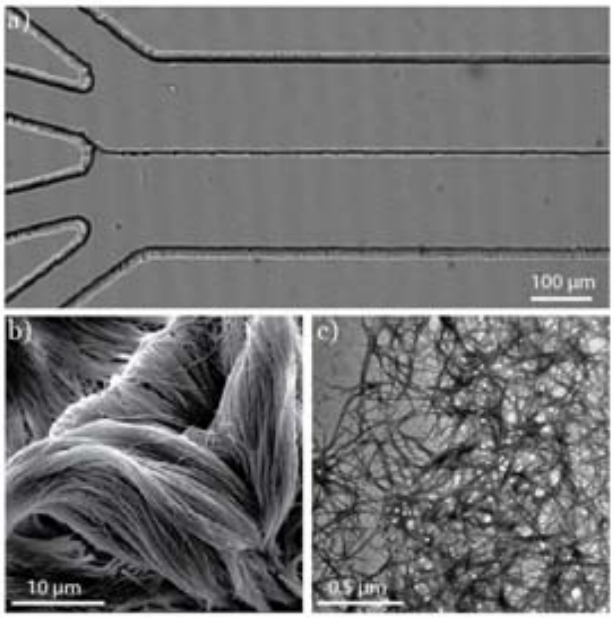

Figure 4.10. a) Optical microscope image of bundels of Cu(II)-Asp nanofibers generated inside the chip demonstrating the centered assembly along the main channel lenght. b) SEM image of the Cu(II)-Asp nanofibers fabricated in the microreactor. c) TEM image of the resulting bundles of Ag(I)-Cys just after their elution from the chip.

The second class of nanofibers made of amino acids was formed by Ag(I) ions linked by the amino acid Cys. Compared to Asp, Cys also has a third functional group, a thiol group, which can coordinate with metal ions. Following the same methodology but injecting aqueous solutions of silver nitrate and Cys in the microreactor, we could synthesized Ag(I)-Cys nanofibers with a diameter between 10 and 50 nm (Figure 4.10.c). The formation of these nanofibers is rather remarkable, considering that they were not formed when the two reagents were mixed under agitation. Under these more conventional conditions, the Ag(I)-Cys coordination polymer was shaped as a membrane instead of nanofibers (see Figure S.10. of S.I.) This observation confirms the possibility to use microfluidics to discover nanoscale coordination polymers with different morphologies, which special conditions shows a high tendency to form 1D nanostructures.

The formation of Cu(II)-Asp and Ag(I)-Cys CPs was confirmed by characterizing the resulting nanofibers by electron microscopy (SEM and TEM) (Figure 4.10 b-c), by EDX microanalysis that corroborated the presence of copper and silver in the respective nanofibers (see Figure S.6. of S.I.) and by infrared spectroscopy that confirmed the coordination of the Asp ligand to the Cu (II) metal ion through the carboxylate groups and Cys to Ag (I) through the sulphur atom and carboxylic group of the Cys (see Figure S.8. of S.I.).

These two examples show that microfluidics, besides being an effective approach to produce nanostructures, offers another advantage over convectional synthetic approaches. The precise command over the reaction zone makes it possible to control the position within the reactor where the assembly of molecules and metal ions into nanofibers occurs and therefore, where the nanofibers are synthesized. This control on the location will be very important in the following Chapters to further characterize and study the synthesized CP nanostructures.

Finally, the generality and efficacy of microfluidics for the nanofabrication of coordination polymer 1D nanostructures was confirmed by creating Zn(II)-4'4-bipyridine (4,4'-bipy) nanofibers. These nanofibers were obtained when an aqueous solution of zinc nitrate (100 mM) and another solution containing 4,4'-bipy (100 mM) in ethanol were injected in the microfluidic platform. The resulting Zn(II)-4,4'-bipy nanofibers had diameters between 10 and 75 nm. The coordinative polymerization of Zn(II) metal ions through 4,4'-bipy ligands was also confirmed by energy dispersive X-ray (EDX), that corroborates the presence of zinc in the nanofibers and by IR spectroscopy that confirms the coordination of the Zn(II) to the pyridine ring of the 4,4'-bipy (see Figure 4.11).

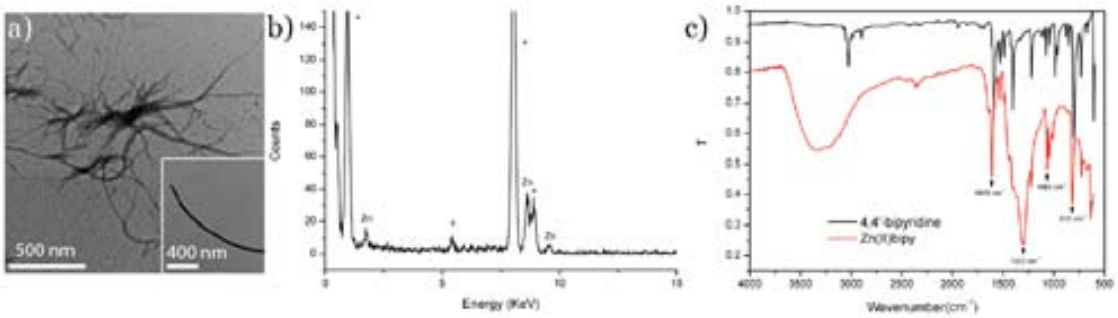

Figure 4.11. a) TEM image of Zn(II)-4,4'-bipy nanofibers just after their elution from the chip. The inset corresponds the magnification of the nanofibers. b) EDX spectrum of Zn(II)-4,4'-bipy. The peaks marked by a star symbol correspond to the TEM grid. c) Infrared spectra of Zn(II)-4,4'-bipy nanofibers and 4,4'-bipyridine.

To conclude, in this Chapter, we have demonstrated that microfluidics is a promising technology for the straightforward production not only of coordination polymers but also for their nanostructuration in the form of nanofibers. Moreover, this methodology enables a fast, better-controlled synthesis and possesses the ability to govern the formation pathway of the assembled structures by varying flow-rate conditions. Considering the amount of research focused on developing new methods for synthesizing nanoscale coordination polymers, microfluidics will certainly expand the possibilities for fabrication of functional molecular nano-assemblies that are not easily constructed by traditional techniques. In the next chapter, it is shown how these coordination polymer nanofibers can be further used as scaffolds to template the growth of functional superstructures made of inorganic nanoparticles.[38]

V. References

(1) Whitesides, G. M. The Origins and the Future of Microfluidics. *Nature* **2006**, *442*, 368–373.

(2) Elvira, K. S.; i Solvas, X. C.; Wootton, R. C. R.; deMello, A. J. The Past, Present and Potential for Microfluidic Reactor Technology in Chemical Synthesis. *Nat. Chem.* **2013**, *5*, 905–915.

(3) Horvath, C.; Lipsky, S. R. Column Design in High Pressure Liquid Chromatography. *J. Chromatogr. Sci.* **1969**, *7*, 109–116.

(4) Srinivasan, R.; Firebaugh, S. L.; Hsing, I.-M.; Ryley, J.; Harold, M. P.; Jensen, K. F.; Schmidt, M. A. Chemical Performance and High Temperature Characterization of Micromachined Chemical Reactors. In; IEEE; Vol. 1, pp. 163–166.

(5) Harrison, D. J.; Fluri, K.; Seiler, K.; Fan, Z.; Effenhauser, C. S.; Manz, A. Micromachining a Miniaturized Capillary Electrophoresis-Based Chemical Analysis System on a Chip. *Science* **1993**, *261*, 895–897.

(6) Kappos, D. J. Who Will Bankroll the Next Big Idea? *Sci. Am.* **2013**, *309*, 58–61.

(7) Mitchell, M. C.; Spikmans, V.; Manz, A.; Mello, A. J. de. Microchip-Based Synthesis and Total Analysis Systems (μ-SYNTAS):chemical Microprocessing for Generation and Analysis of Compound Libraries. *J. Chem. Soc. [Perkin 1]* **2001**, 514–518.

(8) deMello, A. J. Control and Detection of Chemical Reactions in Microfluidic Systems. *Nature* **2006**, *442*, 394–402.

(9) Woias, P. Micropumps—past, Progress and Future Prospects. *Sens. Actuators B Chem.* **2005**, *105*, 28–38.

(10) Terry, S. C.; Jerman, J. H.; Angell, J. B. A Gas Chromatographic Air Analyzer Fabricated on a Silicon Wafer. *IEEE Trans. Electron Devices* **1979**, *26*, 1880–1886.

(11) Manz, A.; Graber, N.; Widmer, H. M. Miniaturized Total Chemical Analysis Systems: A Novel Concept for Chemical Sensing. *Sens. Actuators B Chem.* **1990**, *1*, 244–248.

(12) Xia, Y.; Whitesides, G. M. Soft Lithography. *Annu. Rev. Mater. Sci.* **1998**, *28*, 153–184.

(13) *Lab on a Chip Technology*; Caister Academic Press: Norfolk, UK, 2009.

(14) Buechler, K. F.; Moi, S.; Noar, B.; McGrath, D.; Villela, J.; Clancy, M.; Shenhav, A.; Colleymore, A.; Valkirs, G.; Lee, T. Simultaneous Detection of Seven Drugs of Abuse by the Triage Panel for Drugs of Abuse. *Clin. Chem.* **1992**, *38*, 1678–1684.

(15) Chin, C. D.; Linder, V.; Sia, S. K. Commercialization of Microfluidic Point-of-Care Diagnostic Devices. *Lab. Chip* **2012**, *12*, 2118-2134.

(16) Foudeh, A. M.; Fatanat Didar, T.; Veres, T.; Tabrizian, M. Microfluidic Designs and Techniques Using Lab-on-a-Chip Devices for Pathogen Detection for Point-of-Care Diagnostics. *Lab. Chip* **2012**, *12*, 3249–3266.

(17) Manz, A.; Harrison, D. J.; Verpoorte, E. M. J.; Fettinger, J. C.; Paulus, A.; Lüdi, H.; Widmer, H. M. Planar Chips Technology for Miniaturization and Integration of Separation Techniques into Monitoring Systems: Capillary Electrophoresis on a Chip. *J. Chromatogr. A* **1992**, *593*, 253–258.

(18) Fu, A. Y.; Spence, C.; Scherer, A.; Arnold, F. H.; Quake, S. R. A Microfabricated Fluorescence-Activated Cell Sorter. *Nat. Biotechnol.* **1999**, *17*, 1109–1111.

(19) Puigmartí-Luis, J. Microfluidic Platforms: A Mainstream Technology for the Preparation of Crystals. *Chem. Soc. Rev.* **2014**, 43,2253-2271.

(20) Shestopalov, I.; Tice, J. D.; Ismagilov, R. F. Multi-Step Synthesis of Nanoparticles Performed on Millisecond Time Scale in a Microfluidic Droplet-Based System. *Lab. Chip* **2004**, *4*, 316–321.

(21) Hansen, C. L.; Skordalakes, E.; Berger, J. M.; Quake, S. R. A Robust and Scalable Microfluidic Metering Method That Allows Protein Crystal Growth by Free Interface Diffusion. *Proc. Natl. Acad. Sci.* **2002**, *99*, 16531–16536.

(22) Hansen, C. L.; Sommer, M. O. A.; Quake, S. R. Systematic Investigation of Protein Phase Behavior with a Microfluidic Formulator. *Proc. Natl. Acad. Sci. U. S. A.* **2004**, *101*, 14431–14436.

(23) Zhou, X.; Lau, L.; Lam, W. W. L.; Au, S. W. N.; Zheng, B. Nanoliter Dispensing Method by Degassed Poly(dimethylsiloxane) Microchannels and Its Application in Protein Crystallization. *Anal. Chem.* **2007**, *79*, 4924–4930.

(24) Witters, D.; Vergauwe, N.; Ameloot, R.; Vermeir, S.; De Vos, D.; Puers, R.; Sels, B.; Lammertyn, J. Digital Microfluidic High-Throughput Printing of Single Metal-Organic Framework Crystals. *Adv. Mater.* **2012**, *24*, 1316–1320.

(25) Ameloot, R.; Vermoortele, F.; Vanhove, W.; Roeffaers, M. B. J.; Sels, B. F.; De Vos, D. E. Interfacial Synthesis of Hollow Metal–organic Framework Capsules Demonstrating Selective Permeability. *Nat. Chem.* **2011**, *3*, 382–387.

(26) Faustini, M.; Kim, J.; Jeong, G.-Y.; Kim, J. Y.; Moon, H. R.; Ahn, W.-S.; Kim, D.-P. Microfluidic Approach toward Continuous and Ultrafast Synthesis of Metal–Organic Framework Crystals and Hetero Structures in Confined Microdroplets. *J. Am. Chem. Soc.* **2013**, *135*, 14619–14626.

(27) Paseta, L.; Seoane, B.; Julve, D.; Sebastian, V.; Tellez, C.; Coronas, J. Accelerating the Controlled Synthesis of MOFs by a Microfluidic Approach: A Nanoliter Continuous Reactor. *ACS Appl. Mater. Interfaces* **2013**, 19, 9405-9410.

(28) Ismagilov, R. F.; Stroock, A. D.; Kenis, P. J. A.; Whitesides, G.; Stone, H. A. Experimental and Theoretical Scaling Laws for Transverse Diffusive Broadening in Two-Phase Laminar Flows in Microchannels. *Appl. Phys. Lett.* **2000**, *76*, 2376–2378.

(29) Dertinger, S. K. W.; Chiu, D. T.; Jeon, N. L.; Whitesides, G. M. Generation of Gradients Having Complex Shapes Using Microfluidic Networks. *Anal. Chem.* **2001**, *73*, 1240–1246.

(30) Bahrami, M.; Yovanovich, M. M.; Culham, J. R. Pressure Drop of Fully-Developed, Laminar Flow in Microchannels of Arbitrary Cross-Section. *J. Fluids Eng.* **2006**, *128*, 1036-1044.

(31) Fuerstman, M. J.; Lai, A.; Thurlow, M. E.; Shevkoplyas, S. S.; Stone, H. A.; Whitesides, G. M. The Pressure Drop along Rectangular Microchannels Containing Bubbles. *Lab. Chip* **2007**, *7*, 1479-1489.

(32) Xia, Y.; Whitesides, G. M. SOFT LITHOGRAPHY. *Annu. Rev. Mater. Sci.* **1998**, *28*, 153–184.

(33) Dittrich, P. S.; Heule, M.; Renaud, P.; Manz, A. On-Chip Extrusion of Lipid Vesicles and Tubes through Microsized Apertures. *Lab. Chip* **2006**, *6*, 488-493.

(34) Kenis, P. J. Microfabrication Inside Capillaries Using Multiphase Laminar Flow Patterning. *Science* **1999**, *285*, 83–85.

(35) Edel, J. B.; Fortt, R.; deMello, J. C.; deMello, A. J. Microfluidic Routes to the Controlled Production of nanoparticles. *Chem. Commun.* **2002**, 1136–1137.

(36) Watts, P.; Haswell, S. J. Chemical Synthesis in Microreactors. *Methods Mol. Biol. Clifton NJ* **2010**, *583*, 109–120.

(37) Sultana, M.; Jensen, K. F. Microfluidic Continuous Seeded Crystallization: Extraction of Growth Kinetics and Impact of Impurity on Morphology. *Cryst. Growth Des.* **2012**, *12*, 6260–6266.

(38) Puigmartí-Luis, J.; Schaffhauser, D.; Burg, B. R.; Dittrich, P. S. A Microfluidic Approach for the Formation of Conductive Nanowires and Hollow Hybrid Structures. *Adv. Mater.* **2010**, *22*, 2255–2259.

Publication 3. "Coordination polymer nanofibers generated by microfluidics synthesis." J. Puigmartí-Luis, M. Rubio-Martínez, U. Hartfelder, I.Imaz, D. Maspoch, P.S. Dittrich. *J. Am. Chem.Soc.* **2011**, 133, 4216-4219.

JACS
JOURNAL OF THE AMERICAN CHEMICAL SOCIETY

COMMUNICATION

pubs.acs.org/JACS

Coordination Polymer Nanofibers Generated by Microfluidic Synthesis

Josep Puigmartí-Luis,[†] Marta Rubio-Martínez,[‡] Urs Hartfelder,[†] Inhar Imaz,[‡] Daniel Maspoch,*[,‡] and Petra S. Dittrich*[,†]

[†]Department of Chemistry and Applied Biosciences, ETH Zürich, Wolfgang-Pauli-Strasse 10, CH-8093 Zurich, Switzerland
[‡]CIN2(ICN-CSIC), Catalan Institute of Nanotechnology, Esfera UAB, 08193 Bellaterra, Spain

Supporting Information

ABSTRACT: One-dimensional coordination polymer nanostructures are an emerging class of nanoscale materials with many potential applications. Here, we report the first case of coordination polymer nanofibers assembled using microfluidic technologies. Unlike common synthetic procedures, this approach enables parallel synthesis with an unprecedented level of control over the coordination pathway and facilitates the formation of 1D coordination polymer assemblies at the nanometer length scale. Finally, these nanostructures, which are not easily constructed with traditional methods, can be used for various applications, for example as templates to grow and organize functional inorganic nanoparticles.

In the past decade, huge efforts have been focused on developing new methods for the controlled formation of one-dimensional (1D) nanoscale structures, such as wires, rods, tubes, and fibers, because they play important roles in many applications, including electronics, optics, magnetic devices, drug delivery, and sensors.[1] Nanoscale coordination polymers are an important emerging class of 1D nanomaterials with the intriguing prospect to obtain tailorable morphologies and properties by careful selection of both metal ions and organic ligands.[2−7] Thus, the design of 1D nanoscale materials containing organic−inorganic components can be particularly interesting for fabricating a new generation of technologically important functional nanomaterials,[2−5] and for creating novel synthetic biomimetic approaches[6] and functional gels.[7] To date, the most common approach for the synthesis of these structures is based on the self-assembly of metal ions and multitopic organic ligands in solution under certain conditions (solvents, temperature, etc.)[2,3] or employing advanced fabrication methods, such as electrospinning and ultrasound.[4,5] However, although these approaches are very powerful strategies, more general methods for controlling and guiding the assembly of metal ions and organic molecules to novel 1D coordination polymer structures at the nanometer length scale remain challenging.[2]

In this regard, lab-on-a-chip approaches have recently attracted tremendous interest for fabricating 1D nanostructures.[8] Compared to conventional methods, excellent and unique properties appear when scaling-down dimensions inside a microreactor. In particular, the presence of laminar flow makes microfluidic technologies ideal synthetic and assembly tools due to the superior control over the reaction zone.[9] Under laminar flow conditions, a stable interface between two reactive streams can be established, while mixing happens exclusively through diffusion. The diffusion and hence the reaction area of different species can be predicted as well as the residence time of species in the microreactor. Therefore the reaction time can be modulated by varying flow rates.[10] While the laminar flow in a microfluidic reactor has been exploited to induce redox and polymerization reactions at the interface of two co-flowing reactant streams to create fibers and wires in the microscale range, we herein demonstrate that microfluidics is as well a straightforward route for controlling the assembly of metal ions and organic building blocks to form 1D coordination polymer nanostructures (Scheme 1). The formation of coordination polymer nanofibers is presented for various compounds: Cu(II) ions and the amino acid aspartate (Asp), Ag(I) ions and the amino acid cysteine (Cys), and Zn(II) ions and the ditopic 4,4′-bipyridine (4,4′-bipy) ligand. The formation of long Cu-Asp nanofibers has recently been shown in a time-consuming bulk reaction,[11] which can be massively accelerated in the microdevice to occur within microseconds (∼280 μs), where the reaction occurs through the entire length of the microchannel (9 mm) at predefined locations and with a preferred orientation. Moreover, Ag(I)-Cys and Zn(II)-4,4′-bipy are novel types of 1D metal-containing nanofibers that cannot be formed in bulk synthetic approaches. Hence, microfluidic-based fabrication can yield nanoscale coordination polymers with

Scheme 1. Fabrication of 1D Coordination Polymer Nanostructures Using Laminar Flow in a Microfluidic Platform

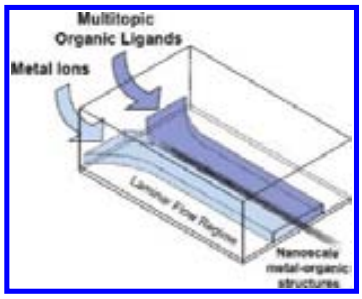

Received: December 2, 2010
Published: March 08, 2011

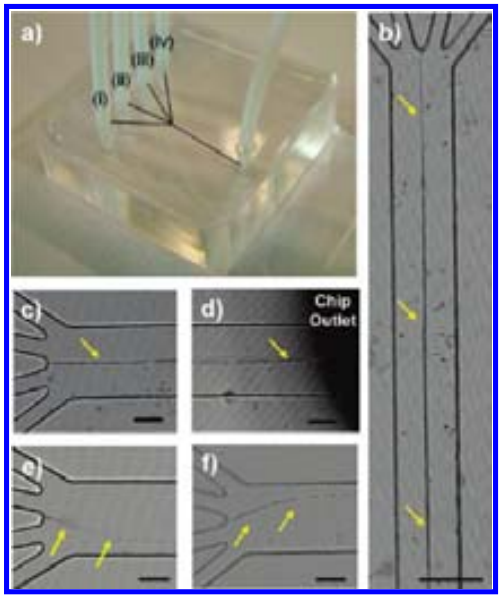

Figure 1. (a) Photograph of the microreactor used in the fabrication of nanoscale coordination polymer fibers. The microreactor contains four inlets channels for supplying the reactants solutions ((ii) and (iii)) and the sheath aqueous flows ((i) and (iv)). (b−f) Optical microscope images of bundles of Cu(II)-Asp nanofibers (yellow arrows) generated inside the chip. (b) Low-magnification optical image of a synthesis performed at [100; 100; 100; 100] (note the broadening of the reaction zone due to diffusion). (c,d) Optical microscope images demonstrating the centered assembly along the main channel length. (e,f) Optical microscope images showing guided assembly when changing the flow rate configuration to [20; 20; 200; 200] and [200; 200; 20; 20], respectively. The scale bar in (b) is 250 μm, and in (c−f) the scale bar is 100 μm.

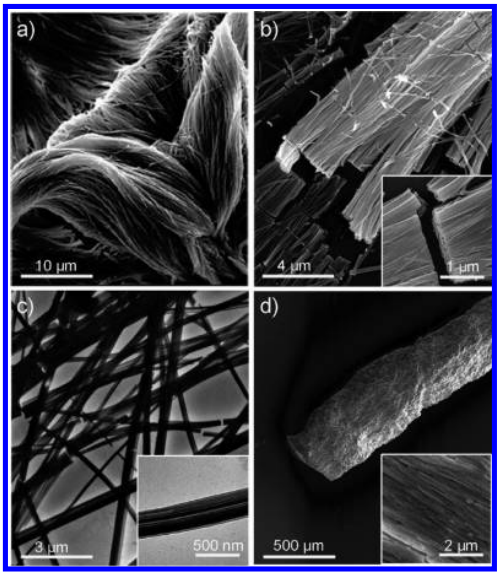

Figure 2. Cu(II)-Asp nanofibers fabricated in the microreactor. (a,b) SEM images of nanofiber bundles synthesized at different concentrations of precursors: (a) 150 mM and (b) 15 mM $Cu(NO_3)_2 \cdot 3H_2O$. (c) TEM image of these fibers synthesized using a $Cu(NO_3)_2 \cdot 3H_2O$ concentration of 150 mM. The inset is a high-magnification image of a single nanofiber. (d) SEM images of a Cu(II)-Asp-based xerogel produced in the microreactor and synthesized at a concentration of 1.5 M $Cu(NO_3)_2 \cdot 3H_2O$. The inset is a high-magnification image, showing the well-aligned nanofibers.

morphologies and therefore properties that are unequivocally different from those offered by standard synthetic methods.

In a typical synthetic procedure, Cu(II)-Asp nanofibers were initially prepared by injecting two aqueous solutions, one containing $Cu(NO_3)_2 \cdot 3H_2O$ (1.5 mM) and the second containing L-Asp (1.0 mM) and NaOH (2.5 mM), into a microfluidic platform with four input channels via a syringe pump system at a flow rate of 100 μL/min (Figure 1a). Both Asp and Cu(II) solutions were injected in the central channels (channels (ii) and (iii) in Figure 1a, respectively), and the formation of Cu(II)-Asp nanofibers through the entire length (9 mm) of the main channel (Figure 1b−d) was accomplished by flowing two aqueous auxiliary streams operating at same flow rate of 100 μL/min (channels (i) and (iv) in Figure 1a). We define the flow rates (all μL/min) in the different channels by using the following abbreviation: flow (i), Q_i; flow (ii), Q_{ii}; flow (iii), Q_{iii}; and flow (iv), Q_{iv}. Unlike in bulk methods, this methodology enables precisely control of the interface position. Therefore, one can guide the position of the assembly of metal ions and organic ligands along the main channel length by varying the flow rates. When all flow rates are fixed at 100 μL/min, i.e., [100; 100; 100; 100], Cu(II)-Asp nanofibers are assembled in the center of the main channel (Figure 1b−d). However, the formation of these fibers is directed to positions close to the channel walls by changing two flow rates, either Q_i and Q_{ii} or Q_{iii} and Q_{iv}, from 100 μL/min to 20 μL/min.

Figure 2 shows typical scanning (SEM) and transmission (TEM) electron microscopy images of these structures fabricated using laminar flow and collected at the end of the main channel. The formation of bundles of well-aligned nanofibers with diameters ranging from 50 to 200 nm can be found. In addition, further characterization by powder X-ray diffraction (PXRD), infrared (IR) spectroscopy, and elemental analysis confirmed the formation of Cu(II)-Asp coordination chains identical to those previously reported.[11] The formation of these fibers was also studied by systematically varying the concentrations of both precursor solutions from 1.5 M to 1.5 mM. Under the studied conditions, the formation of fibers was verified, and no significant differences concerning morphology were evidenced (Supporting Information [SI], Figure S2). However, when the microfluidic synthesis was conducted at flow rates [100; 100; 100; 100] and concentrations higher than 1 M, a Cu(II)-Asp based gel was directly eluted from the chip (Figure 2d). A SEM image of the Cu(II)-Asp xerogel directly synthesized in the microreactor shows the good alignment of Cu(II)-Asp nanofibers (inset in Figure 2d; SI, Figure S3). This result confirms that microfluidics is an excellent fabrication technique to control not only the position but also the orientation of metal−organic nanofibers, thus making it possible to envisage the future fabrication of nanofibers with superior performance in comparison with those showing non-oriented geometries, as well as their integration in devices.[12,13]

The generality and efficacy of the nanofabrication of 1D metal−organic structures using laminar flow in microfluidic devices were studied by generating a second and third type of coordination polymer nanofibers. In the first case, aqueous solutions of $Ag(NO_3)$ (1 mM) and Cys (1 mM) were separately injected in channels (ii) and (iii) at a flow rate of 100 μL/min. Again, two aqueous auxiliary streams were injected in channels

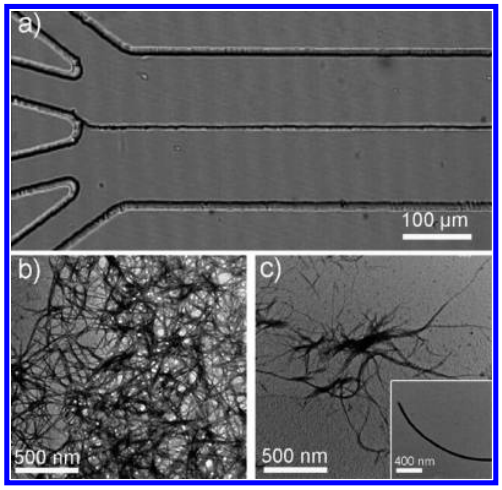

Figure 3. (a) Optical microscope image showing the guided assembly of 1D nanostructure bundles created at the interface between aqueous Ag(I) metal ions and Cys solutions. (b,c) TEM images of the resulting bundles of Ag(I)-Cys (b) and Zn(II)-4,4′-bipy (c) nanofibers just after their elution from the chip. The inset is a high-magnification image of a single Zn(II)-4,4′-bipy nanofiber.

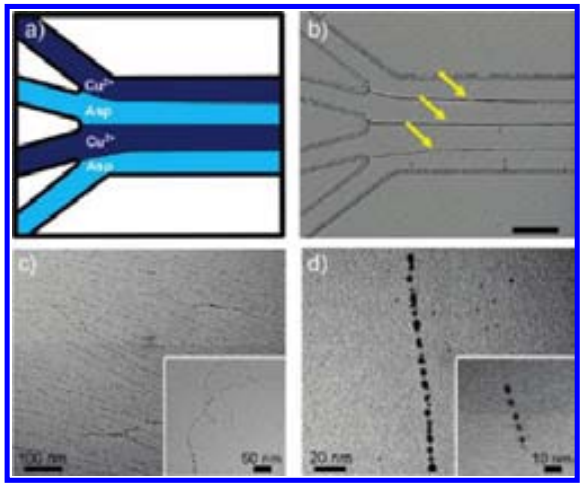

Figure 4. (a) Illustration and (b) optical microscope image of the parallel synthesis of Cu(II)-Asp nanofibers. The scale bar is 100 mm. (c,d) TEM images of the synthesized chain-like superstructures composed of Ag_2S nanoparticles using Ag(I)-Cys nanofibers as templates.

(i) and (iv) at the same flow rate of 100 μL/min. Figure 3a shows the microfluidic guided assembly of 1D Ag(I)-Cys structures at the interface of both reactant flows along the entire length of the main channel. Detailed inspection by TEM of the eluted structures demonstrated them to be constituted of bundles of Ag(I)-Cys nanofibers (Figure 3b; SI, Figure S4). These fibers have diameters between 10 and 50 nm. Similar 1D nanostructures were also obtained when an aqueous solution of $Zn(NO_3)_2 \cdot 6H_2O$ (100 mM) and another solution containing 4,4′-bipy (100 mM) in ethanol were injected in the microfluidic platform. As shown in Figure 3c, the resulting Zn(II)-4,4′-bipy nanofibers have diameters between 10 and 75 nm (SI, Figure S5). In both cases, the coordinative polymerization of Ag(I) and Zn(II) metal ions through Cys and 4,4′-bipy ligands, respectively, was studied by energy dispersive X-ray (EDX) and IR spectroscopy. First, the EDX spectrum of Ag(I)-Cys fibers corroborates the presence of silver, nitrogen, carbon, and sulfur, whereas zinc, nitrogen, and carbon are observed for the Zn(II)-4,4′-bipy fibers (SI, Figures S6 and S7). The IR spectrum of Ag(I)-Cys fibers confirms the coordination of Cys ligands to the Ag(I) metal ions, as evidenced by the absence of the bands for the S−H group stretching vibration (2546 cm^{-1}), the O−H bending vibration (1419 cm^{-1}), the C−O stretching vibration (1295 cm^{-1}), and the C−O−H combining vibration (1344 cm^{-1}; SI, Figure S8). Interestingly, this IR spectrum is similar to that recently reported for Ag(I)-Cys small particles, in which a 1D metal−organic structure resulting from the coordination of Ag(I) metal ions through the sulfur atom and weak bonding through the carboxylic group was proposed.[14] Similarly, the IR spectrum of Zn(II)-4,4′-bipy nanofibers includes bands in the range 1639−1333 cm^{-1} associated with the pyridine ring stretching vibrations and bands at 1302 and 812 cm^{-1}, which are attributed to the presence of coordinated nitrate groups (SI, Figure S9).[15]

Unlike Cu(II)-Asp nanofibers, the use of conventional methods based on fast mixing of precursor solutions under conditions identical to those used in microfluidic synthesis but with continuous stirring did not lead to the formation of long Ag(I)-Cys and Zn(II)-4,4′-bipy nanofibers. For the Ag(I)-Cys system, the bulk synthesis leads to the formation of membrane-like structures, whereas wider 1D needle-like crystals are formed for the Zn(II)-4,4′-bipy system (SI, Figures S10 and S11). Based on these results, formation of metal−organic polymers using laminar flow in microfluidic platforms seems an effective way for constraining reaction environments and favoring the supramolecular assembly in the form of long 1D nanoscale structures.

An exciting possibility of this fabrication approach using laminar flow is the potential to use the additional channels (i) and (iv) of the microfluidic platform (Figure 1a) to inject reactants and test the capacity of microfluidics to be used as a parallel synthetic methodology for fabricating such 1D metal-containing structures at different pathways inside the main channel. To explore this approach, two aqueous Cu(II) solutions were injected in channels (ii) and (iv), whereas the aqueous Asp solutions were injected in channels (i) and (iii) (Figure 4a). Immediately, as shown in Figure 4b, bundles of Cu(II)-Asp nanofibers were generated at the three interfaces between the four alternating reactant flows. This parallel fabrication should be particularly useful for scaling-up the production and shows promise for synthesizing different types of metal−organic nanostructures at once and even producing metal−organic gels composed of different types of fibers.

All of the data presented thus far point to the ability to form coordination polymer nanofibers and gels using microfluidic synthesis, a capability that could become important for synthesizing unique metal-containing nanostructures with novel functionalities. For example, to test whether these coordination polymer nanofibers can be used as templates for controlling the growth of inorganic nanoparticles, we exposed the Ag(I)-Cys nanofibers collected from the main channel of the microfluidic platform to electron radiation in TEM. Under these conditions, a typical TEM image reveals the formation and organization of semiconductor silver sulfide nanoparticles following the shape of these templates.[16] The resulting nanoparticle superstructures appear in chains composed of individual Ag_2S nanoparticles in

the acanthite phase with diameters between 4 and 9 nm (Figure 4c,d), as confirmed by PXRD[17] and electron diffractions performed via high-resolution TEM and EDX microanalysis (SI, Figures S12−14). Considering that the Ag(I)-Cys nanofibers cannot be easily constructed by traditional techniques or bulk synthetic methods, microfluidic synthesis can be particularly interesting toward the synthesis of new functional 1D inorganic assemblies with important applications in the areas of nanoscale electronics and molecular sensing.[18]

In summary, we have presented a new route for a straightforward production of metal-containing nanofibers using microfluidic technologies as a method for guided assembly. We have demonstrated that this methodology enables a fast, better-controlled synthesis and possesses the ability to dictate the formation pathway of the assembled structures simply by varying flow-rate conditions. Considering that many researchers are focused on developing new methods for synthesizing nanoscale coordination polymers,[2,3] we believe that microfluidics will certainly expand the tools for the fabrication of functional molecular nanoassemblies that are not easily constructed by traditional techniques. Therefore, we believe that this study opens up new opportunities in the design and alignment of (bio)organic−inorganic structures. Ongoing research focuses on the integration of these nanoscale metal−organic materials to other microfabricated structures (e.g., electrodes) for further electrical characterization and applications in the field of nanosensing devices, where anisotropic nanostructures would serve as a convenient building block.

■ ASSOCIATED CONTENT

Supporting Information. Detailed experimental section, SEM and TEM images and EDX and IR spectra of coordination polymer nanofibers, optical and TEM images of materials obtained in bulk reactions, and PXRD, electron diffraction, and EDX spectra of Ag_2S nanoparticles. This material is available free of charge via the Internet at http://pubs.acs.org.

■ AUTHOR INFORMATION

Corresponding Author
dittrich@org.chem.ethz.ch; daniel.maspoch.icn@uab.es

■ ACKNOWLEDGMENT

This work was funded by the European Research Council under the 7th Framework Programme (ERC Starting Grant, project no. 203428, "nμ-LIPIDS"), VALTEC08-2-003, and MAT-2009-13977-C03. J.P.-L. thanks for the ETH fellowship. D.M. and I. I. thank the Ministerio de Ciencia e Innovación for RyC contracts. M.R.-M. thanks the Institut Català de Nanotecnologia for research fellowships. We thank the Servei de Microscopia of the UAB, the FIRST clean room facilities, and the Electron Microscopy Center of the ETH Zurich for their facilities. Phillip Kuhn and Andreas Cavegn are also acknowledged for their help with figures design.

■ REFERENCES

(1) (a) Schoonbeek, F. S.; van Esch, J. H.; Wegewijs, B.; Rep, D. B. A.; de Haas, M. P.; Klapwijk, T. M.; Kellogg, R. M.; Feringa, B. L. *Angew. Chem. Int. Ed.* **1999**, *38*, 1393–1397. (b) Joachim, C.; Gimzewski, J. K.; Aviram, A. *Nature* **2000**, *408*, 541–548. (c) Huang, Y.; Duan, X. F.; Cui, Y.; Lauhon, L. J.; Kim, K. H.; Lieber, C. M. *Science* **2001**, *294*, 1313–1317. (d) Ulijn, R. V.; Smith, A. M. *Chem. Soc. Rev.* **2008**, *37*, 664–675. (e) Papapostolou, D.; Howorka, S. *Mol. BioSyst.* **2009**, *5*, 723–732. (f) Amabilino, D. B.; Puigmarti-Luis, J. *Soft Mater.* **2010**, *6*, 1605–1612.

(2) (a) Spokoyny, A. M.; Kim, D.; Sumrein, A.; Mirkin, C. A. *Chem. Soc. Rev.* **2009**, *38*, 1218–1227. (b) Lin, W.; Rieter, W. J.; Taylor, K. M. L. *Angew. Chem. Int. Ed.* **2009**, *48*, 650–658. (c) Hui, J. K.-H.; MacLachlan, M. J. *Coord. Chem. Rev.* **2010**, *254*, 2363–2390. (d) Carné, A.; Carbonell, C.; Imaz, I.; Maspoch, D. *Chem. Soc. Rev.* **2011**, *40*, 291–305.

(3) (a) Hou, S.; Harrell, C. C.; Trofin, L.; Kohli, P.; Martin, C. R. *J. Am. Chem. Soc.* **2004**, *126*, 5674–5675. (b) Rieter, W. J.; Taylor, K. M. L.; An, H.; Lin, W.; Lin, W. *J. Am. Chem. Soc.* **2006**, *128*, 9024–9025. (c) Jung, S.; Oh, M. *Angew. Chem. Int. Ed.* **2008**, *47*, 2049–2051. (d) Zhang, X.; Chen, Z.-K.; Loh, K. P. *J. Am. Chem. Soc.* **2009**, *131*, 7210–7211.

(4) McDowell, J. J.; Zacharia, N. S.; Puzzo, D.; Manners, I.; Ozin, G. A. *J. Am. Chem. Soc.* **2010**, *132*, 3236–3236.

(5) (a) Chen, Z.; Foster, M. D.; Zhou, W.; Fong, H.; Reneker, D. H.; Resendes, R.; Manners, I. *Macromolecules* **2001**, *34*, 6156–6158. (b) Wang, J.; Dai, L.; Gao, Q.; Wu, P.; Wang, X. *Eur. Polym. J.* **2008**, *44*, 602–607. (c) Zhang, S.; Yang, S.; Lan, J.; Tang, Y.; Xue, Y.; You, J. *J. Am. Chem. Soc.* **2009**, *131*, 1689–1691. (d) Batabyal, S. K.; Peedikakkal, A. M. P.; Ramakrishna, S.; Sow, C. H.; Vittal, J. J. *Macromol. Rapid Commun.* **2009**, *30*, 1356–1361.

(6) Pires, M. M.; Przybyla, D. E.; Chmielewski, J. *Angew. Chem. Int. Ed.* **2009**, *48*, 7813–7817.

(7) (a) Beck, J. B.; Rowan, S. J. *J. Am. Chem. Soc.* **2003**, *125*, 13922–13923. (b) Kawano, S.-i.; Fujita, N.; Shinkai, S. *J. Am. Chem. Soc.* **2004**, *126*, 8592–8593. (c) Kuroiwa, K.; Shibata, T.; Takada, A.; Nemoto, N.; Kimizuka, N. *J. Am. Chem. Soc.* **2004**, *126*, 2016–2021. (d) Hui, J. K-H.; Yu, Z.; MacLahlan, M. J. *Angew. Chem. Int. Ed.* **2007**, *46*, 7980–7983. (e) Tu, T.; Assenmacher, W.; Peterlik, H.; Weisbarth, R.; Nieger, M.; Dötz, K. H. *Angew. Chem. Int. Ed.* **2007**, *46*, 6368–6371.

(8) (a) Kenis, P. J. A.; Ismagilov, R. F.; Whitesides, G. M. *Science* **1999**, *285*, 83–85. (b) Brazhnik, K. P.; Vreeland, W. N.; Hutchison, J. B.; Kishore, R.; Wells, J.; Helmerson, K.; Locascio, L. E. *Langmuir* **2005**, *21*, 10814–10817. (c) Dittrich, P. S.; Heule, M.; Renaudb, P.; Manz, A. *Lab Chip* **2006**, *6*, 488–493. (d) Wang, J.; Bunimovich, Y. L.; Sui, G.; Savvas, S.; Wang, J.; Guo, Y.; Heath, J. R.; Tseng, H.-R. *Chem. Commun.* **2006**, 3075–3084. (e) Gao, Y.; Chen, L. *Lab Chip* **2008**, *8*, 1695–1699. (f) Thangawng, A. L.; Howell, P. B., Jr.; Richards, J. J.; Erickson, J. S.; Ligler, F. S. *Lab Chip* **2009**, *9*, 3126–3130. (g) Puigmartí-Luis, J.; Schaffhauser, D.; Burg, B. R.; Dittrich, P. S. *Adv. Mater.* **2010**, *22*, 2255–2259.

(9) Atencia, J.; Beebe, D. J. *Nature* **2005**, *437*, 648–655.

(10) Ismagilov, R. F.; Stroock, A. D.; Kenis, P. J. A.; Whitesides, G. M.; Stone, H. A. *Appl. Phys. Lett.* **2000**, *76*, 2376–2378.

(11) Imaz, I.; Rubio-Martinez, M.; Saletra, W. J.; Amabilino, D. B.; Maspoch, D. *J. Am. Chem. Soc.* **2009**, *131*, 18222–18223.

(12) (a) Mor, G. K.; Shankar, K.; Paulose, M.; Varghese, O. K.; Grimes, C. A. *Nano Lett.* **2006**, *6*, 215–218. (b) Tang, Y. B.; Chen, Z. H.; Song, H. S.; Lee, C. S.; Cong, H. T.; Cheng, H. M.; Zhang, W. J.; Bello, I.; Lee, S. T. *Nano Lett.* **2008**, *8*, 4191–4195.

(13) (a) Wittmann, J. C.; Smith, P. *Nature* **1991**, *352*, 414–417. (b) Kuykendall, T.; Pauzauskie, P. J.; Zhang, Y.; Goldberger, J.; Sirbuly, D.; Denlinger, J.; Yang, P. *Nature Mater.* **2004**, *3*, 524–528. (c) Zhu, K.; Neale, N. R.; Miedaner, A.; Frank, A. J. *Nano Lett.* **2007**, *7*, 69–74.

(14) Nan, J.; Yan, X.-P. *Chem. Eur. J.* **2010**, *16*, 423–427.

(15) (a) Curtis, N. F.; Curtis, Y. M. *Inorg. Chem.* **1965**, *4*, 804–809. (b) Kim, J.; Lee, U.; Koo, B. K. *Bull. Korean Chem. Soc.* **2006**, *27*, 918–920.

(16) (a) Wang, C.; Zhang, X.; Qian, X.; Wang, W.; Qian, Y. *Mater. Res. Bull.* **1998**, *33*, 1083–1086. (b) Lu, Q.; Gao, F.; Zhao, D. *Angew. Chem. Int. Ed.* **2002**, *41*, 1932–1934.

(17) (a) Yvon, K.; Jeitschko, W.; Parthe, E. *J. Appl. Crystallogr.* **1977**, *10*, 73–74. (b) Aleali, H.; Sarkhosh, L.; Karimzadeh, R.; Mansour, N. *Phys. Status Solidi B* **2011**, *248*, 680–685.

(18) Nie, Z. H.; Petukhova, A.; Kumacheva, E. *Nature Nanotechnol.* **2010**, *5*, 15–25.

(Supporting Information)

Coordination Polymer Nanofibers Generated by Microfluidic Synthesis

Josep Puigmartí-Luis,[†] Marta Rubio-Martínez,[‡] Urs Hartfelder,[†] Inhar Imaz,[‡] Daniel Maspoch,[*,‡] and Petra S. Dittrich[*,†]

Department of Chemistry and Applied Biosciences, ETH Zürich, Wolfgang-Pauli-Str. 10, CH-8093 Zurich, Switzerland, and CIN2 (ICN-CSIC), Catalan Institute of Nanotechnology, Campus UAB, 08193 Bellaterra (Barcelona) Spain.

E-mail: dittrich@org.chem.ethz.ch, daniel.maspoch.icn@uab.es

S1. Experimental section

Fabrication of the microfluidic device

The microreactor was prepared in poly(dimethylsiloxane)(PDMS) by soft lithography as described elsewhere [(a) X. Xia, G. M. Whitesides, *Annu. Rev. Mater. Sci.* 1998, *28*, 153-184; (b) P. S. Dittrich, M. Heule, P. Renaud, A. Manz, *Lab Chip* 2006, *6*, 488-493.]. The dimensions of the microchannels were 50 μm x 50 μm for the four input microchannels, and 250 μm x 50 μm for the main reactor channel. The total length of the main reactor channel was 9 mm.

Preparation of 1D metal-organic nanofibers using laminar flow

In a typical procedure, the synthesis of 1D metal-organic nanofibers by means of laminar flow was performed by injecting two solutions, one containing the metal ion salt and the second containing the organic ligand, via a syringe pump system into the central two channels of the microfluidic platform at a certain flow rate (typically 100 μL/min). Two auxiliary streams composed of the same solvent used in the adjacent central channel, but without precursors, were injected in the side channels. The solutions used for synthesizing the 1D metal-organic nanofibers were:

i) *Cu(II)-Asp nanofibers:* $Cu(NO_3)_2 \cdot 3H_2O$ (3.62 g, 15 mmol) was dissolved in deionized water (10 mL), giving a 1.5 M solution. This solution was volumetrically diluted with deionized water to give 0.15 M, 0.015 M and 0.0015 M solutions. On the other hand, L-aspartic acid (1.33 g, 10 mmol) and NaOH (0.80 g, 20 mmol) were dissolved in deionized water (10 mL), giving a 1 M solution of L-aspartate ligand. This solution was further diluted with deionized water to give 0.1 M, 0.01 M and 0.001 M solutions as needed for the respective microfluidic synthesis.

ii) *Ag(I)-Cys nanofibers:* $Ag(NO_3)$ (0.17 g, 1 mmol) was dissolved in 10 mL of deionized water (0.1 M). This solution was volumetrically diluted to a solution with concentration of 0.001 M. On the other hand, L-cysteine (0.12 g, 1 mmol) was dissolved in deionized water (10 mL), and the resulting solution was volumetrically diluted to a 0.001 M solution.

iii) *Zn(II)-4,4'-bipy nanofibers:* $Zn(NO_3)_2 \cdot 6H_2O$ (0.29 g, 1 mmol) was dissolved in 10 mL of deionized water (0.1 M). The 4,4'-bipy solution was prepared by dissolving 0.15 g (1 mmol) of 4,4'-bipy in 10 mL ethanol (0.1 M).

Preparation of Ag(I)-Cys membrane-like structures and Zn(II)-4,4'-bipy needle-like crystals

Ag(I)-Cys membrane-like structures were fabricated by addition of an aqueous solution (5 mL) of $Ag(NO_3)$ (84 mg, 0.5 mmol) to an aqueous solution (5 mL) of Cys amino acid (60 mg, 0.5 mmol) under stirring at room temperature. Similarly, needle-like crystals of Zn(II)-4,4'-bipy were synthesized by addition of an aqueous solution (2.5 mL) of $Zn(NO_3)_2 \cdot 6H_2O$ (17 mg, 0.6 mmol) to an ethanolic solution (2.5 mL) of 4,4'-bipy ligand (94 mg, 0.6 mmol) under stirring at room temperature. In both cases, the precipitation of a white solid was immediately observed.

Characterization

Infrared (IR) spectra were performed on a FTIR Tensor 27 InfraRed spectrophotometer (Bruker) equipped with a Bruker Golden Gate diamond ATR (Attenuated Total Reflection) cell. Scanning electron microscopy (SEM) images were collected on a scanning electron microscope (HITACHI S-570) at acceleration voltages of 10-15 kV. Aluminium was used as support. Transmission electron microscopy (TEM) images were obtained with a JEOL JEM 2010F. The measurements were performed at room temperature and a voltage of 200 kV. The X-ray EDX microanalysis was performed on an Oxford Instruments INCA Energy TEM system, which performs the elemental qualitative and quantitative analyses. Optical images of the microfluidic device were obtained with an Olympus IX70 inverted microscope and a CCD camera and other optical images presented in the supporting information were registered using a Zeiss Axio Observer Z-1 inverted optical/fluorescence microscope with motorized XY stage, Hg lamp excitation source, AxioCam HRc digital camera and standard filters.

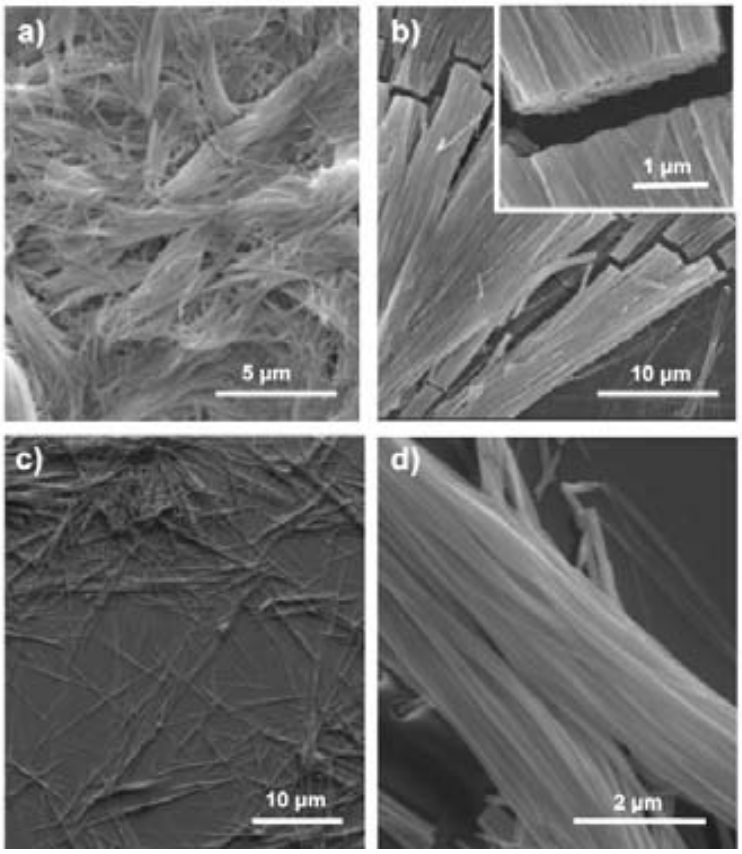

Figure S2. (a-c) SEM images of bunches of Cu(II)-Asp nanowires produced in a micro-reactor at different concentrations of $Cu(NO_3)_2 \cdot 3H_2O$; 150 mM, 15 mM and 1.5 mM, respectively. (d) SEM image of a bundle of Cu(II)-Asp nanowires produced on a non-bonded chip. The image is obtained after the removal of the PDMS. Notice the alignment and the homogeneity of the nanowires. The concentration is 150 mM of $Cu(NO_3)_2 \cdot 3H_2O$.

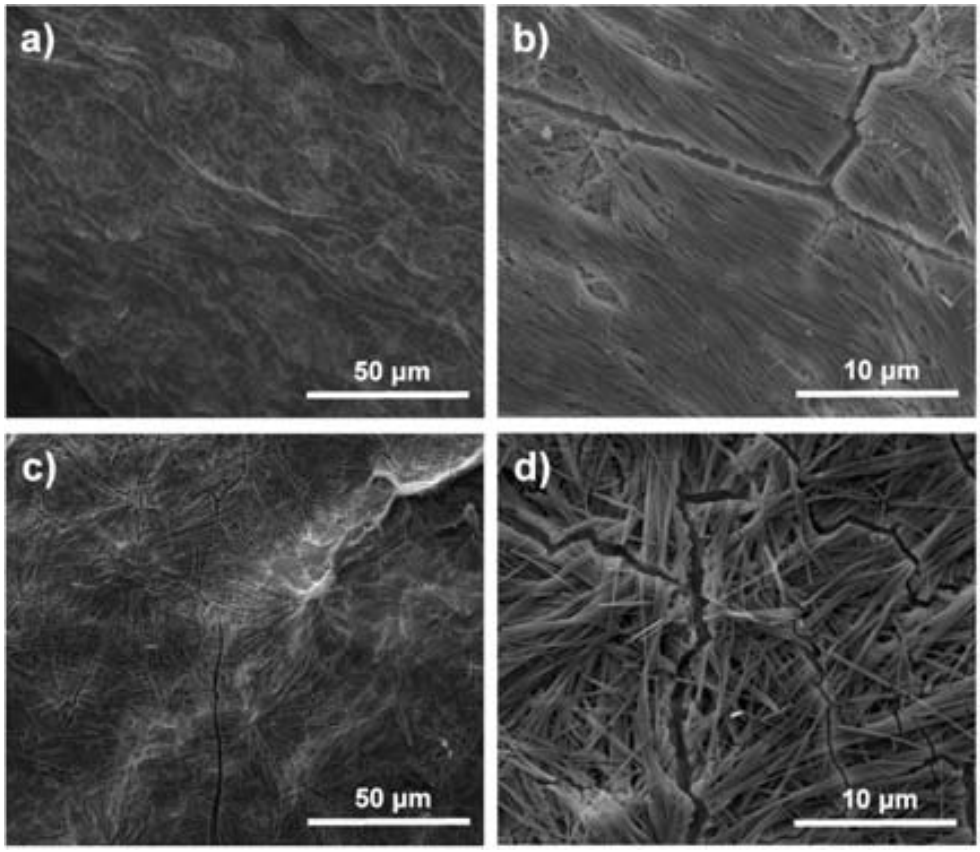

Figure S3. SEM images of Cu(II)-Asp based xerogels produced by using (a) and (b) microfluidics and (c) and (d) bulk conventional synthesis. Note the well-alignment of Cu(II)-Asp nanofibers in the xerogels fabricated by microfluidics.

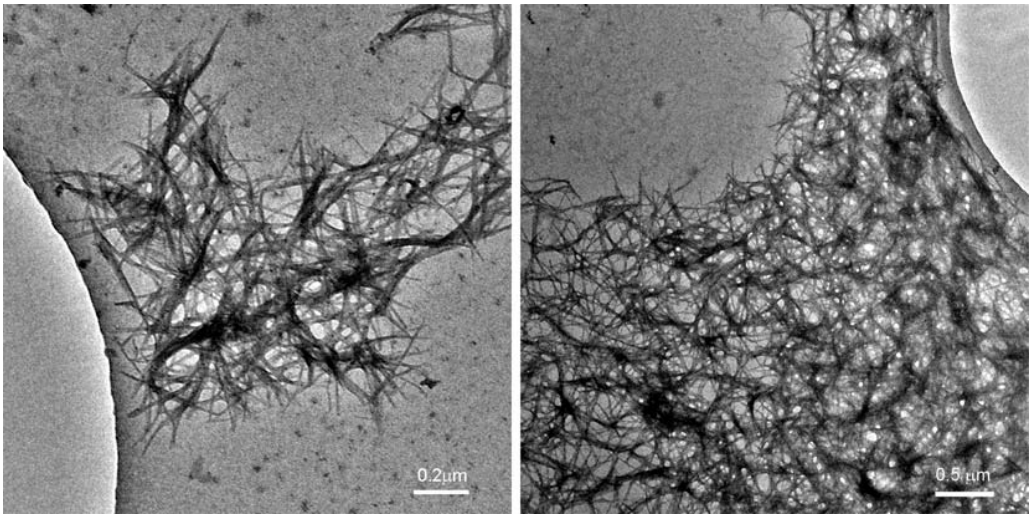

Figure S4. TEM images of Ag(I)-Cys nanofibers. The samples were prepared by drop-casting the eluted solution from the chip over holy carbon grid.

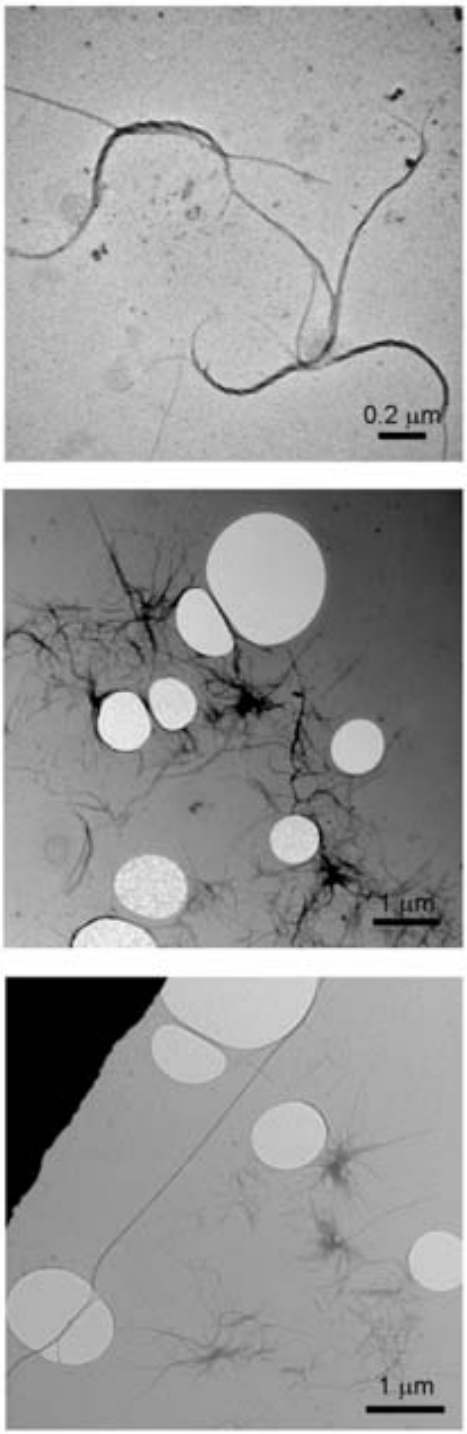

Figure S5. TEM images of Zn(II)-4,4'-bipy nanofibers produced using laminar flow in the microfluidic devices.

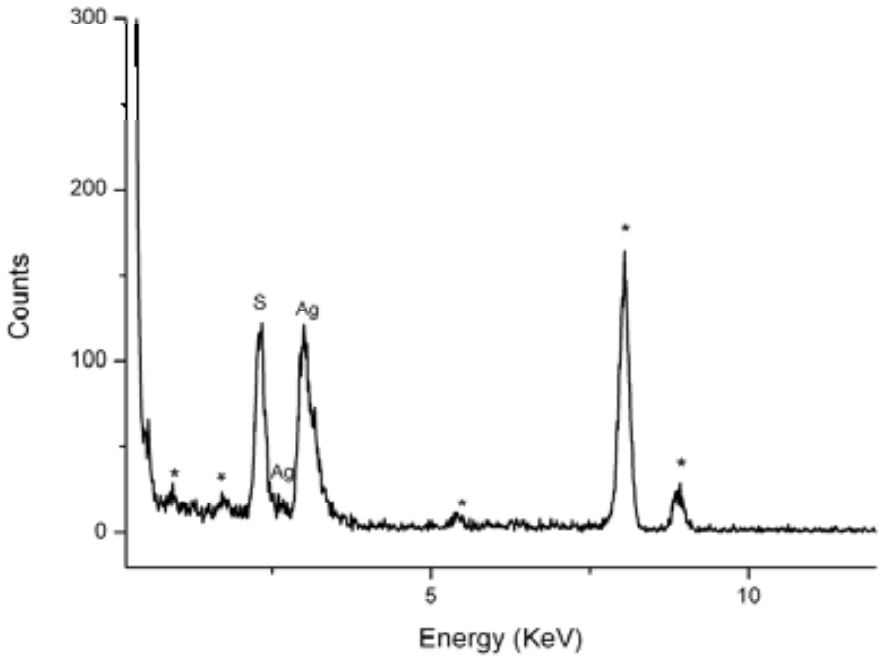

Figure S6. EDX spectrum of Ag(I)-Cys nanofibers showing the presence of silver and sulphur. (The peaks marked by a star symbol correspond to the TEM grid).

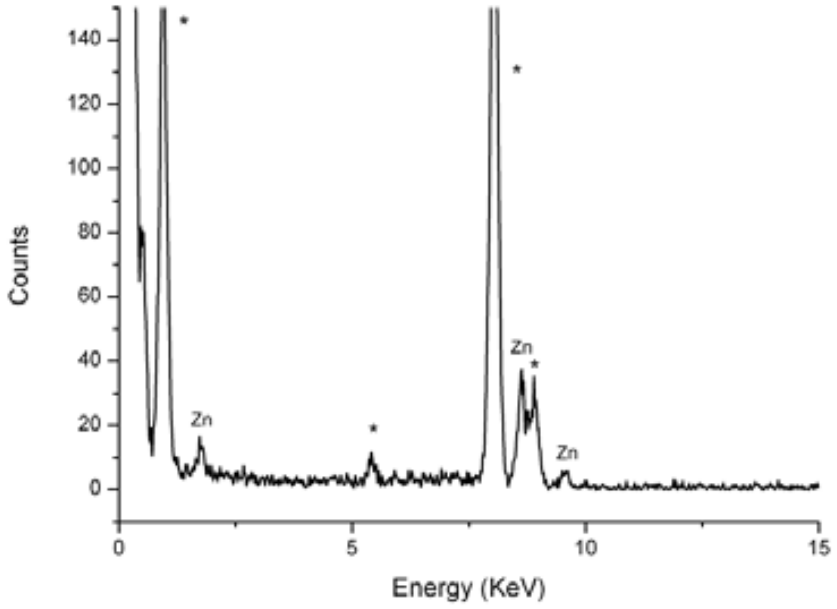

Figure S7. EDX spectrum of Zn(II)-4,4'-bipy nanofibers showing the presence of zinc. (The peaks marked by a star symbol correspond to the TEM grid).

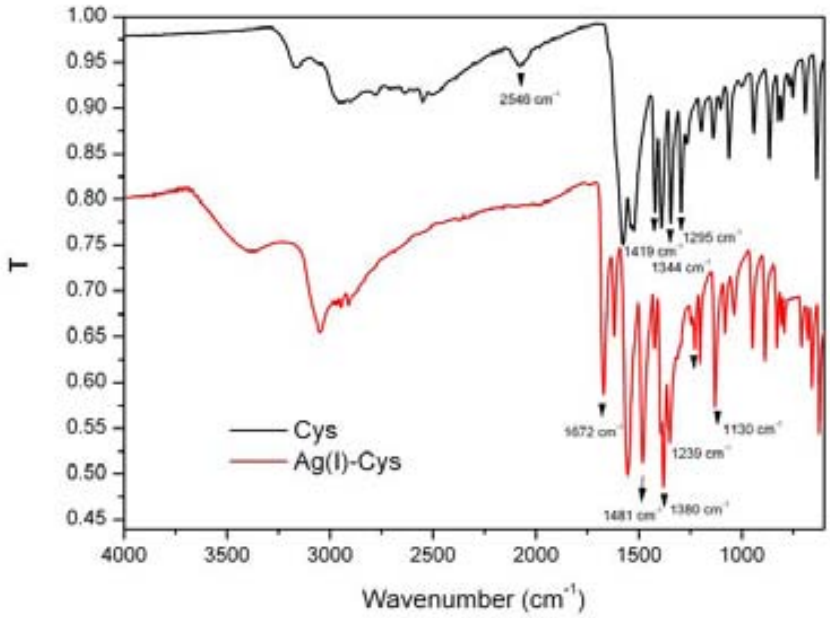

Figure S8. Infrared spectra of Ag(I)-Cys nanofibers and cysteine.

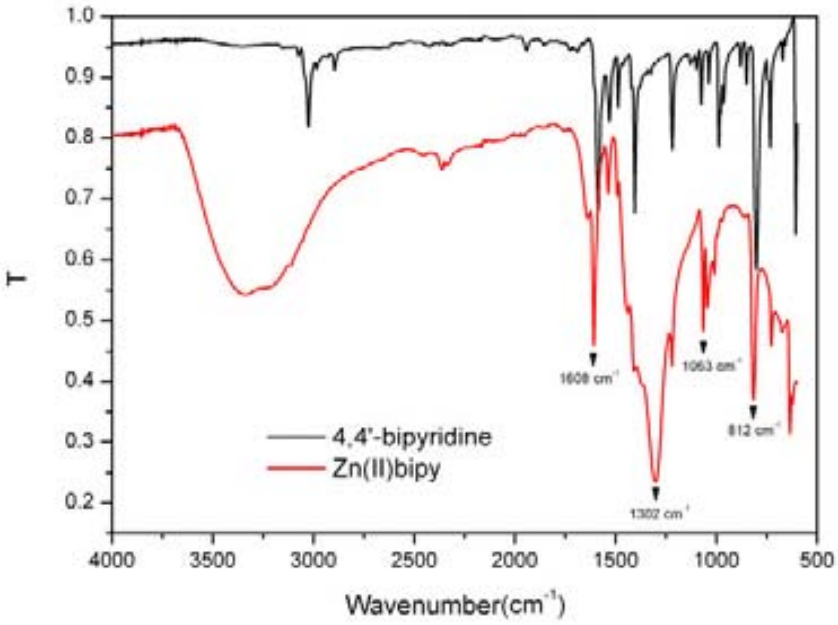

Figure S9. Infrared spectra of Zn(II)-4,4'-bipy nanofibers and 4,4-bipyridine.

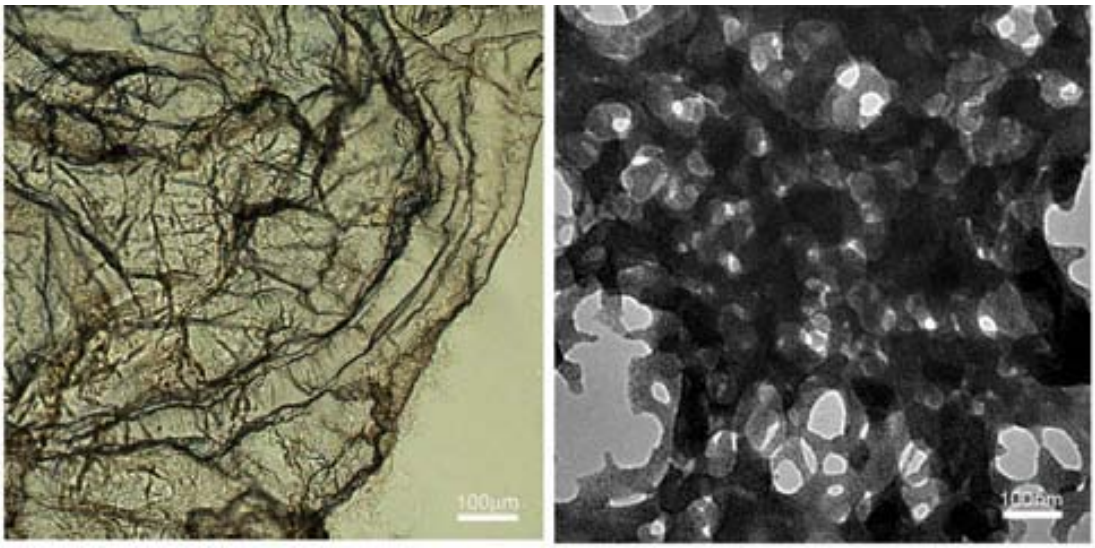

Figure S10. Optical microscope (left) and TEM (right) images of Ag(I)-Cys membrane-like structures synthesized using conventional synthesis.

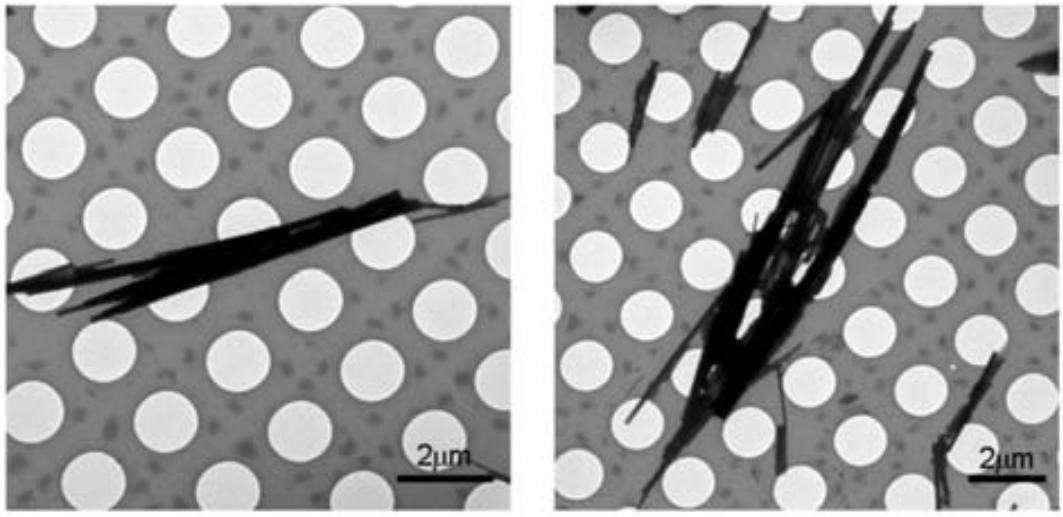

Figure S11. TEM images of Zn(II)-4,4'-bipy needle-like crystals obtained using conventional synthesis.

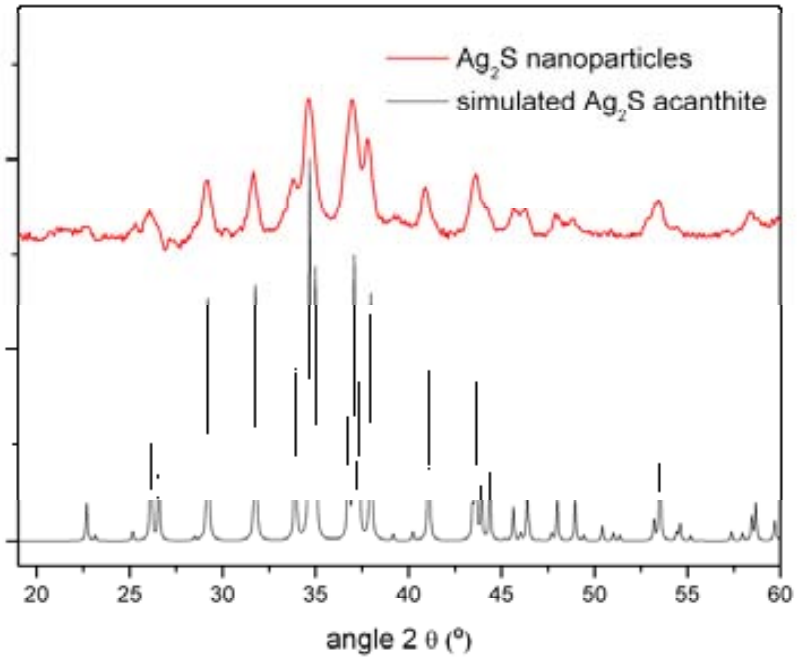

Figure S12. XRPD patterns of Ag_2S nanoparticles obtained from the Ag(I)-Cys nanofibers compared with the simulated XRPD of Ag_2S nanoparticles in the acanthite phase.

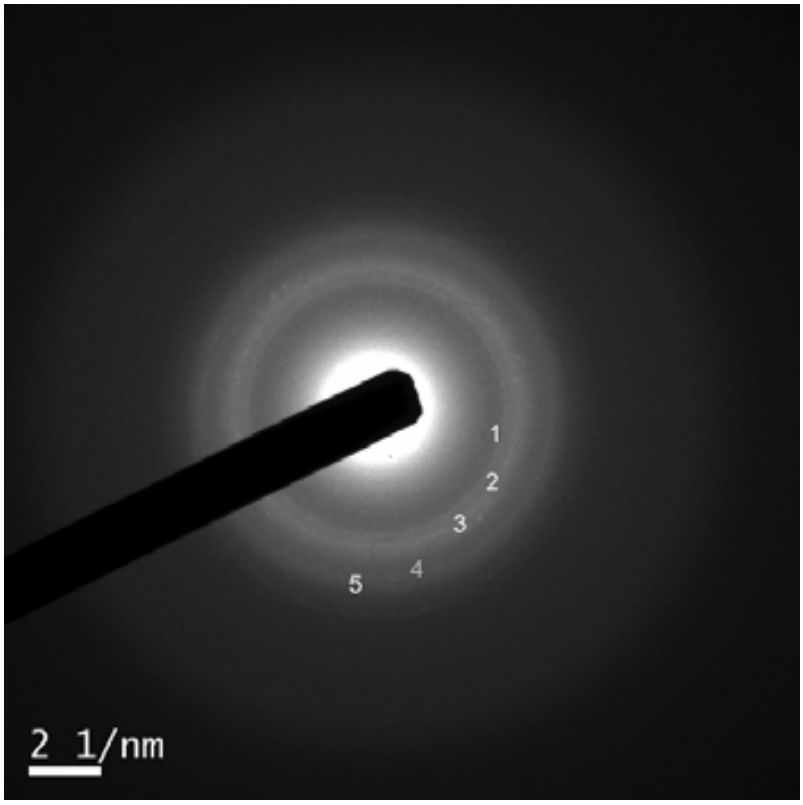

Selected reflections	Reticular distances (nm)	
	Literature for acanthite phase of Ag_2S*	Synthesized Ag_2S nanoparticles
1	2.837	2.862
2	2.603	2.611
3	2.439	2.443
4	2.086	2.060
5	1.966	1.960

* Parthe et al., *J. Appl. Cryst.* **1977**, *10*, 73.

Figure S13. Diffraction pattern and reticular distance table of synthesized Ag_2S nanoparticles compared to the theoretical values for acanthite phase of Ag_2S.

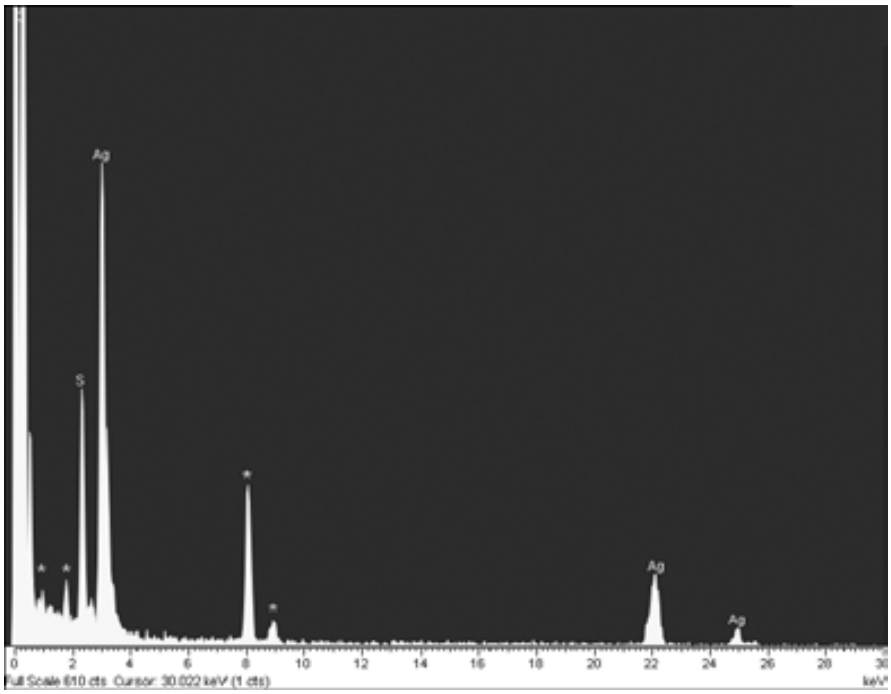

Figure S14. EDX spectrum of synthesized Ag_2S nanoparticles showing the presence of silver and sulphur. (The peaks marked by a star symbol correspond to the TEM grid).

Chapter 5:

Metal-Amino Acid Nanostructures as New Templates for Inorganic Nanoparticle Superstructures Synthesis

In this Chapter, we show that metal-AA CP nanofibers can be used as templates to synthesize and assemble inorganic nanoparticles into 1D superstructures using the internal metal ions of the CP and their fibrillar morphology. With this approach, 1D Ag_2S nanoparticle superstructures were synthesized by exposing the microfluidic-synthesized Ag(I)-Cys nanofibers to e-beam bombardment. We also show that this template synthesis can be localized at precise positions by using microfluidic technology with micro-engineered fluidic clamps incorporated. This technology allows i) guiding and localizing the formation of Ag(I)-Cys nanofibers; ii) localizing the synthesis of 1D Ag nanoparticle superstructures using these fibers as templates; iii) using these Ag nanoparticle superstructures as second templates to synthesize conductive Ag(I)-TCNQ crystals; and iv) measuring *in situ* the conductivity properties of these Ag(I)-TCNQ crystals by localizing this template-synthetic process onto electrodes. These results are included in the article presented in Chapter 4 and in the article entitled "Localized template growth of functional nanofibers from an metal-amino acid-supported framework in a microfluidic chip", ACS Nano 2014.

I. Coordination polymers as a template-directed approach towards inorganic nanoparticles

Inorganic nanoparticles are ubiquitous in material sciences because of their numerous technological applications in several domains of science and industry.[1–3] The interest for nanoparticles stems from the fact that new properties are acquired at this length scale, and that these properties change with their size. Another key factor that dramatically alters the final properties of inorganic nanoparticles is their shape. The importance of the shape was intensely studied at the end of 90's and the beginning of this century. During this period, El-Sayed and co-workers demonstrated that the catalytic activity of platinum nanoparticles depends on their shape.[4] They confirmed that platinum nanoparticles of different shapes but identical size show different catalytic activity, and that this activity dependes on the percentage of atoms present at the edges and corners of the particle: better catalytic activities were detected for larger percentages. Mirkin and co-workers also showed that the shape can modify the optical properties of inorganic nanoparticles by developing a photoinduced method that allowed the conversion of large quantities of silver nanospheres into triangular nanoprisms. They observed that this change from an isotropic to anisotropic shape has a strong impact on the plasmon resonances of the nanoparticles and hence their interactions with light: the original spherical particles Rayleigh light-scatter in the blue, while the nanoprisms exhibit scattering in the red, as is shown in Figure 5.1.[5] Another characteristic example of how the shape influences the properties of inorganic nanoparticles is the case of

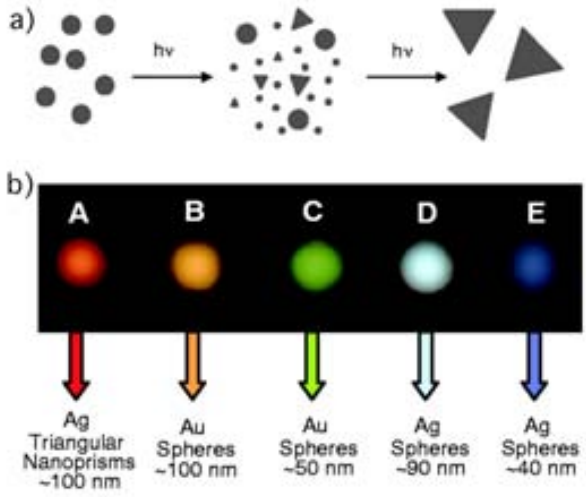

Figure 5.1. a) Schematic representation of the formation of silver nanoprisms. Once the spherical particles and small nanoclusters are consumed, the reaction terminates. b) Digital image of the Rayleigh light-scattering of different particles deposited on a microscope glass slide. Figure adapted from ref 5.

ZnO. It is known that the optical, semiconducting, catalytic, magnetic and piezoelectric properties of ZnO nanoparticles strongly depend on their rod-like or spherical morphology.[6]

Owing to this correlation, inorganic nanoparticles have to be synthesized not only controlling their size but also their shape. Today, many different approaches are used to achieve this control. The most common strategies are sol-gel process, micellar synthesis, precipitation methods and hydrothermal synthesis. Recently, the "template-synthesis" has also been proposed for the controlled synthesis of inorganic nanoparticles. The advantage of the template synthesis resides in the transmission of structural information from the initial template to the final nanostructure. A template can transmit its external structure (for example, a fibrilar morphology) or its internal structure (for example, porosity) to the resulting nanoparticles and thus, providing them with additional functionalities.

The template synthesis of inorganic nanoparticles normally consists of three steps. First, the nanoparticle precursors are deposited around, onto, or inside a template. Then, the inorganic nanoparticles are synthesized on/in the template by exposing this template to the reaction conditions needed for the synthesis of the intended nanoparticles. Finally, the template is removed. This process allows the synthesis of nanoparticles with special morphologies or nanoparticles that are self-assembled into well-defined superstructures.[7,8]

Another possibility is to use a template that is formed by the elements needed for the synthesis of the inorganic nanoparticles. In this case, the exposure of this template to certain reaction conditions, for example high temperatures, can induce the template formation of inorganic nanoparticles. Very recently, it has been proposed that CPs could be an excellent type of sacrificial templates.[9–11] CPs are composed of metal ions and organic molecules; hence, they can be ideal sources of metal ions and carbon for the fabrication of inorganic nanostructures. Recent studies, in which CPs have been used as templates for the creation of metal oxide or carbon nanoparticles via thermal decomposition under controlled atmospheres, have confirmed this hypothesis.[12–14] These solid–solid transformation processes using CP templates are normally based on a simple calcination (see Figure 5.2). In this calcination process, the structure and composition of the resulting nanoparticles is dependent on the reaction conditions, such as temperature, irradiation and atmosphere. Today, several inorganic materials, including nanoparticles and 1D nanoparticle superstructures, have been synthesized using a calcination process.

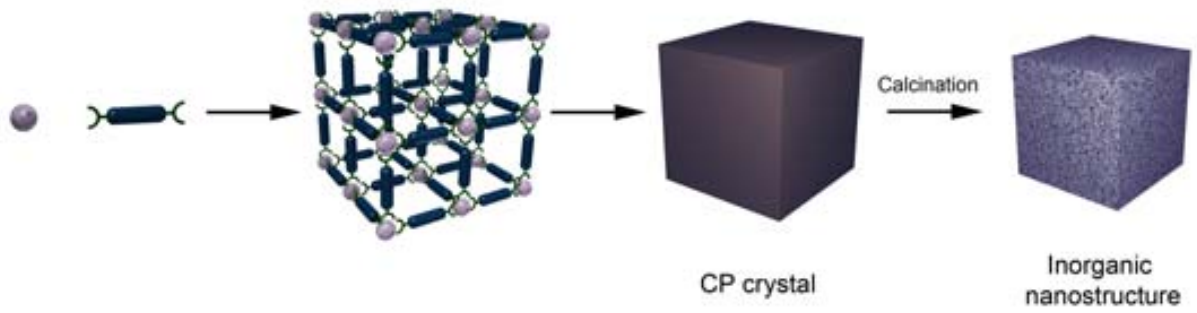

Figure 5.2. Schematic representation of the synthetic procedure for the preparation of inorganic nanoparticles using CPs as templates.

I.1. Synthesis of inorganic particles using CP crystals as sacrificial templates

The first use of CP crystals as templates for inorganic particles was reported in 2009 by Oh and co-workers.[15] This pioneering work was based on the calcination of different CP nanocrystals composed of H_2BDC and In(III) ions to prepare hexagonally shaped hollow and non-hollow In_2O_3 rods. In_2O_3 particles have been widely used in solar cells, gas sensor, optoelectronic devices and photocatalysis.[16–18] The authors demonstrated the synthesis of three In_2O_3 nanoparticles with different morphologies (hexagons, ellipsoids and rods) by calcination of three different CPs with the same morphologies.[19] It is interesting to note that the final shape of the resulting nanoparticles was dictated by the initial shape of the CP. They also established that the composition and porosity of the precursor CPs affect the resulting In_2O_3 structure, especially in its hollow character. Figure 5.3 shows the different In_2O_3 nanoparticles obtained by calcination of CP crystals.

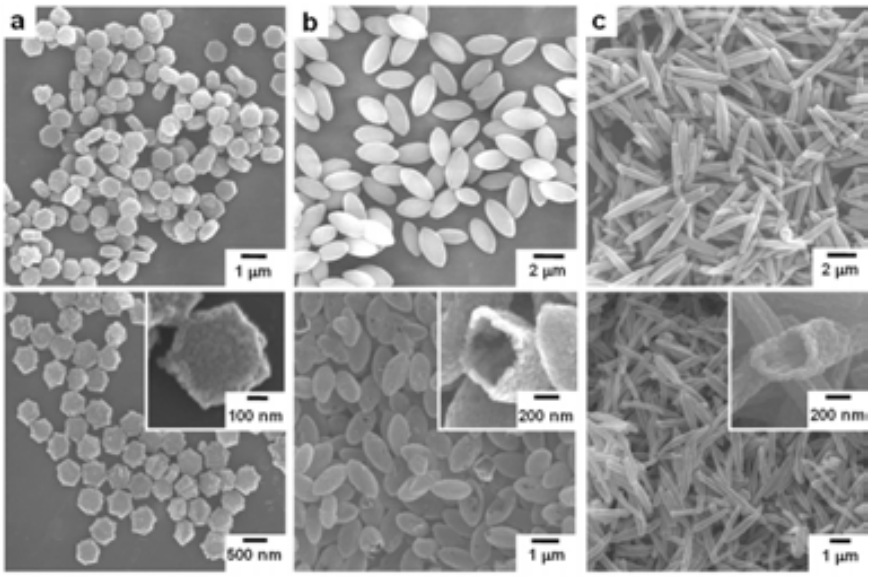

Figure 5.3. a) SEM images of the non-hollow hexagonal disk-shaped CP precursor before calcination (top) and images of the resulting In_2O_3 nanoparticles after calcination (bottom). b) Hollow ellipsoid-shaped CP before (top) and after (bottom) calcination. c) Rod shaped CP before (top) and after (bottom) calcination. Figure adapted from ref 15.

Another example reported by Oh and co-workers showed the synthesis of ZnO hexagonal rings following a three-step process (see Figure 5.4).[20] In a first step, hexagonal disks of a Zn(II)-based CP were synthesized by mixing a carboxy-functionalized organic ligand, N,N"-phenylenebis(salicylideneimine)dicarboxylic acid, and H_2BDC in a 1:5 molar ratio) and Zn(II) ions at a stoichiometric ratio (see Figure 5.4.a). Then, upon a heat treatment (120°C), a secondary CP was grown around the initial disks with no change in the disk thickness and resulting in an amorphous hexagonal ring (see Figure 5.4.b-c). Finally, the calcination of the resulting hexagonal rings at 550°C led to the formation of polycrystalline ZnO ring-like structures, which became hollow after removing the initial CP template using polar organic solvents.

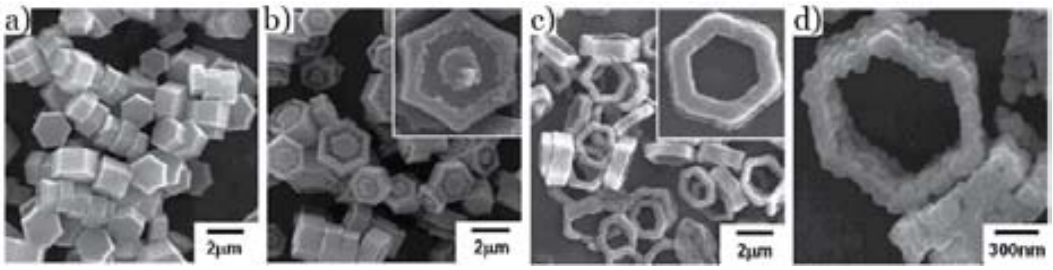

Figure 5.4. SEM images of the different stages of the formation of the hexagonal ZnO rings using a combination of template-directed coordination polymer growth and thermal decomposition. a) Image of the initial formed hexagonal CPs disks. b), c) CPs structures formed at the latters stages of the growth process during heat-up. d) High-magnification SEM image of the ZnO rings formed after calcination. Figure adapted from ref 20.

The same authors also extended this approach to other metal ions, such as iron.[21] Hematite (α-Fe_2O_3) or magnetite (Fe_3O_4) nanorods were synthesized by calcination of Fe-MIL-88B nanorods (see Figure 5.5). They obtained hematite nanorods performing one-step calcination in the presence of air, whereas magnetite nanorods were prepared by a two-step calcination. The two-step process consisted of a first calcination of the CP nanorods at low temperature in air (to adjust the amount of organic residues within the particles) followed by a second calcination at high temperature under a nitrogen atmosphere. In this second step, the hematite phase was transformed to the magnetite phase.

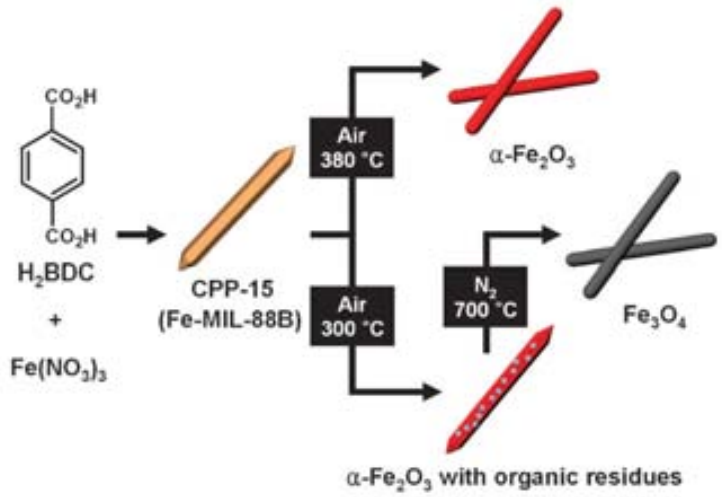

Figure 5.5. The selective preparation of hematite (α-Fe_2O_3) and magnetite (Fe_3O_4) nanorods from Fe-MIL-88B nanorods. Figure adapted from ref. 21.

Recently, it has been found that Prussian Blue (PB) crystals are one of the most suitable candidates to produce microporous magnetic Fe(III) oxides particles with promising applications such as catalysis and biomedical applications.[22–24] For example, Hu *et al.* prepared hierarchical magnetic Fe(III) oxide nanoparticles by calcination of PB, and furthermore showed that the heating rate affects the morphological features of these nanoparticles.[25] They observed that at low heating rates (1 °C min^{-1}), Fe(III) oxides nanoparticles with smooth surfaces were obtained. However, at high heating rates (10 °C min^{-1}), the synthesized nanoparticles exhibited a hierarchical structure with a magnetic response at room temperature. It is interesting to note that the nanoporous architecture of CPs can also favour the formation of porous inorganic nanoparticles. One recent example, reported by Wu and co-workers, used ZIF-67 with a rhombic dodecahedral morphology to obtain porous Co_3O_4 hollow dodecahedra.[26] These anisotropic hollow structures were obtained by heating the ZIF-67 crystals at 350°C. Interestingly, these hollow structures exhibited high lithium storage capacities and excellent cycling performance as anode materials for lithium batteries.

Finally, apart from the metal ions present in CPs, the porous architecture of CPs can also be used as a template to generate carbon-based porous nanostructures. In this approach, CP crystals with high thermal stability can be utilized both as a sacrificial template and a secondary carbon precursor to construct highly porous carbon. The first example showing the use of a porous CP crystal as a template for preparing nanoporous carbon was reported by Xu and co-workers.[27] MOF-5 was used as the template and furfuryl alcohol (FA) as the carbon precursor. The degassed MOF-5 was heated at 150°C for 48 h under an atmosphere of FA vapour, during which FA polymerized in the pores of MOF-5. The carbonization of the PFA/MOF-5 composite was performed at 1000°C for 8 h. The resulting nanoporous carbon exhibited a high surface area, hydrogen adsorption capacity and an excellent electrochemical performance as an electrode material for electrochemical double-layered capacitors.

I.2. Synthesis of inorganic particle superstructures using CP fibers as templates

As seen above, the final shape of the inorganic nanoparticles depends on the initial morphology of the CP-based template. In this sense, the use of other morphologies such as 1D fibers shows promise to be used as template not only to synthesize inorganic nanoparticles but also to assemble then into 1D chains or superstructures.

To date, only few examples showing the use of CP nanofibers as templates to produce inorganic nanoparticle superstructures have been reported; and all of them have been published in parallel to the work presented in this Chapter. An early example of the template-directed synthesis using CP nanofibers was reported by Li and co-workers.[28] They first synthesized helical CP nanofibers associating the Congo red dye with Ag(I) ions. Then, they exposed these fibers to visible light for 48 h to induce the photo-reduction of the Ag(I) ions of the Ag(I)-CongoRed nanofibers and therefore, produce metallic Ag nanoparticle chains (see Figure 5.6).

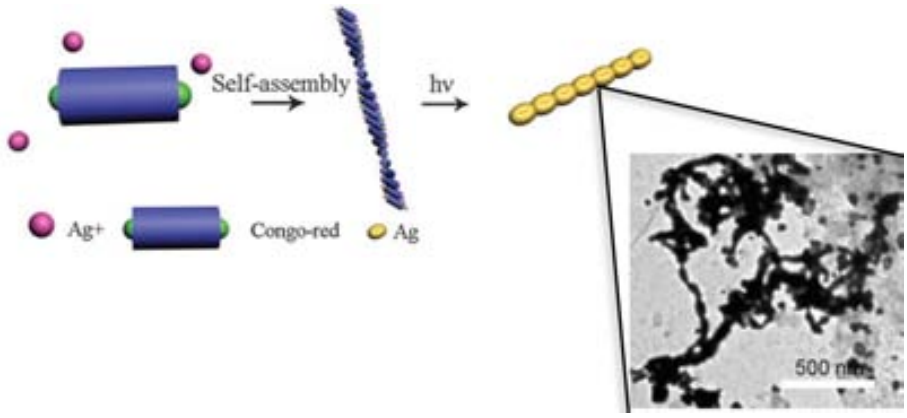

Figure 5.6. Schematic illustration of the formation of Ag(I) nanoparticle chains with their corresponding TEM image. Figure adapted from ref. 32.

More recently, the same authors have reported a second example that uses CP nanohelices made of Ag(I) ions and melamine as templates to synthesize Ag nanoparticle superstructures.[29] In a first step, CP helices were assembled via asymmetric coordination between $AgNO_3$ and melamine by a simple mixing of both components under dark conditions at room temperature (see Figure 5.7.a). Once synthesized, these nanohelices were exposed to UV-Vis light for 48 hours, leading to the formation of Ag nanoparticle nanochains (see Figure 5.7.b).

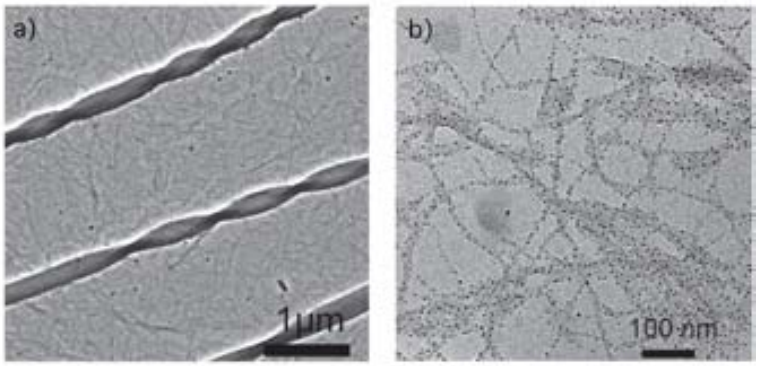

Figure 5.7. a) TEM image of the helical Ag(I)-melamine fibers. b) TEM image of the Ag nanoparticle superstructures synthesized after photo-reduction of the Ag(I)-melamine fibers for 48 hours. Figure adapted from ref. 29.

II. Our results: Metal-AA nanofibers as new templates to create inorganic nanoparticle superstructures

In the previous Chapter, we showed that by using microfluidics as a synthetic approach it was possible to create Ag(I)-Cys nanofibers, which is remarkable considering that they are not formed when the two reagents are mixed under agitation. Here, we show that these Ag(I)-Cys nanofibers can be used as a template for controlling the growth and assembly of inorganic nanoparticles stimulated by electron bombardment in a TEM setup. This bombardment leads to the decomposition of the CP and to the formation of well-organized 1D Ag_2S-nanoparticles chains/superstructures following the shape of the nanofiber templates (see Figure 5.8. a-b).

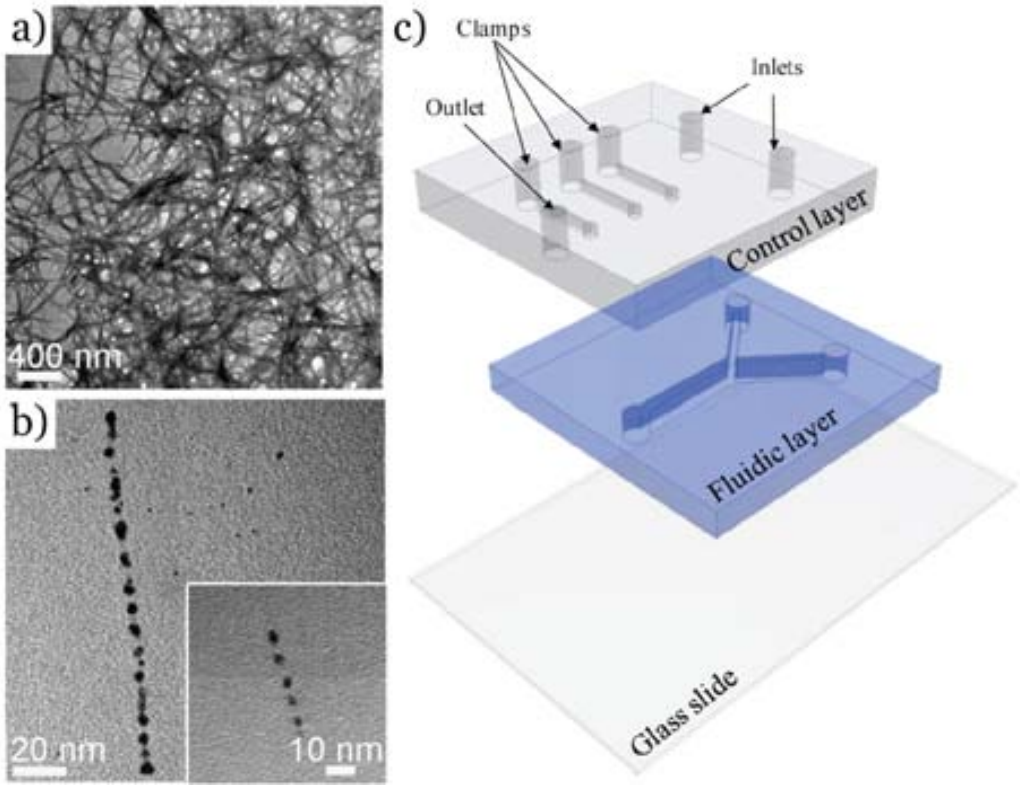

Figure 5.8. a) TEM image of the resulting bundles of Ag(I)-Cys just after their elution from the chip. b) TEM image of the synthesized chain-like superstructures composed of Ag2S nanoparticles using Ag(I)-Cys nanofibers as templates. c) Schematic view of the two-layer polydimethylsiloxane-based (PDMS) microfluidic chip used in the experiment composed by three microengineered pneumatic clamps.

The potential use of Ag(I)-Cys nanofibers as templates to produce Ag_2S nanoparticle superstructures prompted us to further develop the microfluidic technology by incorporating microengineered fluidic clamps (Figure 5.8.c) to precisely control the position where the

template synthesis takes place. This control is crucial if one wants (i) to expand the formation of other types of inorganic nanoparticle superstructures (*e.g*. Ag nanoparticle superstructures), (ii) to use these superstructures as second templates to grow conductive CP crystals and (iii) to be able to measure *in situ* the conductivity properties. All these results are collected in the article entitled "Localized template growth of functional nanofibers from an metal-amino acid-supported framework in a microfluidic chip".

In the first part of this work, a microengineered fluidic clamp based chip was designed and fabricated. Details of the fabrication of this chip can be found in the Materials and Methods Section of the article. Briefly, the chip consisted of two layers of PDMS where the bottom-layer was designed to accommodate the fluidic channel and the top control layer was used to partially squeeze using nitrogen gas the fluidic channel toward the glass substrate, acting as pneumatic clamps.

The Ag(I)-Cys nanofibers were synthesized following the same procedure described in Chapter 4, by injecting two aqueous reagents solutions of $AgNO_3$ and Cys through the fluidic channels. Once we synthesized the Ag(I)-Cys nanofibers, they were localized on the glass substrate using the pneumatic clamps at 3 bars (see Figure 5.9.a). This entrapment allowed the washing of the surplus reagents by a pure water flow. It also opens the possibility to localize the template-synthesis of the inorganic nanoparticle superstructures from the CP nanofibers. In order to reduce the Ag(I) ions of the immobilized Ag(I)-Cys nanofibers to metallic Ag, a saturated ascorbic solution in EtOH was added to the microfluidic platform while reducing the clamp pressure to 1 bar to favour the chemical treatment. As shown in Figure 5.9.b, this reduction and consequent formation of Ag nanoparticles (confirmed by XRPD in bulk experiments, (see Figure S.1 of S.I. of the article) was accompanied by a colour change from white to dark brown. Afterwards, the excess of ascorbic acid was removed in another cleaning step with water with the clamps activated at 3 bar to avoid movement of the fibers.

To further show control on the template-synthesis process, we used such Ag nanoparticle superstructures as second templates to grow a second CP. Here, the oxidation of the Ag nanoparticles with tetracyanoquinodinemethane (TCNQ) was performed in acetone, activating the clamps again at 1 bar (see Figure 5.9.c). We observed that the Ag nanoparticle superstructures act as nucleation sites for the growth of blue-purple Ag(I)-TCNQ charge transfer complexes. The formation of crystals of Ag(I)-TCNQ was confirmed by reproducing the same reaction on large surfaces, which XRPD indicated the formation of the tetragonal phase of the Ag(I)-TCNQ complex (see Figure S.1 of S.I. of the article). Furthermore, SEM measurements of the microfluidic-synthesized Ag(I)-TCNQ crystals

revealed the formation wire-like nanocrystals with a diameter range from 60 to 250 nm and a length longer than 10 μm (see Figure 3 of the article).

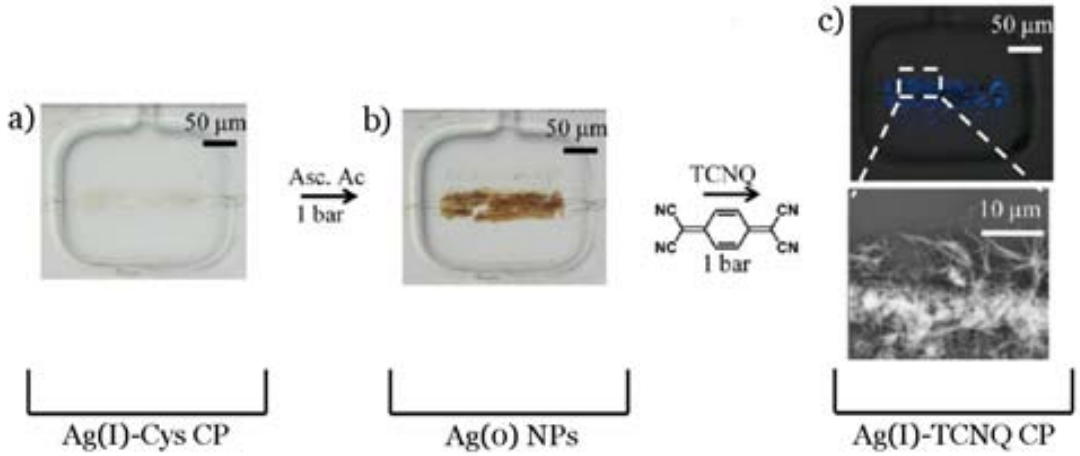

Figure 5.9. a) An optical image showing the trapped Ag(I)-Cys CP synthesized using microfluidic. b) Microscope image of reduced Ag(I)-Cys CP using ascorbic acid as reductor. c) Polarized microscope image of Ag(I)-TCNQ nanowires bundles together with a SEM image showing the nanometer scale Ag(I)-TCNQ wires that are grown.

Additionally, this microfluidic setup allows the positioning of the synthesized fibers at different locations on the chip by controlling the clamp pressure and varying of the relative flow rates of the precursor solutions. In this way, it was possible to grow the Ag(I)-TCNQ nanowire bundles, using the five synthetic steps explained above, onto an electrode array which is incorporated in a second microfluidic design. The pressure exerted by the clamps not only localized the fibers but also facilitated their integration into a functional interfaced system (see Figure 5.10.a). To confirm this integration of the Ag(I)-TCNQ nanowire bundles, microscale two-point electrical measurements and current sensing atomic force microscopy (CS-AFM) studies were undertaken. These I-V measurements uncovered that Ag(I)-TCNQ nanowires show high (ON) and (OFF) current states which can be switched by controlling the voltage applied to the electrodes. In Figure 5.10.c the non-linear I-V behavior typical for a semiconducting charge transfer complex is shown. The hysteresis behavior clearly reveals the switching between ON-OFF states due to high-applied voltages (see Figure 5.10.b). The current signal response measured in a reversible voltage cycle with different voltage steps, 2, 4, and 6 V shows that the switching can be controlled. At first, the system is in an OFF state up to 4 V, while at 6 V a two-fold increase in the current (ON) was observed. The sequential measurement at 4 V confirms the switch to an ON state indicating a reversible hysteretic switching behavior of the Ag(I)-TCNQ material, confirming that this assembly could act as a memory element (see Figure 5.10.c).

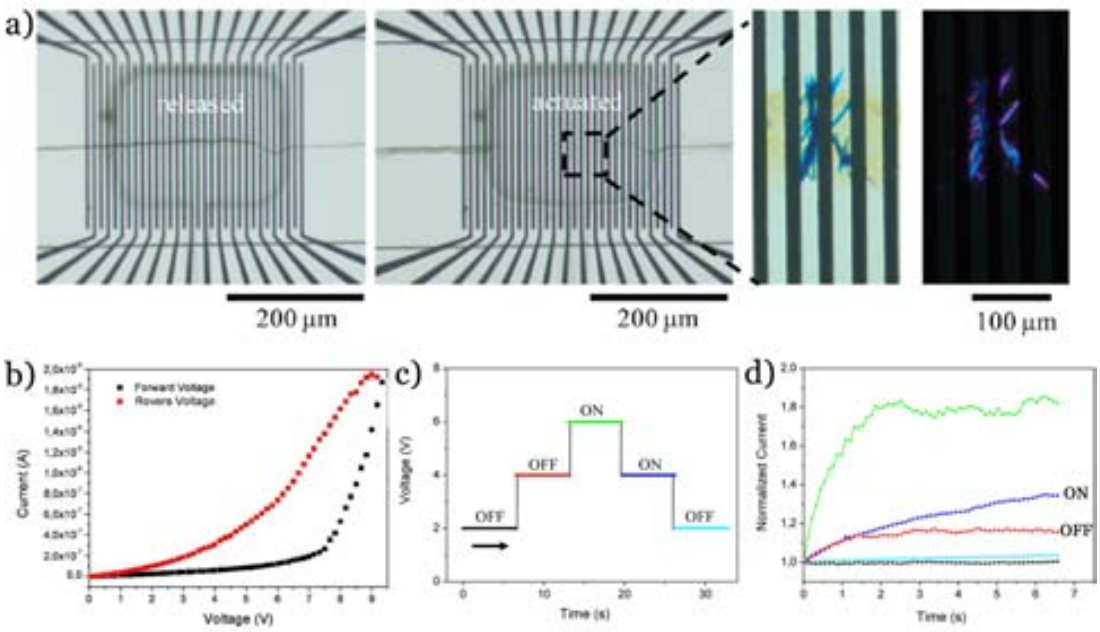

Figure 5.10. a) Optical microscope images showing the synthesis of Ag(I)-Cys CP over a patterned electrode surface (left), a micrograph of the pneumatic actuation (center) together with a optical image of Ag(I)-TCNQ nanowires bundles (right). b) I-V sweeps measured on Ag(I)-TCNQ showing a hysteresis in the current transport after applying a forward (black curve) and reverse (red curve) voltage, confirming the ON and OFF states of the Ag(I)-TCNQ nanowire bundles. (c) Schematic illustration of the reversible voltage cycle applied to the Ag(I)-TCNQ nanowires and in (d) the normalized current signal response measured.

To conclude, in this Chapter, we have demonstrated the use of metal-AA nanofibers as single scaffolds to produce superstructures made of inorganic nanoparticles via thermal reduction. Taking advantage of microfluidics, we aim to control the precise location of the templated synthesis of the superstructures made of Ag nanoparticles, thereby allowing the direct measurement of their conductivity properties as well as their re-use as a template to grow conductive Ag(I)-TCNQ crystals.

III. References

(1) Auffan, M.; Rose, J.; Bottero, J.-Y.; Lowry, G. V.; Jolivet, J.-P.; Wiesner, M. R. Towards a Definition of Inorganic Nanoparticles from an Environmental, Health and Safety Perspective. *Nat. Nanotechnol.* **2009**, *4*, 634–641.

(2) Lohse, S. E.; Murphy, C. J. Applications of Colloidal Inorganic Nanoparticles: From Medicine to Energy. *J. Am. Chem. Soc.* **2012**, *134*, 15607–15620.

(3) Nie, Z.; Petukhova, A.; Kumacheva, E. Properties and Emerging Applications of Self-Assembled Structures Made from Inorganic Nanoparticles. *Nat. Nanotechnol.* **2010**, *5*, 15–25.

(4) Narayanan, R.; El-Sayed, M. A. Shape-Dependent Catalytic Activity of Platinum Nanoparticles in Colloidal Solution. *Nano Lett.* **2004**, *4*, 1343–1348.

(5) Jin, R.; Cao, Y.; Mirkin, C. A.; Kelly, K. L.; Schatz, G. C.; Zheng, J. G. Photoinduced Conversion of Silver Nanospheres to Nanoprisms. *Science* **2001**, *294*, 1901–1903.

(6) *Zinc Oxide Bulk, Thin Films and Nanostructures: Processing, Properties and Applications*; Jagadish, C.; Pearton, S. J., Eds.; Elsevier: Amsterdam ; Boston, 2006.

(7) Katz, E.; Willner, I. Integrated Nanoparticle-Biomolecule Hybrid Systems: Synthesis, Properties, and Applications. *Angew. Chem. Int. Ed.* **2004**, *43*, 6042–6108.

(8) Ofir, Y.; Samanta, B.; Rotello, V. M. Polymer and Biopolymer Mediated Self-Assembly of Gold Nanoparticles. *Chem. Soc. Rev.* **2008**, *37*, 1814–1825.

(9) Jung, S.; Oh, M. Monitoring Shape Transformation from Nanowires to Nanocubes and Size-Controlled Formation of Coordination Polymer Particles. *Angew. Chem. Int. Ed.* **2008**, *47*, 2049–2051.

(10) Oh, M.; Mirkin, C. A. Chemically Tailorable Colloidal Particles from Infinite Coordination Polymers. *Nature* **2005**, *438*, 651–654.

(11) Sun, X.; Dong, S.; Wang, E. Coordination-Induced Formation of Submicrometer-Scale, Monodisperse, Spherical Colloids of Organic–Inorganic Hybrid Materials at Room Temperature. *J. Am. Chem. Soc.* **2005**, *127*, 13102–13103.

(12) Zhong, S.-L.; Luo, L.-F.; Wang, L.; Zhang, L.-F. $DyPO_4$ Flower-like Superstructures and Macroporous Microstructures from Dysprosium-Based Coordination Polymer Wires. *Powder Technol.* **2012**, *230*, 151–157.

(13) Park, J.-U.; Lee, H. J.; Cho, W.; Jo, C.; Oh, M. Facile Synthetic Route for Thickness and Composition Tunable Hollow Metal Oxide Spheres from Silica-Templated Coordination Polymers. *Adv. Mater.* **2011**, *23*, 3161–3164.

(14) Zheng, Y.; Liu, K.; Qiao, H.; Zhang, Y.; Song, Y.; Yang, M.; Huang, Y.; Guo, N.; Jia, Y.; You, H. Facile Synthesis and Catalytic Properties of CeO_2 with Tunable Morphologies from

Thermal Transformation of Cerium Benzendicarboxylate Complexes. *CrystEngComm* **2011**, *13*, 1786–1788.

(15) Cho, W.; Lee, Y. H.; Lee, H. J.; Oh, M. Systematic Transformation of Coordination Polymer Particles to Hollow and Non-Hollow In_2O_3 with Pre-Defined Morphology. *Chem. Commun.* **2009**, 4756–4758.

(16) Zhang, D.; Liu, Z.; Li, C.; Tang, T.; Liu, X.; Han, S.; Lei, B.; Zhou, C. Detection of NO2 down to Ppb Levels Using Individual and Multiple In_2O_3 Nanowire Devices. *Nano Lett.* **2004**, *4*, 1919–1924.

(17) Pinna, N.; Neri, G.; Antonietti, M.; Niederberger, M. Nonaqueous Synthesis of Nanocrystalline Semiconducting Metal Oxides for Gas Sensing. *Angew. Chem. Int. Ed.* **2004**, *43*, 4345–4349.

(18) Li, C.; Zhang, D.; Han, S.; Liu, X.; Tang, T.; Zhou, C. Diameter-Controlled Growth of Single-Crystalline In2O3 Nanowires and Their Electronic Properties. *Adv. Mater.* **2003**, *15*, 143–146.

(19) Cho, W.; Lee, H. J.; Oh, M. Growth-Controlled Formation of Porous Coordination Polymer Particles. *J. Am. Chem. Soc.* **2008**, *130*, 16943–16946.

(20) Jung, S.; Cho, W.; Lee, H. J.; Oh, M. Self-Template-Directed Formation of Coordination-Polymer Hexagonal Tubes and Rings, and Their Calcination to ZnO Rings. *Angew. Chem. Int. Ed.* **2009**, *48*, 1459–1462.

(21) Cho, W.; Park, S.; Oh, M. Coordination Polymer Nanorods of Fe-MIL-88B and Their Utilization for Selective Preparation of Hematite and Magnetite Nanorods. *Chem. Commun.* **2011**, *47*, 4138–4140.

(22) Machala, L.; Zoppellaro, G.; Tuček, J.; Šafářová, K.; Marušák, Z.; Filip, J.; Pechoušek, J.; Zbořil, R. Thermal Decomposition of Prussian Blue Microcrystals and Nanocrystals – Iron(III) Oxide Polymorphism Control through Reactant Particle Size. *RSC Adv.* **2013**, *3*, 19591-19595.

(23) Shi, F.; Tse, M. K.; Pohl, M.-M.; Brückner, A.; Zhang, S.; Beller, M. Tuning Catalytic Activity between Homogeneous and Heterogeneous Catalysis: Improved Activity and Selectivity of Free Nano-Fe2O3 in Selective Oxidations. *Angew. Chem. Int. Ed.* **2007**, *46*, 8866–8868.

(24) Hsu, M.-H.; Su, Y.-C. Iron-Oxide Embedded Solid Lipid Nanoparticles for Magnetically Controlled Heating and Drug Delivery. *Biomed. Microdevices* **2008**, *10*, 785–793.

(25) Hu, M.; Jiang, J.-S.; Bu, F.-X.; Cheng, X.-L.; Lin, C.-C.; Zeng, Y. Hierarchical Magnetic Iron (III) Oxides Prepared by Solid-State Thermal Decomposition of Coordination Polymers. *RSC Adv.* **2012**, *2*, 4782-4784.

(26) Wu, R.; Qian, X.; Rui, X.; Liu, H.; Yadian, B.; Zhou, K.; Wei, J.; Yan, Q.; Feng, X.-Q.; Long, Y.; *et al.* Zeolitic Imidazolate Framework 67-Derived High Symmetric Porous Co_3O_4 Hollow Dodecahedra with Highly Enhanced Lithium Storage Capability. *Small* **2014**, DOI:10.1002/smll.201303520.

(27) Liu, B.; Shioyama, H.; Akita, T.; Xu, Q. Metal-Organic Framework as a Template for Porous Carbon Synthesis. *J. Am. Chem. Soc.* **2008**, *130*, 5390–5391.

(28) Fei, J.; Cui, Y.; Wang, A.; Zhu, P.; Li, J. Noble Metal Nanochains through Helical Self-Assembly. *Chem. Commun.* **2010**, *46*, 2310.

(29) Fei, J.; Gao, L.; Zhao, J.; Du, C.; Li, J. Responsive Helical Self-Assembly of $AgNO_3$ and Melamine Through Asymmetric Coordination for Ag Nanochain Synthesis. *Small* **2013**, *9*, 1021–1024.

Publication 4. "Localized, stepwise template growth of functional nanowires from an amino-acid supported framework in a microfluidic chip". J. Puigmartí-Luis, M. Rubio-Martínez, I.Imaz, B. Z. Cvetkovic, L. Abad, A. Perez del Pino, D. Maspoch, D. B. Amabilino. *ACS nano*. **2014**, 8, 818-826.

Localized, Stepwise Template Growth of Functional Nanowires from an Amino Acid-Supported Framework in a Microfluidic Chip

Josep Puigmartí-Luis,[†,*] Marta Rubio-Martínez,[‡] Inhar Imaz,[‡] Benjamin Z. Cvetković,[§] Llibertat Abad,[⊥] Angel Pérez del Pino,[†] Daniel Maspoch,[‡,∥] and David B. Amabilino[†,*]

[†]Institut de Ciència de Materials de Barcelona (ICMAB-CSIC), Campus Universitari de Bellaterra, 08193 Bellaterra, Spain, [‡]ICN2—Institut Catala de Nanociencia i Nanotecnologia, Campus Universitari de Bellaterra, 08193 Bellaterra (Barcelona), Spain, [§]Laboratory for Waste Management, Department for Nuclear Energy and Safety Research, Paul Scherrer Institut, Villigen, Switzerland, [⊥]Institut de Microelectrònica de Barcelona, IMB-CNM (CSIC), Campus Universitari de Bellaterra, 08193 Bellaterra, Barcelona, Spain, and [∥]Institució Catalana de Recerca i Estudis Avançats (ICREA) 08100 Barcelona, Spain

ABSTRACT A spatially controlled synthesis of nanowire bundles of the functional crystalline coordination polymer (CP) Ag(I)TCNQ (tetracyanoquinodimethane) from previously fabricated and trapped monovalent silver CP (Ag(I)Cys (cysteine)) using a room-temperature microfluidic-assisted templated growth method is demonstrated. The incorporation of microengineered pneumatic clamps in a two-layer polydimethylsiloxane-based (PDMS) microfluidic platform was used. Apart from guiding the formation of the Ag(I)Cys coordination polymer, this microfluidic approach enables a local trapping of the *in situ* synthesized structures with a simple pneumatic clamp actuation. This method not only enables continuous and multiple chemical events to be conducted upon the trapped structures, but the excellent fluid handling ensures a precise chemical activation of the amino acid-supported framework in a position controlled by interface and clamp location that leads to a site-specific growth of Ag(I)TCNQ nanowire bundles. The synthesis is conducted stepwise starting with Ag(I)Cys CPs, going through silver metal, and back to a functional CP (Ag(I)TCNQ); that is, a novel microfluidic controlled ligand exchange (CP → NP → CP) is presented. Additionally, the pneumatic clamps can be employed further to integrate the conductive Ag(I)TCNQ nanowire bundles onto electrode arrays located on a surface, hence facilitating the construction of the final functional interfaced systems from solution specifically with no need for postassembly manipulation. This localized self-supported growth of functional matter from an amino acid-based CP shows how sequential localized chemistry in a fluid cell can be used to integrate molecular systems onto device platforms using a chip incorporating microengineered pneumatic tools. The control of clamp pressure and in parallel the variation of relative flow rates of source solutions permit deposition of materials at different locations on a chip that could be useful for device array preparation. The *in situ* reaction and washing procedures make this approach a powerful one for the fabrication of multicomponent complex nanomaterials using a soft bottom-up approach.

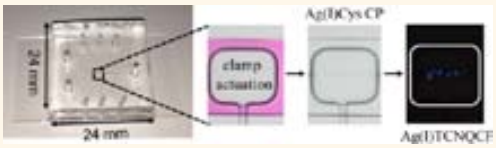

KEYWORDS: molecular nanomaterials · flow · template synthesis · amino acids · molecular electronics

The localization and integration of functional materials on surfaces is important for rapid device fabrication,[1] and bottom-up chemical approaches are particularly attractive. Among the several approaches employed so far, templated growth techniques have proven to be the most effective methods to localize and control the growth of monodisperse functional structures with nanoscale spatial resolution.[2,3] Nonetheless, in many cases, these approaches are time-consuming, labor intensive, and frequently require the use of expensive equipment. Therefore, a longstanding challenge in the field is to develop new approaches where sequential multiple chemical modifications can be performed under controlled mild conditions economically without the need for postassembly manipulation that could affect the performance of the material. Recently, for example, the templated growth approach to functional nanocrystals with the assistance of biomolecules has gained much attention owing to the ease with which extremely complex structures can be constructed from the bottom-up in a flexible manner with no need of expensive equipment and under mild conditions.[4,5] Biomolecular scaffolding of functional assemblies is an attractive and an emerging field of research in which a wide number of functional structures can be used for nanotechnological applications

* Address correspondence to jpuigmarti@icmab.es, amabilino@icmab.es.

Received for review October 21, 2013 and accepted December 19, 2013.

Published online December 19, 2013
10.1021/nn4054864

and device fabrication.[6−9] Within the various biomolecular scaffolding approaches, a set of coordination polymers (CPs) involving peptide-supported frameworks have proven to be relevant materials for a controlled template growth of functional superstructures at both, micro- and nanoscale dimensions.[10] Typically, CPs are crystalline materials that are composed of metal ion nodes coordinated to organic ligands.[11,12] While significant research efforts are focused in the development of novel synthetic methods for new CPs and while modification of the structure and composition of CPs is necessary in order to expand their number of functions to go beyond the state-of-the-art in certain applications, very little is known in terms of CPs acting as template scaffolds for the growth of functional materials that could be useful for introducing components in devices in a bottom-up way.

Common and straightforward methods employed so far to induce novel functions to CPs include establishing functional organic linkers in the structure[13,14] or inducing photochemical processes that can favor the reduction of the metal ions which act as nodes or connectors. For example, a direct-writing of microscopic metallic silver patterns inside single metal−organic crystals employing a laser beam approach has been reported recently.[15] Moreover, Cohen and co-workers have effectively reported postsynthetic organic linker modification approaches to porous CP crystals.[16−20] These studies have demonstrated effectively that tunable chemical and physical properties (*e.g.*, hydrophobicity or microporosity, respectively) can be modulated when CP crystals are subjected to postsynthetic modifications. Despite the progress achieved in this area, a major challenge that remains is to define rational and systematic methods that can enable the synthesis of novel functional structures grown from CP scaffolds and which could display distinct functionality to the former building blocks. For example, we have recently described the formation of Ag_2S semiconductor nanoparticles from a silver-cysteine (Ag(I)Cys) based CP after e-beam exposure.[21] Nonetheless, it should be emphasized that to impart functionality to CPs by treating and tuning their building block composition chemically is still largely unexplored.

Here we provide the first strong evidence that CPs can be used as scaffolds to template the growth of functional nanometer scale matter through sequential chemical reactions, and we further explore this templated growth mechanism with a two-layer microfluidic platform incorporating microengineered fluidic clamps, where a spatially resolved crystal template growth process is accomplished. In contrast to other templated growth routes where microscale porous CP crystals are modified by CP-on-CP heteroepitaxy,[22,23] or where CPs are grown on microscale nucleation agents,[24] we prove a silver-tetracyanoquinodimethane (Ag(I)TCNQ) templated crystal growth from a previously formed and immobilized amino acid-supported framework (Ag(I)Cys) which acts as the backbone scaffold in the process. Ag(I)TCNQ CPs are well-known charge transfer complexes with very interesting electroactive properties, for instance, for the fabrication of organic memory elements thanks to the existence of two reversible and stable electronic states. That is, the resistivity of this charge transfer complex switches from a high conductive state (ON state) to a low conductive state (OFF state) while changing the voltage applied to the complex.[24,25] In addition, the approach used to localize growth involves square-shaped microengineered fluidic clamps that can be actuated over electrode arrays located at the bottom of the fluidic layer which permitted the integration of Ag(I)TCNQ nanowire bundles to read-out components and at desired locations on a surface. To the best of our knowledge, there are no examples reported so far which combine sequential chemical event treatments, a functional crystal template growth method, where a microfluidic assisted ligand exchange is favored, and the actuation of microengineered pneumatic tools toward the assembly of fully integrated systems on surfaces. Thus, devices can be prepared on-chip from solution, with components at specific locations and that require no further manipulation that might affect the molecular material that is used.

RESULTS AND DISCUSSION

Double-layer microfluidic chips with square-shaped embedded deformable features were employed in our research. As shown in Figure 1a, the chips consisted of two layers of polydimethylsiloxane (PDMS) where the bottom-layer was designed to accommodate the fluidic channel and a top control layer was used to partially squeeze (using nitrogen gas) the fluidic channel toward the glass substrate (see Materials and Methods section for further details). This partial deformation of the fluidic layer resulted in what are effectively microengineered fluidic clamps (Figure 1). Determining the performance of these clamps and the behavior of the laminar flow upon clamp pressurization with nitrogen gas was necessary prior to Ag(I)Cys CP trapping. We studied the efficiency of the device with the injection of an aqueous solution of rhodamine dye through the fluidic layer. Figure 1b shows an optical micrograph of the main channel of the microfluidic chip filled with the dye and the square-shaped embedded deformable clamps which were not actuated. After actuation of a single square-shaped clamp with nitrogen gas (3 bar), the membrane of PDMS between the gas and fluid channel deflected toward the glass substrate deflecting the fluid flow regime in the actuated region (Figure 1(c)). Nonetheless, the dye stream could still flow through the clamp sides as shown in Figure 1c with black arrows. This noninterrupted flow condition

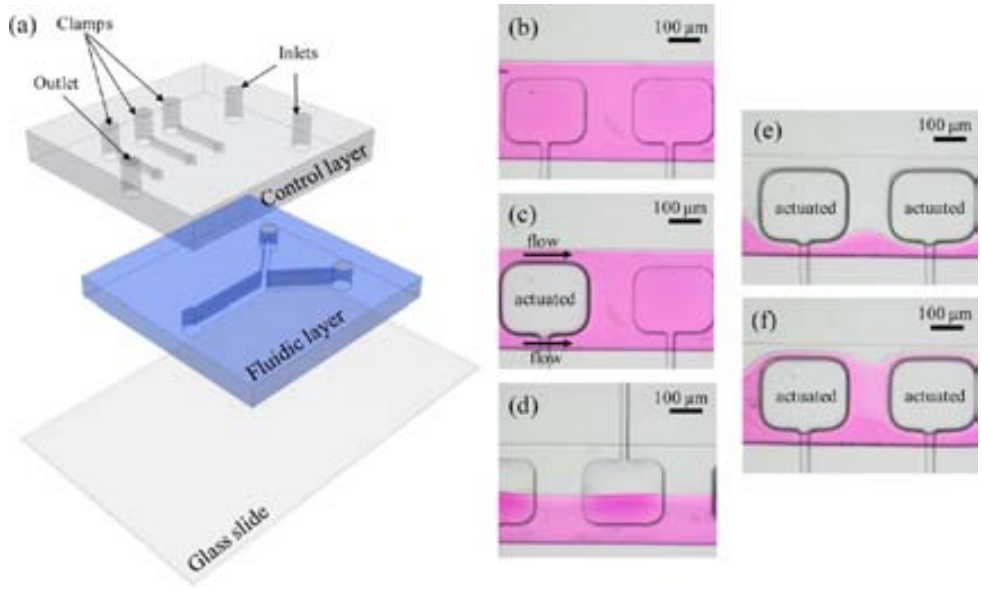

Figure 1. (a) Schematic view of the multilayer microfluidic chip used in our experiments. (b) Optical microscope image of the microfluidic chip filled with an aqueous solution of rhodamine dye. (c) An optical micrograph showing the actuation of the pneumatic clamp located on the left. The arrows indicate the fluid flow around the squared-shape valve design. (d) Optical microscope image of the laminar flow regime achieved by coflowing a water stream to the dye flow. (e and f) optical microscope images showing the tuning of the dye solution–water interface by varying one fluid flow rate when the valves are actuated. In panel e the dye flow rate is higher (30 μL/min) than the water flow rate (10 μL/min), whereas in panel f, the opposite is true.

is essential in order to allow an online, continuous, and sequential chemical event treatment of the trapped Ag(I)Cys CPs (*vide infra*). We further demonstrated the laminar flow regime with the injection of a second fluid stream; water (Figure 1d). When the clamps were actuated under a laminar flow regime, a precise guiding of the water and dye interface could be achieved by varying the relative flow rates. Figure 1e and Figure 1f show that when the flow rate of the dye solution stream is lower, a down-shifted guiding of the interface could be accomplished; whereas at higher dye flow rates the interface was shifted upward in the optical micrograph image. This accurate control of the interface position inside the microfluidic channel is very promising for a precise localization of the coordination pathway which leads to the formation of Ag(I)Cys CP (*vide infra*).

With this microengineered fluidic clamp-based chip in hand, we employed it both to localize *in situ* synthesis of the Ag(I)Cys CP and to induce a site-specific growth of functional Ag(I)TCNQ nanowire bundles on the underlying surface. In a typical experiment two aqueous reagent solutions, $Ag(NO_3)$ (2.5 mM) and Cys (2.5 mM), were injected through the fluidic channel at flow rates of 50 μL/min. The concentration of the reagent precursors was optimized to avoid channel clogging. Figure 2a shows a sequence of optical microscope images of the interface of the two coflowing reagent streams where the formation of Ag(I)Cys CP occurred (indicated with green arrows). Actuation of a microfluidic pneumatic clamp at 3 bar enabled both a localized trapping of Ag(I)Cys CP on the glass substrate surface (Figure 2b) and a successful removal of all surplus reagents solutions used during the synthesis of Ag(I)Cys CP, washed away with a flow of pure water (Figure 2i). Afterward, a saturated ascorbic acid solution in EtOH was added to the microfluidic platform (10 μL/min) in order to reduce the monovalent silver salt to the metal. To favor a precise chemical treatment of the trapped Ag(I)Cys CP underneath the clamped area, the clamp pressure was reduced to 1 bar (Figure 2ii). As shown in Figure 2b, a clear color change to a darker brown was demonstrated after treating the trapped Ag(I)Cys CP with the solution of ascorbic acid for approximately 2 min. The color change was attributed to the reduction of Ag(I) to metallic silver (Ag(0)) by the ascorbic acid, a supposition that was corroborated with bulk powder X-ray diffraction (PXRD) studies (Supporting Information, Figure S1), and in accord with previous observations.[26−29] It is worth noting that the color change assigned to the silver reduction was only observed underneath the clamp area, thereby demonstrating the localized chemical treatment enabled by the present approach (Figure 2c). After this reduction step, a washing procedure with ethanol was necessary in order to eliminate the excess ascorbic acid in the microfluidic channel (Figure 2iii). An increase of the clamp pressure to 3 bar was necessary during this rinsing process in order to avoid the movement and elution of the material. Washing steps between consecutive chemical reactions turned out to be crucial as they ensure that no additional

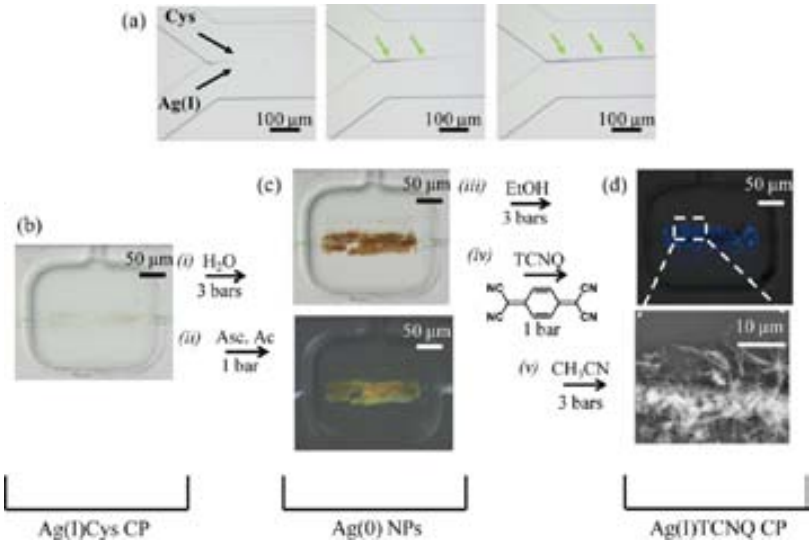

Figure 2. (a) A sequence of optical microscope images showing the assembly of Ag(I)Cys CP at the interface of Ag(NO_3) and Cys aqueous reagent streams. The yellow arrows indicate the Ag(I)Cys CP assembled at the interface of the two coflowing streams. From panels b to d, optical microscope images showing the five consecutive chemical events (i, ii, iii, iv, and v) that lead ultimately to the self-supported growth of Ag(I)TCNQ nanowires. (b) An optical micrograph showing trapped Ag(I)Cys CP. (c) A nonpolarized microscope image (top) and a polarized microscope image (bottom) of reduced Ag(I)Cys CP. (d) Polarized microscope image of Ag(I)TCNQ nanowires bundles (top) together with a SEM image showing the nanometer scale Ag(I)TCNQ wires that are grown (bottom).

reactions with surplus reagents could occur. Next, an oxidation of the deposited Ag(0) with TCNQ in acetonitrile was conducted after the clamp pressure was again set to 1 bar. In fact, the Ag(0) deposit acts as nucleation sites for the Ag(I)TCNQ charge transfer complex growth. The confirmation of the formation of the crystalline Ag(I)-TCNQ CPs was immediately clear under inspection with a polarizing optical microscope where polarization-dependent crystal colors were observed. Figure 2d (top) shows an optical microscope image taken using crossed polarizers showing a deep blue-purple color which is attributed to the crystalline Ag(I)TCNQ CPs. Furthermore, PXRD analysis on the sample removed from the chip corroborated the formation of the Ag(I)TCNQ complex in its tetragonal phase, which has been reported (Supporting Information, Figure S1).[30] To demonstrate that the crystalline Ag(I)TCNQ CP was formed from reduced Ag(I)Cys CP, a control experiment was performed where the chemical treatment with saturated ascorbic acid solution was omitted. In this case, no Ag(I)-TCNQ CPs were observed even after a long treatment time with a TCNQ solution. These results clearly evidence that the reduction of silver metal ions is necessary for Ag(I)TCNQ charge transfer complex growth. To avoid formation of TCNQ crystals after solvent evaporation, pure acetonitrile was injected into the microfluidic platform to wash away the remaining TCNQ solution while the clamp pressure was switched to 3 bar again (Figure 2v). Because it is inherently difficult to distinguish nanoscale Ag(I)TCNQ CP structures under the optical microscope, scanning electron microscopy (SEM) studies on released nonbonded

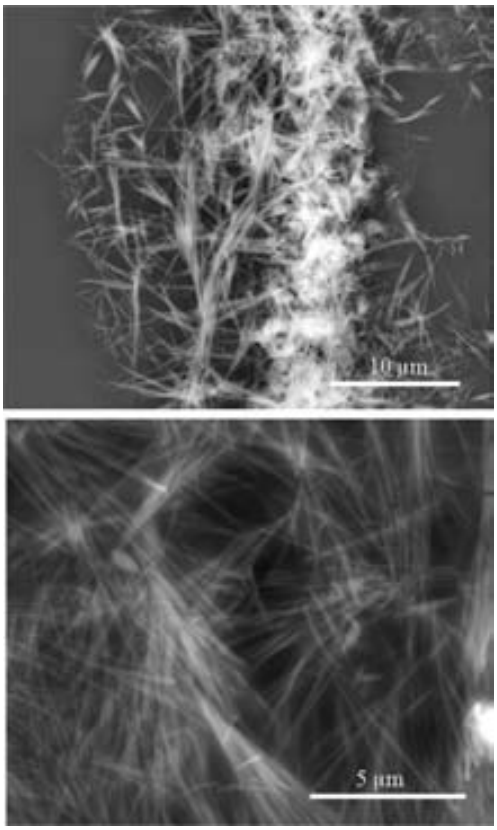

Figure 3. SEM images of Ag(I)TCNQ nanowire bundles synthesized with the presented clamp-based microfluidic approach.

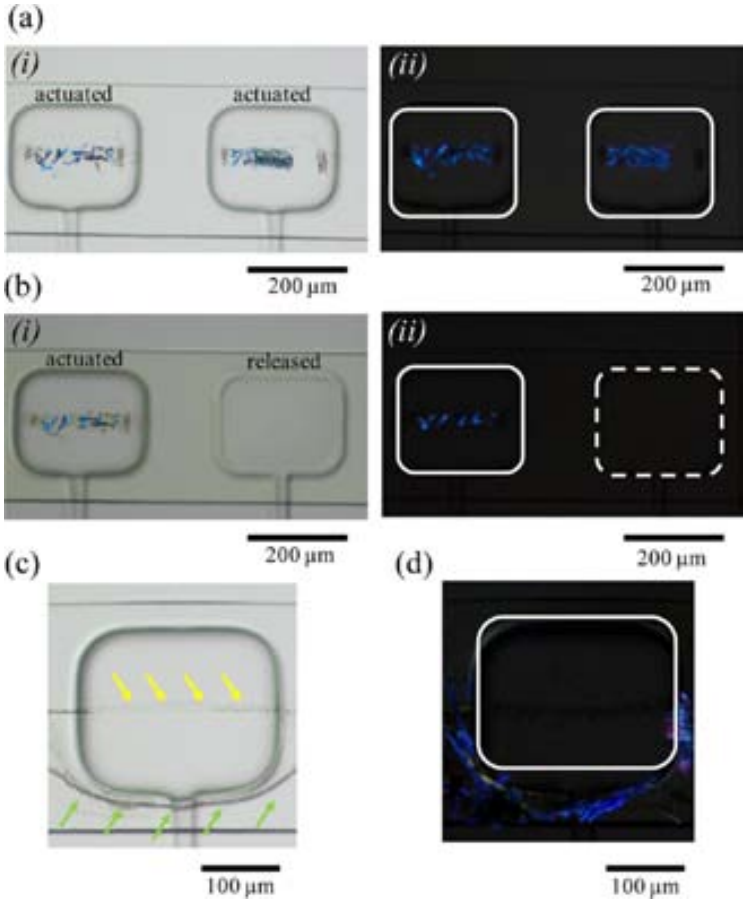

Figure 4. (a) Optical graphs showing a sequential templated growth of Ag(I)TCNQ nanowire bundles at different latitudes in the channel, (i) without, and (ii) with crossed polarizers. (b) (i) Micrograph showing the release of one valve, the second valve, and the wash away process of the Ag(I)TCNQ nanowire bundles located underneath. In panel ii, the same optical microscope image but with crossed polarizers. Notice that the squared-shape feature represented with a dash line represents the situation where the clamp is released, and with a solid line when it is actuated. (c) Optical microscope image of a double Ag(I)Cys CP guided assembly one synthesized before clamp actuation (yellow arrows), and the second after its actuation (green arrows). (d) Micrograph under crossed polarizers showing the templated growth of Ag(I)TCNQ nanowire bundles only on the Ag(I)Cys CP outside the clamp region.

chips were conducted. Clearly, SEM characterization demonstrated the nanoscale nature of the crystalline Ag(I)TCNQ CPs grown with this microfluidic-assisted template method where a localized ligand exchange is facilitated (Figure 2d, bottom image, and Figure 3). Typical diameters of these Ag(I)TCNQ nanowires range from 60 to 250 nm, and the length can be longer than 10 μm.

A parallelized Ag(I)TCNQ patterning on a glass surface was also demonstrated with this clamp-based approach. Figure 4a shows optical micrographs of the Ag(I)TCNQ CPs grown and located precisely underneath two clamp patches. Images with parallel and crossed polarizers are shown in Figure 4a,i and Figure 4a,ii, respectively. By releasing the second valve and additionally increasing the acetonitrile flow rate from 10 μL/min to 50 μL/min and above, a controlled removal of Ag(I)TCNQ from the glass surface was demonstrated (Figure 4b,i and 4b,ii). Interestingly, if the flow rates were interrupted, the two valves could be released and the Ag(I)TCNQ CPs remained in place and on the surface (Supporting Information, Figure S2). This result was very important not just to show the potential of the template growth approach toward surface patterning, but to further demonstrate the possibility of integrating the Ag(I)TCNQ nanowires onto electrode arrays located on the glass surface (vide infra).

Additionally, by controlling the clamp pressure and the interface position during the formation of the Ag(I)Cys CP, a precise templated growth of Ag(I)TCNQ could be achieved. Figure 4c shows an optical micrograph of Ag(I)Cys CP formed under laminar flow conditions, which was trapped by the clamp actuation (indicated with yellow arrows in the figure), and Ag(I)Cys CP formed outside the clamp region after this was actuated (denoted with green arrows). We demonstrated that when all five consecutive chemical events described in Figure 2, from i to v, were conducted with a clamp pressure of 3 bar, an accurate templated Ag(I)TCNQ

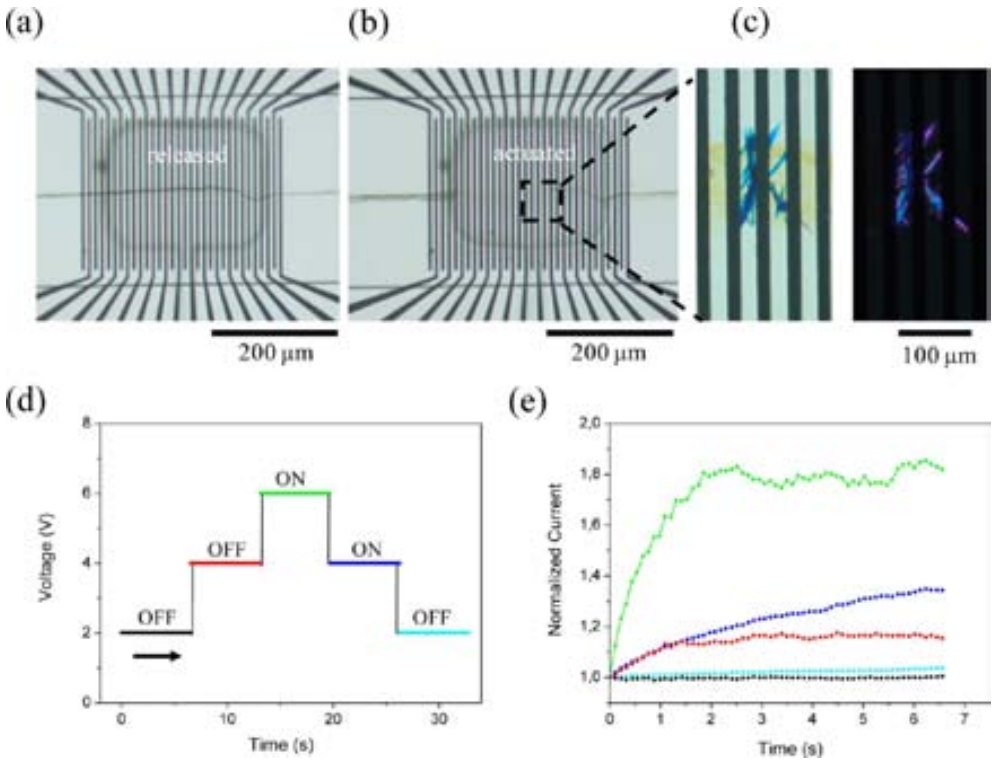

Figure 5. (a) Optical microscope image showing the synthesis of Ag(I)Cys CP over a patterned electrode surface, and in (b) a micrograph upon the pneumatic actuation. (c) Optical microscope images of Ag(I)TCNQ nanowire bundles under nonpolarized light (top) and under cross-polarized illumination (bottom). (d) Schematic illustration of the reversible voltage cycle applied to the Ag(I)TCNQ nanowires and in (e) the normalized current signal response measured.

growth was accomplished only on the Ag(I)Cys CP located outside the valve region (Figure 4d). This localized site-specific templated growth is extremely encouraging because it provides the best evidence of the control enabled by the present approach toward a precise crystal template growth process due to its excellent fluid control. Importantly, in the present case, the template growth process was performed at lower flow rates of both reactants and washing solvents (maximum 2 μL/min) in order to avoid the elution of Ag(I)Cys CP from the chip. Notice that even though the flow rates used during the five consecutive chemical events were low, the Ag(I)Cys CP located outside the clamp region moved slightly from its initial position (Figure 4b,ii). Besides thermal vapor deposition methods, the number of template techniques which facilitate rapid and consecutive chemical events to be addressed at specific locations and with excellent fluid handling conditions is very limited. To the best of our knowledge, there are no other methods described where an amino acid-supported framework is employed for the synthesis of functional crystalline matter with such a control in both the location of the scaffold enabling the template growth, and guiding the consecutive chemical events in a "one-pot" format.

Studies conducted with lower concentrations of $Ag(NO_3)$ (1.0 mM) and Cys (1.0 mM) precursor solutions corroborated the formation of a smaller number of Ag(I)TCNQ nanowires from the trapped Ag(I)Cys CP, probably due to the lower amount of Ag(I)Cys CP trapped under these conditions (Supporting Information, Figure S3). Interestingly, adjusting the concentration to 1.0 mM enabled a clear time-sequence analysis of the oxidation process (Supporting Information, Figure S4). In these investigations, it was demonstrated, under optical microscope visualization, that around 30 min were necessary to conclude crystalline Ag(I)TCNQ charge transfer complex growth. Moreover, these studies indicated that with this approach a continuous growth of Ag(I)TCNQ nanowire bundles up to 40 μm far away from its initial interface was possible. The small number of Ag(I)TCNQ nanowires at this concentration facilitated this study. Notably, no observation of Ag(I)TCNQ CPs was evidenced at a lower concentration of reagents (data not shown), hence delimiting the concentration range of the precursor solutions from which a clear appreciation of the growth process was feasible.

As stated above, pneumatic clamp actuation can also be employed for a selective localization and integration of Ag(I)TCNQ charge transfer complexes on patterned electrode surfaces. In these experiments, a glass surface containing an electrode array was used during the templated growth process. The electrode

array was perfectly aligned below the square-shape valves in order to favor Ag(I)TCNQ integration (Figure 5, and Supporting Information, Figure S5a). To confirm the integration of Ag(I)TCNQ nanowire bundles to the electrode array, microscale two-point electrical measurements (Figure 5 and Supporting Information, Figure S5b), and current sensing atomic force microscopy (CS AFM) studies were conducted on different samples (Supporting Information, Figure S5c). Figure 5 shows, from panels a to c, an Ag(I)TCNQ template growth process conducted on a patterned electrode glass surface. Figure 5d presents a schematic illustration of a reversible voltage cycle applied to the Ag(I)TCNQ nanowires, and Figure 5e shows a representative and normalized current signal response measured at different voltage steps, 2, 4, and 6 V. Figure 5e clearly supports the assertion that the Ag(I)TCNQ bundles grown with this methodology have indeed high (ON) and low (OFF) current states which can be accurately switched by controlling the voltage applied to the electrodes. A characteristic two-order-fold increase in current (ON state) was evidenced at 6 V,[31] therefore confirming the effective assembly of functional Ag(I)TCNQ memory elements with this microfluidic-assisted template method. In contrast, at 4 V the current change between the ON and OFF states was lower than at 6 V, indicating the reversible hysteretic switching behavior of the Ag(I)TCNQ material (see also Supporting Information, Figure S5b). Furthermore, CS AFM studies confirmed beyond doubt the integration of Ag(I)TCNQ nanowire bundles to the electrode array with the acquisition of current maps where nanowire features were clearly appreciated (Supporting Information, Figure S5c).

CONCLUSIONS

Both continuous chemical events and a controlled crystal template growth are possible with a clamp-based microfluidic approach. We have thus proven that microengineered pneumatic clamps can be exploited for functions which go far beyond a simple trapping of *in situ* formed structures. A unique and straightforward synthetic route for producing functional and crystalline Ag(I)TCNQ nanowire bundles from an amino acid-supported coordination framework (Ag(I)Cys CP) has been described, where mild conditions were used. The Ag(I)TCNQ nanowire bundles were generated online within a single microfluidic channel and on surface. Furthermore, a precise localization and integration of conductive Ag(I)TCNQ nanowire bundles to electrode arrays located underneath the clamp area was demonstrated. Thus, unlike other techniques where the material is formed upon evaporation,[32] where electrodes are evaporated onto existing nanostructures,[31] or where electrophoretic methods are used to align orientation but not position,[33] this soft bottom-up approach allows the parallel template formation of molecular nanostructures from solution on device surfaces with no need for postassembly manipulation to reach the functioning system.

It is important to note that the control of clamp pressure and in parallel the variation of relative flow rates of source solutions can in principle lead to spatially controlled deposition of materials at different locations on a chip. The *in situ* reaction and washing procedures make this approach a powerful one for the fabrication of multicomponent complex systems. We envision the use of the present method to a variety of other systems and structures, therefore expanding and opening up new powerful routes for a localized synthesis and integration of other functional hybrid systems which could further be employed in optoelectronic applications, sensing, and catalysis. Indeed, the results presented here should also open new possibilities in the ambitious route of biomolecular scaffolding and device fabrication.

MATERIALS AND METHODS

All reagents were purchased from Sigma-Aldrich Co. High purity solvents were purchased from Teknokroma, and used without further purification. Deionized Millipore Milli-Q water was used in all experiments.

Fabrication of patterned electrode surfaces on glass coverslips. The electrodes consisted of a chromium adhesion layer (Cr (10 nm)) and a top platinum layer (Pt) 100 nm thick. These electrodes were fabricated on substrates of glass coverslips with standard UV-photolithography and lift-off using acetate transparency as a mask (JD Photo-Tools, UK) and 1.7 μm thin AZ 5214 E photoresist (Clariant, GmbH).

Two-layer microfluidic chip assembly. The two polydimethylsiloxane (PDMS) layers were fabricated on silicon wafers (Okmetic, Finland) with SU8-2025 as photoresist (Microchemicals, GmbH) using conventional soft lithography techniques.[25] Both, the fluid and control layer had features 50 μm high as confirmed by profilometry measurements. The top (control) layer was fabricated by a replication molding technique,[34] where a PDMS oligomer and hardener mixture (5:1 in weight) was poured onto the "control layer" wafer bearing the SU-8 features and polymerized at 80 °C for 30 min. Next, the bottom (fluid channel) layer was spin-coated at 2000 rpm for 1 min with a PDMS oligomer and hardener mixture 20:1, respectively. After spinning the PDMS mixture, the "fluidic" master was cured at 80 °C over 10 min. Later, 1.0 mm holes were punched in the control layer with a biopsy punch (Miltex GmbH) and this was then assembled on top of the cured fluidic layer present in the "fluidic" master. The two layers were then placed in an oven at 80 °C overnight in order to enable the bonding process. After that, the two bonded layers were removed from the "fluidic" master and 1.5 mm holes were punch in the fluidic layer. A final assembly of the two bonded layers to a glass coverslip (24 mm × 60 mm) was finally achieved through oxygen plasma activation of the two parts.

Instrumentation. Pt−Cr electrodes and fluidic masters were obtained by standard photolithography by using a DELTA 80 spinner (Süss), a Karl Suss MA/BA6 mask aligner, and an electron-assisted metal evaporator UNIVEX 450B (Oerlikon Leybold Vacuum). X-ray powder diffraction (XRPD) measurements were performed with an X'Pert PRO MPD diffractometer (Panalytical).

SEM measurements. All SEM images presented in this work were acquired on a SEM QUANTA FEI 200 FEG-ESEM operating in a low vacuum mode. In all cases the samples were measured as prepared with no need of metal deposition on the samples.

Electrical characterization and CS AFM studies. Two-point electrical characterizations were performed using a two channel Keithley 2612 SourceMeter and were measured under ambient conditions. On the other hand, CS AFM studies were performed on a 5500LS SPM system from Agilent Technologies using the Resiscope module. Unlike the two-point electrical characterization, a nanoscaled conducting tip was biased to the electrode array patterned on the glass coverslip. In this case, the current flowing through the electrodes to the integrated Ag(I)TCNQ nanowire bundles was measured with a conductive grounded tip at each point of the image, thus providing a current map image of the region scanned.

Conflict of Interest: The authors declare no competing financial interest.

Supporting Information Available: Additional optical micrographs, X-ray diffractograms of the materials, as well as electrical characterization of Ag(I)TCNQ prepared here. This material is available free of charge *via* the Internet at http://pubs.acs.org.

Acknowledgment. This research was supported by the MINECO, Spain (Projects CTQ2010-16339, MAT2012-30994, and CTQ2011-16009-E)), and the DGR, Catalonia (Project 2009 SGR 158). J.P.L. and I.I. thank the MINECO for a Ramón y Cajal Contract (RYC-2011-08071 and RYC-2010-06530, respectively). J.P.L. also thanks funding from the European Community's Seventh Framework Programme under Grant Agreement No. PCIG-11-GA-2012-32139, (project MuLoPla). Ll. Abad gratefully acknowledges a JAE-Doc contract from CSIC partially funded by European Social Fund (ESF). The authors also thank Dr. Francisco Javier del Campo for useful discussions and the GICSERV-B Program: 8th call, IMB-CNM-CSIC, Spain (Project NGG-261).

REFERENCES AND NOTES

1. Briseno, A. L.; Mannsfeld, S. C. B.; Ling, M. M.; Liu, Sh.; Tseng, R. J.; Reese, C.; Roberts, M. E.; Yang, Y.; Wudl, F.; Bao, Z. Patterning Organic Single-Crystal Transistor Arrays. *Nature* **2006**, *444*, 913–917.
2. Xia, Y.; Yang, P.; Sun, Y.; Wu, Y.; Mayers, B.; Gates, B.; Yin, Y.; Kim, F.; Yan, H. One-Dimensional Nanostructures: Synthesis, Characterization, and Applications. *Adv. Mater.* **2003**, *15*, 353–389.
3. Wang, X.; Summers, C. J.; Wang, Z. L. Large-Scale Hexagonal-Patterned Growth of Aligned ZnO Nanorods for Nano-Optoelectronics and Nanosensor Arrays. *Nano Lett.* **2004**, *4*, 423–426.
4. Reches, M.; Gazit, E. Casting Metal Nanowires within Discrete Self-Assembled Peptide Nanotubes. *Science* **2003**, *300*, 625–627.
5. Zhang, L.; Li, N.; Gao, F.; Hou, L.; Xu, Z. Insulin Amyloid Fibrils: An Excellent Platform for Controlled Synthesis of Ultrathin Superlong Platinum Nanowires with High Electrocatalytic Activity. *J. Am. Chem. Soc.* **2012**, *134*, 11326–11329.
6. Huang, Z.; Pu, F.; Hu, D.; Wang, C.; Ren, J.; Qu, X. Site-Specific DNA-Programmed Growth of Fluorescent and Functional Silver Nanoclusters. *Chem.—Eur. J.* **2011**, *17*, 3774–3780.
7. Zhao, X.; Pan, F.; Xu, H.; Yaseen, M.; Shan, H.; Hauser, C. A. E.; Zhang, S.; Lu, J. R. Molecular Self-Assembly and Applications of Designer Peptide Amphiphiles. *Chem. Soc. Rev.* **2010**, *39*, 3480–3498.
8. Woolfson, D. N.; Mahmoud, Z. N. More Than Just Bare Scaffolds: Towards Multi-Component and Decorated Fibrous Biomaterials. *Chem. Soc. Rev.* **2010**, *39*, 3464–3479.
9. Pu, F.; Liu, X.; Xu, B.; Ren, J.; Qu, X. Miniaturization of Metal–Biomolecule Frameworks Based on Stereoselective Self-Assembly and Potential Application in Water Treatment and as Antibacterial Agents. *Chem.—Eur. J.* **2012**, *18*, 4322–4328.
10. Rubio-Martínez, M.; Puigmartí-Luis, J.; Imaz, I.; Dittrich, P. S.; Maspoch, D. "Dual-Template" Synthesis of One-Dimensional Conductive Nanoparticle Superstructures from Coordination Metal–Peptide Polymer Crystals. *Small* **2013**, 10.1002/smll.201301338.
11. Kitagawa, S.; Kitaura, R.; Noro, S.-i. Functional Porous Coordination Polymers. *Angew. Chem., Int. Ed.* **2004**, *43*, 2334–2375.
12. Yaghi, O. M.; O'Keeffe, M.; Ockwig, N. W.; Chae, H. K.; Eddaoudi, M.; Kim, J. Reticular Synthesis and the Design of New Materials. *Nature* **2003**, *423*, 705–714.
13. Narayan, T. C.; Miyakai, T.; Seki, Sh.; Dincă, M. Tetrathiafulvalene-Based Microporous Metal–Organic Framework. *J. Am. Chem. Soc.* **2012**, *134*, 12932–12935.
14. Deng, H.; Grunder, S.; Cordova, K. E.; Valente, C.; Furukawa, H.; Hmadeh, M.; Gándara, F.; Whalley, A. C.; Liu, Z.; Asahina, S.; et al. Large-Pore Apertures in a Series of Metal–Organic Frameworks. *Science* **2012**, *336*, 1018–1023.
15. Ameloot, R.; Roeffaers, M. B. J.; De Cremer, G.; Vermoortele, F.; Hofkens, J.; Sels, B. F.; De Vos, D. E. Metal–Organic Framework Single Crystals as Photoactive Matrices for the Generation of Metallic Microstructures. *Adv. Mater.* **2011**, *23*, 1788–1791.
16. Wang, Z.; Cohen, S. M. Postsynthetic Covalent Modification of a Neutral Metal–Organic Framework. *J. Am. Chem. Soc.* **2007**, *129*, 12368–12369.
17. Wang, Z.; Cohen, S. M. Tandem Modification of Metal–Organic Frameworks by a Postsynthetic Approach. *Angew. Chem., Int. Ed.* **2008**, *47*, 4699–4702.
18. Tanabe, K. K.; Wang, Z.; Cohen, S. M. Systematic Functionalization of a Metal–Organic Framework *via* a Postsynthetic Modification Approach. *J. Am. Chem. Soc.* **2008**, *130*, 8508–8517.
19. Nguyen, J. G.; Cohen, S. M. Moisture-Resistant and Superhydrophobic Metal–Organic Frameworks Obtained *via* Postsynthetic Modification. *J. Am. Chem. Soc.* **2010**, *132*, 4560–4561.
20. Puigmarti-Luis, J.; Rubio-Martinez, M.; Hartfelder, U.; Imaz, I.; Maspoch, D.; Dittrich, P. S. Coordination Polymer Nanowires Generated by Microfluidic Synthesis. *J. Am. Chem. Soc.* **2011**, *133*, 4216–4219.
21. Furukawa, S.; Hirai, K.; Nakagawa, K.; Takashima, Y.; Matsuda, R.; Tsuruoka, T.; Kondo, M.; Haruki, R.; Tanaka, D.; Sakamoto, H.; *et al.* Heterogeneously Hybridized Porous Coordination Polymer Crystals: Fabrication of Heterometallic Core-Shell Single Crystals with an In-Plane Rotational Epitaxial Relationship. *Angew. Chem., Int. Ed.* **2009**, *48*, 1766–1770.
22. Hirai, K.; Furukawa, S.; Kondo, M.; Uehara, H.; Sakata, O.; Kitagawa, S. Sequential Functionalization of Porous Coordination Polymer Crystals. *Angew. Chem., Int. Ed.* **2011**, *50*, 8057–8061.
23. Falcaro, P.; Hill, A. J.; Nairn, K. M.; Jasieniak, J.; Mardel, J. I.; Bastow, T. J.; Mayo, S. C.; Gimona, D.; Gomez, H. J.; Whitfield, R.; *et al.* A New Method to Position and Functionalize Metal–Organic Framework Crystals. *Nat. Commun.* **2011**, *2*, 237 (8 pages).
24. Chen, X.; Zheng, G.; Cutler, J. I.; Jang, J.-W.; Mirkin, C. A. In-Wire Conversion of a Metal Nanorod Segment into an Organic Semiconductor. *Small* **2009**, *5*, 1527–1530.
25. Cvetković, B. Z.; Puigmartí-Luis, J.; Schaffhauser, D.; Ryll, T.; Schmid, S.; Dittrich, P. S. Confined Synthesis and Integration of Functional Materials in Sub-nanoliter Volumes. *ACS Nano* **2013**, *7*, 183–190.
26. Velikov, K. P.; Zegers, G. E.; van Blaaderen, A. Synthesis and Characterization of Large Colloidal Silver Particles. *Langmuir* **2003**, *19*, 1384–1389.
27. Sondi, I.; Goia, D. V.; Matijević, E. Preparation of Highly Concentrated Stable Dispersions of Uniform Silver Nanoparticles. *J. Colloid Interface Sci.* **2003**, *260*, 75–81.
28. Rodríguez-González, B.; Burrows, A.; Watanabe, M.; Kiely, C. J.; Liz Marzán, L. M. Multishell Bimetallic AuAg Nanoparticles: Synthesis, Structure and Optical Properties. *J. Mater. Chem.* **2005**, *15*, 1755–1759.
29. Ma, Y.; Li, W.; Cho, E. C.; Li, Z.; Yu, T.; Zeng, J.; Xie, Z.; Xia, Y. Au@Ag Core–Shell Nanocubes with Finely Tuned and

Well-Controlled Sizes, Shell Thicknesses, and Optical Properties. *ACS Nano* **2010**, *4*, 6725–6734.
30. O'Kane, A.; Clerac, R.; Zhao, H. H.; Ouyang, X.; Galan-Mascaros, J. R.; Heintz, R.; Dunbar, K. R. New Crystalline Polymers of Ag(TCNQ) and Ag(TCNQF4): Structures and Magnetic Properties. *J. Solid State Chem.* **2000**, *152*, 159–173.
31. Ren, L.; Fu, L.; Liu, Y.; Chen, S.; Liu, Z. Electrochemical Synthesis of High-Quality Ag(I)TCNQ Nanowires Using Carbon Nanotube Electrodes. *Adv. Mater.* **2009**, *21*, 4742–4746.
32. Xiao, K.; Tao, J.; Puretzky, A. A.; Ivanov, I. N.; Retterer, S. T.; Pennycook, S. J.; Geohegan, D. B. Selective Patterned Growth of Single-Crystal Ag−TCNQ Nanowires for Devices by Vapor−Solid Chemical Reaction. *Adv. Funct. Mater.* **2008**, *18*, 3043–3048.
33. Xiao, J.; Yin, Z.; Wu, Y.; Guo, J.; Cheng, Y.; Li, H.; Huang, Y.; Zhang, Q.; Ma, J.; Boey, F.; *et al*. Chemical Reaction between Ag Nanoparticles and TCNQ Microparticles in Aqueous Solution. *Small* **2011**, *7*, 1242–1246.
34. Xia, Y.; Whitesides, G. M. Soft Lithography. *Annu. Rev. Mater. Sci.* **1998**, *28*, 153–184.

Supporting Information for:

Localized, Stepwise Template Growth of Functional Nanowires from an Amino Acid-Supported Framework in a Microfluidic Chip

Josep Puigmartí-Luis,[†,] Marta Rubio-Martínez,[‡] Inhar Imaz,[‡] Benjamin Z. Cvetković,[§] Llibertat Abad,[⊥] Angel Pérez del Pino,[†] Daniel Maspoch,[‡,∥] David B. Amabilino[†,*]*

[†]Institut de Ciència de Materials de Barcelona (ICMAB-CSIC), Campus Universitari de Bellaterra, 08193 Bellaterra, Spain, [‡]ICN2—Institut Catala de Nanociencia i Nanotecnologia, Campus Universitari de Bellaterra, 08193 Bellaterra (Barcelona), Spain, [§]Laboratory for Waste Management, Department for Nuclear Energy and Safety Research, Paul Scherrer Institut, Villigen, Switzerland, [⊥]Institut de Microelectrònica de Barcelona, IMB-CNM (CSIC), Campus Universitari de Bellaterra, 08193 Bellaterra, Barcelona, Spain, and [∥]Institució Catalana de Recerca i Estudis Avançats (ICREA) 08100 Barcelona, Spain.

Figure S1. Photographs showing the sequential chemical event treatments in bulk experiments: (a) Ag(I)Cys CP on a glass cover slip; (b) Ag(I)Cys CP treated with ascorbic acid (reduced Ag(I)Cys CP); and (c) Ag(I)TCNQ formed from the oxidation of reduced Ag(I)Cys CP with a saturated TCNQ acetonitrile solution. The Ag(I)Cys CP was synthesized by the addition of an aqueous solution of $Ag(NO_3)$ (84 mg, 0.5 mmol) to an aqueous solution of Cys (60 mg, 0.5 mmol). (d) Powder X-ray Diffraction (PXRD) spectra of Ag(I)Cys (pink colour), reduced Ag(I)Cys (orange) in which the characteristic peak 2□ = 38.1 º corresponding to Ag(111) cubic phase is clearly observed, and Ag(I)TCNQ nanowires (blue), which matches with the previously reported tetragonal phase of Ag(I)TCNQ (black). Moreover, a PXRD spectra of reduced Ag(I)Cys at higher angles (from 2□ = 10º to 80º) is also shown to further confirm the formation of Ag(0) nanoparticules. The (+) indicates characteristic silver metal peak (Ag(0)), and the (*) points out peaks corresponding to pure TCNQ.

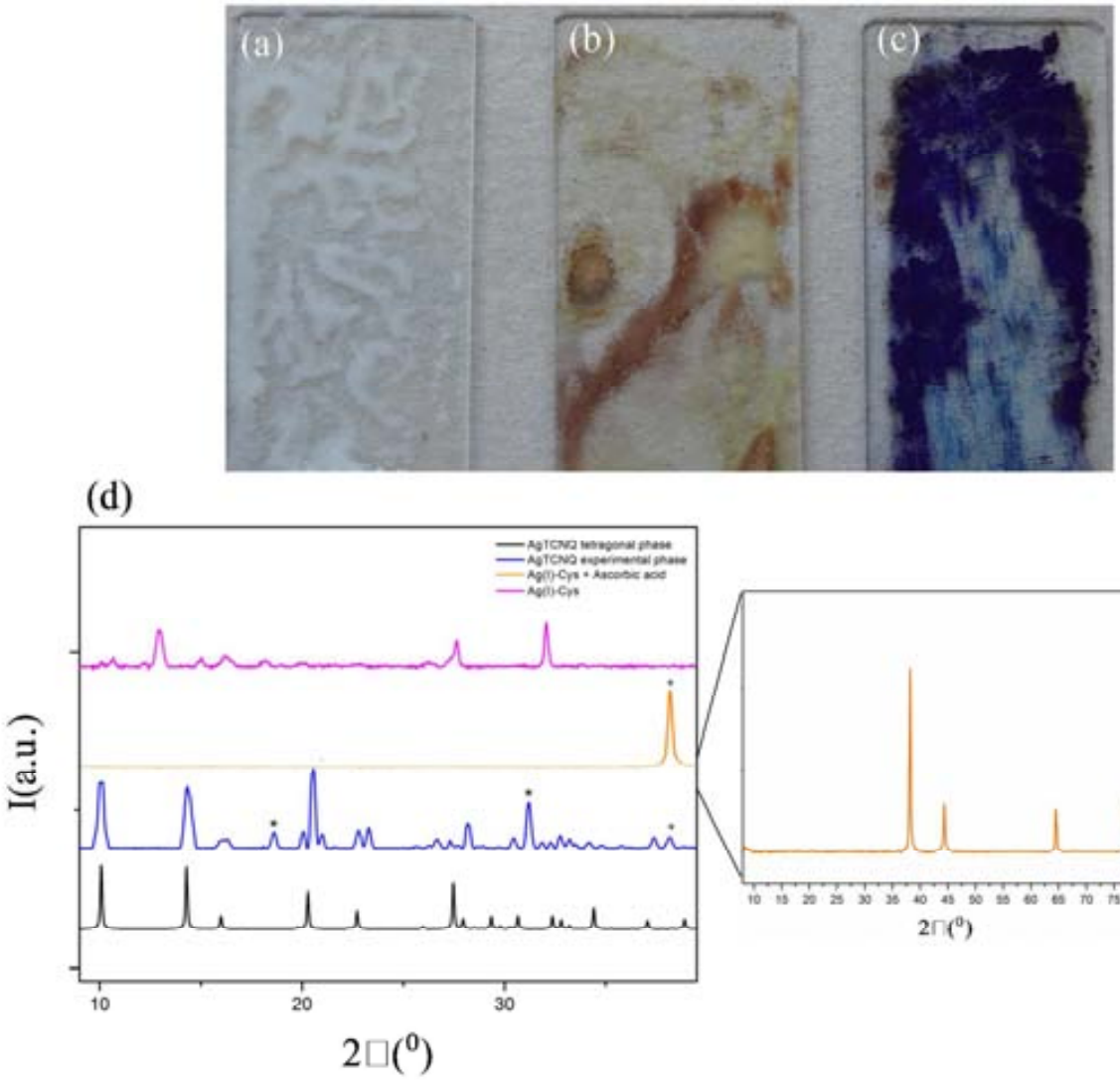
(a)
(b)
(c)
(d)
AgTCNQ tetragonal phase
AgTCNQ experimental phase
Ag(I)-Cys + Ascorbic acid
Ag(I)-Cys
I(a.u.)
10
20
30
2□(⁰)
10 15 20 25 30 35 40 45 50 55 60 65 70 75 80
2□(⁰)

3

Figure S2. Optical microscope image showing Ag(I)TCNQ nanowire bundles on a glass surface after releasing the clamp pressure. Notice that the square-shape valve designs are out of focus and that Ag(I)TCNQ nanowire bundles are in the focal plane on the glass substrate.

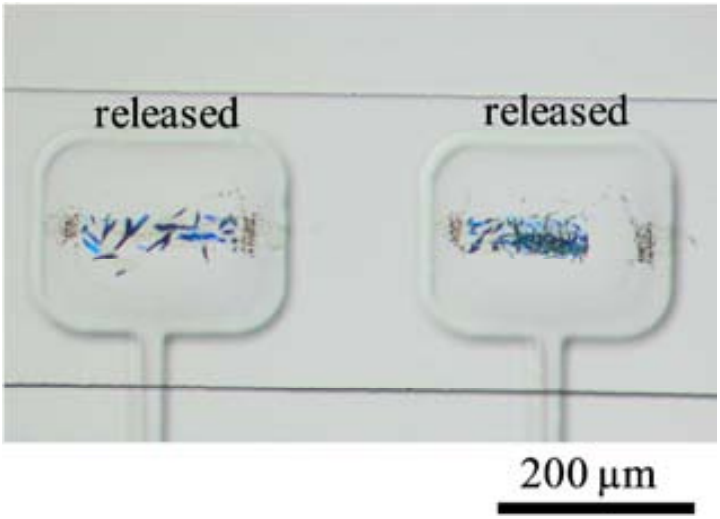

Figure S3. Polarized optical microscope image of Ag(I)TCNQ template crystal growth from Ag(I)Cys CP assembled with 1.0 mM precursor solutions.

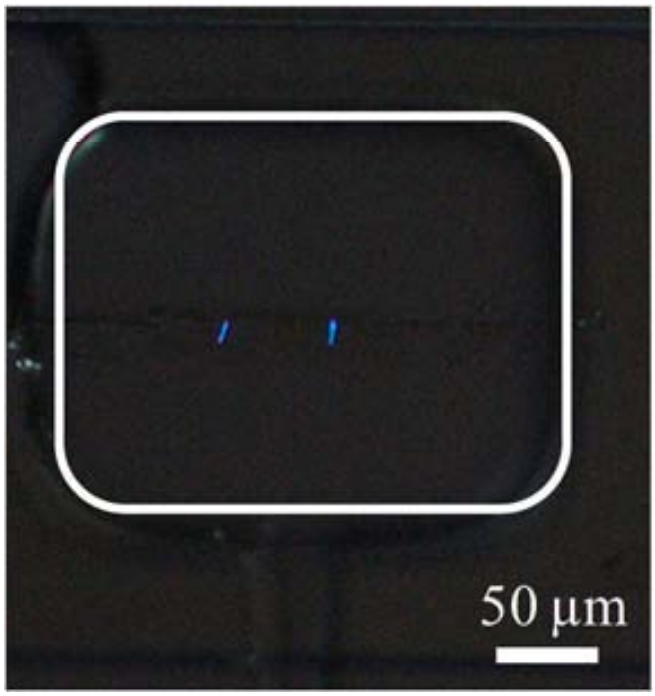

Figure S4. Optical microscope images showing: (a) trapped Ag(I)Cys CP, (b) reduced Ag(I)Cys CP, and from (c) to (f) a time-line study of Ag(I)TCNQ template crystal growth conducted under crossed polarizers. The concentration of both regent precursors ($Ag(NO_3)$ and Cys) was 1.0 mM in this study.

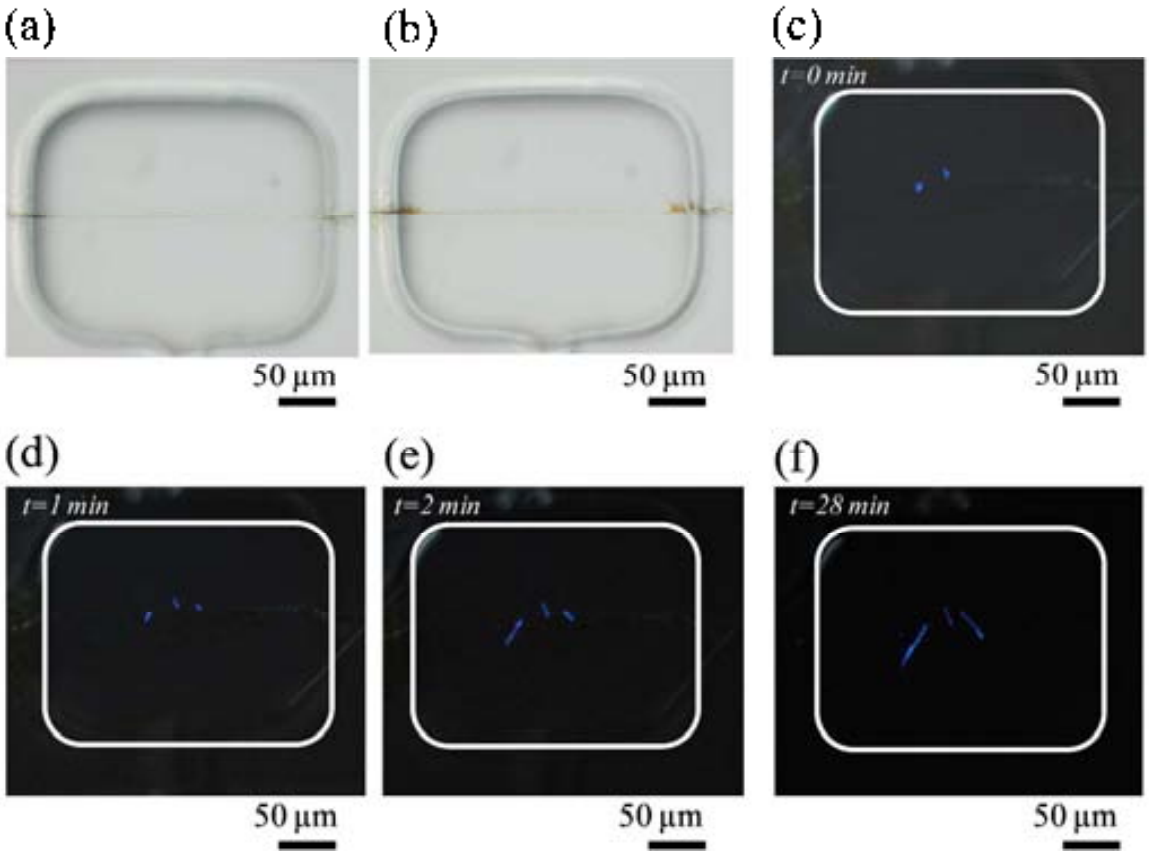

Figure S5. (a) Optical microscope image of Ag(I)TCNQ nanowire bundles trapped over an electrode array. (b) I-V sweeps measured on Ag(I)TCNQ nanowire bundles generated with this microfluidic-assisted template method. The I-V sweep reveals a nonlinear behavior which is expected for a semiconductor charge transfer complex (black curve). However, notice the hysteresis in the Ag(I)TCNQ current transport after applying a forward (black curve) and reverse (red curve) voltage sweep. A characteristic hysteresis current signal was acquired, therefore confirming the ON and OFF states of the Ag(I)TCNQ nanowire bundles. (c) Schematic illustration showing the set-up employed to perform CS AFM studies on trapped an integrated Ag(I)TCNQ nanowire bundles, and a 3D current map measured on top of one electrode area where conductive Ag(I)TCNQ nanowires can be identified clearly.

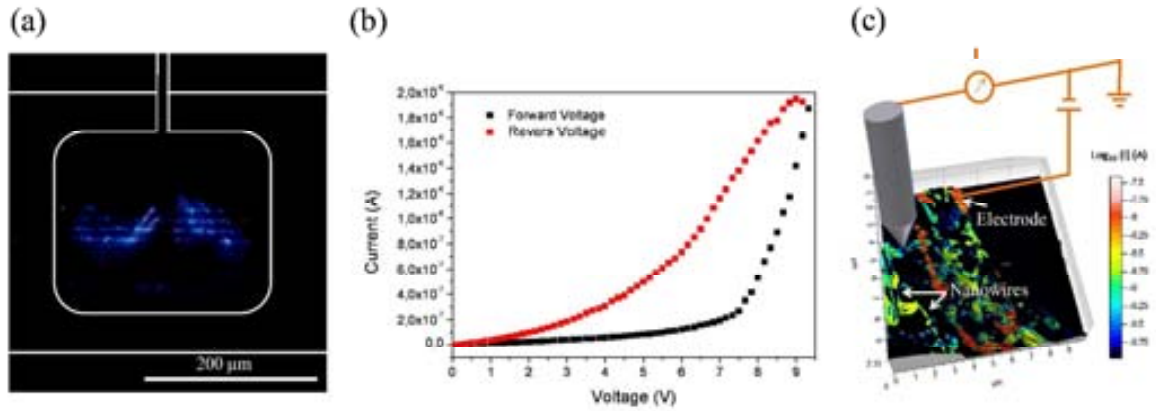

Chapter 6:

Metal-peptide Nanostructures as Dual Templates for Conductive Inorganic Superstructure Synthesis

In this Chapter, we show that 1D coordination polymer crystals, formed by metal ions and peptides afford a novel class of peptide-supported frameworks that can act as dual templates for the synthesis and assembly of two types of inorganic nanoparticles: one on their surface (crystal face) and the other within their internal structures leading to the formation of multifunctional superstructures. These results are included in the article: *"Dual-template" Synthesis of one-dimensional conductive nanoparticle superstructures from coordination metal-peptide polymer crystals*", Small 2013.

I. From biomineralization to controlled inorganic-organic hybrid nanostructures

"Biomineralization links soft organic tissues, which are compositionally akin to the atmosphere and oceans, with the hard materials of the solid Earth. It provides organisms with skeletons and shells while they are alive, and when they die these are deposited as sediment in environments from river plains to the deep ocean floor. It is also these hard, resistant products of life, which are mainly responsible for the Earth's fossil record. Consequently, biomineralization involves biologists, chemists, and geologists in interdisciplinary studies at one of the interfaces between Earth and life." [1]

Biomineralization is defined as the study of the formation, structure and properties of inorganic solids created in biological systems. In other words it refers to the processes by which organism form minerals. Living organisms use various strategies to create highly ordered and hierarchical mineral structures under physiologic conditions with temperatures and pressures much lower than those required to form the same mineralized structures by chemical synthesis.[2] The principle of biomineralization is based on the specific molecular interactions at inorganic-organic interfaces where nucleation, growth, morphology, and assembly of the inorganic crystals are regulated by an organic matrix. Electrostatic binding or association, metal-coordination, geometric matching (epitaxis) and stereochemical correspondence play a crucial role in these recognition and controlled growth processes.[3]

From an historic point of view, microbial stromalites can be considered as the first evidence of biomineralization processes that occured 3500 billion years ago.[4] They consist of layered calcium carbonates sedimentary structures created by the trapping, binding and cementation of sedimentary grains by biofilms of microorganisms. Millions of years later, there are more than 60 different biologically produced minerals.[5] Weiner *et al.* classified the names and corresponding chemical compositions of minerals produced by organisms (table 1).[6]

Table 6.1. The chemical compositions and names of minerals produced by biologically induced and controlled mineralization processes.

Name	Mineral
Carbonates	Calcite, Mg-calcite, Aragonite, Vaterite, Monohydrocalcite, Protodolomite, Hydrocerussite, Amorphous Calcium Carbonate
Phosphates	Octacalcium phosphate, Brushite, Francolite, dahllite, Whitlockkite, Struvite, Vivianite, Amorphous calcium phosphate, Amorphous calcium pyrophosphate
Sulfates	Gypsum, Barite, Celestite, Jarosite
Sulfides	Pyrite, Hydrotoilite, Sphalerite, Galena, Greigite, Mackninawite, Amorphous Pyrrhotute, Acanthite
Arsenates	Orpiment
Hydrated Silica	Amorphous Silica
Chlorides	Atacamite
Fluorides	Fluorite, Hieratite
Metals	Sulfur
Oxides	Magnetite, Amorphous Ilmenite, Amorphous Iron oxide, Amorphous Manganese oxide
Hydroxides	Goethite, Lepidocrocite, Ferrihydrite, Todorokite, Birnessite
Organic crystals	Earlandite, Whewellite, Weddelite, Glushinskite, Manganese Oxalate, Sodium urte, Uric acid, Ca-tartrate, Ca-malate, Paraffin Hydrocarbon, Guanine

Among biominerals, those created by molluscs are undoubtedly one of the most illustrative examples of hybrid natural-inorganic systems. Molluscs use a highly cross-linked protein layer (periostracum) as well as their epithelial cells of the mantle to produce shells or nacres that contain a single calcium carbonate crystalline phase (see Figure 6.1.a).[7] They elaborate a matrix comprising various macromolecules where the minerals are formed. The major components of this matrix are polysaccharide b-chitin, a relatively hydrophobic silk protein, and a complex assemblage of hydrophilic proteins, many of which are unusually rich in aspartic acid. The final stage of the process is the formation of the mineral itself within the matrix. The mineral found in mature mollusc shells is most often aragonite, sometimes calcite or the same shell may have layers of calcite and layers of aragonite. Beyond the archetypal case of molluscs other examples have been described in the literature. For example, Magnetotactic bacteria produce Fe_3O_4 or Fe_3S_4 nanoparticles with well-defined sizes and shapes to recognize magnetic fields for alignment and migration (see Figure 6.1.b).[8]

Furthermore some marine sponges produce silica spicules possessing light-guiding characteristics with lengths of up to 3 m (see Figure 6.1.c).[9]

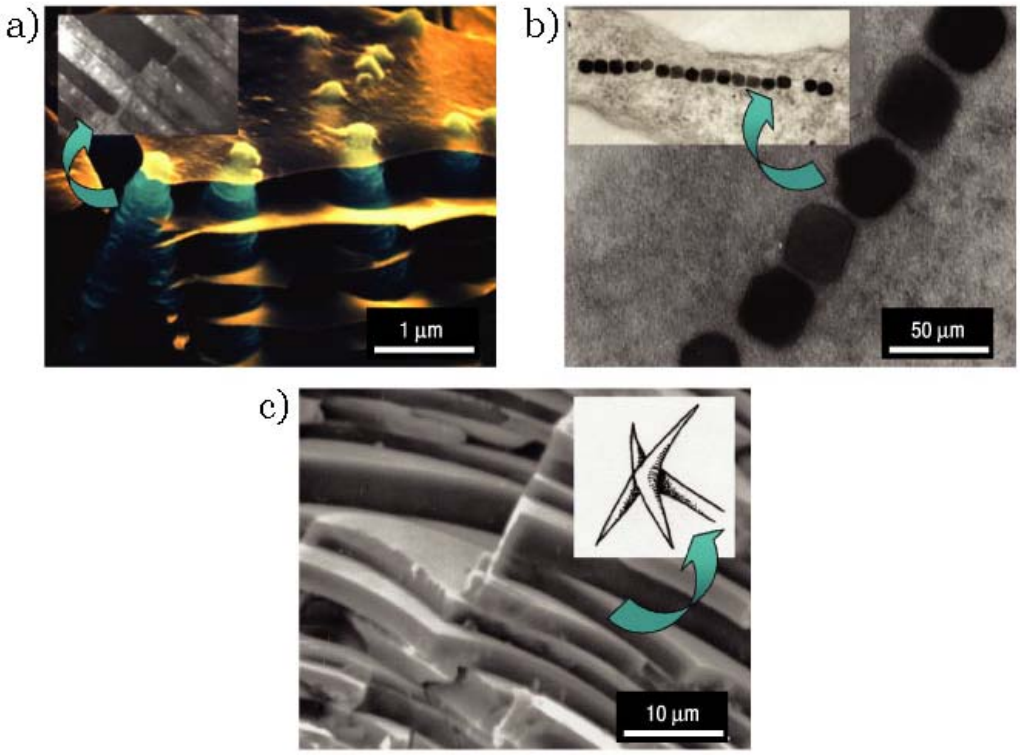

Figure 6.1. a) SEM image of a growth edge of abalone shell, a sea snail i.e. a marine molluscs (*Haliotis rufescens*) displaying aragonite platelets (blue) separated by an organic film (orange) that eventually becomes nacre (mother-of-pearl). b) TEM image of magnetite nanoparticles formed by a magnetotactic bacterium (*Aquaspirillum magnetotacticum*) c) SEM image of the sponge spicule of Rosella a marine sponge that has layered silica with excellent optical and mechanical properties. Figure adapted from ref 9.

All these examples illustrate that the intrinsic structure and compositions of biomolecules play a critical role in the formation of inorganic nanostructures within organisms. Different examples suggest that coordination environments in the mineral phase are simulated by metal-ion binding to appropriate ligands exposed at the organic surface: For instance, carbonate and phosphate biominerals are often associated with carboxylate-rich (aspartate and glutamate) and phosphorylated proteins respectively. Recently, Sommerdijk and co-workers found experimental evidence of the close interaction between metal ions and biomolecules visualizing the prenucleation clusters of $CaCO_3$ employing a model system based on cryogenic TEM (cryoTEM).[10] They showed that the formation of apatite crystals from simulated body fluid (SBF) at physiological temperature in the presence of an arachidic acid monolayer proceeds through a multistage process that involves the formation and aggregation of prenucleation clusters (see Figure 6.2).

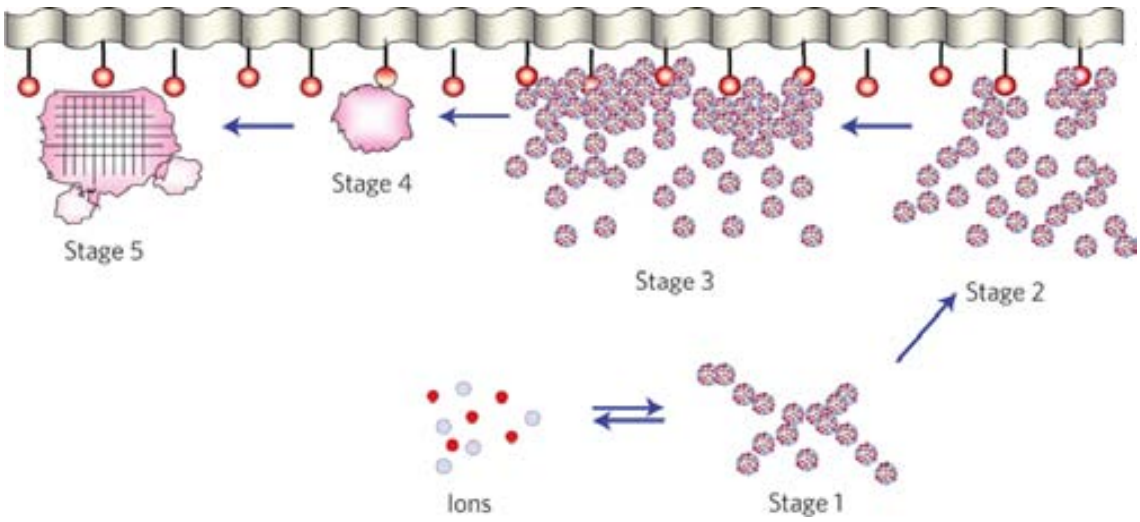

Figure 6.2. Schematic representation of the different stages of surface-directed mineralization of calcium phosphate from simulated body fluid (SBF) at 37 °C. Stage 1: the prenucleation clusters present in the SBF. Stage 2: parts of the cluster aggregates that are in contact with the organic films start to densify by adapting a closer packing of the clusters. Stage 3: the continuation of this densification process leads to defined domains of closely associated clusters with diameters of 50nm attached to the monolayer. Stage 4: these domains transform into dense spherical particles with diameters of 40-80nm. Stage 5: after 12h, these particles have developed into spherical crystals with an average diameter of 120nm. Figure adapted from ref 10.

Inspired by these natural phenomena many research groups have tried to establish a biomimetic approach to develop new strategies in the controlled synthesis of inorganic nanophases.[11] Thus, during the past decades, many inorganic crystals or hybrid inorganic/organic materials with special sizes, shapes, organizations, complex forms and hierarchies have been synthesized with the assistance of various templates, such as synthetic polymers, self-assembled peptides and proteins.[3] In this context the work done by Stephen Mann and his group deserves a special mention. They published several groundbreaking works, reporting, among other examples, for the first time the synthesis and assembly of mesostructured silica with lipid helicoids and TMV liquid crystals (see Figure 6.3.a.),[12] the DNA-driven self-assembly of gold nanorods (see Figure 6.3.b.),[13] or the synthesis of metallic nanowires arrays within cross-linked protein crystals (see Figure 6.3.c.).[14] One of their most interesting examples is the use of TMV hollow cylinders as a biotemplates for the controlled formation and organization of Pt, Au or Ag nanoparticles (see Figure 6.3.d.).[15] For Pt and Au metal ions the mechanism was based on the chemical reduction of $[PtCl6]^{2-}$ or $[AuCl4]^{-}$ complexes at acidic pH leading to the decoration of the external surface of the TMV rods with metallic nanoparticles less than 10 nm in size. In contrast for Ag, the photochemical reduction of Ag(I) salts at pH 7 resulted in nucleation and constrained growth of discrete Ag nanoparticles aligned within the 4 nm-wide internal channel. Another recent example, reported by Sleiman *et al.* is the synthesis of DNA nanotubes with different longitudinal

variations intercalating two different sizes of DNA triangles along the tube length.[16] The interlinkage of the different sized triangles in the presence of Au nanoparticles leads to the formation of a three duplex hybrid DNA strands. These nanotubes can be opened when specific DNA strands are added to release the gold nanoparticles cargo spontaneously.

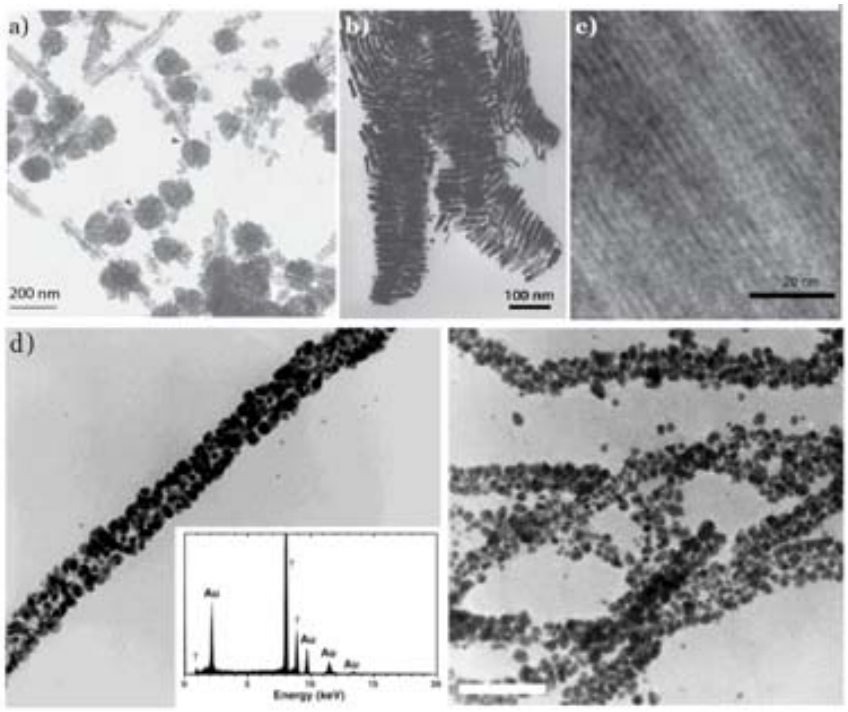

Figure 6.3. TEM images of a) silica-TMV nanoparticles showing radially patterned interiors, along with thread-like co-aligned mesostructures.[12] b) bundles of DNA-linked gold nanorods.[13] c) dense metallic nanofilaments of chemically reduced Au-containing cross-linked lysozyme crystals.[14] d) TEM image of gold nanoparticles produced in the presence of TMV with the corresponding EDXA spectrum showing the presence of gold and copper.[15]

In literature numerous other examples can been found, like the biomineralization of cage-like proteins[17] ,spherical viruses[18] or biomolecules, such as oligonucleotides[19] as well as the use of antibodies[20] to interconnect metallic/semiconductor nanoparticles in solution or to position nanoparticles on solid surfaces.[21]

II. Peptide-based scaffolds for the assembly of inorganic nanoparticles

As we have discussed in the first section of this chapter, living organism produce nanostructured materials. In most of these natural systems the peptide sequence plays a capital role in controlling the biomineralization of inorganic structures: Organisms use the interactions between peptides moieties and inorganic species to create ordered composites. Inspired by these natural systems and mechanisms, scientists isolated and extracted natural peptides, which have been identified as source of biomineralization in living organisms, and used them to synthesize new inorganic materials.[22,23] As detailed in the first chapter of this PhD Thesis, peptides are polymeric biomolecules made of amino acids. Peptides undergo distinctive sequence-specific self-assembly and have recognition properties, which makes them perfect candidates for directing the growth and assembly of inorganic nanostructures. To create these special inorganic nanostructures, three principal strategies have been used: (i) the peptides based growth of nanoparticles or peptide-based biomineralization, (ii) peptide based scaffolds for the assembly of inorganic nanoparticles and (iii) the mixed simultaneous biomineralization and assembly of inorganic nanoparticles.

II.1. Peptide-based biomineralization

A large number of peptide-based methods have been used to control the growth of inorganic nanostructures or biomineralization processes. For example Valiyaveettil *et al.* studied the *in vitro* mineralization of the peptide pelovaterin, extracted from eggshells of pelodiscus sinensis (Chinese soft-shelled turtle).[24] It is a glycine rich peptide with 42 amino acid residues and 3 disulfide bonds. They demonstrated that this peptide directs the formation of a metastable vaterite phase. With a peptide concentration of 5–100 μg mL^{-1}, floret-shaped crystals are formed, while spherical particles (25–30 μm) of vaterite were observed exclusively at higher peptide concentrations (≥ 0.5 mg mL^{-1}). The diameter of the spheres decreased significantly and some spheres fused together to form larger aggregates when the peptide concentration was further increased.

Beyond natural peptides that induce biomineralization processes, artificial peptides can be also envisaged. Indeed, one of the limitations of the use natural peptides is the

restricted diversity in the biomineralization process. Some peptides are generally specific for controlling the nucleation of some inorganic materials such as calcium carbonate, silica and iron oxide but there are many others useful inorganic compositions such as platinum, silver and cadmium sulphide that do not exist in biological systems. One approach to obtain these peptides is to use a combinatorial libraries (phage display or cell surface display) in order to develop new peptides that exhibit sequence-specific affinities for unnatural inorganic materials.[25] The approach is based on the introduction of DNA fragments with random sequences into certain genes within phage genomes or bacterial plasmids. These sequences code for the expression of particular peptide sequences on the surface of the phage or bacterium. Millions of different phages or cells, each with different peptides on their surfaces, are exposed to specific inorganic materials. Stringency washes are used to remove phages or cells from the inorganic surface. In order to choose the sequences favourable to interact to inorganic materials, those phage or cells lacking surface peptides that strongly interact with the inorganic material are removed. To perform a laboratory analysis (phage display), the eluted i.e. interacting phages are multiplied in a bacterial host. Similarly, the eluted cells are cultured for cell-surface display. Those phages or cells are then re-exposed to the inorganic material. This cycle is repeated with successively more rigorous washes until only phages or cells having surface peptides with very high affinities to the specific inorganic material remain. The peptide sequences are determined by decoding the viral or bacterial genome. Using this approach, Adschiri and co-workers isolated five peptides which have affinities for ZnO.[26] They immobilized ZnO particles on a gold-coated polypropylene plate and studied which peptide is selective in binding ZnO, but not ZnS or Eu_2O_3. They obtained that adding the GGGSC sequence to the carboxyl terminus of the peptide, the resultant peptide promoted the synthesis of flowerlike ZnO nanostructures at room temperature. This combinatorial library approach afforded new peptides with affinities with inorganic materials and used to create new inorganic structures such as Cu_2O,[27] GeO_2,[28] Fe_2O_3,[29] $CaCo_3$[30] among others.

Finally, beyond the natural and “pseudo-natural” approach (genetic engineering) where the design is quite limited and controlled by the living organism (virus, phage) researchers have also tried to rationalize the synthesis of peptides and to adapt them to the synthesis inorganic nanostructures. For example, Naik and co-workers designed and used the peptide AYSSGAPPMPPF to understand the role of the peptide in the formation of discrete gold nanoparticles.[31] They studied which key amino acid residues within the peptide sequence mediate the formation of gold nanoparticles (see Figure 6.4.). They found that an alanine-substituted peptide (AYSSGAPPAPPF) exhibited the highest affinity for gold, while a proline-substituted peptide (AY**PP**GAPPMPPF) showed almost no affinity. Other peptides,

including ASSSGAPPMPPF, A**M**SSGAPPYPPF, and PSPGSAYAPFPM, all displayed moderate-binding affinities. On the basis of their observations, they concluded that the hydroxy groups present on the serine and tyrosine residues were likely required for these peptides to have strong binding affinities to the surfaces of the gold nanoparticles.

Au-peptide NP	Sequence	Au NP binding (%)*	Absorbance (nm)	TEM Au NP size (nm)	CPS Au NP† size (nm)
A3	AYSSGAPPMPPF	-‡	523	12.8 ± 2.9	8.6 ± 0.8
A3-S	A**S**SSGAPPMPPF	NA	NA	NA	NA
A3-X	A**M**SSGAPP**Y**PPF	9.6 ± 3.5	521	12.9 ± 2.8	8.4 ± 1.0
A3-A	AYSSGAPP**A**PPF	16.1 ± 3.8	527	8.3 ± 3.6	12.6 ± 1.9
A3-P	AY**PP**GAPPMPPF	1.6 ± 1.0	522	9.1 ± 6.4	20.4 ± 5.1
A3-W	PSPGSAYAPFPM	9.9 ± 3.9	538	13.6 ± 3.1	18.9 ± 3.3

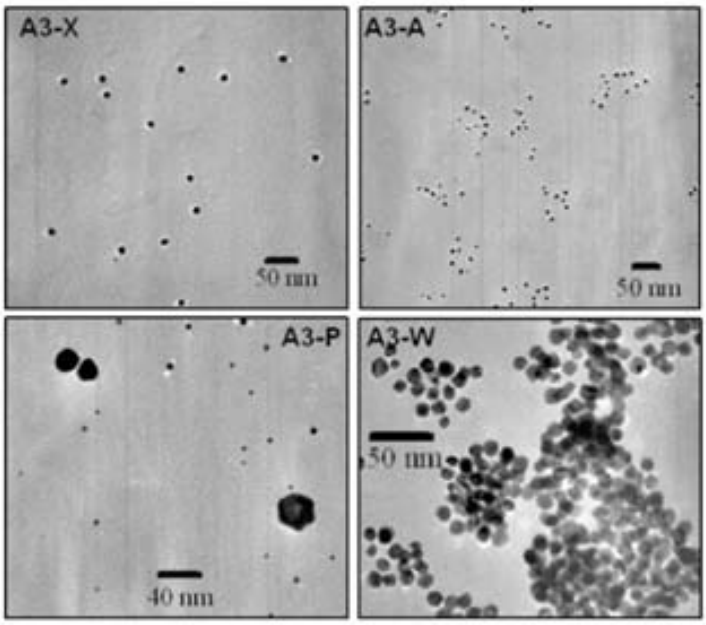

Figure 6.4. Experimental table with the 6 different modified peptides with the corresponding TEM images showing the formation of gold nanoparticles using modified peptides. (NA, not applicable). Image adapted from ref.[31]

II.2. Peptide-based scaffolds

The specific self-assembly and recognition capabilities of peptides can also be used to direct to growth and assembly of nanoparticle superstructures by using them as scafolds.[23,32] Many inorganic nanoparticle superstructures in form of spheres, chains or helices have built using (i) pure or (ii) conjugate peptides in this way:

II.2a. Pure peptides

Pure peptides have many different types of functional groups that can interact with nanoparticles. The critical key to control these assemblies is to define the nature of this interaction: that can be electrostatic interaction, metal-coordination or peptide folding.

In general, many colloidal inorganic nanoparticles present negative superficial charges. In order to associate nanoparticles and peptides, positively charged peptides have been designed and synthesized. For example, Pochan *et al.* constructed chains of gold nanoparticles using this approach (see Figure 6.5).[34] They used the polypeptide 17H6 with regularly spaced positively charged histidine patches along the fiber axis, which then was mixed with negatively charged gold nanoparticles. As a result, the nanoparticles were immobilized in a regular arrangement on the fibril template though electrostatic interactions. Using the same approach Wang et al. protonated at acidic pH the RGYFWAGDYNYF peptides that tends to self-assemble in nanofibers, and mixed it with 3.6 nm gold nanoparticles in solutions. The nanoparticles attached to the peptide fibers forming double-helical arrays. If the same reaction is performed at basic pH at which the peptide is not protonated, this self-assembly is not observed confirming the electrostatic nature of this association.

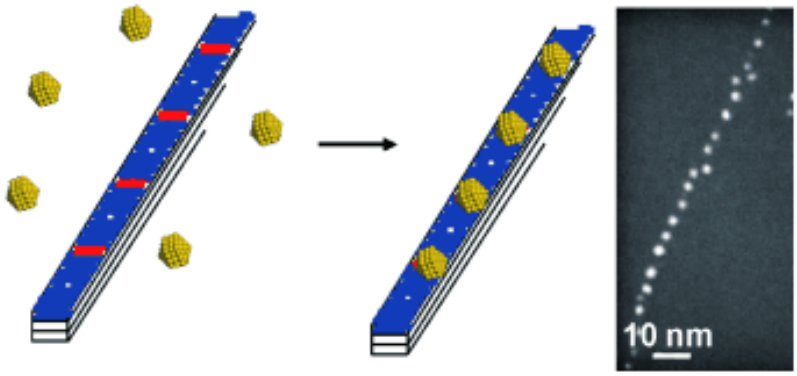

Figure 6.5. Mechanism for electrostatic assemble of negatively charged gold nanoparticles on positively charged histidine patches in 17H6 fibrils and TEM image showing controlled axial nanoparticle positioning. Figure adapted from ref.[34]

II.2b. Conjugated peptides

One very successful strategy to tailor the self-assembly properties of peptides is modifying them by attaching molecules to their structure thereby adding new functional groups. For instance, the use of peptide amphiphiles is a useful strategy for obtaining nanoparticle superstructures with complex shapes and various nanoparticle compositions. Stupp and co-workers reported the use of peptide-amphiphile (PA) nanofibers displaying S(P)RGD peptide sequences (S(P)=phosphoserine) on their exterior as templates for the mineralization of cadmium sulphide (CdS) nanocrystals.[35] Metal salts are directly added to the suspensions of the peptide at different ratios and exposed to hydrogen sulfide gas (H_2S). The metal cations, which bound to the peptide, served as nucleation sites for the mineralization of nanoparticles onto the fibers. At low Cd:PA ratios, 1D nanoparticle arrays nucleate and decorate the PA fibers with individual CdS nanocrystals of 3-5 nm. In some cases, gaps of 2-3 nm between two rows of CdS nanoparticles were observed and correspond approximately to the dimensions of the hydrophobic core of the fibre. When they increased the Cd:PA ratio, the PA fibers were completely encapsulated by a continuous polycrystalline coating of 5-7 nm semiconductor CdS grains. In this method the binding affinity between the peptide and the metal ion is the key factor in promoting the synthesis and assembly of the nanoparticles.

II.2c. Combined biomineralization and self-assembly

Recently it was demonstrated that, in some cases peptide-based structures can combine the biomineralization and the self- assembly process. Various complex multistep syntheses have been explored in order to create in situ nanoparticles assemblies. Very recently, and in parallel with the work presented in this chapter, Rosi and co-workers developed a peptide-based methodology where these two processes occur simultaneously.[36] This method relies on the use of peptide conjugates to direct the synthesis and assembly of the nanoparticles in a one-pot reaction. They selected a water-soluble peptide AYSSGAPPMPPF (PEP), which is able to mineralize chloroauric acid and functionalized the amino terminus of the peptide with a hydrophobic aliphatic C_{12} tail creating an amphiphile peptide. This C_{12}-PEP in the presence of a HEPES buffer and chloroauric acid directs the formation and assembly of 1D left-handed gold nanoparticle double helices with an excellent local order (see Figure 6.6).

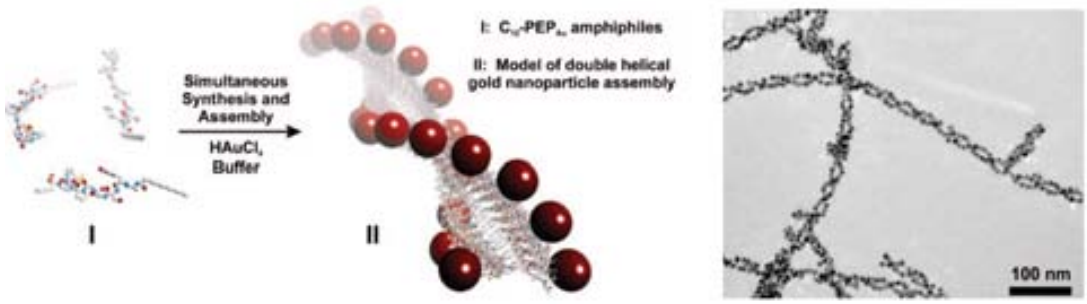

Figure 6.6. Schematic representation and TEM image of the formation of left-handed gold nanoparticle double helices combining the peptide self-assembly and the peptide-based biomineralization in one step. Figure adapted from ref.[36]

III. Our results: Metal-peptide templates for the synthesis of inorganic nanoparticle superstructures

The article presented in this chapter, "*'Dual-template' synthesis of one-dimensional conductive nanoparticle superstructures from coordination metal-peptide polymer crystals*", shows how we can take advantage from the metal-directed self-assembly of peptides and the ability of peptides to create inorganic nanoparticles based superstructures to create a novel class of peptide-supported frameworks that act as dual templates. It describes the coordination of metal ions Ag(I) and peptides (DLL, Aspartic-Leucine-Leucine) to form 1D coordination metal-peptide polymer crystals as well as the synthesis and assembly of different inorganic nanoparticles on their surface and within their internal structures.

In order to achieve this objective we designed a specific peptide sequence that allows using CPs as scaffolds. Three key criteria had to be fulfilled: Firstly (i), the peptide had to be able to bridge Ag(I) metal ions to form extended coordination networks. Therefore, two carboxylic groups were used at separate positions of the sequence (see Figure 6.7.a). Secondly, (ii) the peptide had to be able to direct the assembly of inorganic nanoparticles onto the crystals.[37,38] Considering that amino groups and leucine amino acids help form inorganic nanoparticle superstructures made from peptide scaffolds, we designed the tripeptide sequence DLL to increase the density of amino groups (one per repeating unit of -Ag(I)-DLL-) and leucine units (two per -Ag(I)-DLL-) in the extended coordination network (and consequently, on the crystal surface). And thirdly (iii), the prepared nanostructures had to be stable in water; therefore, we incorporated two consecutive leucine units into the

peptide sequence to confer the resulting crystals with hydrophobicity. Although the peptide was water soluble, it underwent a rapid coordination assembly upon reaction with $AgNO_3$ (diffusion of an ethanolic solution of $AgNO_3$ into an aqueous solution of DLL at pH 7 in the dark). The obtained fibers were characterized by Field-Emission SEM (FESEM) and the analysis revealed numerous rectangular, wire-like, belt-shaped Ag(I)-DLL sub-micrometre crystals, with typical lengths in the tens to hundreds of micrometers (see figure 6.7.b-d). XRPD confirmed the crystalline character of these belts (see Figure 2.d of the article) and energy dispersive X-ray (EDX) analysis confirmed the presence of silver within the assembled belts (see Figure S4 of the S.I. from the article). The infrared spectrum indicated that the two terminal carboxylate groups had coordinated to the Ag(I) ions (see Figure S5 of the Supporting Information of the article). These data together with the elemental analysis confirm that the ratio between Ag(I) ions and DLL is 2:1.

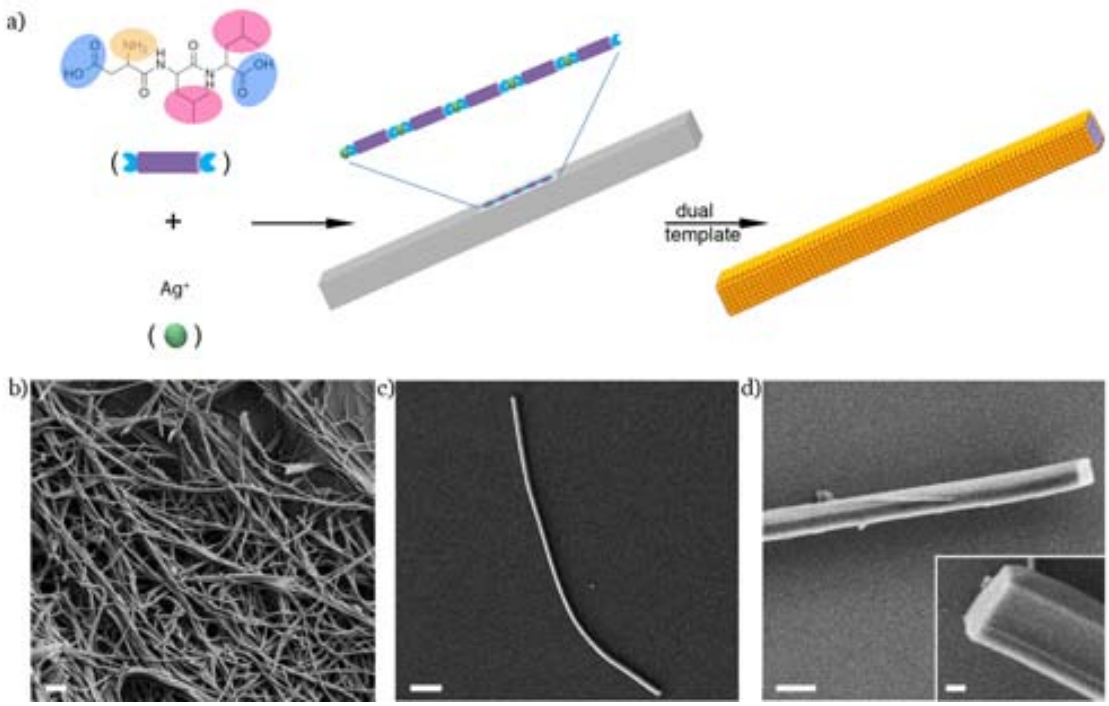

Figure 6.7. a) Schematic representation of the designed peptide DLL, highlighting the functional groups that participate in the linkage of Ag(I) ions to form the Ag(I)-DLL coordination belts and provide the characteristics to act as dual scaffolds for the formation of multicomponent self-assembled nanoparticle structures (blue, carboxylate groups; orange, amino group; pink, hydrophobic part of leucine amino acid). b-d) Representative FESEM images of the synthesised Ag(I)-DLL belts. inset d, Zoom on a terminal section of an Ag(I)-DLL belt, showing the rectangle-like cross-section of the belt. Scale bars: 500 nm (b-d) and 100 nm (inset d).

With these Ag-DLL belt-like crystals, we take advantage of the self-assembly and recognition capacities of peptides, and the selective reduction of metal ions to metal atoms, in order to grow and assemble inorganic nanoparticles along them. By modulating

experimental conditions such as temperature and pH (see Figure 6.8. (i) and (ii) respectively) precise control over the growth process can be achieved: firstly inside the structures themselves and then on their surfaces. To reduce the Ag(I) and form Ag nanoparticles along the entire length of the belt interior, the pristine belts were exposed to heat (see figure 6.8.c) At 250 °C, 1D assemblies comprising randomly positioned Ag nanoparticles were obtained along the belt (mean nanoparticle diameter as calculated by the Scherrer equation: 27 nm; see Figure S7 of the Supporting Information from the article).

In parallel, we synthesized Ag(I)-DLL belts coated with Ag_2O nanoparticles. A solution of DLL at pH 10.5 was mixed with a solution of $AgNO_3$ in water/ethanol (1:2) at pH 7.0, and the resulting black dispersion was left in the dark for 24 hours. Under these conditions, the Ag(I)-DLL assembly occurred and simultaneously acted as a template for the formation of Ag_2O nanoparticles yielding wire-like Ag_2O@Ag(I)-DLL superstructures. FESEM and TEM analysis of the Ag_2O@Ag(I)-DLL showed a uniform coating of Ag_2O nanoparticles (density: 700 particles/μm² mean nanoparticle diameter: 39 ± 11 nm). The XRPD patterns from the Ag_2O@Ag(I)-DLL superstructures further indicated that Ag_2O nanoparticles were formed and that the Ag(I)-DLL coordination network was preserved. This process can be attributed to the biomineralization process descried previously.

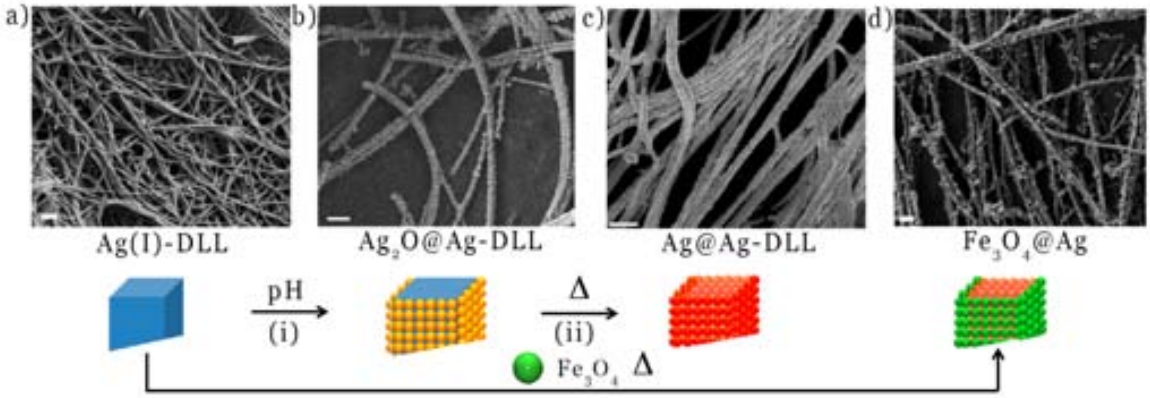

Figure 6.8. Schematic representation of the different metal-peptide templates covered with inorganic nanoparticles, representative FESEM images are shown. a) Ag(I)-DLL. b) Ag_2O@Ag-DLL. c) Ag@Ag- and d) Fe_3O_4@Ag-nanoparticle structures.

After coating the Ag(I)-DLL belts with Ag_2O nanoparticles, we then heated the Ag_2O@Ag(I)-DLL superstructures to different temperatures: 150 °C ,200 °C and 250 °C. At 150°C, the Ag_2O nanoparticles began to reduce to metallic Ag nanoparticles. This thermal reduction process could be seen in a XRPD analysis (see Figure 3c of the article): the XRPD patterns of the Ag_2O@Ag(I)-DLL superstructures heated to 150 °C and 200 °C lacked the characteristic peaks of Ag_2O nanoparticles, but included the peaks characteristic of fcc-Ag nanoparticles. After heating the Ag@Ag(I)-DLL superstructures further, to 250 °C, we

observed by SEM and XRPD the expected confined thermal reduction of the Ag(I) ions that comprise the internal Ag(I)-DLL coordination network into closely packed Ag nanoparticles Ag@Ag-nanoparticle superstructures.

Our results up to this point prompted us to investigate whether we could exploit the external nanoparticle assembly and the internal nanoparticle formation to design and construct multicomponent, and therefore multifunctional, self-assembled nanoparticle structures. To test this, the Ag(I)-DLL belts were coated with magnetic Fe_3O_4 nanoparticles by submerging them into an aqueous dispersion of Fe_3O_4nanoparticles for 1 h. The resulting brown Fe_3O_4@Ag(I)-DLL structures were separated out by gravity decantation, and then redispersed in water. Characterization by FESEM, TEM and XRPD revealed that the belts were indeed partially coated with Fe_3O_4 nanoparticles (density: ~350 particle/μm^2; mean nanoparticle diameter: 35 ± 9 nm; see Figure 5a and 5d of the article). Interestingly, the resulting Fe_3O_4@Ag(I)-DLL structures incorporated the magnetic properties of the nanoparticles, as demonstrated by the fact they could be easily guided by a magnet (Figure 6.9.a).

Following the dual-template strategy, the Fe_3O_4@Ag(I)-DLL structures were then heated to 250 ºC to induce thermal reduction of the internal Ag(I) ions. This afforded wire-like self-assembled Fe_3O_4@Ag-nanoparticle structures (Figure 5e of the article). The XRPD pattern showed the characteristic peaks of fcc-Ag and Fe_3O_4, and lacked those corresponding to the Ag(I)-DLL. Additionally, EDX analysis performed on a single Fe_3O_4@Ag-nanoparticle assembly confirmed the presence of both metallic silver and metallic iron (Figure S9 of the article).

We then decided to ascertain the magnetism of the Fe_3O_4@Ag-nanoparticle assemblies. These were first redispersed in an aqueous solution, and then attracted by a magnet (Figure 6.9). As shown in the images, the templated internal Ag nanoparticles are well confined and closely packed, conditions that favour electrical conductivity in these superstructures. To test this we assessed their electronic transport properties by randomly placing Ag_2O@Ag(I)-DLL structures over platinum patterned electrodes, and then heating them from 100 ºC to 250 ºC. Indeed, measurements of the electronic transport properties of both Ag@Ag-nanoparticle and Fe_3O_4@Ag-nanoparticle superstructures confirmed that they are conductive.

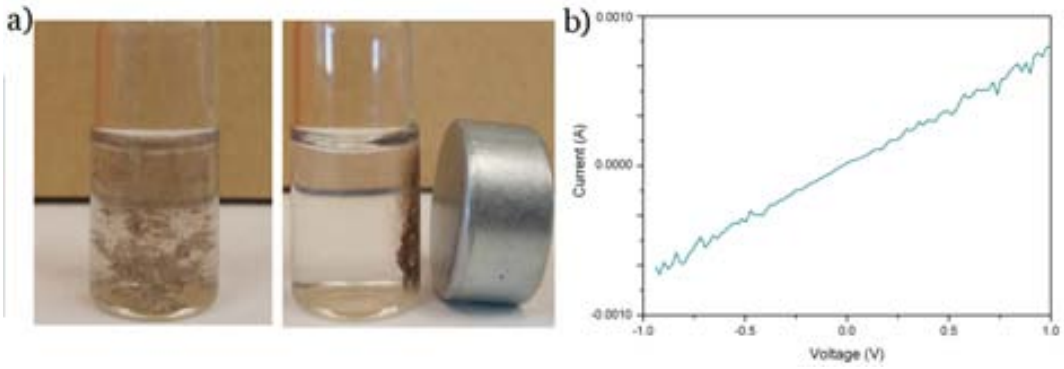

Figure 6.9. a) Photographs showing the attraction of Fe_3O_4@Ag(I)-DLL structures in an aqueous solution to a magnet at room temperature (left, absence of magnet; right, presence of magnet). b) *I-V* sweep (average of 20 measurements) of Fe_3O_4@Ag-nanoparticle structures.

To conclude, we synthesized a novel class of peptide-supported frameworks that can act as dual templates enabling the synthesis of different inorganic nanoparticles on their surface as well as within their internal structures. As proof-of-concept, this dual-templating approach allows the creation of very long (> 100 μm) self-assembled Ag@Ag-nanoparticle superstructures and polymetallic multifunctional Fe_3O_4@Ag-nanoparticle composites combines the magnetic and conductive properties of the two-nanoparticle types.

IV. References

(1) Kristiansen, J. Leadbeater, B. S. C. & Riding, R. (eds). Biomineralization in Lower Plants and Animals. *Nord. J. Bot.* **1987**, *7*, 608–608.

(2) Skinner, H. C. W.; Jahren, A. H. Biomineralization. In *Treatise on Geochemistry*; Elsevier, 2007; pp. 1–69.

(3) Mann, S. Molecular Tectonics in Biomineralization and Biomimetic Materials Chemistry. *Nature* **1993**, *365*, 499–505.

(4) Allwood, A. C.; Walter, M. R.; Kamber, B. S.; Marshall, C. P.; Burch, I. W. Stromatolite Reef from the Early Archaean Era of Australia. *Nature* **2006**, *441*, 714–718.

(5) Sigel, A.; Sigel, H.; Sigel, R. K. O. *Biomineralization: From Nature to Application*; Chichester, West Sussex, England; Hoboken, NJ, 2008.

(6) Weiner, S. An Overview of Biomineralization Processes and the Problem of the Vital Effect. *Rev. Mineral. Geochem.* **2003**, *54*, 1–29.

(7) Mayer, G.; Sarikaya, M. Rigid Biological Composite Materials: Structural Examples for Biomimetic Design. *Exp. Mech.* **2002**, *42*, 395–403.

(8) Biomimetics: Design and Processing of Materials by Sarikaya, Mehmet & Ilhan A. Aksay: American Institute of Physics, Woodbury, New York, U.S.A. 9781563961960 Hardcover, First Edition - Aspen Book Shop http://www.abebooks.com/Biomimetics-Design-Processing-Materials-Sarikaya-Mehmet/8536731334/bd (accessed Mar 10, 2014).

(9) M. Sarikaya, H. F. Biomimetic Model of a Sponge-Spicular Optical Fiber—mechanical Properties and Structure. *J. Mater. Res.* **2001**, *16*, 1420 – 1428.

(10) Dey, A.; Bomans, P. H. H.; Müller, F. A.; Will, J.; Frederik, P. M.; de With, G.; Sommerdijk, N. A. J. M. The Role of Prenucleation Clusters in Surface-Induced Calcium Phosphate Crystallization. *Nat. Mater.* **2010**, *9*, 1010–1014.

(11) Mann, S.; Archibald, D. D.; Didymus, J. M.; Douglas, T.; Heywood, B. R.; Meldrum, F. C.; Reeves, N. J. Crystallization at Inorganic-Organic Interfaces: Biominerals and Biomimetic Synthesis. *Science* **1993**, *261*, 1286–1292.

(12) Fowler, C. E.; Shenton, W.; Stubbs, G.; Mann, S. Tobacco Mosaic Virus Liquid Crystals as Templates for the Interior Design of Silica Mesophases and Nanoparticles. *Adv. Mater.* **2001**, *13*, 1266.

(13) Dujardin, E.; Mann, S.; Hsin, L.-B.; Wang, C. R. C. DNA-Driven Self-Assembly of Gold Nanorods. *Chem. Commun.* **2001**, 1264–1265.

(14) Guli, M.; Lambert, E.; Li, M.; Mann, S. Template-Directed Synthesis of Nanoplasmonic Arrays by Intracrystalline Metalization of Cross-Linked Lysozyme Crystals. *Angew. Chem.* **2010**, *122*, 530–533.

(15) Dujardin, E.; Peet, C.; Stubbs, G.; Culver, J. N.; Mann, S. Organization of Metallic Nanoparticles Using Tobacco Mosaic Virus Templates. *Nano Lett.* **2003**, *3*, 413–417.
(16) Lo, P. K.; Karam, P.; Aldaye, F. A.; McLaughlin, C. K.; Hamblin, G. D.; Cosa, G.; Sleiman, H. F. Loading and Selective Release of Cargo in DNA Nanotubes with Longitudinal Variation. *Nat. Chem.* **2010**, *2*, 319–328.
(17) Meldrum, F. C.; Wade, V. J.; Nimmo, D. L.; Heywood, B. R.; Mann, S. Synthesis of Inorganic Nanophase Materials in Supramolecular Protein Cages. *Nature* **1991**, *349*, 684–687.
(18) Huang, Y.; Chiang, C.-Y.; Lee, S. K.; Gao, Y.; Hu, E. L.; Yoreo, J. D.; Belcher, A. M. Programmable Assembly of Nanoarchitectures Using Genetically Engineered Viruses. *Nano Lett.* **2005**, *5*, 1429–1434.
(19) Alivisatos, A. P.; Johnsson, K. P.; Peng, X.; Wilson, T. E.; Loweth, C. J.; Bruchez, M. P.; Schultz, P. G. Organization of "Nanocrystal Molecules" Using DNA. *Nature* **1996**, *382*, 609–611.
(20) Shenton, W.; Davis, S. A.; Mann, S. Directed Self-Assembly of Nanoparticles into Macroscopic Materials Using Antibody–Antigen Recognition. *Adv. Mater.* **1999**, *11*, 449–452.
(21) Willner, I.; Willner, B. Biomolecule-Based Nanomaterials and Nanostructures. *Nano Lett.* **2010**, *10*, 3805–3815.
(22) Dickerson, M. B.; Sandhage, K. H.; Naik, R. R. Protein- and Peptide-Directed Syntheses of Inorganic Materials. *Chem. Rev.* **2008**, *108*, 4935–4978.
(23) Chen, C.-L.; Rosi, N. L. Peptide-Based Methods for the Preparation of Nanostructured Inorganic Materials. *Angew. Chem. Int. Ed.* **2010**, *49*, 1924–1942.
(24) Lakshminarayanan, R.; Chi-Jin, E. O.; Loh, X. J.; Kini, R. M.; Valiyaveettil, S. Purification and Characterization of a Vaterite-Inducing Peptide, Pelovaterin, from the Eggshells of Pelodiscus Sinensis (Chinese Soft-Shelled Turtle). *Biomacromolecules* **2005**, *6*, 1429–1437.
(25) Sarikaya, M.; Tamerler, C.; Jen, A. K.-Y.; Schulten, K.; Baneyx, F. Molecular Biomimetics: Nanotechnology through Biology. *Nat. Mater.* **2003**, *2*, 577–585.
(26) Umetsu, M.; Mizuta, M.; Tsumoto, K.; Ohara, S.; Takami, S.; Watanabe, H.; Kumagai, I.; Adschiri, T. Bioassisted Room-Temperature Immobilization and Mineralization of Zinc Oxide—The Structural Ordering of ZnO Nanoparticles into a Flower-Type Morphology. *Adv. Mater.* **2005**, *17*, 2571–2575.
(27) Thai, C. K.; Dai, H.; Sastry, M. S. R.; Sarikaya, M.; Schwartz, D. T.; Baneyx, F. Identification and Characterization of Cu2O- and ZnO-Binding Polypeptides by Escherichia Coli Cell Surface Display: Toward an Understanding of Metal Oxide Binding. *Biotechnol. Bioeng.* **2004**, *87*, 129–137.

(28) Dickerson, M. B.; Naik, R. R.; Stone, M. O.; Cai, Y.; Sandhage, K. H. Identification of Peptides That Promote the Rapid Precipitation of Germania Nanoparticle Networks via Use of a Peptide Display Library. *Chem. Commun.* **2004**, 1776–1777.

(29) Brown, S. Engineered Iron Oxide-Adhesion Mutants of the Escherichia Coli Phage Lambda Receptor. *Proc. Natl. Acad. Sci. U. S. A.* **1992**, *89*, 8651–8655.

(30) Li, C.; Botsaris, G. D.; Kaplan, D. L. Selective in Vitro Effect of Peptides on Calcium Carbonate Crystallization. *Cryst. Growth Des.* **2002**, *2*, 387–393.

(31) Tomczak, M. M.; Slocik, J. M.; Stone, M. O.; Naik, R. R. Bio-Based Approaches to Inorganic Material Synthesis. *Biochem. Soc. Trans.* **2007**, *35*, 512–515.

(32) Ulijn, R. V.; Smith, A. M. Designing Peptide Based Nanomaterials. *Chem. Soc. Rev.* **2008**, *37*, 664–675.

(33) Reches, M.; Gazit, E. Casting Metal Nanowires Within Discrete Self-Assembled Peptide Nanotubes. *Science* **2003**, *300*, 625–627.

(34) Sharma, N.; Top, A.; Kiick, K. L.; Pochan, D. J. One-Dimensional Gold Nanoparticle Arrays by Electrostatically Directed Organization Using Polypeptide Self-Assembly. *Angew. Chem. Int. Ed.* **2009**, *48*, 7078–7082.

(35) Sone, E. D.; Stupp, S. I. Semiconductor-Encapsulated Peptide-Amphiphile Nanofibers. *J. Am. Chem. Soc.* **2004**, *126*, 12756–12757.

(36) Chen, C.-L.; Zhang, P.; Rosi, N. L. A New Peptide-Based Method for the Design and Synthesis of Nanoparticle Superstructures: Construction of Highly Ordered Gold Nanoparticle Double Helices. *J. Am. Chem. Soc.* **2008**, *130*, 13555–13557.

(37) Hwang, L.; Zhao, G.; Zhang, P.; Rosi, N. L. Size-Controlled Peptide-Directed Synthesis of Hollow Spherical Gold Nanoparticle Superstructures. *Small Weinh. Bergstr. Ger.* **2011**, *7*, 1938–1942.

(38) Lee, E.; Kim, D.-H.; Woo, Y.; Hur, H.-G.; Lim, Y. Solution Structure of Peptide AG4 Used to Form Silver Nanoparticles. *Biochem. Biophys. Res. Commun.* **2008**, *376*, 595–598.

Publication 5. ""Dual-template" Synthesis of one-dimensional conductive nanoparticle superstructures from coordination metal-peptide polymer crystals" M. Rubio-Martinez, J. Puigmartí-Luís, I. Imaz, Petra S. Dittrich, D. Maspoch, *Small* **2013**, 24, 4160-4167.

small

Nanoparticle Superstructures

"Dual-Template" Synthesis of One-Dimensional Conductive Nanoparticle Superstructures from Coordination Metal–Peptide Polymer Crystals

*Marta Rubio-Martínez, Josep Puigmartí-Luis, Inhar Imaz, Petra S. Dittrich, and Daniel Maspoch**

***B**ottom-up fabrication of self-assembled structures made of nanoparticles may lead to new materials, arrays and devices with great promise for myriad applications. Here a new class of metal–peptide scaffolds is reported: coordination polymer Ag(I)-DLL belt-like crystals, which enable the dual-template synthesis of more sophisticated nanoparticle superstructures. In these biorelated scaffolds, the self-assembly and recognition capacities of peptides and the selective reduction of Ag(I) ions to Ag are simultaneously exploited to control the growth and assembly of inorganic nanoparticles: first on their surfaces, and then inside the structures themselves. The templated internal Ag nanoparticles are well confined and closely packed, conditions that favour electrical conductivity in the superstructures. It is anticipated that these Ag(I)-DLL belts could be applied to create long (>100 μm) conductive Ag@Ag nanoparticle superstructures and polymetallic, multifunctional Fe_3O_4@Ag nanoparticle composites that marry the magnetic and conductive properties of the two nanoparticle types.*

1. Introduction

Self-assembled biomaterials are outstanding scaffolds for the controlled bottom-up fabrication of novel functional self-assembled nanoparticle structures and devices.[1–5] Examples include the synthesis of inorganic nanoparticles (e.g. iron sulphide, manganese, uranium-oxo, and iron oxide [magnetite] nanoparticles) in protein or virus-protein cages (e.g. ferritin and cowpea chlorotic mottle virus),[6–9] and the synthesis of inorganic nanowires using Tobacco Mosaic viruses,[10,11] M13 bacteriophages,[12] insulin fibrils,[13] DNA[14,15] and amyloid fibers.[16] Peptides are particularly important biological templates: owing to their specific self-assembly and recognition capacities, they can direct the growth and assembly of nanoparticle superstructures.[17] A landmark in the use of self-assembled peptides as template scaffolds was the demonstration by Gazit et al. that Phe-Phe nanotubes can be used to form silver nanowires within their pores.[18] Fibers/fibrils made from amphiphilic peptides have also been used to control the growth and assembly of inorganic nanoparticles on their surfaces, thereby creating a template for one-dimensional nanoparticle superstructures.[19,20] Other

M. Rubio-Martínez, Dr. I. Imaz, Prof. D. Maspoch
ICN2 - Institut Catala de Nanociencia i Nanotecnologia
Esfera UAB, 08193 Bellaterra (Barcelona), Spain
E-mail: daniel.maspoch@icn.cat
Prof. D. Maspoch
Institució Catalana de Recerca i Estudis Avançats (ICREA)
08100 Barcelona, Spain

Dr. J. Puigmartí-Luis
Institut de Ciència de Materials (ICMAB-CSIC)
Esfera UAB, 08193 Bellaterra, Spain
Dr. J. Puigmartí-Luis, Prof. P. S. Dittrich
Department of Chemistry and Applied Biosciences
ETH Zürich, Wolfgang-Pauli-Strasse 10
CH-8093 Zürich, Switzerland

DOI: 10.1002/smll.201301338

self-assembled peptides (e.g. T1 and 17H6) have also been reported to fabricate nanoparticle assemblies.[21,22] However, despite the wide range of inorganic assemblies enabled by these scaffolds, using them to develop more complex multifunctional and multicomponent nanoparticle superstructures is replete with challenges, such as obtaining high-density nanoparticle coatings; preparing long continuous nanoparticle assemblies; and controlling the simultaneous growth and assembly of nanoparticles of various compositions and properties on the structure surfaces. The last of these tasks will certainly open new avenues for the rational design of well-defined polymetallic, multifunctional superstructures made from different types of nanoparticles.

Here, we demonstrate a "dual-template" strategy for the fabrication of wire-like nanoparticle superstructures via stepwise growth and/or assembly of inorganic nanoparticles using supramolecular metal–peptide scaffolds. The coordination of metal ions and peptides to form 1D coordination polymer crystals affords a novel class of peptide-supported frameworks that act as dual templates: they enable synthesis and assembly of different inorganic nanoparticles on their surface (crystal face) as well as within their internal structures, unlike in commonly used peptide-based approaches. Surprisingly, these peptide-supported frameworks direct the nucleation, growth and/or assembly of inorganic nanoparticles on their surfaces as accurately as do pure self-assembled peptide nanostructures. Furthermore, the inside of coordination peptide scaffolds can serve as a site for synthesis inorganic nanoparticles, via reduction (e.g. thermal or photo) of the metal ions inside the scaffold structure.[23,24] As proof-of-concept, we synthesised crystalline belts of the coordination polymer Ag(I)-DLL, in which the tripeptide ligand DLL is coordinated at each end to a silver ion, and then used these belts as scaffolds to build conductive, wire-like superstructures comprising Ag nanoparticles synthesised both on and in the belts. The external Ag nanoparticles were prepared by directing the nucleation and growth of Ag_2O nanoparticles on the belt surface, and then reducing them thermally to metallic silver, whereas the internal ones -which were constrained and closely packed- were prepared by thermal reduction of the Ag(I) ions comprising the belt. Inspired by this dual-template nanoparticle synthesis, we extended the chemistry to create multicomponent Fe_3O_4@Ag nanoparticle superstructures in which we selectively assembled Fe_3O_4 nanoparticles on the surface of Ag(I)-DLL belts and prepared closely packed Ag nanoparticles inside the belts. The results presented herein demonstrate a rational route to the dual-template synthesis of more complex bimetallic assemblies with modifiable properties, including electrical conductivity and magnetism, and offer valuable insight into multifunctional nanostructures.

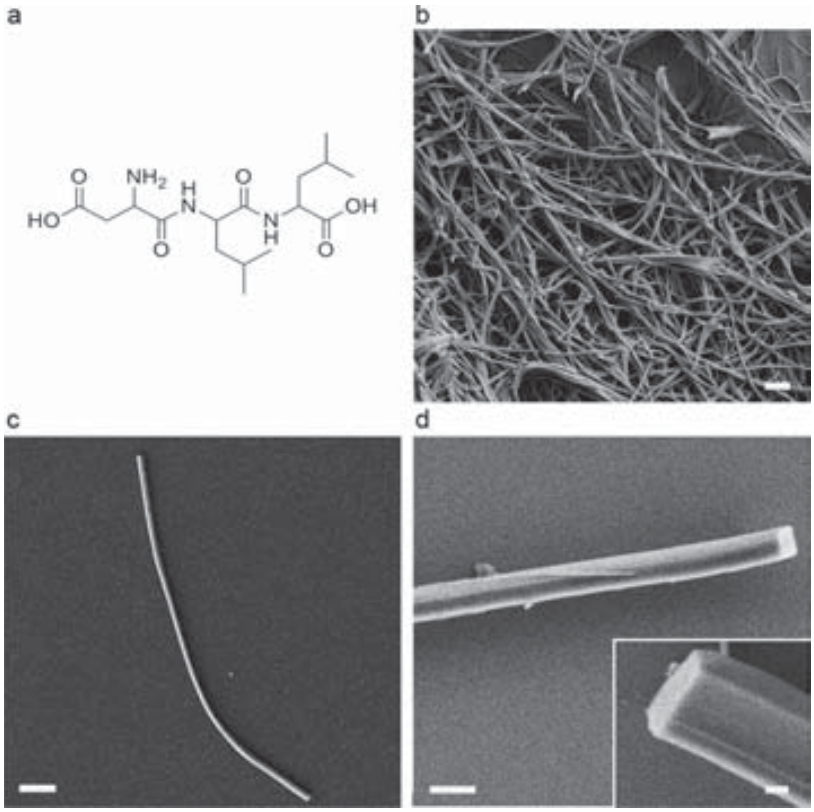

Figure 1. a) Representation of the designed tripeptide DLL. b–d) Representative FESEM images of the synthesised Ag(I)-DLL belts; (inset) Zoom on a terminal section of an Ag(I)-DLL belt, showing the rectangle-like cross-section of the belt. Scale bars: 500 nm (b–d) and 100 nm (inset d).

2. Results and Discussion

2.1. Design, Synthesis, and Characterisation of Ag(I)-DLL Belt-Like Crystals

In order to make Ag(I)-peptide coordination crystals and use them as dual scaffolds, we engineered three features into the peptide sequence (**Figure 1**a). Firstly, the peptide had to be able to bridge Ag(I) metal ions to form extended coordination networks. Therefore, two carboxylic groups were used at separate positions of the sequence. Secondly, the peptide had to be able to direct the assembly of inorganic nanoparticles onto the crystals. Considering that amino groups and leucine amino acids help form inorganic nanoparticle superstructures made from peptide scaffolds,[25–28] we designed the tripeptide sequence DLL (see Figure S1 of the Supporting Information) to increase the density of amino groups (one per repeating unit of -Ag(I)-DLL-) and leucine units (two per -Ag(I)-DLL-) in the extended coordination network (and consequently, on the crystal surface). And thirdly, the prepared nanostructures had to be stable in water; therefore, we incorporated two consecutive leucine units into the peptide sequence to confer

small 2013,
DOI: 10.1002/smll.201301338

the resulting crystals with hydrophobicity.[29] Although the peptide was water soluble, it underwent rapid coordination assembly upon reaction with $AgNO_3$ (diffusion of an ethanolic solution of $AgNO_3$ into an aqueous solution of DLL at pH 7 in the dark). The resulting white solid was then collected by filtration, washed three times with water, and finally, redispersed in water. Field-emission scanning electron microscopy (FESEM) and transmission electron microscopy (TEM) analyses, combined with X-ray powder diffraction (XRPD), revealed numerous rectangular, wire-like, belt-shaped Ag(I)-DLL sub-micrometre crystals, with typical lengths in the tens to hundreds of micrometers (Figures 1b,c). Each belt was uniform in width along its entire length, with typical widths ranging from 200 nm to 2 μm (Figures 1c,d). Interestingly, we were able to control the dimensions of the belts by controlling the speed of reagent addition: we obtained smaller nanobelts (length < 10 μm; width = 50 to 200 nm) by rapidly mixing the two solutions with stirring than when we had when we combined them by diffusion (see Figure S3 of the Supporting Information). Even though XRPD confirmed the crystalline character of these belts, their single crystal structure determination, and therefore, a detailed analysis of the structural connectivity was not feasible due to their small diameter. Energy dispersive X-ray (EDX) analysis confirmed the presence of silver within the assembled belts (see Figure S4 of the Supporting Information). The infrared spectrum exhibited typical two bands in the NH stretching region at 3380 and 3259 cm^{-1}, which are characteristic of primary (NH_2) amines rather than their zwitterionic (NH_3^+) form. This observation together with the presence of both broad asymmetric and symmetric COO^- bands (1640 and 1390 cm^{-1}) indicated that the two terminal carboxylate groups had coordinated to the Ag(I) ions (see Figure S5 of the Supporting Information).[30,31] These data together with the elemental analysis, which confirms that the ratio between Ag(I) ions and DLL is 2:1, and the thermogravimetric studies (see Figure S6 of the Supporting Information), which shows the absence of solvent molecules, enable us to tentatively suggest the formation of [Ag_2(DLL)] coordination polymer.

2.2. Dual-Template Synthesis of Ag@Ag Nanoparticle Superstructures

To reduce Ag(I) ions of Ag(I)-DLL belts to form Ag nanoparticles along the entire length of the belt interior, the neat belts were exposed to heat. To study this phenomenon, a solid sample of neat Ag(I)-DLL belts was sequentially heated at 100 °C, 150 °C, 200 °C, and 250 °C (30 min at each temperature), and monitored by FESEM and XRPD throughout the heating process (**Figure 2**a). Initially, FESEM images and XRPD spectra did not reveal any differences from heating at 150 °C. However at 200 °C, Ag nanoparticles (average diameter: 6 to 60 nm) began to form within the Ag(I)-DLL belts (Figures 2a,d), a process that was accompanied by a certain loss of crystallinity. At 250 °C, 1-D assemblies comprising randomly positioned Ag nanoparticles (mean nanoparticle diameter as calculated by the Scherrer equation: 27 nm; see Figure S7 of the Supporting Information) along the belt were obtained (Figure 2b). Some of these went on to form continuous, closely packed Ag superstructures (Figure 2c, top), and others were highly interrupted (Figure 2c, bottom). At this temperature, XRPD confirmed the formation of fcc-Ag nanoparticles accompanied by a complete loss of Ag(I)-DLL crystallinity between 200 and 250 °C, due to decomposition of the coordination network (Figure 2d), as further confirmed by thermogravimetric analysis.

In parallel, we synthesised Ag(I)-DLL belts coated with Ag_2O nanoparticles. A solution of DLL at pH 10.5 was mixed

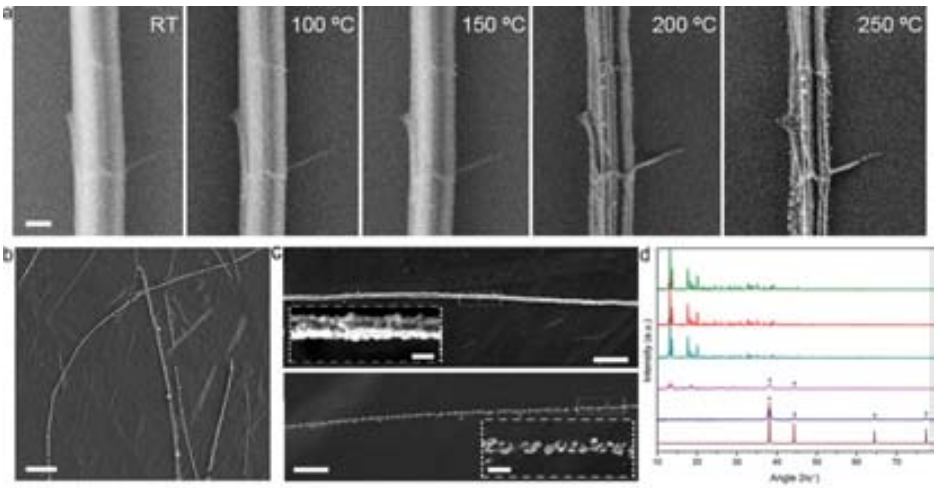

Figure 2. a) Sequential FESEM images of an isolated Ag(I)-DLL belt illustrating the templated growth of Ag nanoparticles after annealing by sequential heating from room temperature to 100, 150, 200, and 250 °C (30 min at each temperature; from left to right). b) Representative FESEM image of Ag assemblies, showing the formation of either continuous or discontinuous Ag-nanoparticle superstructures. c) Representative FESEM images of two individual continuous (top) and discontinuous (bottom) Ag-nanoparticle superstructures. d) XRPD spectra of Ag(I)-DLL belts at room temperature (green) and after heating for 30 min at each of the following temperatures sequentially: 100 °C (red), 150 °C (turquoise), 200 °C (pink) and 250 °C (blue). The bottom spectrum corresponds to the simulated XRPD pattern of fcc-Ag structure. The peaks marked with stars correspond to the fcc-Ag phase. Scale bars: 200 nm (a, inset c) and 1 μm (b,c).

DOI: 10.1002/smll.201301338

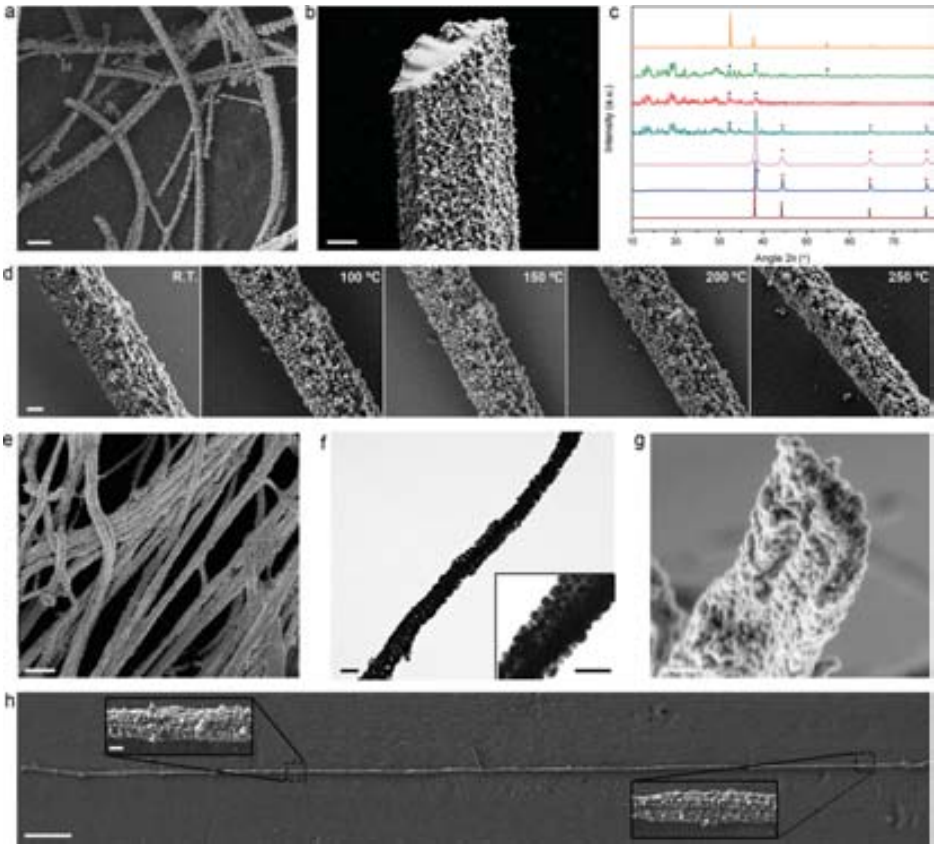

Figure 3. a) Representative FESEM image of Ag_2O@Ag(I)-DLL superstructures, showing the uniformity of the Ag_2O nanoparticle coating. b) FESEM image of a rectangular cross-section of an Ag_2O@Ag(I)-DLL superstructure, showing the external surface coated with Ag_2O nanoparticles. c) XRPD spectra of Ag_2O@Ag(I)-DLL superstructures at room temperature (green) and after 30 min heating at each of the following temperatures sequentially: 100 °C (red), 150 °C (turquoise), 200 °C (pink) and 250 °C (blue). The top and bottom patterns correspond to the theoretical cubic structure of Ag_2O (orange) and fcc-Ag (brown), respectively. The peaks marked with black stars correspond to the cubic structure of Ag_2O, and marked with red stars, to the fcc-Ag phase. d) Sequential FESEM images of an isolated Ag_2O@Ag(I)-DLL superstructure sequentially heated from room temperature to 100, 150, 200 and 250 °C (30 min at each temperature; from left to right). e) Representative FESEM image of continuous Ag@Ag-nanoparticle superstructures. f) Representative TEM image of an individual Ag@Ag-nanoparticle superstructure. g) FESEM image of a cross-section view of an Ag@Ag-nanoparticle superstructure, showing the external-internal growth of Ag nanoparticles. h) Representative FESEM image of a long (~250 μm) Ag@Ag-nanoparticle superstructure. Scale bars: 200 nm (b,d,f,g), 400 nm (a,e), 10 μm (h) and 2 μm (inset h).

with a solution of $AgNO_3$ in water/ethanol (1:2) at pH 7.0, and the resulting black dispersion was left in the dark for 24 hours. Under these conditions, Ag(I)-DLL assembly and template formation of Ag_2O nanoparticles occurred simultaneously to yield wire-like Ag_2O@Ag(I)-DLL superstructures. Self-assembled structures identical to those above could as well be prepared by dispersing neat Ag(I)-DLL belts into an aqueous solution of $AgNO_3$ at pH 8.0. FESEM and TEM analysis of Ag_2O@Ag(I)-DLL showed a uniform coating of Ag_2O nanoparticles (density ~ 700 particles/μm^2; mean nanoparticle diameter: 39 ± 11 nm; **Figure 3**a). Additionally, a cross-sectional FESEM image of a superstructure end revealed that the cross-sections of the Ag(I)-DLL internal belts had remained rectangular, and that all of the Ag_2O nanoparticles had assembled on the external surfaces (Figure 3b). The XRPD patterns from the Ag_2O@Ag(I)-DLL superstructures further indicated that Ag_2O nanoparticles had been formed and that the Ag(I)-DLL coordination network had been preserved; however, they also revealed that crystallinity had slightly diminished during the nanoparticle formation (Figure 3c).

To demonstrate that the Ag_2O nanoparticles had not been formed from the Ag(I) ions in the Ag(I)-DLL belts, we performed a control experiment. Pre-synthesised belts were dispersed in water at pH 10.5 without $AgNO_3$. After 24 h, the dispersion did not exhibit any significant changes, and FESEM and XRPD analysis confirmed the absence of Ag_2O nanoparticles on the belt surfaces (see Figure S9 of the Supporting Information).

After coating the Ag(I)-DLL belts with Ag_2O nanoparticles, we then heated the Ag_2O@Ag(I)-DLL superstructures to 150 °C (Figure 3d). At this temperature, the Ag_2O nanoparticles began to reduce into Ag nanoparticles.[32] This thermal reduction process was proven by XRPD analysis (Figure 3c): the XRPD patterns of the Ag_2O@Ag(I)-DLL superstructures heated to between 150 °C and 200 °C lacked the characteristic peaks of Ag_2O nanoparticles, but included the peaks characteristic of fcc-Ag nanoparticles. Interestingly, this

small 2013,
DOI: 10.1002/smll.201301338

small

reduction of Ag_2O to Ag did not change the internal structure of the Ag(I)-DLL belt, as supported by XRPD comparison of heated and non-heated samples, thus confirming the high chemical stability of the belt surface, and therefore, its amenability as a template for the nucleation and assembly of nanoparticles of other compositions. After heating the Ag@Ag(I)-DLL superstructures further, to 250 °C, we observed the expected confined thermal reduction of the Ag(I) ions that comprise the internal Ag(I)-DLL coordination network into closely packed Ag nanoparticles (Figure 3c; mean nanoparticle diameter as calculated by the Scherrer equation: 39 nm; see Figure S7 of the Supporting Information) to well-defined, dual-templated and continuous Ag@Ag-nanoparticle superstructures (Figure 3e). To further verify the dual-template formation of these self-assembled nanoparticle structures, they were studied by TEM and cross-sectional FESEM (Figures 3f,g), which revealed that both the external and the internal Ag nanoparticles were highly dense.

Considering the above results, when heated neat Ag(I)-DLL belts to 250 °C, either continuous or interrupted Ag nanoparticles assemblies are formed.[33] However, when Ag_2O nanoparticles are assembled on the surface of Ag(I)-DLL belts and the resulting Ag_2O@Ag(I)-DLL superstructures are heated up to 250 °C, functional dual-templated and close-packed Ag@Ag nanoparticle assemblies, which can be longer than 100 μm (see Figure 3h for a representative Ag@Ag-nanoparticle superstructure with a length of ~250 μm; also see Figure S10 of the Supporting Information), are generated. This thermally-induced, external-internal Ag nanoparticle reduction enabled us to reproducibly create highly uniform self-assembled structures of closely packed metallic Ag that may have applications as conductive 1-D nanomaterials.

2.3. Conductivity Properties of Ag@Ag Nanoparticle Superstructures

To test the conductivity of the Ag@Ag nanoparticle assemblies, we assessed their electronic transport properties. We randomly placed Ag_2O@Ag(I)-DLL superstructures over platinum patterned electrodes, and then heated them from 100 °C to 250 °C. These superstructures showed no electrical response at 100 °C. However, an increasing proportion of them began to conduct electric current from 125 °C to 200 °C, a result which is consistent with the thermal reduction of external Ag_2O to Ag nanoparticles that we had previously detected in this temperature range (**Figure 4**a). The percentage of conductive superstructures continuously increased, ultimately reaching 100% at 250 °C, the temperature at which we were able to reproducibly create the dual-templated continuous Ag@Ag-nanoparticle superstructures.

To further evaluate the uniformity of dual-templated Ag@Ag-nanoparticle assemblies along their entire length, we guided and integrated Ag_2O@Ag(I)-DLL superstructures onto platinum patterned electrodes surfaces through the use of capillarity forces acting in microfluidic channels and constrained microchannel geometries (Figure 4b). Figure 4c shows an optical microscopy image of a Ag_2O@Ag(I)-DLL superstructure (length: ca. 150 μm) located between different

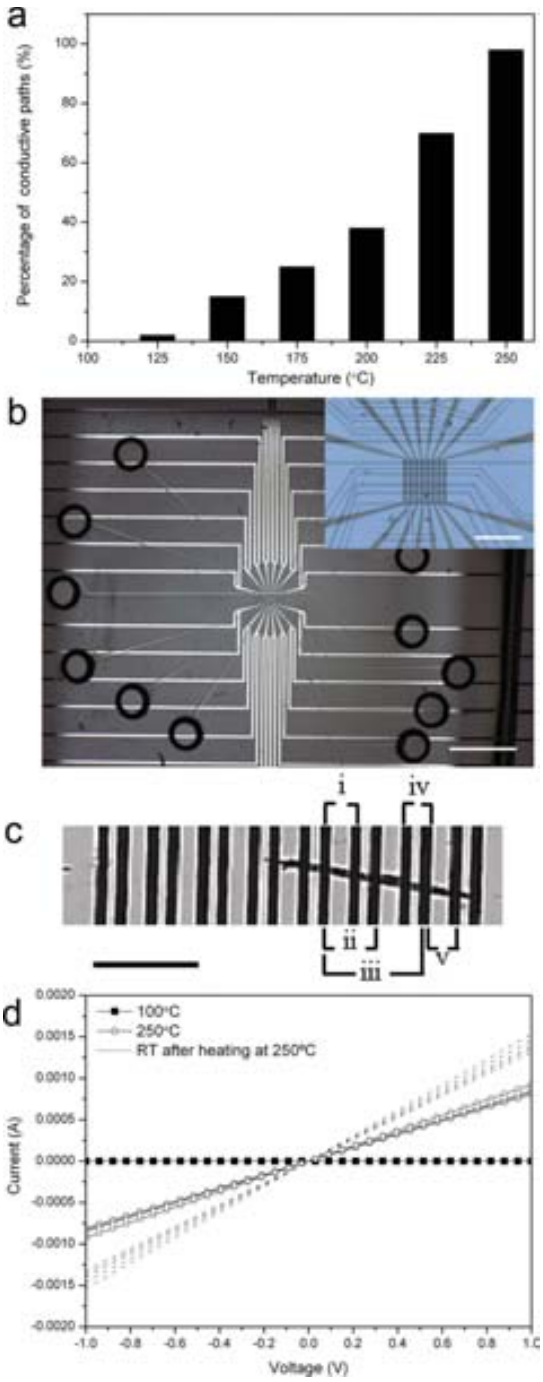

Figure 4. a) Percentage of conductive paths at a given temperature for Ag_2O@Ag(I)-DLL superstructures (calculated from 147 electrode pairs). b) Optical microscope image of a microfluidic network located on top of a patterned electrode glass-slide. Inset b, zoom on the interdigitated electrode area. The electrode pairs were prefabricated with a gap of 10 μm. c) Optical microscopy image of a single Ag@Ag nanoparticle superstructure, synthesised by heating (to 250 °C) a Ag_2O@Ag(I)-DLL superstructure that had previously been positioned on a patterned electrode surface. The five longitudinal sections of the superstructure that were electrically measured during the thermal treatment are denoted as (i) to (v). d) Measured *I*–*V* sweeps of the five sections shown in (c) at 100 °C; at 250 °C; and at room temperature after previously being heated at 250 °C. Scale bars: 3 mm (b), 400 μm (inset) and 100 μm (c).

DOI: 10.1002/smll.201301338

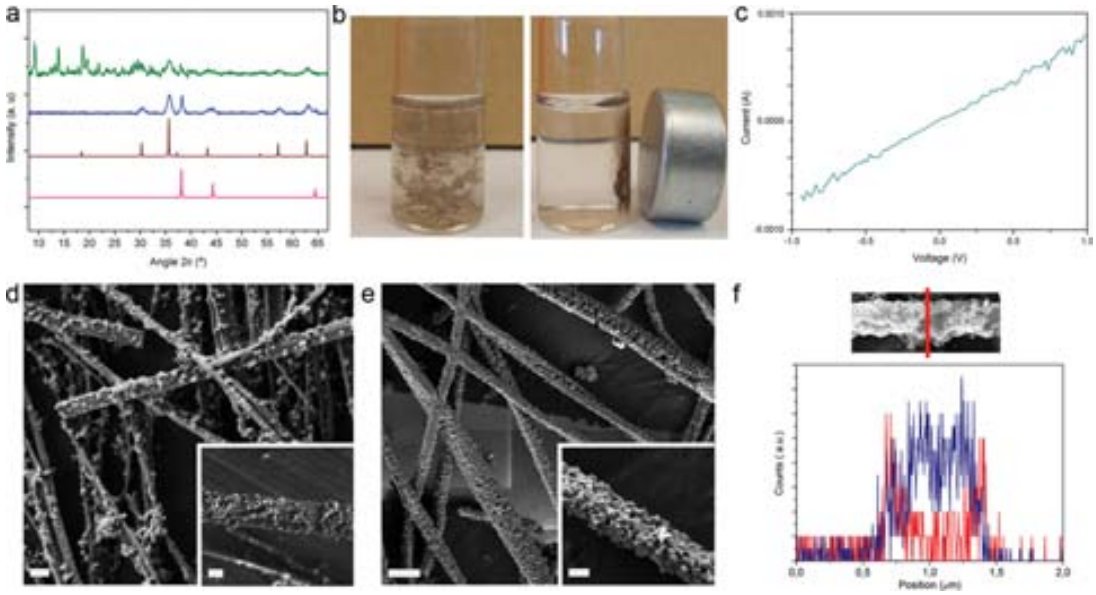

Figure 5. a) XRPD patterns of Fe_3O_4@Ag(I)-DLL superstructures at room temperature (green) and heated to 250 °C (blue). The brown and pink XRPD patterns correspond to the theoretical fcc-Ag and magnetite, respectively. b) Photographs showing the attraction of Fe_3O_4@Ag(I)-DLL superstructures in an aqueous solution to a magnet at room temperature (left, absence of magnet; right, presence of magnet). c) *I–V* sweep (average of 20 measurements) of Fe_3O_4@Ag nanoparticle superstructures. d) Representative FESEM images of Fe_3O_4@Ag(I)-DLL superstructures. e) Representative FESEM images of Fe_3O_4@Ag nanoparticle superstructures. f) EDX spectrum profile scanning for "core-shell" Fe_3O_4@Ag nanoparticle superstructures. Red: iron; blue: silver. Scale bars: 200 nm.

electrode pairs. Through this integration, the *I–V* characteristics at five different longitudinal sections (Figure 4c, *i* to *v*) of this superstructure heated to 250 °C were studied in a two-point configuration. After 30 minutes at 250 °C, all studied sections became conductive with a resistance value of 1 kΩ approximately (*i.e.* 1.2×10^2 S/cm), hence confirming the uniform formation of metallically continuous and electrically active Ag@Ag-nanoparticles superstructures. Furthermore, when the Ag@Ag-nanoparticle superstructures were cooled down to room temperature, their *I–V* characteristics still showed an ohmic behavior (Figure 4d) and a lower resistance (approx. 700 Ω, 2.4×10^2 S/cm), as expected for a metal. Whereby the electrical conductivity found is lower than that of the bulk silver metal (6.2×10^5 S/cm)[34] -presumably due to its grain-boundary structure-, the conductivity of Ag@Ag superstructures is higher than most of the reported values for silver-based nanoparticle composites,[35] or silver-based nanowire composites.[36]

2.4. Conductive and Magnetic Fe_3O_4@Ag Nanoparticle Superstructures

Our results up to this point prompted us to investigate whether we could exploit the external nanoparticle assembly and the internal nanoparticle formation to design and construct multicomponent (and therefore, multifunctional) self-assembled nanoparticle structures. To test this, Ag(I)-DLL belts were coated with magnetic Fe_3O_4 nanoparticles (by submerging them into an aqueous dispersion of these nanoparticles for 1 h). The resulting brown Fe_3O_4@Ag(I)-DLL superstructures were separated out by gravity decantation, and then redispersed in water. Characterization by FESEM, TEM and XRPD revealed that the belts were indeed partially coated with Fe_3O_4 nanoparticles (density ~ 350 particle/μm^2; mean nanoparticle diameter: 35 ± 9 nm; **Figure 5**a and d). Interestingly, the resulting Fe_3O_4@Ag(I)-DLL superstructures incorporated the magnetic properties of the nanoparticles, as demonstrated by the fact they could be easily guided by a magnet (Figure 5b). These were confirmed to be non-conductive (data not shown). Following the dual-template strategy, the Fe_3O_4@Ag(I)-DLL superstructures were then heated to 250 °C to induce thermal reduction of the internal Ag(I) ions. This afforded wire-like self-assembled Fe_3O_4@Ag nanoparticle superstructures (Figure 5e). The XRPD pattern showed the characteristic peaks of fcc-Ag and Fe_3O_4, and lacked those corresponding to the Ag(I)-DLL. Additionally, EDX mapping performed on a single Fe_3O_4@Ag-nanoparticle assembly indicated the formation of dual-templated "core–shell" superstructures, as evidenced by the detection of higher concentrations of iron atoms at the tips of the superstructure and the detection of silver atoms at the middle of the superstructure (Figure 5f).

We then decided to ascertain the magnetism and the electrical conductivity of the Fe_3O_4@Ag nanoparticle assemblies. These were first redispersed in an aqueous solution, and then magnetically attracted by a magnet (see Figure S12 of the Supporting Information). In parallel, they were tested by two-terminal current–voltage measurements, which indicated that they were conductive with a resistance value of 1.5 kΩ approximately (Figure 5c). Strikingly, this multifunctional dual-template assembly did not affect the magnetism or the

small 2013,
DOI: 10.1002/smll.201301338

small

I–V characteristics of the Fe_3O_4@Ag nanoparticle assemblies, which exhibited an ohmic response, just as the Ag@Ag nanoparticle superstructures had.

3. Conclusion

In summary, we have demonstrated that the growth of various inorganic nanoparticles both on the surface and inside micrometre-long 1-D supramolecular scaffolds can be templated by coordination metal–peptide [Ag(I)-DLL] belt-like crystals. Particularly promising is the ability to control and confine the assembly of two different classes of inorganic nanoparticles, thereby opening up new avenues for designing more sophisticated multicomponent nanoparticle superstructures that combine the properties derived from both types of nanoparticles, such as the synthesised magnetic and conductive Fe_3O_4@Ag-nanoparticle assemblies. As this class of supramolecular metal–peptide scaffolds can be made from a wide range of peptides and metal ions, which can be converted into metal atoms or metal oxides (e.g. Fe(III) to α-Fe_2O_3 or to Fe_3O_4;[37] Zn(II) to ZnO;[38] In(III) to In_2O_3;[39] and Gd(III) to Gd_2O_3),[40] our dual-template approach can be adapted to fabricate a diverse array of multifunctional self-assembled nanoparticle structures.

4. Experimental Section

Materials: The reagents silver nitrate ($AgNO_3$), sodium hydroxide (NaOH), ferric chloride hexahydrate ($FeCl_3 \cdot 6H_2O$) and ferrous chloride tetrahydrate ($FeCl_2 \cdot 4H_2O$) were purchased from Sigma-Aldrich Co. The peptide DLL, comprising one aspartic acid (D) residue and two leucine (L) residues, was designed by us and synthesised by GenScript USA Inc. Fe_3O_4 nanoparticles were prepared as described elsewhere.[41] High purity EtOH was purchased from Teknokroma, and used without further purification. Deionised Millipore Milli-Q water was used in all experiments.

Preparation of Ag(I)-DLL Belts by Diffusion: DLL (8.8 mg, 0.025 mmol) was dissolved in 2.5 mL of water, and the final pH was brought to 7 with aqueous NaOH (1% w/w). In parallel, a solution of $AgNO_3$ (8.25 mg, 0.05 mmol) was dissolved in water/ethanol (1:2). The two solutions were carefully transferred to a test tube, generating two layers separated by an interface. After 1 week in the dark (to avoid the formation of Ag_2O nanoparticles), long belts with a diameter ranging from 200 nm to 2 µm appeared at the interface. Anal. (%) Calcd. for $C_{16}H_{27}N_3O_6Ag_2$: C, 33.51; H, 4.75; N, 7,33; Ag, 37,7. Found: C, 33.24; H, 4,72; N, 7,13; Ag, 36,8.

Preparation of Ag(I)-DLL Belts by Fast Addition: Ag(I)-DLL belts were prepared by fast addition 3 mL of a solution of $AgNO_3$ (16.5 mg, 0.1 mmol) in water/ethanol (1:2) to 5 mL aqueous solution of DLL (17.5 mg, 0.05 mmol) at pH 7 under stirring and dark conditions at room temperature. Dendritic growth of white belts was immediately observed.

Preparation of Nanoparticle Superstructures: Ag_2O@Ag(I)-DLL superstructures were prepared using the same diffusion method employed to synthesise the neat Ag(I)-DLL belts, except that the pH of the DLL solution was brought to 10.5 with aqueous NaOH (1% w/w). Fe_3O_4@Ag(I)-DLL superstructures were prepared by adding an aqueous dispersion of Fe_3O_4 nanoparticles into an aqueous dispersion of neat Ag(I)-DLL belts. This mixture was left for 1 h, and the resulting Fe_3O_4@Ag(I)-DLL superstructures were separated by gravity decantation, and then redispersed in water. Ag, Ag@Ag and Fe_3O_4@Ag nanoparticle assemblies were obtained by heating Ag(I)-DLL belts, Ag_2O@Ag(I)-DLL superstructures and Fe_3O_4@Ag(I)-DLL superstructures, respectively, to 250 °C at a heating rate of 1 °C/min.

Characterisation: Infrared (IR) spectra were recorded on a Tensor 27FTIR spectrophotometer (Bruker) equipped with a Golden Gate diamond ATR (Attenuated Total Reflection) cell (Bruker). ^1H NMR and ^{13}C NMR spectra were recorded on Bruker DPX360 (360 Mhz) spectrometer. Proton and carbon chemical shifts are reported in ppm. All spectra have been registered at 298 K. Elemental analysis and ICP-OES were performed with a CHNS Thermo Scientific Flash 2000 elemental analyzer and a Perkin-Elmer Optima 4300DV model, respectively. High-resolution mass spectrum (HRMS) was recorded in a Bruker micrOTOF-Q II spectrometer. Scanning Electron Microscopy (SEM) images were collected on an EI Merlin Field–Emission microscope (Zeiss) at acceleration voltages of 0.2–30 kV. Aluminium was used as support. Transmission electron microscopy (TEM) images were obtained on a JEM 1400 microscope (Jeol). The measurements were performed at room temperature and a voltage of 140 kV. The X-ray EDX microanalysis was performed with an INCA energy SEM system (Oxford Instruments). X-ray powder diffraction (XRPD) measurements were performed with an X'Pert PRO MPD diffractometer (Panalytical). In order to estimate the particle size, Scherrer's equation was used. For this purpose, the (111), (200), (220), and (311) peaks of the Ag fcc structure were selected. Thermal reduction reactions were run in a UNE300 oven (Memmert). To assess the electrical conductivity of samples, the source–drain current was determined at a given temperature while the applied source–drain voltage was swept in a two-point configuration. The temperature was raised to 300 °C, in increments of 25 °C. All samples were maintained on a hot plate for 30 minutes at each temperature just before measurement. The microfluidic channels employed in our experiments were moulded into polydimethylsiloxane (PDMS, SYLGARD® 184 Silicone Elastomer Kit) using an SU-8 (2015, Microchem) master form fabricated with standard photolithographic techniques. Before attaching the cured and structured PDMS mould to a patterned electrode surface, inlet holes connecting to the microfluidic channels were punched with a Biopsy puncher. Non-bonded chips were used, which enabled peeling of the PDMS mould before the thermal treatment processes were conducted on the localized superstructures. The microfluidic channels were filled with a suspension of the studied superstructures by capillary forces.

Supporting Information

Supporting Information is available from the Wiley Online Library or from the author. It includes FESEM images, EDX and IR spectra, XRPD pattern and thermogravimetric analysis of Ag(I)-DLL belts, TEM images of Ag_2O@Ag(I)-DLL superstructures, FESEM images of long, close-packed and continuous Ag@Ag nanoparticle and Fe_3O_4@Ag nanoparticle superstructures, EDX spectrum of

DOI: 10.1002/smll.201301338

Fe_3O_4@Ag(I)-DLL superstructures, and conductivity study of a single Ag(I)-DLL belt.

Acknowledgements

The authors acknowledge the financial support from MINECO-Spain, under projects MAT2012-30994 and CTQ2011-16009-E. The authors thank the Microscopy Service of the UAB. I. I. and J. P. L. thank the MINECO for RyC contracts. M. R. M. thanks the ICN2 for her research fellowship. The authors also thank Dr. Ángel Pérez del Pino for kindly supplying the Keithley sourcemeter used in the experiments.

[1] Z. Nie, A. Petukhova, E. Kumacheva, *Nat. Nanotechnol.* **2010**, *5*, 15.
[2] S. Mann, *Nat. Mater.* **2009**, *8*, 781.
[3] S. Zhang, *Nat. Biotechnol.* **2003**, *21*, 1171.
[4] N. C. Seeman, A. M. Belcher, *Proc. Natl. Acad. Sci. USA* **2002**, *99*, 6451.
[5] Y. Gao, Z. Tang, *Small* **2011**, *7*, 2133.
[6] D. Papapostolou, S. Howorka, *Mol. Bio Syst.* **2009**, *5*, 723.
[7] F. C. Meldrum, V. J. Wade, D. L. Nimmo, B. R. Heywood, S. Mann, *Science* **1991**, *349*, 684.
[8] F. C. Meldrum, B. R. Heywood, S. Mann, *Science* **1992**, *257*, 522.
[9] T. Douglas, M. Young, *Nat.* **1998**, *393*, 152.
[10] W. Shenton, T. Douglas, M. Young, G. Stubbs, S. Mann, *Adv. Mater.* **1999**, *11*, 253.
[11] R. J. Tseng, C. Tsai, L. Ma, J. Ouyang, C. S. Ozkan, Y. Yang, *Nat. Nanotechnol.* **2006**, *1*, 72.
[12] C. Mao, C. E. Flynn, A. Hayhurst, R. Sweeney, J. Qi, G. Georgiou, B. Iverson, A. M. Belcher, *Proc. Natl. Acad. Sci. USA* **2003**,*100*, 6946.
[13] F. Leroux, M. Gysemans, S. Bals, K. J. Batenburg, J. Snauwaert, T. Verbiest, C. Van Haesendonck, G. Van Tendeloo, *Adv. Mater.* **2010**, *22*, 2193.
[14] M. G. Warner, J. E. Hutchison, *Nat. Mater.* **2003**, *2*, 272.
[15] H. D. A. Mohamed, S. M. D. Watson, B. R. Horrocks, A. Houlton, *Nanoscale* **2012**, *4*, 5936.
[16] T. Scheibel, R. Parthasarathy, G. Sawicki, X.-M. Lin, H. Jaeger, S. T. Lindquist, *Proc. Natl. Acad. Sci. USA* **2003**, *100*, 4527.
[17] C. L. Chen, N. L. Rosi, *Angew. Chem. Int. Ed.* **2010**, *49*, 1924.
[18] M. Reches, E. Gazit, *Science* **2003**, *300*, 625.
[19] J. D. Hartgerink, E. Beniash, S. I. Stupp, *Science* **2001**, *294*, 1684.
[20] C. L. Chen, N. L. Rosi, *J. Am. Chem. Soc.* **2010**, *132*, 6902.
[21] X. Fu, Y. Wang, L. Huang, Y. Sha, L. Gui, L. Lai, Y. Tang, *Adv. Mater.* **2003**, *15*, 902.
[22] N. Sharma, A. Top, K. L. Kiick, D. J. Pochan, *Angew. Chem. Int. Ed.* **2009**, *48*, 7078.
[23] L. Liang-Shi, S. Stupp, *Angew. Chem. Int. Ed.* **2005**, *44*, 1833.
[24] K. T. Nam, A. M. Belcher, *ACS Nano* **2008**, *7*, 1480.
[25] L. Hwang, G. P. Zhao, P. J. Zhang, N. L. Rosi, *Small* **2011**, *7*, 1939.
[26] P. Pengo, L. Baltzer, L. Pasquato, P. Scrimin, *Angew. Chem. Int. Ed.* **2007**, *46*, 400.
[27] C. Chiu, L. Ruan, Y. Huang, *Chem. Soc. Rev.* 2013, DOI: 10.1039/c2cs35347d.
[28] E. Lee, D. H. Kim, Y. Woo, H. G. Hur, Y. Lim, *Biochem. Biophys. Res. Commun.* **2008**, *376*, 595.
[29] Y. Liu, W. Xuan, Y. Cui, *Adv. Mater.* **2012**, *22*, 4112.
[30] T. Khuge, M. Bette, C. Vetter, J. Schmidt, D. T. Steinborn, *J. Organomet. Chem.* **2012**, *75*, 93.
[31] L. Antolini, G. Marcotrigiano, L. Menabue, G. C. Pellacani, M. Saladini, *Inorg. Chem.* **1982**, *21*, 2263.
[32] S. Chun, D. Grudinin, D. Lee, S. H. Kim, G. R. Yi, I. Hwang, *Chem. Mater.* **2009**, *21*, 343.
[33] It is important to note here that upon heating the Ag(I)-DLL belts up to 250 °C, only the continuous single-templated Ag assemblies were electrically conductive, with a conductivity value of 1.0×10^3 S/cm approximately (see Figure S13 of the Supporting Information). Indeed, in the same voltage range (–1 V to 1 V), the conductivity increased (approx. 1.4×10^3 S/cm) as the temperature was decreased, thus inferring a typical metallic behaviour.
[34] Y. Sun, Y. Yin, B. T. Mayers, T. Herricks, Y. Xia, *Chem. Mater.* **2002**, *14*, 4736.
[35] H. P. Wu, J. F. Liu, X. J. Wu, M. Y. Ge, Y. W. Wang, G. Q. Zhang, J. Z. Jiang, *Int. J. Adhes. Adhes.* **2006**, *26*, 617.
[36] I. Moreno, N. Navascues, S. Irusta, J. Santamaría, *IOP Conf. Ser.: Mater. Sci. Eng.* **2012**, *40*, 012001.
[37] W. Cho, S. Park, M. Oh, *Chem. Commun.* **2011**, 4138.
[38] H. J. Lee, W. Cho, M. Oh, *Chem. Commun.* **2012**, 221.
[39] W. Cho, Y. H. Lee, H. J. Lee, M. Oh, *Chem. Commun.* **2009**, 4756.
[40] H. J. Lee, J. U. Park, S. Choi, J. Son, M. Oh, *Small* **2013**, *9*, 561.
[41] S. Garcia-Jimeno, J. Estelrich, *Colloids Surf. A* **2013**, *420*, 74.

Received: April 30, 2013
Published online:

NANO MICRO small

Supporting Information

for *Small*, DOI: 10.1002/smll.201301338

"Dual-Template" Synthesis of One-Dimensional Conductive Nanoparticle Superstructures from Coordination Metal–Peptide Polymer Crystals

*Marta Rubio-Martínez, Josep Puigmartí-Luis, Inhar Imaz, Petra S. Dittrich, and Daniel Maspoch**

NANO small MICRO

SUPPORTING INFORMATION

"Dual-Template" Synthesis of One-Dimensional Conductive Nanoparticle Superstructures from Coordination Metal-Peptide Polymer Crystals

Marta Rubio-Martínez, Josep Puigmartí-Luis, Inhar Imaz, Petra S. Dittrich and Daniel Maspoch*

Figure S1. a,b) ^{1}H-NMR and ^{13}C-NMR spectra of DLL. c) Infrared spectrum of DLL peptide. d) High resolution mass spectra of DLL in positive ionization mode. HRMS (ESI+): calcd for $C_{16}H_{29}N_3O_6$: 382.1949 [M+Na$^+$]; found 382.1949.

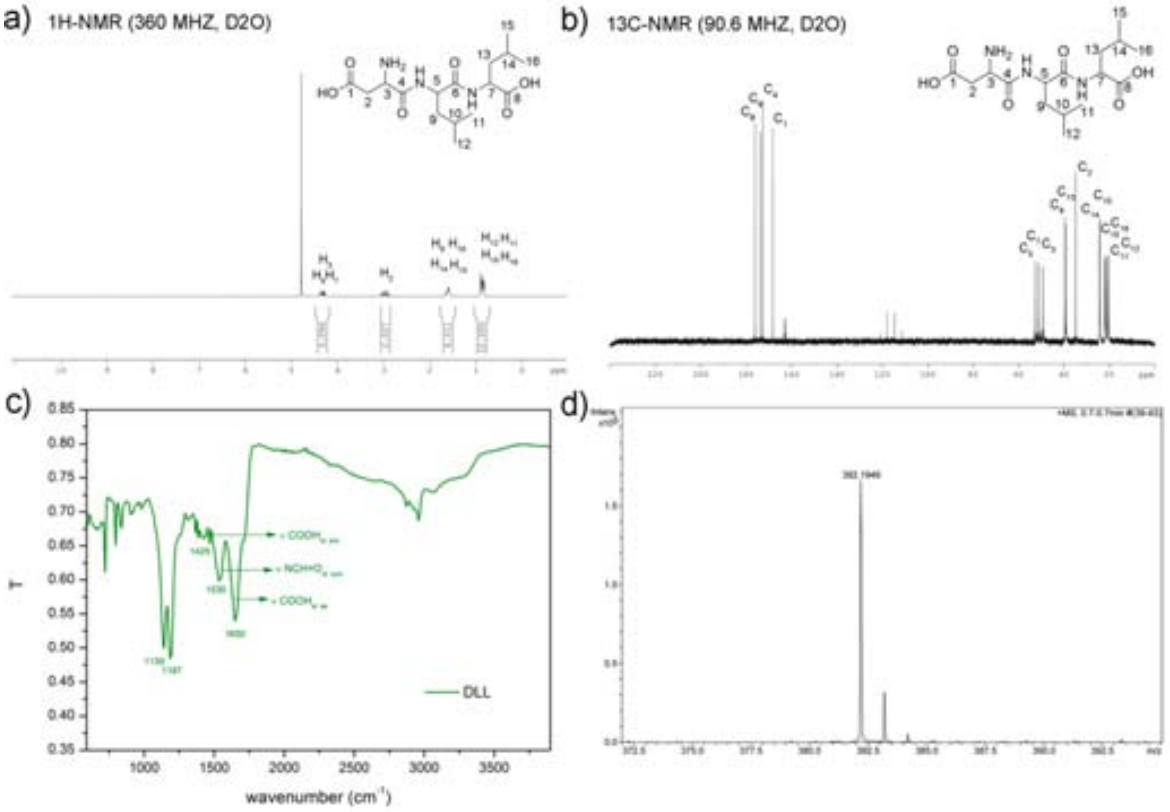

Figure S2. FESEM images of Ag(I)-DLL belts synthesised by diffusion.

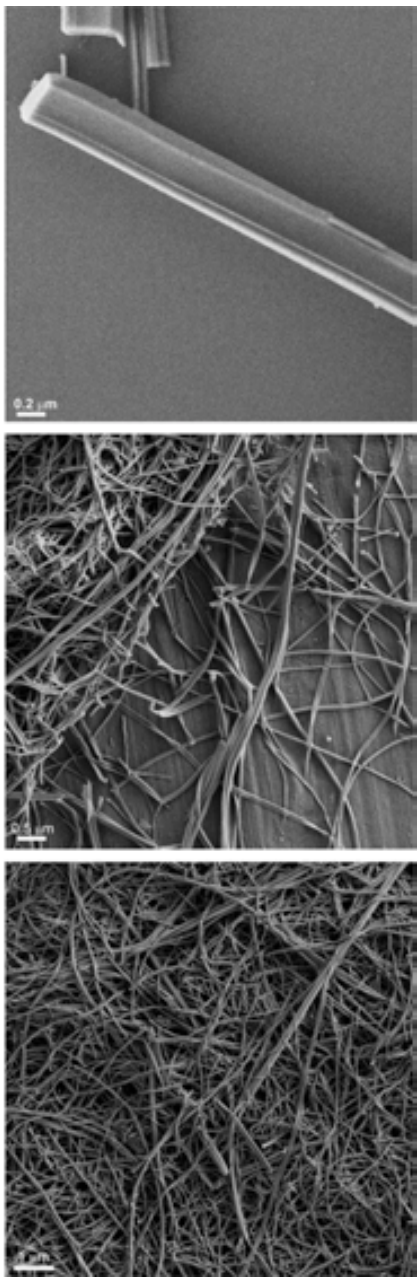

Figure S3. Representative FESEM images of Ag(I)-DLL nanobelts synthesised by fast addition. Scale bar: 1μm. XRPD pattern of Ag(I)-DLL nanobelts synthesised by fast addition (red) in comparison with those synthesised by diffusion (blue).

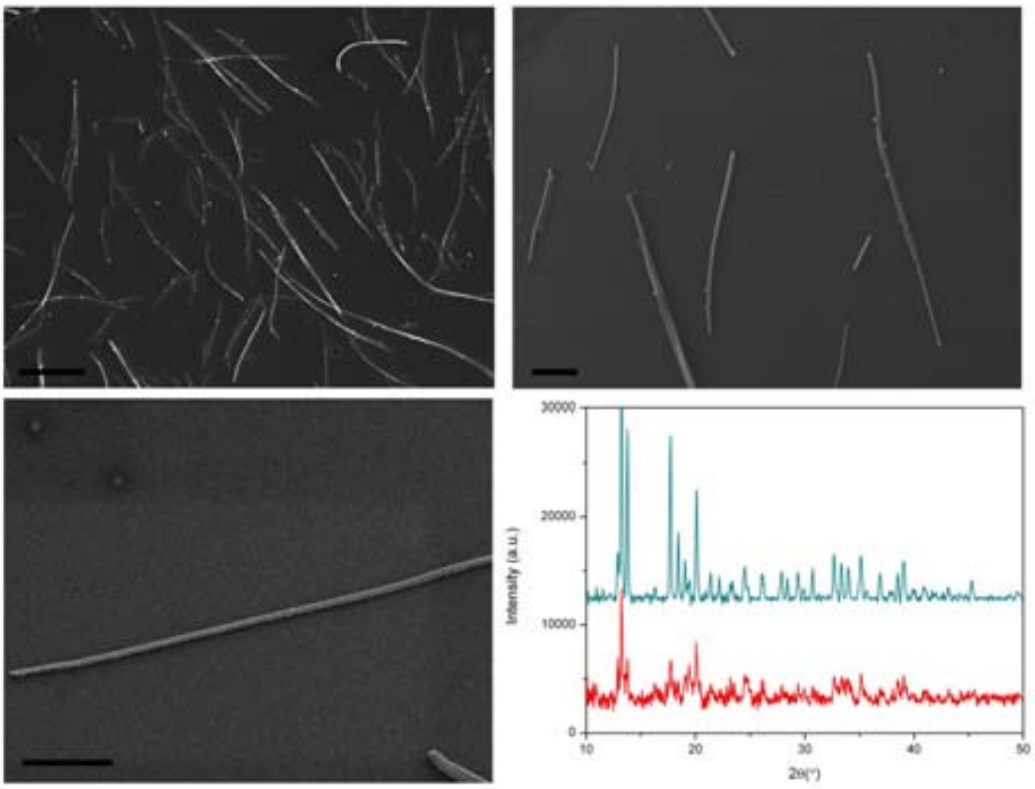

Figure S4. EDX spectrum of Ag(I)-DLL belts, indicating the presence of silver (the copper peak corresponds to the TEM grid).

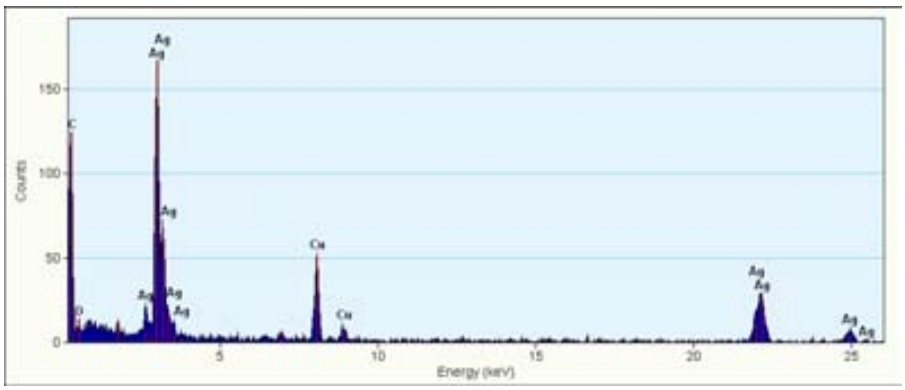

Figure S5. Infrared spectra of DLL peptide (green) and synthesised Ag(I)-DLL belts (red).

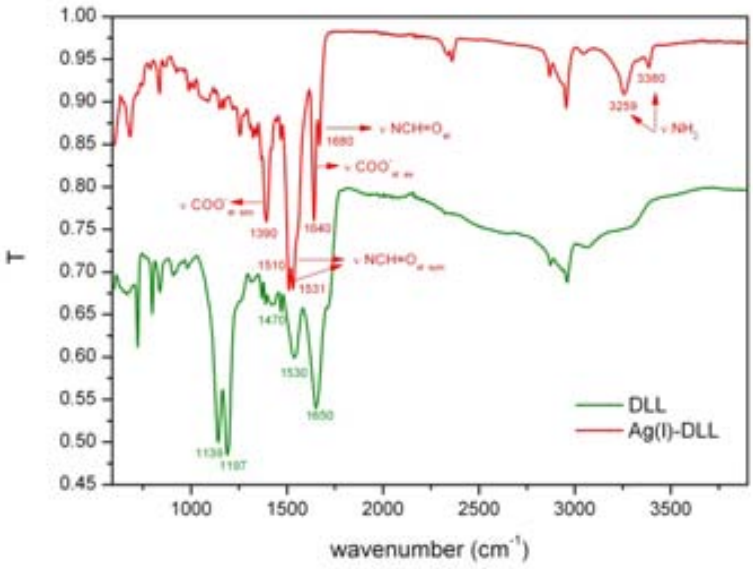

Figure S6. Thermogravimetric analysis of Ag(I)-DLL belts (heating rate: 0.5 ºC/min).

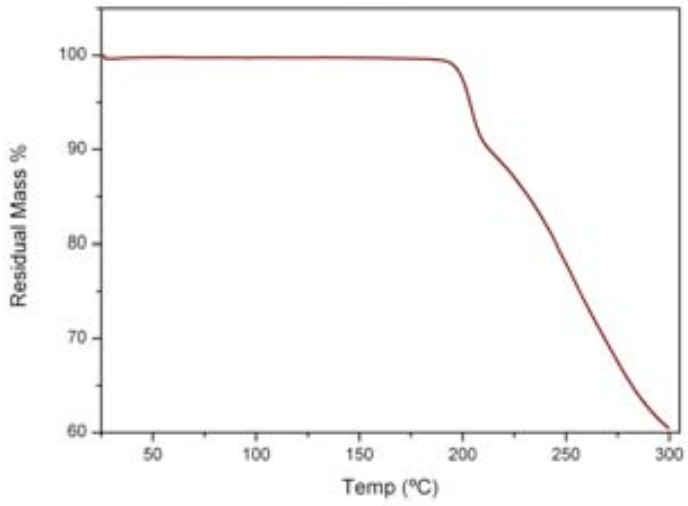

Figure S7. Tables resuming the different peak broadening and the corresponding calculated nanoparticle size of Ag-nanoparticle (a) and Ag@Ag superstructures (b) under the following conditions: Anode material: Copper (Cu); K-Alpha1 (Å): 1.540598; K-Alpha2 (Å): 1.544426; K-A.2/K-A.1 ratio: 0.500000; K-Alpha (Å): 1.541874; K-Beta (Å): 1.392250; Calculations based on: K-Alpha1; Shape factor K: 0.90. XRPD patterns of macroscopic silver sample (pink), Ag-nanoparticle superstructures (blue, a) and Ag@Ag-nanoparticle superstructures (blue, b).

a)

B obs. (2θ, °)	B std. (2θ, °)	Peak Position (2θ, °)	B struct. (2θ, °)	Crystallite size (nm)
0.610	0.310	38.110	0.300	28
0.690	0.370	44.300	0.320	26.8
0.750	0.440	64.400	0.310	30.3
0.990	0.540	77.400	0.450	22.6

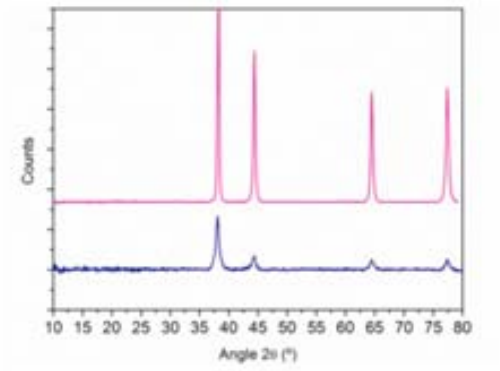

b)

B obs (2θ,°)	B std (2θ,°)	Peak position (2θ,°)	B struct. (2θ,°)	Crystallite size (nm)
0.52	0.31	38.10	0.21	40
0.62	0.37	44.28	0.25	34.3
0.70	0.44	64.62	0.26	36.2
0.76	0.54	77.3	0.22	46.2

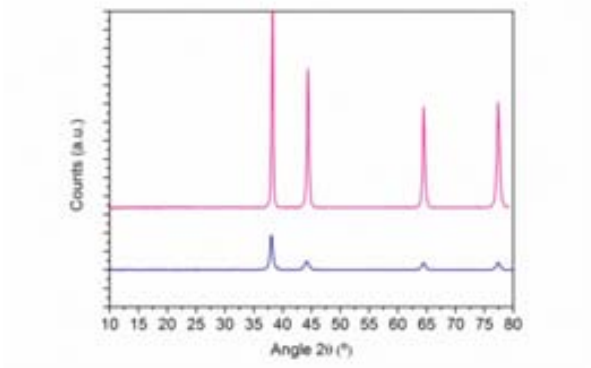

Figure S8. Representative TEM images of Ag_2O@Ag(I)-DLL superstructures.

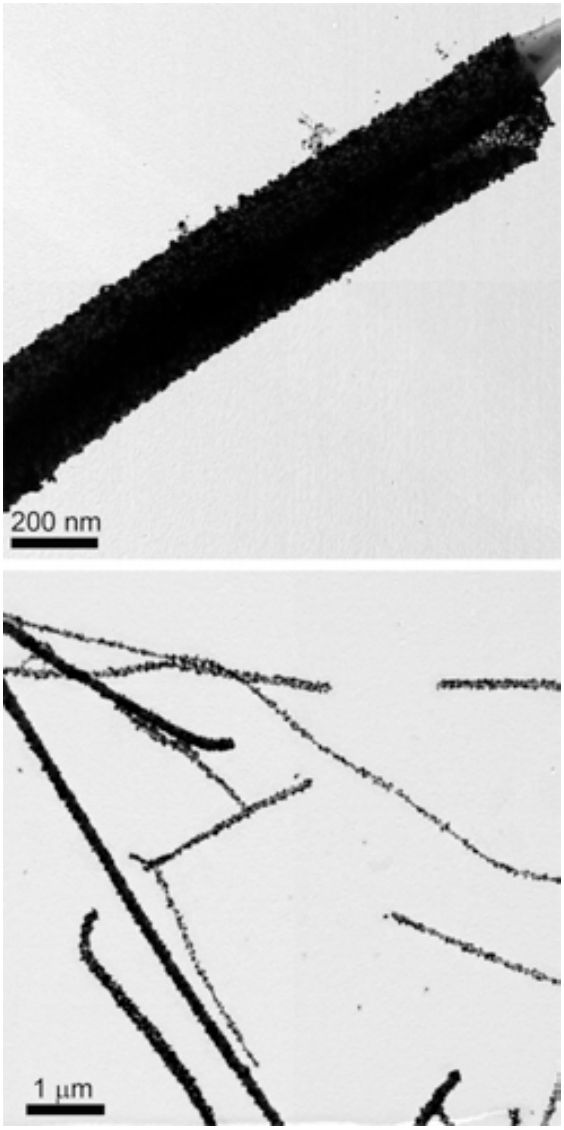

Figure S9. Representative FESEM image (a) and XRPD pattern (b) of Ag(I)-DLL belts after 24 hours at pH 10.5.

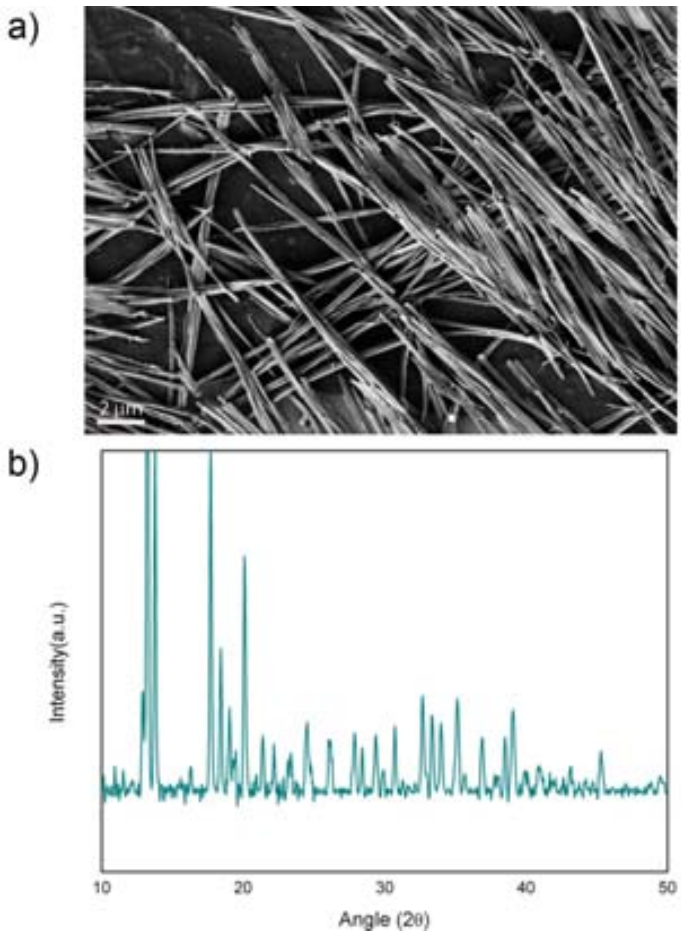

Figure S10. Representative FESEM images of very long, close-packed and continuous Ag@Ag-nanoparticle superstructures. Scale bar: 20 μm and 2 μm (insets).

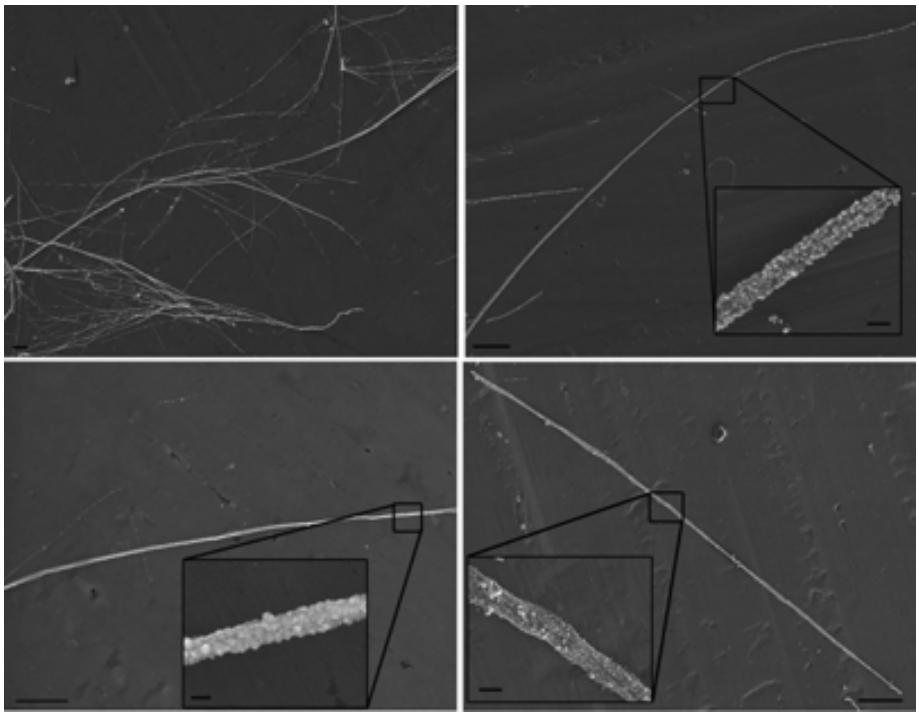

Figure S11. EDX spectrum of Fe_3O_4@Ag(I)-DLL superstructures, indicating the presence of silver and iron (the aluminium peak corresponds to the SEM support).

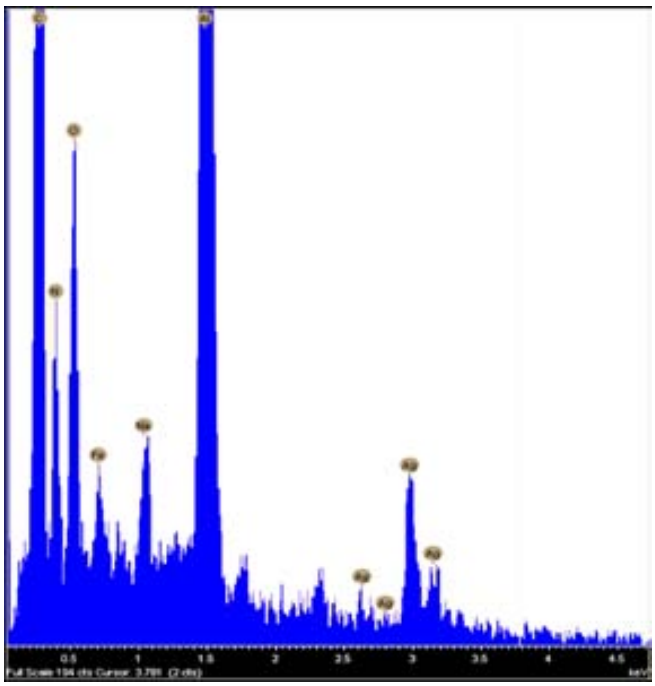

Figure S12. Photos showing the magnetic attraction of Fe_3O_4@Ag-nanoparticle assemblies dispersed in water when they are exposed to a magnet (top left, absence of magnet; top right, presence of magnet). Corresponding FESEM image of collected Fe_3O_4@Ag-nanoparticle assemblies by a magnet. Scale bars: 2 μm.

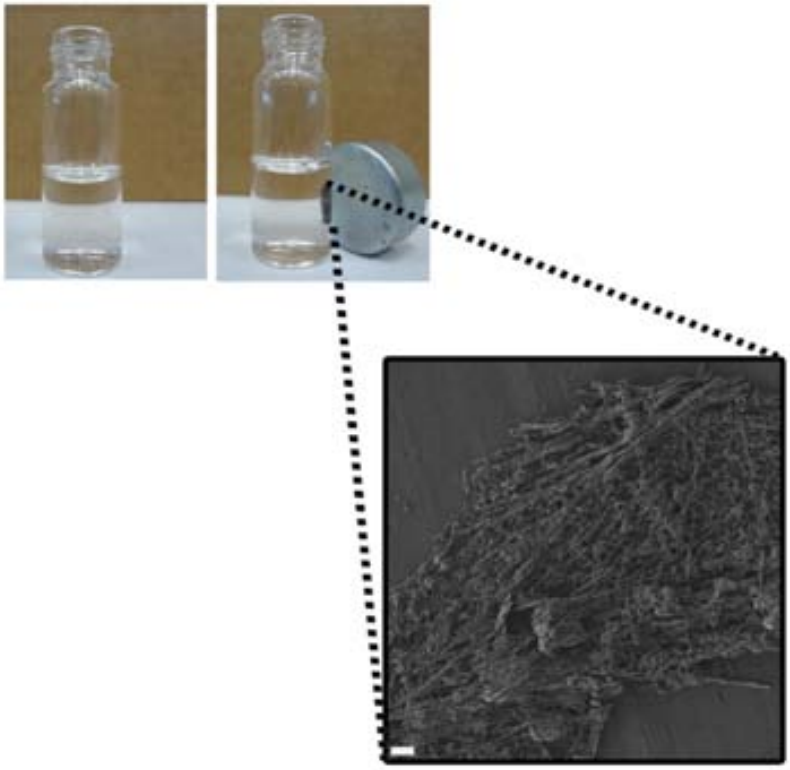

Figure S13. Optical microscopy image of a single Ag(I)-DLL belt bridging the (ii) electrode pair, and plot showing the *I-V* sweeps of the (ii) electrode pair at different temperatures. The (i) electrode pair was also measured during the annealing process: as expected, it did not exhibit any current dependence.

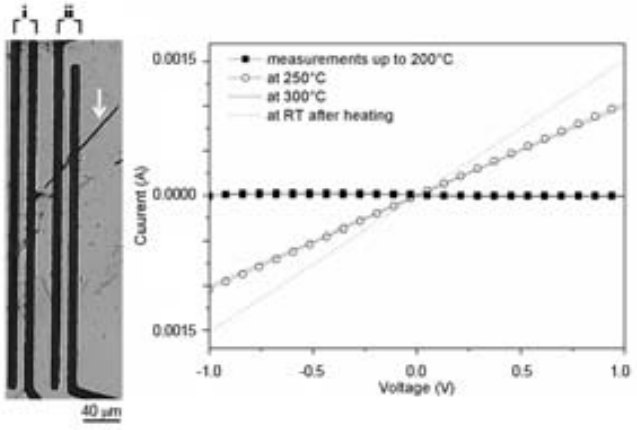

Conclusions

The main objective of this PhD Thesis was the design and synthesis of a new family of nanoscale biomolecule based coordination polymers (BioCPs) together with the development of new synthetic methodologies that enable an advanced control of the self-assembly of BioCPs into 1-D nanostructures.

In the first part of this work we demonstrated that 1-D nanostructures based on metal-AA coordination polymers can be built using metal-coordination interaction as driving force. We took advantage of the well-known capacity of L- or D-aspartic acid (Asp) to generate biorelated CP i.e. long chiral metal–organic nanofibers by reacting them with Cu(II) metal ions. The length and composition of the resulting Cu(II)-Asp nanofibers could be tuned using different synthetic conditions from the fast precipitation to slow diffusion techniques allowing the synthesis of nanofibers with lengths up to 1 cm.

This metal-AA system was used to explore the large possibilities that microfluidics offer as a new tool to control the assembly of metal ion and biomolecules and to create new nanostructures. We demonstrated that this technology, based on the manipulation of fluids at the microscale under laminar flow, enables a fast better-controlled synthesis and possesses the ability to dictate the formation pathway of the assembled structures simply by varying the flow-rate conditions. An exciting possibility of this fabrication approach is the potential to use the additional channels of the microfluidic platform to inject reactants and test the capacity of microfluidics to be used as a parallel synthetic methodology for the fabrication of 1-D metal containing structures at different pathways inside the main channel. Microfluidics proved a versatile and effective way for constraining the reaction environment to favor supramolecular assembly in an elongated 1-D shape. We demonstrated this by synthesizing two more CPs, Zn(II)-4,4'-bipy and Ag(I)-Cys which show different morphologies when they are prepared in batch conditions. The Zn(II)-4,4'-bipy form crystals and Ag(I)-cys form membrane like structures in batch conditions whereas by microfluidics we obtained fibrilar structures.

Exceptionally, these coordination polymer nanofibers can be used as templates for controlling the growth of inorganic nanoparticles. We exposed the Ag(I)-Cys nanofibers collected from the main channel of the microfluidic platform to

TEM electron radiation and obtained the formation of semiconductor silver sulphide nanoparticles chains following the shape of the CP templates.

We further exploited the template properties of Ag(I)-Cys nanofibers and used them to direct the growth and assembly of inorganic nanoparticles along the fibrilar structure using a reduction agent (ascorbic acid) of the metal ions inside the scaffold structure. Microfluidics allows us to precisely control the location of the templated synthesis of the superstructures made of Ag nanoparticles, thereby permitting the direct measurement of their conductivity properties as well as their re-use as a template to grow conductive Ag(I)-tetracyanoquinodinemethane (TCNQ) CP crystals.

Finally we increased the complexity of the BioCPs by using peptides as building blocks. We designed and synthesized 1-D nanobelts exploiting the inherent recognition-template characteristics of peptides. This new class of metal-peptide scaffolds, Ag(I)-DLL belt like crystals, act as dual-templates for the synthesis and assembly of two types of inorganic nanoparticles, one on their surface (crystal face) and the other within their internal structures leading to the formation of multifunctional superstructures. Using to the recognition capacities of the DLL peptide we could successfully cover the exterior of these 1-D nanobelt with Fe_3O_4 nanoparticles, while the selective reduction of the interior Ag(I) ions to Ag lead to the formation of Ag nanoparticles. These internal Ag nanoparticles are well confined and closely packed conditions that favour electrical conductivity in the superstructures. These Ag(I)-DLL belts could be applied to create long (> 100 μm) conductive Ag@Ag nanoparticle superstructures and polymetallic, multifunctional Fe_3O_4@Ag nanoparticle composites that combine the magnetic and conductive properties of the two nanoparticle types.

All the results obtained during this PhD show the high potential of metal-biomolecules association to create new types of nanostructures. Combined with the high level of synthetic control offered by microfluidics these new materials allow opening up new promising pathways for localized synthesis and integration of functional hybrid systems, which could be employed further in optoelectronic applications, sensing, and catalysis. Indeed, the results presented here should also open new possibilities in the ambitious route of biomolecular scaffolding and device fabrication.

Appendix

In the appendix of this PhD Thesis three additional works are presented. These manuscripts are related to the main objectives in a broader sense, but nonetheless add insights to the fields of coordination polymers.

The first work presented was elaborated during my Master Thesis. It was focused on the synthesis and development of new type of metal-organic nanospheres to be used as drug delivery nanocarriers. We demonstrated the release of four different drugs from coordination polymer capsules, and their potential anticancer efficacies in vitro. These results have been reported in the manuscript entitled "Coordination polymer particles as potential drug delivery systems" Chem. Comm. (2010)

A second work reviews the synthesis and characterization of metal-AA nanofibers using microfluidics as a synthetic approach. An article entitled "Metal-biomolecule nanostructures" written by invitation of the Societat Catalana de Quimica (RSCQ) thanks to the award received in the "VII Trobada de Joves Investigadors" Conference.

The last work showcases the potential of microfluidics to control the crystal growth of coordination polymer crystals. We synthesize a new coordination polymer the Cu(II)-4-4'-bipy plate-like single crystals. Furthermore, we showed that the ability to control the contact time between the two reactive streams with a resolution of microseconds allows the freezing of the different stages of the crystallization of CPs, leading to the formation of different crystal shapes, ranging from needles, to frames, to plate-like single crystals. These results have been reported in the manuscript which it is under preparation entitled "Trapping the morphological transitions of a coordination polymer by microfluidics: from needles to frames to plate like single crystals".

.

Coordination polymer particles as potential drug delivery systems†

Inhar Imaz,[a] Marta Rubio-Martínez,[a] Lorena García-Fernández,[a] Francisca García,[b] Daniel Ruiz-Molina,[a] Jordi Hernando,[c] Victor Puntes[a] and Daniel Maspoch*[a]

Received 12th February 2010, Accepted 5th May 2010
First published as an Advance Article on the web 20th May 2010
DOI: 10.1039/c003084h

Micro- and nanoscale coordination polymer particles can be used for encapsulating and delivering drugs. *In vitro* cancer cell cytotoxicity assays showed that these capsules readily release doxorubicin, which shows anticancer efficacy. The results from this work open up new avenues for metal–organic capsules to be used as potential drug delivery systems.

Micro- and nanomaterials able to encapsulate pharmaceutical agents have been actively explored as carriers for therapy to achieve a prolonged and better controlled drug administration.[1] To date, the vast majority of carriers are based on dendrimers,[2] liposomes,[3] organic polymeric[4] and inorganic particles.[5] In this field, we have recently described a general method for encapsulating desired species into micro- and nanoscale coordination polymer particles[6] *via* a coordination polymerization followed by a fast precipitation,[7] and have demonstrated its utility by entrapping organic dyes, quantum dots and magnetic nanoparticles into blue fluorescent spheres (hereafter referred to as Zn(bix)) created by connecting Zn^{2+} metal ions through 1,4-bis(imidazol-1-ylmethyl)benzene (bix) organic ligands. Owing to their small size and ability for entrapping a wide variety of substances, we believe that coordination polymer nanospheres also show promise for encapsulating drugs and thus being used as novel functional carriers for drug delivery.

Thus far, some advances have been made in using metal–organic frameworks (MOFs) as drug delivery systems.[8–10] Férey's group first described promising adsorption and release properties of ibuprofen on bulk hybrid inorganic–organic solids,[8] whereas Lin *et al.* have structured a Pt-based drug at the nanoscale by using it as one building block for creating the framework of a coordination polymer.[9] Very recently, Horcajada, Gref and co-workers have also shown that porous crystalline nano-MOFs can adsorb and release several drugs, thus acting as potential non-toxic drug nanocarriers.[10] Herein we wish to report an alternative general methodology for *in situ* encapsulating unmodified drugs into metal–organic frameworks in the form of micro- and nanoscale spherical particles (Fig. 1a). Doxorubicin (DOX), SN-38, camptothecin (CPT) and daunomycin (DAU) were chosen as archetypical drugs because of their current use for cancer therapy and fluorescence properties that facilitate their monitorization.[11] The encapsulation of all these drugs, their release and initial *in vitro* cellular studies serve as excellent tests to preliminary illustrate the use of coordination polymer spheres as drug delivery systems.

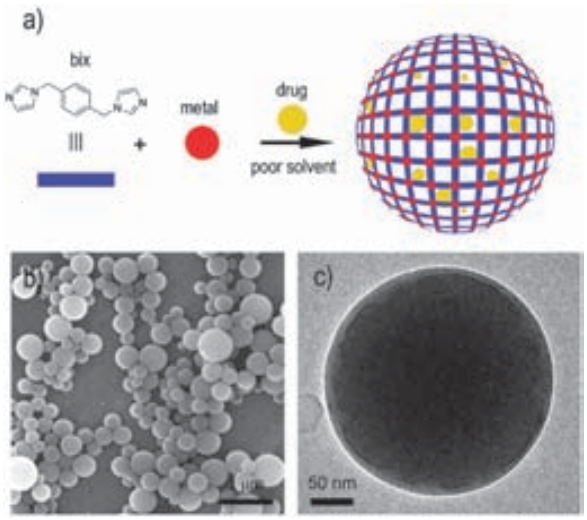

Fig. 1 (a) Schematic illustration describing the encapsulation of drugs into metal–organic spheres created by the connection of metal ions, such as Zn^{2+}, through multitopic organic ligands, such as bix. (b) SEM and (c) TEM images of a representative colloidal solution of DOX/Zn(bix) spheres.

In a typical experiment, metal–organic Zn(bix) spheres with encapsulated DOX [DOX/Zn(bix)], SN-38 [SN-38/Zn(bix)], CPT [CPT/Zn(bix)] and DAU [DAU/Zn(bix)] were prepared by addition of an aqueous solution of $Zn(NO_3)_2{\cdot}6H_2O$ to an ethanolic solution of bix containing the drug ($c \sim 3.3 \times 10^{-3}$ M) under stirring at room temperature. The resulting spheres were then purified by centrifugation and washed several times with ethanol. This process was repeated until no fluorescence signal from free, non-encapsulated drug was detected in the supernatant solution. Fig. 1b and c show representative scanning (SEM) and transmission (TEM) electron microscopy images of the resulting coordination polymer spherical capsules, whose diameter was controlled from 100 to 1500 nm by adjusting the initial concentrations of the reactants.[6]

The entrapment of DOX, CPT, SN-38 and DAU into these spheres was confirmed by both absorption and fluorescence measurements, and encapsulation efficiencies up to 21% of the initial drug concentration were measured. In all cases, the fluorescence emission spectrum of the colloids matches that of

[a] *Centro de Investigación en Nanociencia y Nanotecnología (ICN-CSIC) Campus UAB, 08193 Bellaterra, Spain. E-mail: daniel.maspoch.icn@uab.es*
[b] *Departament de Química, Universitat Autònoma de Barcelona, Campus UAB, 08193-Bellaterra, Spain*
[c] *Institut de biotecnologia i de biomedicina, Campus UAB, 08193-Bellaterra, Spain*

† Electronic supplementary information (ESI) available: Detailed synthetic and experimental procedures, SEM, TEM, fluorescence optical and DLS images, and *in vitro* cytotoxicity assay curves. See DOI: 10.1039/c003084h

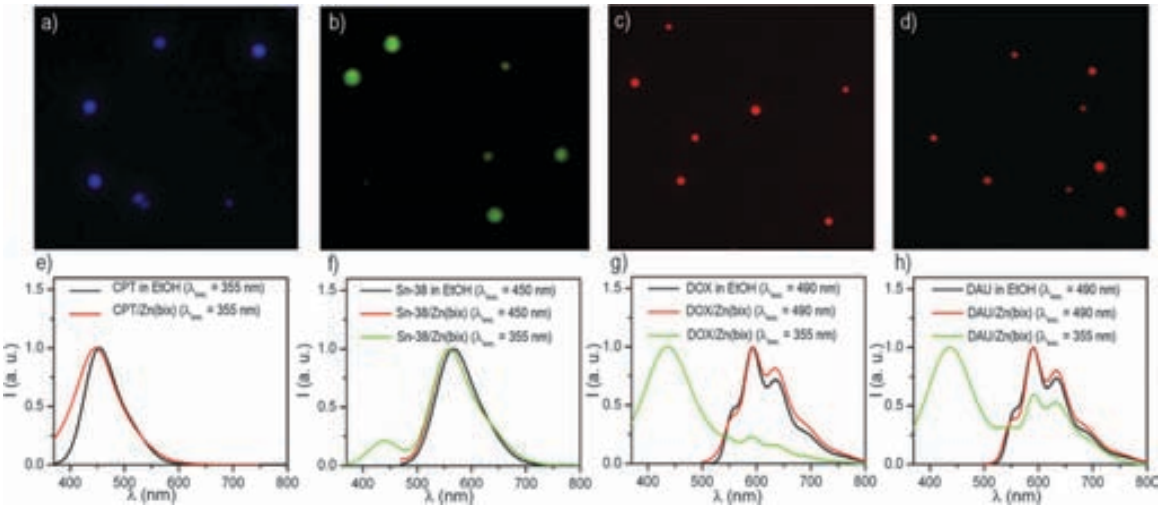

Fig. 2 (a–d) Fluorescence optical microscope images of (a) CPT/Zn(bix), (b) SN-38/Zn(bix), (c) DOX/Zn(bix), and (d) DAU/Zn(bix) spheres. (e–h) Fluorescence emission spectra of (e) free CPT and CPT/Zn(bix) (collected at λ_{exc} = 355 nm), (f) free SN-38 and SN-38/Zn(bix) (collected at λ_{exc} = 450 and 355 nm), (g) free DOX and DOX/Zn(bix) (collected at λ_{exc} = 490 and 355 nm), and (h) free DAU and DAU/Zn(bix) (collected at λ_{exc} = 490 and 355 nm).

free DOX, DAU, SN-38 and CPT (Fig. 2e–h), which results in blue [CPT/Zn(bix)], green [SN-38/Zn(bix)] and red [DOX/Zn(bix) and DAU/Zn(bix)] emitting spheres upon selective excitation of the drug (Fig. 2a–d). Furthermore, since bare Zn(bix) particles already show blue luminescence when excited at 355 nm, broadband fluorescence spectra are measured upon UV excitation, which show contributions from both the drug and Zn(bix) spheres emission (Fig. 2e–h).

To investigate the drug release from coordination polymer particles, we first prepared colloidal solutions of 300 ± 23 m in diameter DOX/Zn(bix) and SN-38/Zn(bix) spheres in phosphate buffered saline solution (PBS) at pH = 7.4, and the resulting colloids were placed in a dialysis bag (cut-off molecular weight: 3500) at 37 °C. Both dispersions were dialyzed against 100 mL of PBS for 48 hours. The DOX and SN-38 release profiles measured by fluorescence spectroscopy are depicted in Fig. 3a. At 37 °C, Zn(bix) spheres containing those drugs showed a fast release of ~ 80% at 8 hours, followed by an additional release of ~ 15% over the next 2 days. The DOX release from Zn(bix) spheres was also perceptive with naked eyes because the initial violet-pink colour of the colloid gradually changed to a white colour characteristic of bare Zn(bix) spheres.

A number of factors can contribute to the release of DOX and SN-38 from coordination polymer particles, including desorption of drug adsorbed on the sphere surface, diffusion of drug through the coordination polymeric sphere, and erosion of the sphere. Similar to other encapsulating systems, the fast release can be attributed to both desorption and diffusion of drug as well as to the gradual erosion of Zn(bix) spheres in PBS for subsequent diffusion from the surface or through developing pores.[12] To confirm the erosion of Zn(bix) spheres at 37 °C, a colloidal PBS solution of DOX/Zn(bix) spheres was maintained at this temperature and sequentially investigated by SEM and dynamic light scattering (DLS). Fig. 3b shows representative SEM images showing the time-dependent degradation of such spheres. As can be seen there, the surface of Zn(bix) spheres becomes gradually rougher and

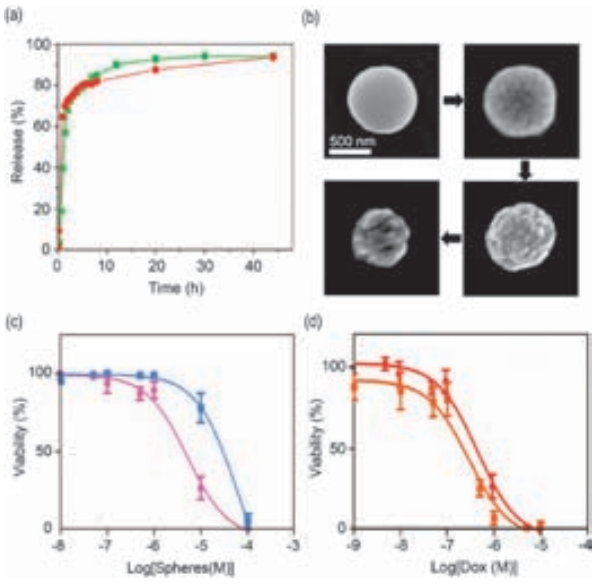

Fig. 3 (a) *In vitro* release profile of DOX and SN-38 from DOX/Zn(bix) (dot, red) and SN-38/Zn(bix) (square, green) spheres incubated in pH 7.2 PBS at 37 °C. (b) SEM micrographs of DOX/Zn(bix) spheres taken at 1, 4, 8, and 24 hours, showing representative degradation in pH 7.4 PBS at 37 °C. (c and d) *In vitro* cytotoxicity assay curves after 24 h for HL60 cells obtained by plotting the cell viability percentage against the (c) Zn(bix) (square, blue) and DOX/Zn(bix) (dot, pink) concentration and (d) the DOX release from DOX/Zn(bix) spheres (dot, red) and DOX (square, orange) concentration.

more cracked, reducing their overall volume with time, as also confirmed by DLS. Noticeably, such process was found to slow down at room temperature.

Our abilities to synthesize coordination polymer spheres for encapsulating drugs and the capacity to release them prompted us to preliminary evaluate their anticancer efficacies. We performed *in vitro* cytotoxicity assays on HL60 (Human promyelocytic leukemia cells) cell line with 24 h and 48 h of

incubation (Fig. 3c). Treatment of HL60 with Zn(bix) and DOX/Zn(bix) spheres did not lead to any appreciable cell death after 24 h and 48 h of incubation at concentrations ranging from 0.01 μM to 0.5 μM. However, between 0.5 μM and 10 μM, some differences were observed between both types of spheres. In this range, the DOX from DOX/Zn(bix) spheres acts on the cells notably reducing the cell-viability down to 25% at 10 μM, whereas the Zn(bix) spheres gave a cell-viability close to 80%. Overall, DOX/Zn(bix) spheres gave a half maximal inhibitory concentration (IC_{50}) of 5.2 μM and 4.5 μM after 24 h and 48 h of incubation, respectively, whereas the non-encapsulated Zn(bix) spheres had respective IC50 values of only 62.5 μM and 99.9 μM. These results demonstrate that at this range the Zn(bix) matrix has a low contribution on the cytotoxic effects, and confirms that delivered DOX from DOX/Zn(bix) spheres is the major responsible of their cytotoxic activity against HL60.

To further evaluate the cytotoxic effect of the DOX released from DOX/Zn(bix) spheres, HL60 cells were also treated with free DOX. Fig. 3d shows the dose response of free DOX and DOX from DOX/Zn(bix) spheres after 24 h of incubation.[13] In both cases, an appreciable cell death was observed at concentrations ranging from 0.1 μM and 10 μM. Indeed, both free DOX and DOX from DOX/Zn(bix) spheres gave similar IC_{50} values of 0.3 μM and 0.4 μM, respectively. These results suggest that DOX/Zn(bix) spheres have similar cytotoxic effects against HL60 than free DOX. Once encapsulated, the DOX released from the metal–organic DOX/Zn(bix) spheres can induce the cell death in cancer cells.

In summary, the presented results show that coordination polymer micro- and nanospheres constitute a novel and promising type of materials to be used as functional matrices for encapsulating a large panel of drugs. We first demonstrate the release of drugs from coordination polymer capsules, and their potential anticancer efficacies *in vitro*. As coordination polymers with a broad range of structures and functionalities can be prepared, this approach could be generalized for obtaining metal–organic delivery systems with novel compositions and functionalities. Future work includes the *in vivo* studies of drug delivery and targeting of coordination polymer particles as well as the development of metal–organic capsules with novel properties and functionalities.

This work was supported by projects VALTEC08-2-003, MAT2009-13977-C03 and CTQ2009-07469. D. M. and I. I. thank the Ministerio de Ciencia y Tecnología for respective RyC and JdC contracts. M. R.-M. and L. G.-F. thank the Institut Català de Nanotecnologia for research fellowships. The authors thank the Servei de Microscopia of the UAB.

Notes and references

1 (*a*) R. Langer, *Nature*, 1998, **392**, 5; (*b*) T. M. Allen and P. R. Cullis, *Science*, 2004, **303**, 1818.
2 (*a*) J. M. J. Fréchet, *J. Polym. Sci., Part A: Polym. Chem.*, 2003, **43**, 3713; (*b*) S. Svenson and D. A. Tomalia, *Adv. Drug Delivery Rev.*, 2005, **57**, 2106.
3 (*a*) F. M. Muggia, J. D. Hainsworth, S. Jeffers, P. Miller, S. Groshen, M. Tan, L. Roman, B. Uziely, L. Muderspach, A. Garcia, A. Burnett, F. A. Greco, C. P. Morrow, L. J. Paradiso and L.-J. Liang, *J. Clin. Oncol.*, 1997, **15**, 987; (*b*) D. D. Lasic and D. Papahadjopoulos, *Science*, 1995, **267**, 1275.
4 (*a*) J. Panyam and V. Labhasetwar, *Adv. Drug Delivery Rev.*, 2003, **55**, 329; (*b*) B. J. Nehilla, P. G. Allen and T. A. Desai, *ACS Nano*, 2008, **2**, 538.
5 (*a*) H. Otsuka, Y. Nagasaki and K. Kataoka, *Adv. Drug Delivery Rev.*, 2003, **55**, 403; (*b*) I. Brigger, C. Dubernet and P. Couvreur, *Adv. Drug Delivery Rev.*, 2002, **54**, 631.
6 (*a*) I. Imaz, J. Hernando, D. Ruiz-Molina and D. Maspoch, *Angew. Chem., Int. Ed.*, 2009, **48**, 2325.
7 (*a*) M. Oh and C. A. Mirkin, *Nature*, 2005, **438**, 651; (*b*) X. Sun, S. Dong and E. Wang, *J. Am. Chem. Soc.*, 2005, **127**, 13102; (*c*) H. Maeda, M. Hasegawa, T. Hashimoto, T. Kakimoto, S. Nishio and T. Nakanishi, *J. Am. Chem. Soc.*, 2006, **128**, 10024; (*d*) K. H. Park, K. Jang, S. U. Son and D. A. Sweigart, *J. Am. Chem. Soc.*, 2006, **128**, 8740; (*e*) H. Wei, B. Li, Y. Du, S. Dong and E. Wang, *Chem. Mater.*, 2007, **19**, 2987; (*f*) S. Jung and M. Oh, *Angew. Chem., Int. Ed.*, 2008, **47**, 2049; (*g*) M. Oh and C. A. Mirkin, *Angew. Chem., Int. Ed.*, 2007, **45**, 5492; (*h*) Y.-M. Jeon, G. S. Armatas, J. Heo, M. G. Kanatzidis and C. A. Mirkin, *Adv. Mater.*, 2008, **20**, 2105; (*i*) I. Imaz, D. Maspoch, C. Rodríguez-Blanco, J.-M. Pérez-Falcón, J. Campo and D. Ruiz-Molina, *Angew. Chem., Int. Ed.*, 2008, **47**, 1860.
8 (*a*) P. Horcajada, C. Serre, M. Vallet-Regí, M. Sebban, F. Taulelle and G. Férey, *Angew. Chem., Int. Ed.*, 2006, **45**, 5974; (*b*) P. Horcajada, C. Serre, G. Maurin, N. A. Ramsahye, F. Balas, M. Vallet-Regi, M. Sebban, F. Taulelle and G. Férey, *J. Am. Chem. Soc.*, 2008, **130**, 6774.
9 W. J. Rieter, K. M. Pott, K. M. L. Taylor and W. Lin, *J. Am. Chem. Soc.*, 2008, **130**, 11584.
10 P. Horcajada, T. Chalati, C. Serre, B. Gillet, C. Sebrie, T. Baati, J. F. Eubank, D. Heurtaux, P. Clayette, C. Kreuz, J.-S. Chang, Y. K. Hwang, V. Marsaud, P.-N. Bories, L. Cynober, S. Gil, G. Férey, P. Couvreur and R. Gref, *Nat. Mater.*, 2010, **9**, 172.
11 (*a*) M. Muggia, J. D. Hainsworth, S. Jeffers, P. Miller, S. Groshen, M. Tan, L. Roman, B. Uziely, L. Muderspach, A. Garcia, A. Burnett, F. A. Greco, C. P. Morrow, L. J. Paradiso and L.-J. Liang, *J. Clin. Oncol.*, 1997, **15**, 987; (*b*) H. L. Wong, R. Bendayan, A. M. Rauth, Y. Li and X. Y. Wu, *Adv. Drug Delivery Rev.*, 2007, **59**, 491.
12 (*a*) R. P. Batycky, J. Hanes, R. Langer and D. A. Edwards, *J. Pharm. Sci.*, 1997, **86**, 1464; (*b*) N. Faisant, J. Siepmann and J. P. Benoit, *Eur. J. Pharm. Sci.*, 2002, **15**, 355; (*c*) J. Wang, B. M. Wang and S. P. Schwendeman, *J. Controlled Release*, 2002, **82**, 289; (*d*) C. Berkland, K. Kim and D. W. Pack, *Pharm. Res.*, 2003, **20**, 1055.
13 The concentration of delivered DOX from DOX/Zn(bix) spheres was calculated according to a maximum encapsulation efficiency of 21% with respect to the initial DOX concentration used for the encapsulation process, and a release of 88% (for 24 h) of the encapsulated DOX, according to the *in vitro* delivery studies.

SUPPORTING INFORMATION

Coordination Polymer Particles as Potential Drug Delivery Systems

Inhar Imaz,[a] Marta Rubio-Martínez,[a] Lorena García-Fernández,[a] Francisca García,[b] Daniel Ruiz-Molina,[a] Jordi Hernando,[c] Victor Puntes,[a] Daniel Maspoch[a]

Centre d'Investigació en Nanociència i Nanotecnologia (ICN-CSIC),[a] Institut de Biotecnologia i Biomedicina,[b] and Departament de Química,[c] Universitat Autònoma de Barcelona, Campus UAB, 08193 Bellaterra, Spain

SUMMARY

S1. Experimental procedures for preparation of Zn(bix) spheres, encapsulation of fluorescent drugs in the Zn(bix) spheres, *in vitro* release studies and *in vitro* cytotoxicity assays

MATERIALS

All reagents were purchased from ALDRICH and used without further purification unless otherwise indicated. All HPLC quality solvents used were purchased from ROMIL, and used without further purification.
The 1,4-bis(imidazol-1-ylmethyl)benzene (bix) was synthesized according to literature procedures P. K. Dhal, F. H. Arnold, *Macromolecules* **1992**, *25*, 7051.

PREPARATION OF Zn(bix) SPHERES

Zn(bix) spheres were fabricated by addition of an aqueous solution (5 mL) of $Zn(NO_3)_2 \cdot 6H_2O$ (150 mg, 0.5 mmol) to an ethanolic solution (25 mL) of bix ligand (121 mg, 0.5 mmol) under stirring at room temperature. Immediately, the precipitation of a white solid was observed. After 1 minute, ethanol (50 mL) was added into the reaction mixture to stabilize the spheres. The resulting spheres were then purified by centrifugation and washing three times with ethanol. Zn(bix) particles were collected as a white solid or redispersed in ethanol to obtain a white colloid. Zn(bix) spheres with different average sizes were prepared using the same synthetic methodology and by simply modifying the concentration of both $Zn(NO_3)_2 \cdot 6H_2O$ and bix ligand. Anal. (%) Calcd. for $C_{14}H_{14}O_6ZnN_6$: C, 39.31; H, 3.30; N, 19.65; Found: C, 40.25; H, 3.57; N, 19.52. IR (ATR, cm^{-1}): 2980 (s), 1618 (s), 1524 (s), 1426 (m), 1332 (s), 1092 (s), 954 (m), 654 (m).

ENCAPSULATION IN Zn(bix) SPHERES

Drug/Zn(bix) spheres were obtained by addition of an aqueous solution (5 mL) of $Zn(NO_3)_2 \cdot 6H_2O$ (150 mg, 0.5 mmol) to an ethanolic solution (25 mL) of Bix (121 mg, 0.5 mmol) containing the drug (DOX, DAU, CPT and SN38) (3.3×10^{-3} M) under vigorous stirring at room temperature. For all drugs, the resulting encapsulated metal-organic systems were purified by centrifugation and washed three times with ethanol. The encapsulated systems were finally redispersed in ethanol or phosphate buffer to obtain the corresponding colloidal solutions.

IN VITRO RELEASE STUDIES

A dialysis bag (cut-off molecular weight: 3500) containing the Drug/Zn(bix) spheres (c ~ 6 mg/mL) dispersed in phosphate buffered saline solution (PBS; pH = 7.4) was placed in 100 mL of PBS (pH = 7.4; dialysate) at 37 ºC under light stirring. Throughout the experimental procedure, the solution inside the dialysis bag was also agitated by magnetic stirring. To determine the increase of Drug concentration diffused through the dialysis bag, 2 mL of external PBS solution were taken from the dialysate at prefixed times, and each aliquot was analyzed by fluorescence spectroscopy. To minimize the effects of Drug decomposition in solution, every four hours the external solution of PBS was changed.

CHARACTERIZATION

Scanning electron microscopy (SEM) images were collected on a scanning electron microscope (HITACHI S-570) at acceleration voltages of 10-15 kV. Aluminium was used as support. Transmission electron microscopy (TEM) images were obtained with a JEOL JEM 2010F. The measurements were performed at room temperature and a voltage of 200 kV. Optical and fluorescence images were obtained using a Zeiss Axio Observer Z-1 inverted optical/fluorescence microscope with motorized XY stage, Hg lamp excitation source, AxioCam HRc digital camera and standard filters. Fluorescence emission spectra of Drugs/Zn(bix) were measured at $\lambda_{exc.}$= 470 nm in PBS by means of a custom-made spectrofluorimeter, where a Brilliant (Quantel) pulsed laser is used as excitation source, and the emitted photons are detected in an Andor ICCD camera coupled to a spectrograph.

IN VITRO CYTOTOXICITY ASSAYS

In order to determine the cytotoxic effects of the metal-organic systems, we first seed the acute promyelocytic leukemia cell line (HL-60, ATCC No. CCL-240) into 96-well plates in a volume of 100 µl with 1 x 10^4 cells per well. Afterwards, the effect of the Zn(bix) and DOX/Zn(bix) spheres in cell viability was evaluated by redispersion of the capsules in culture medium to obtain the final concentrations tested (100 µM, 10 µM, 5 µM, 1 µM, 0,5 µM, 0,1 µM, 0,05 µM and 0,01 µM) in a volume of 100 µl/well, and subsequent addition of these solutions to the seed cells for incubation times of 24 h and 48 h at 37ºC. After the incubation times, 20 µl of MTT solution (EZ4U kit, cell proliferation and cytotoxicity assay, from Biomedica) were added to each well, and after 3 hours of reaction, the cell viability was determined by measuring the absorbance at 450 nm using the *Victor*^{3} multilabel plate reader from PerkinElmer. The cytotoxicity experiments were performed at least three times with four repeated incubations per well plate. From the cytotoxicity assays, viability measurements of cells at variable dose of spheres were used to calculate the IC_{50} in order to obtain the concentration of spheres that gives a response half way between the minimum and the maximum values of viability. For this goal, the

data was analyzed by the software GraphPad Prism 5 to use a nonlinear regression with a pharmacological model of dose response stimulation with variable slope. This model assumes that the dose response curve has a standard slope, equal to a Hill slope (or slope factor) of 1.0.

S2. SEM (Scanning Electron Microscope) and TEM (Transmission Electron Microscope) images of DOX/ZnBix spheres.

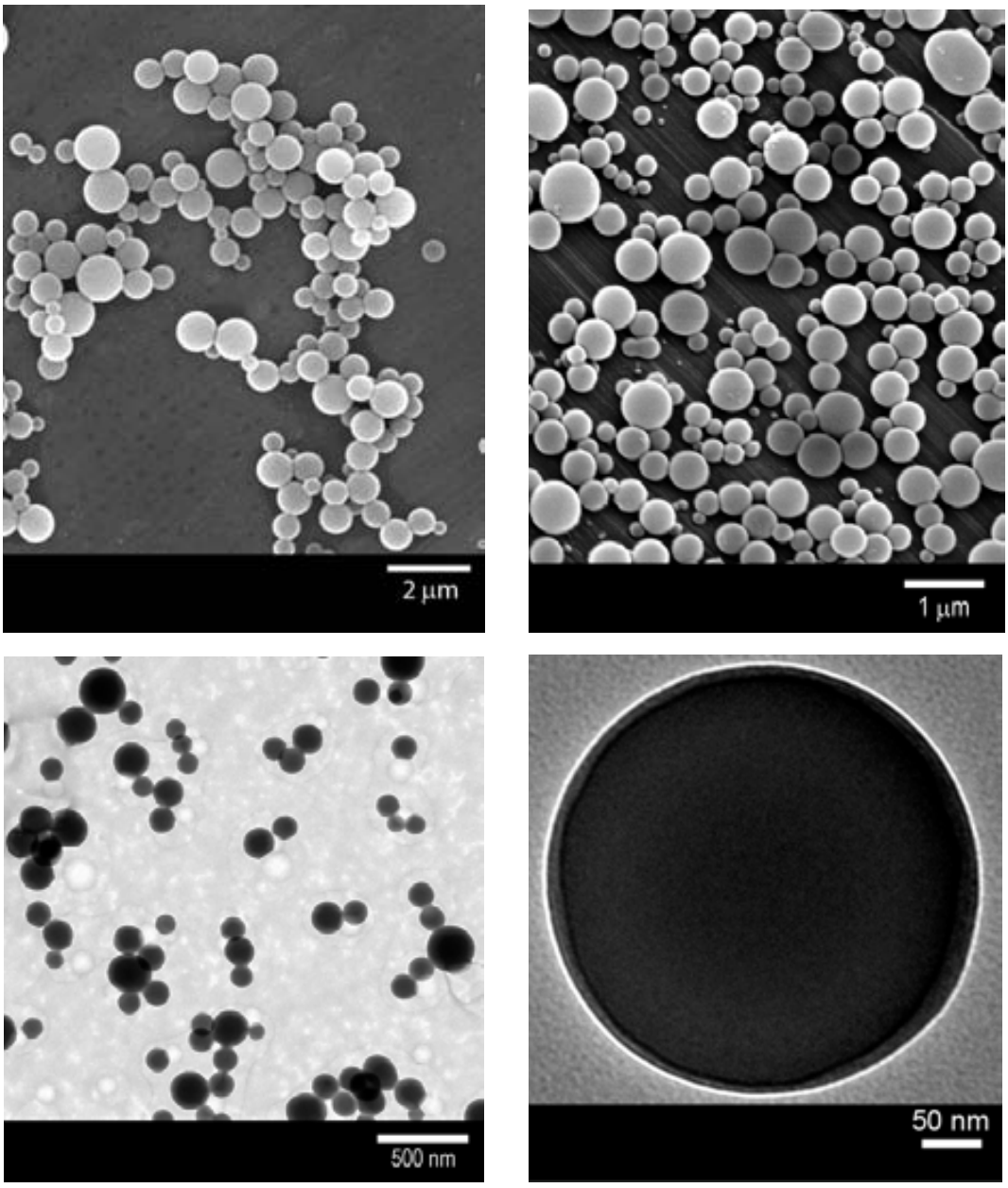

S3. Fluorescence optical microscope images of DOX/Zn(bix), DAU/Zn(bix), CPT/Zn(bix) and SN38/Zn(bix) spheres collected at: DOX/Zn(bix) and DAU/Zn(bix): λ_{exc}= 540 - 552 nm and λ_{em} > 590 nm; CPT/Zn(bix): λ_{exc}= 359 - 371 nm and λ_{em} > 397 nm; SN38/Zn(bix): λ_{exc}= 450 - 490 nm and λ_{em} > 515 nm.

DOX/Zn(bix)

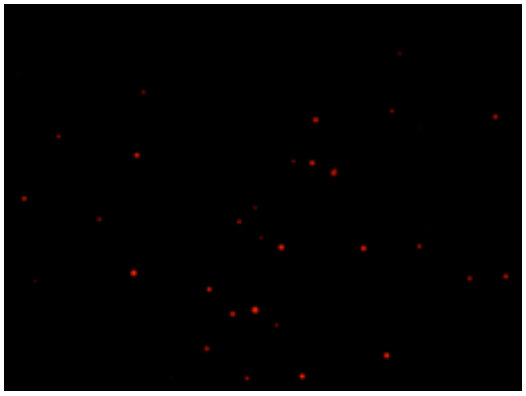

DAU/Zn(bix)

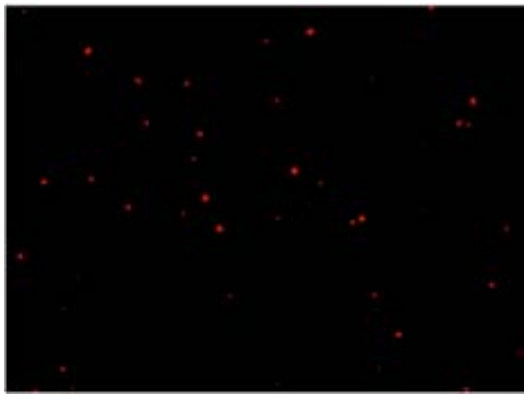

CPT/Zn(bix)

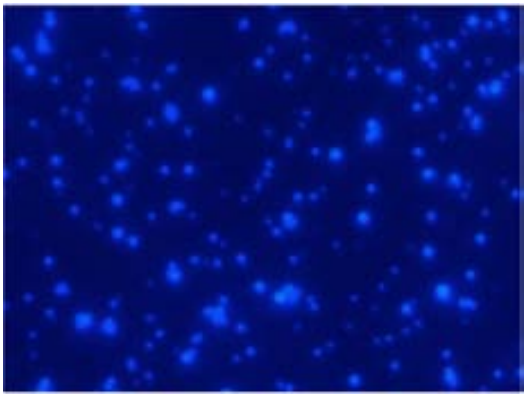

SN38/Zn(bix)

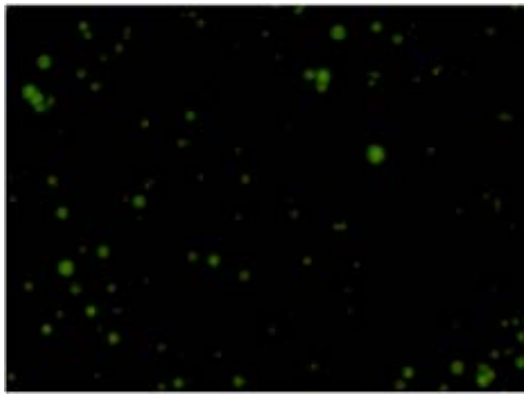

S4. Dynamic light scattering (DLS) measurements of a dispersion of DOX/Zn(bix) spheres in PBS at 37 ºC at different times (0, 8 and 24 hours).

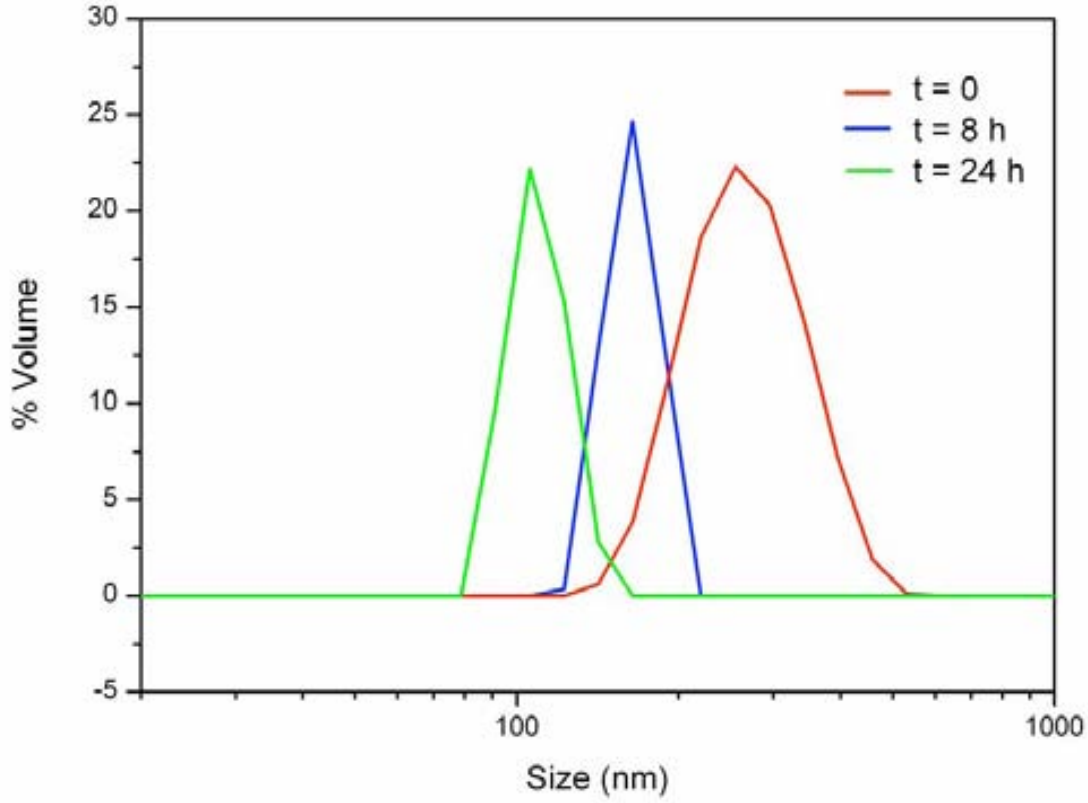

S5. In vitro cytotoxicity assay curves after 48 hours for HL60 cells obtained by plotting the cell viability percentage against Zn(bix) and DOX/Zn(bix) concentration.

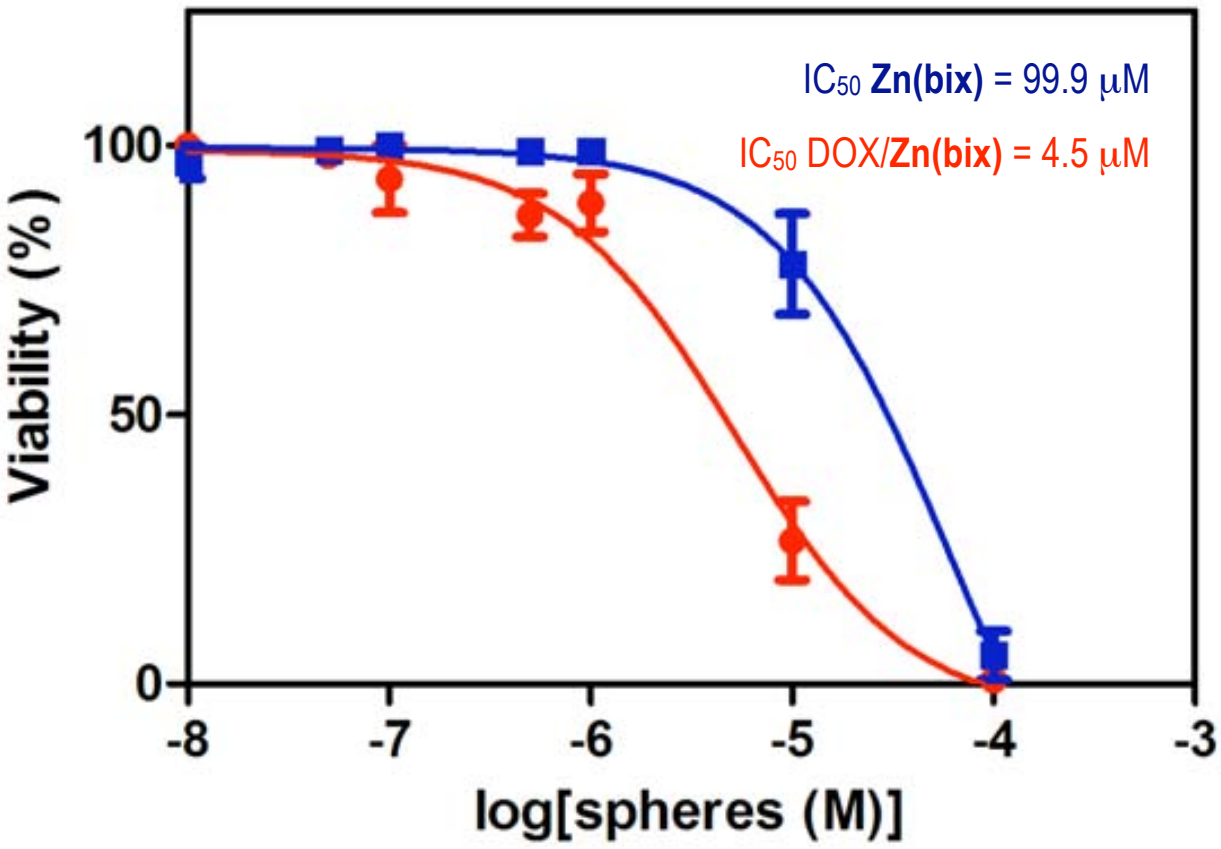

/ 0) / 1 12 + 3 4 5 / 167
1
4
6
7

( )

(

, (-

( ) .

)

01

2 , ,

34 4 1 4 5
5 4 4 34 5 1 54 4
14 5 1 4 5 1 4
1 1 6 4 4 4 1
5 4 4 34 5
5 4 1 5 4
4 4 4 4 1 4 1
34 4 4 5 1 4 4 4 4
4 1 01

15 4 1 1

((

))

)

)

0 5 / + ,

E (

E /

E F G G E/ C 9B1A6 E H

I J 67 A6. B; B 69C D , J 67 A6. B17 C7C

(, -

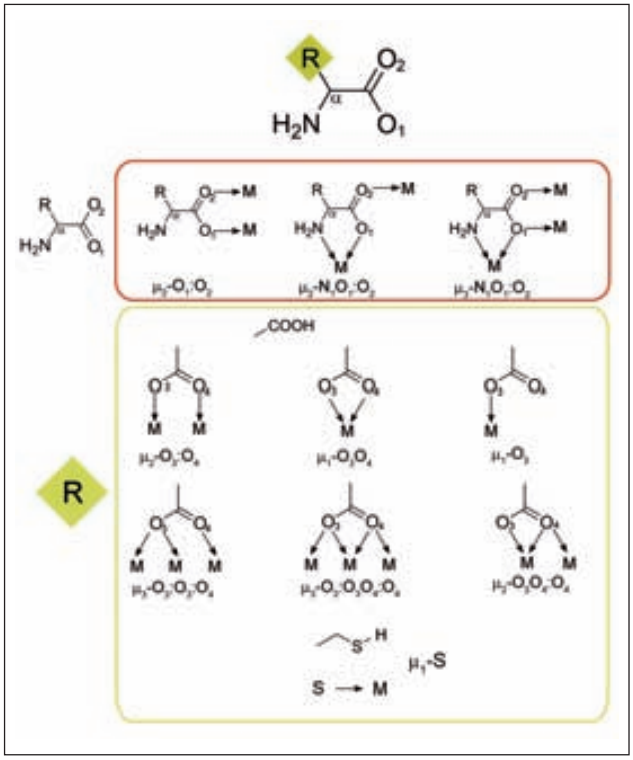
R
O2
α
H2N
O1
COOH
μ1-S
S → M

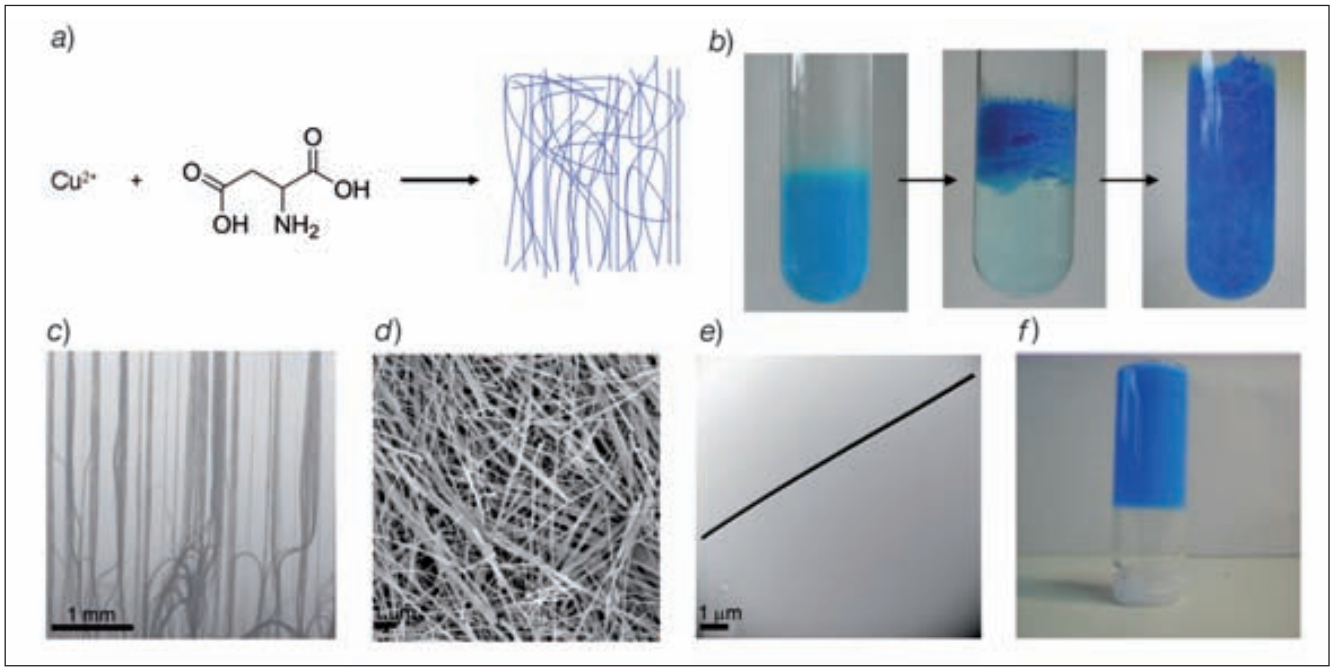

89: : -) E 8: E 8: .:
) E 8: :) E 8: : : / 0 / I) E 8: /:D
-)

/.

αM))
N4ENOE 4N)
) -
) , 08 1:7E
K -
, , ,
F
8 :) , 8 1: -)
) E 8:
) E 8:)
,)
) E 8: 8 4 :C E 8:
1 1)
3 E 8: P 8 5P:
1 ,)
) 3 D
8/ 0: 8/ I:) , E 8: (
) E 8:)
199 499) E - 1;44 1. B; -1
O 1796 1 6; B -1 I ,
) E 8: E 8:
(K 8 1: Æ 8 :8N4 :Ş

) E 8 :

, ,

1 / (K L

8E: (

B)

E 3

E

-) E

, E 8 :A

F)

,

) ,)

)

99C/

) I

4/))

) E 8 : K

/

- .) /

3 , ,

)) (K

19

,

)

) - ,

) ,

5

5

, 11

+

-)

,)( ) E 8 :

14

,

(

E 8 : (, ,

, F (,

. B ,

8 6 : 3) E 8 :

3 6.

/ 0)

) (K

5

,

5)

)

) 5)

D)

))))

)

F) E 8 :

-)))(

8: L

8E :14 I ,) E)

8 : K)

- (

8: E

)) 8: E

19 .9 8 6 : 3)

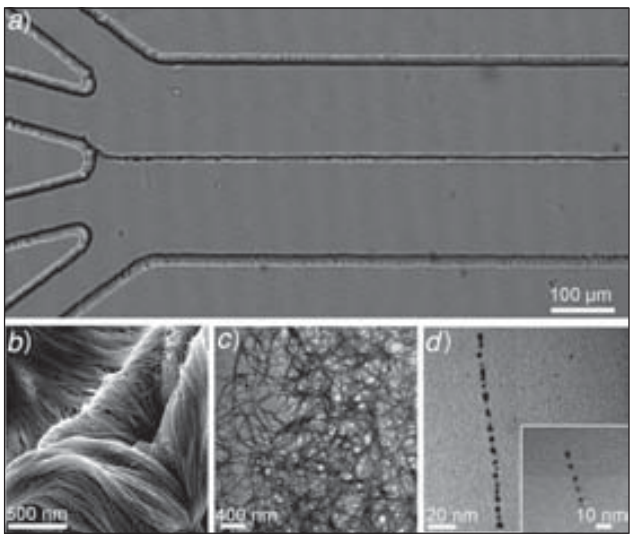

89: :)

E 8 : .: / 0)

E 8 :) : / I

) 8: E) : / I

4

) 8: E

))
)

E

,
-)
)

)
+ ,
( ) 8: E

,
4) , -
8 6 : 14
) ,)

,

L

, L E
2 +
2 + 3 ,
/ E 0 E (
) , / F
G -)

0

1 T U VT 0 V *2* (
34 4667
4 2 WE *5* *3* 4CB1
6 : E VE) E V V/ 5 (
37 4A1 . : W / VT 5 V V
/ W E (*8* 141B : 0 X / V
T / 3 VN VX 3 *9* (**A**
: A947
7 V0) / / V2 V D V
0 3 V/ 5 (*3* C4BC
. E 5 3 VG VX U F V
/ 5 0 (*3* 6; A6
; 2V3 2V 0 (74B
5 19 196B 4914 B9
C V0) / / VX (2 V) 5 GV
/ 5 *9* (*4* 1B444
B / / V) 5 G VX T VH 2
9 (*5* *8* ; C9
A : 5 U 5 VF) D 3 *9* (**A** @
. ACC . : WU W VG U W/ V3 *A(*
: 4C11
19 : 2VG) 5 2 **C** *34* ; 7B
. : N V+ W VT
(*8* 1.
11 : + 3 2V 5 VG G 0 5 V
5 + *: :* 44. . . : T + 2 V
0 DVX / *: 8* B6
14 + 3 2V0) / / VN F V
V/ 5 V5 + *9* (
44 741;

,

D 2 ,

E 4

, 8G 1AB4: H)
F G
E / E 5 /
3))

4 8N + G D K 1ACB: H) 499. F
G , -)
0 E (E 3
-

D 2 , 8 G 1ACB: H F G
84994: Z 3 4996
K E / G 2
H 5 G))
) 5 K
T W F 3 8G : D
) 499B
) 3 499A) IN + D U
(/ / (. . 2 . A / /
. A 0 E (5 G) 8/ E
:
) (K

E 4 8 1AC; : H) 1AAA F
F G 8F G: E /
G 4997 5))) E / W
U F 8E F : E 8E :
0 E (, E / E

Trapping the morphological transitions of a coordination polymer crystal by microfluidics: from needles to frames to plate-like single crystals.

M. Rubio-Martínez, I. Imaz, D B. Amabilino, N. Domingo, J. Puigmartí-Luis, and D. Maspoch.**

Controlling the synthesis of coordination polymers (CPs) and metal-organic frameworks (MOFs) to the micro- and nanometer length scale is an on-going challenge to further expand their scope to myriad applications, from drug-delivery[1] and medical imaging to sensors[2] and membranes[3], and open up novel avenues to more traditional storage[4], capture[5], separation[6] and catalysis applications[7]. Analogously to inorganic nanoparticles, precise control over their composition, size and shape is crucial for optimizing their functions at these length scales. This level of control should be attained by simultaneously advancing on 1) understanding how they are formed (nucleation and crystal growth) and 2) finding new chemical strategies, methodologies and tools that enable a better control of their crystallization.

We propose here that laminar flow microfluidic (LFM) technology can be an alternative approach to control the synthesis of CP/MOF crystals with different, unprecedented shapes at the micro- and nanometer length scale by trapping different stages of their crystal growth. LFM enables the realization of reactions through the formation of a stable interface between two reactive streams into a microchannel, which contact time (residence time into the channel) can be precisely controlled over the microsecond scale by varying their flow rates. LFM has previously been used to demonstrated biological and biochemical processes like polymerase[8] chain reaction or screens for protein crystallization conditions[9] or to induce redox and polymerization reactions at the interface of two co-flowing reactants[10] among other examples. Moreover, a recent study shows as microfluidics is an optimal technology for crystallize and resolved biological macromolecules in situ of the microfluidic chips due to the compatibility of the devices with the collecting of X-ray diffraction.[11] Our group has recently demonstrated that microfluidics technique, besides being a powerful technique to control the assembly of the metal ions and organic building blocks to form nanoscale metal-organic systems, can allow the control and the modification of the morphology of a metal-organic materials compared to conventional synthetic methods.[12]

Here we demonstrated the ability in the control of the contact time between the two reactive streams with a resolution of microseconds which allowing the freezing of the different stages of the crystallization of CPs/MOFs. Considering each one of these stages as an individual *crystallisation frame* of the complete crystallisation process of a certain CP/MOF, one can begin to imagine of using LFM to perform a frame-by-frame study for a better understanding of how these materials crystallize. In addition, controlling the crystallization of CPs/MOFs at different stages of their crystal growth can also allow isolating them into different crystal shapes. We have demonstrated these concepts by choosing a CP/MOF with formula [Cu(4,4'-bpy)] (**1**). It was chosen as the test case scenario because of its fast synthesis when two solutions, one containing the Cu(II) ions and the other containing the 4,4-bipyridine ligand, are put into contact. In particular, macroscopic plate-like crystals of **1** suitable to single-crystal X-ray diffraction were prepared by diffusing an ethanolic solution of 4,4'bipy into an aqueous solution of $Cu(NO_3)_2 \cdot 6H_2O$. **1** shows an infinite coordination polymer with two-dimensional in where the Cu (II) ions have an octahedral coordination with two nitrates groups located in the equatorial plane and the 4,4'bipy molecules occupy the axial position (Figure 1a). This material serves as an excellent model system to evaluate how one can use LFM to monitor the crystal growth of a CP/MOF and isolate its morphological transitions from nanoscale needles to unprecedented hollow frames to plate-like single crystals.

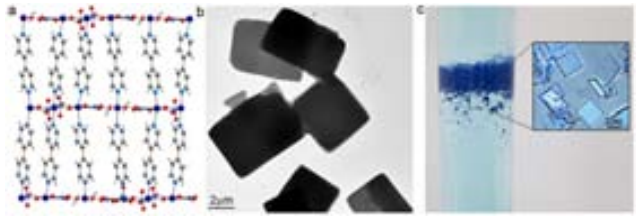

Figure 1. a) View along the b axis of a fragment of the two-dimensional coordination polymer of Cu(II)-4-4'-bipy crystals resolved with synchrotron light. b) TEM image of the crystals demonstrating the plate type shape of the crystals, synthesized using the interfacial coordinative polymerization method in a test tube c) Photograph showing the aqueous/organic interface in which the blue Cu(II)-4-4'-bipy crystals are formed; The inset corresponds to an optical microscope image of the crystals deposited on the walls of the test tube.

The microfluidic-supported synthesis and crystallization of **1** was carried out in a planar microfluidic device that consists of four input channels and one outlet channel, imprinted in poly-dimethylsiloxane (PDMS) and covered by a glass plate.

In a typical experiment, crystals of **1** were prepared by injecting an aqueous solution of $Cu(NO_3)_2 \cdot 3H_2O$ (100 mM) and an ethanolic solution of 4,4'bypi (100 mM) via a syringe pump system. We define the flow rates (all in µL/min) and with the following abbreviation of the channels: flow (1), Q_1; flow (2), Q_2; flow (3),

[*] M. Rubio-Martínez, N. Domingo, I. Imaz, Prof. D. Maspoch
Institut Català de Nanociencia i Nanotecnologia, ICN2,
Esfera UAB, Campus UAB, 08193 Bellaterra, Spain
E-mail: daniel.maspoch@icn.cat
Homepage: www.nanoup.org

J. Puigmartí-Luis
Institut de Ciència de Materials (ICMAB-CSIC) Esfera UAB,
08193 Bellaterra, Spain
E-mail: jpuigmarti@icmab.es

[**] We thank the financial support from MINECO-Spain, under projects MAT2012-30994 and CTQ2011-16009-E. The authors thank the Microscopy Service of the UAB. I.I., N.D. and J.P.L thank the MINECO for RyC contracts. M.R.M. thanks the Catalan Institut of Nanoscience and Nanotechnology for her research fellowship.

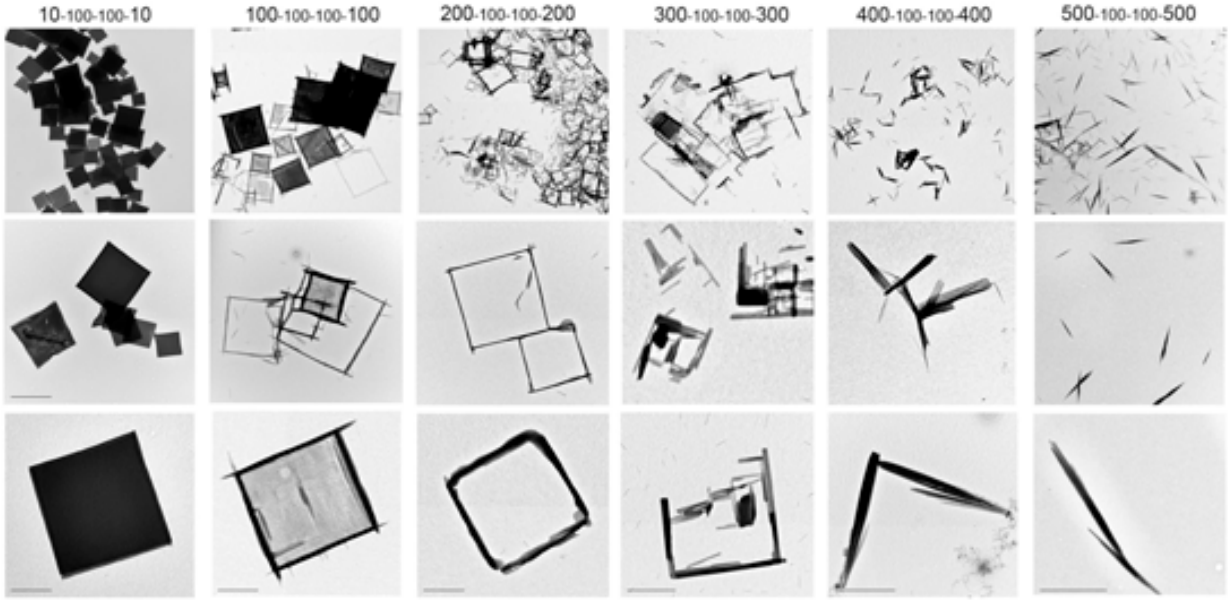

Figure 2. Sequence of FESEM images of Cu(II)-4-4'-bipy crystals fabricated in the micro-reactor at different flow-rate ratios with three different magnification levels, showing the different trapped crystalline phases from needles [500;100;100;500] to single crystal plates [10;100;100;10] (right to left). In the flow rate configuration [200;100;100;200] perfect isolated empty frames were created. The remaining intermediate flow rate-ratios yielded transitional stages, highlighting the crystal growth of the system. As the flow rates of t he auxiliary flows increases, the mechanism formation up to the simplest needles can be captured. The scale bar is 2 μm.

Q_3; and flow 4, Q_4. Cu(II)-4,4'-bipy crystals were initially prepared by injecting a solution of $Cu(NO_3)_2 \cdot 3H_2O$ (100mM) in water in Q_2 and a ethanolic solution of 4,4'-bipy (100mM) in Q_3. Both were accomplished by an auxiliary flow with the corresponding solvents, Q_1 and Q_4 at the same flow rate of the reactants. In this first experiments the different flow rates were fixed at 100 μL/min, i.e. [100;100;100;100]. The crystals growth in the main channel in the interface of Cu(II) and 4,4'-bipy solutions and were collected and analysed by Transmission Electron Microscopy (TEM). A close examination of TEM images revealed a mixture of a majority of squares plates 2.80 ± 0.52 μm and square empty frames 2.95 ± 0.71 μm with an edge around 200 nm of thickness. Although the square plates were expected, because their similarity with the morphology of the crystals obtained by slow formed quasi totally of empty perfect square frames with an average size around 6 μm^2.

Finally at XXXX the frames start to be filled in the flow rate configuration [100;100;100;100]. Under these experimental conditions 60 % of the diffusion techniques, the unexpected presence of empty frames suggested that the use of microfluidics influence dramatically the formation of Cu-4,4'-bipy based coordination polymers. To discard the presence of another phase or the presence of impurities a capillary of the sample in mother liquor (to avoid the presence of reactants due to the evaporation of the solvents) was prepared and X-ray powder diffraction measurement was performed. The resulting pattern reveals a perfect match between the experimental diffractogram of the sample obtained by laminar flow and the diffractogram simulated from the single crystal growth by slow diffusion (see Figure S1 of the Supporting Information). This suggests that the different types of crystals present in the sample correspond to different crystal growth stages of the Cu-4,4'-bipy and that the control of the contact time between the two reactive streams with a resolution of microseconds that offers microfluidics can be used to freeze different stages of the crystallization of CPs/MOFs.

In order to understand the formation of this coordination polymer and dissect the crystal growth mechanism, we perform different experiments, modulating the flow of microfluidics, i.e. the contact time, between 10 and 500 μL/min. We analysed the different samples by TEM. As is shown in figure 2, the differences are considerable (Figure 2). At the higher flow rates (500 μL/min), the sample is only constituted by nanoscopic crystalline needles. The length of the needles is around 500 nm and the diameter around 20 nm. The first frames appear when the experiment is performed at a flow rate of 300 μL/min. The sample analysed by TEM shows the coexistence of needles with incomplete empty frames. These frames present two or three edges but in general there are not complete. The needles disappear at 200 μL/min and the obtained solid in these conditions is frames are empty. Moreover in some of the filled frames the material density (indicated in the TEM images by the different darkness) is higher on the edges of the square frames than in the interior what suggest that in the crystal growth process after the formation of the square frame, the filling of the interior

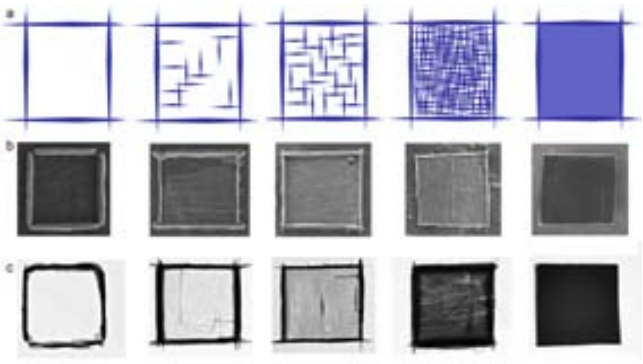

Figure 3. a) Schematic view of an individual frame showing the growth of the needles inside the frame. b) FESEM sequence images in where the details of the surfaces can be appreciate. c) TEM sequence images showing the density of the material in the different stages of growth. The scale bar is 1 μm.

occurs layer by layer. Finally at low flow intensities, that quasi simulate static conditions, all the crystals obtained show square shape as perfectly filled marks. Due to the exceptionality/curiosity of the different collected images and subsequently of the observed phenomena, we certified that the all the shapes observed corresponds to the 4,4'-bipy-Cu coordination polymer solved by single crystal X-ray analysis.

For all the samples we confirmed by X-ray powder diffraction (PXRD) that although the shape is totally different depending on the used flow, the obtained phase is the same (see Figure S1 of the supporting information) preparing a capillary of the wet solid collected from the microfluidics platform. All the diffractogram correspond to the 4,4'-bipy-Cu phase. Complementary characterization of 2-D Cu(II)-4-4'-bipy crystals by infrared (IR) spectroscopy (Figure S2), thermogravimetric analysis (Figure S3) and elemental analysis confirmed the obtaining of the same structure with both synthetic methodologies used. The elemental analysis of the crystals corroborated that Cu(II) ions and 4-4'-bipy ligands are arranged in 2-D structure with the general formula $[Cu(4\text{-}4'\text{-}bipy)_2(NO_3)_2]n$. The chemical composition was determined by energy dispersive X-ray (EDX) spectroscopy, which confirmed the presence of copper, oxygen, nitrogen, and carbon (Figure S4). The coordinative polymerization of Cu(II) metal ion through the 4,4'-bipy ligands was studied by IR spectroscopy. The IR spectrum of Cu(II)-4,4'-bipy includes bands in the range 1639-1333 cm^{-1} associated with the pyridine ring stretching vibrations and bands at 1302 and 812 cm^{-1}, which are attributed to the presence of coordinated nitrate groups.

According to the different electron microscopy studies performed on the samples synthesised at different flow rates, the crystal growth process occurs in two steps. A first step consist on the building of the frame then during the second step the empty frames are filled leading to final square plates.

At the present stage, to fully understand the mechanism of the crystal growth of the final plates obtained, a study by atomic force microscopy (AFM) to complete the SEM study was performed. The crystals obtained by microfluidics using [10;100;100;10], [100;100;100;100] and [200;100;100;200] as a flow rates were deposited in a TEM grid to determine the topography of the crystals. The different surface areas were scanned in AFM non-contact mode. The topography images reveal that the filling process can be considered as a special layer-by-layer process. Each layer is formed following a mechanism, not observed until today to our knowledge, in which a plate or crystalline layer is formed by the simultaneous parallel and perpendicular growth of needles. In general the formation of a single crystal is based on the formation of crystal which growth in one preferential direction, (for example needles that growth in parallel. Each layer exhibit 90º rotation respected the neighbouring once (Figure 4). In conclusion, we described an exciting method based in microfluidics with which is possible to guide the assembling between the metal ion and the organic linker to form coordination polymers. Also this approach allows the obtaining of the desired reaction demonstrate that by changing the flow-rate ratios in the microchannel we are able to control and trapped the different shapes.

We believe that microfluidics is an exciting approach which can overcome an important tool in the synthesis chemistry field in order to dictate the final product and. Also this study opens up new opportunities in the synthesis and crystallization of new materials and especially in this next international crystallographic year.

Experimental Section

The reagents $Cu(NO_3)_2 \cdot 3H_2O$ and 4,4'-bipyridil were obtained from Sigma-Aldrich Co. High purity EtOH was purchased from Teknokroma. Deionised Milipore Mili-Q water was used in all experiments. Infrared (IR) spectra were performed on a FTIR Tensor 27 InfraRed spectrophotometer (Bruker) equipped with a Bruker Golden Gate diamond ATR (Attenuated Total Reflection) cell. Scanning electron microscopy (SEM) images were collected on a scanning electron microscope (ZEISS EI MERLIN FE-SEM) at acceleration voltages of 0.2-30 kV. Aluminium was used as support. Transmission electron microscopy (TEM) images were obtained with a JEOL JEM 1400. The X-Ray EDX microanalysis was performed on an Oxford Instruments INCA energy SEM system. The measurements were performed at room temperature and a voltage of 120 kV. XRD measurements were performed with an X'Pert PRO MPD diffractometer (Panalytical) especially configured for in-plane diffraction. Elemental analysis was performed with CHNS Thermo Scientific Flash 2000 model. For details of the synthesis and experiments, see the Supporting Information. Further details on the crystal structure resolution may be obtained from the Cambridge Crystallographic Data Centre, on quoting the depository number CCDC.

Received: ((will be filled in by the editorial staff))
Published online on ((will be filled in by the editorial staff))

Keywords: Coordination polymer · microfluidic · keyword 3 · keyword 4 · keyword 5

[1] a) P. Horcajada, C. Serre, M. Vallet-Regí, M. Sebban, F. Taulelle, G. Férey, *Angew. Chem. Int. Ed*. **2006**, *45*, 5974-5978. b) D. Zhao, S. Tan, D. Yuan, W. Lu, Y. H. Rezenom, H. Jiang, L. Q. Wang, H. C. Zhou, *Adv. Mater*. **2010**, *23*, 90-93.

[2] a) W. J. Rieter, K. M. L. Taylor, H. An, W. Lin, *J. Am. Chem. Soc.* **2006**, 128, 9024-9025. b) R. V. Uljin, A.M. Smith, *Chem. Soc. Rev*. **2008**, *37*, 664-675.

[3] R. E. Morris, *Nat. Chem*. **2011**, *3*, 347-348.

[4] a) H. Wu, W. Zhou, T. Yildirim, *J. Am. Chem. Soc*. **2007**, *129*, 5314-5315. b) B. Kesanli, Y. Cui, M. R. Smith, E. W. Bittner, B. C. Bockrath, W. Lin, *Angew. Chem. Int. Ed*. **2005**, *44*,72-75. c) R. Lyndon, K. Konstas, B. Ladewig, P. Southon, C. J. Kepert, M. R. Hill, *Angew. Chem. Int. Ed*. **2013**, *52*, 3695-3698. d) J. R. Li, R. J. Kuppler, H. C. Zhou, *Chem. Soc. Rev*. **2009**, *38*, 1477-1504.

[5] Y. Liu, Z. U. Wang, H-C. Zhou, *Greenhouse Gas Sci. Technol*. **2012**, *2*, 239-259.

[6] S. R. Venna, M. A. Carreon, *J. Am. Chem. Soc*. **2009**, *132*, 76-78.

[7] a) C. Janiak, *Dalton Trans*. **2003**, *14*, 2781-2804. b) H. L. Jiang, Q. Xu, *Chem. Commun*. **2011**, *47*, 3354-3370.

[8] R. H. Liu, J. Yang, R. Lenigk, J. Bonanno, P. Grodzinski, *Anal. Chem*. **2004**, 76, 1824-1831.

[9] C. L. Hansen, E. Skordalakes, J. M. Berger, S. R. Quake, *Pros. Natl. Acad. Sci.* **2002**, *99*, 16531-16536.

[10] C. Sauter, K. Dhouib, B. Lorber, *Cryst. Growth Des*. **2007**, *7*, 2247-2250.

[11] F. Pinker, M. Brun, P. Morin, A.-L. Deman, J.-F. Chateaux, V. Oliéric, C. Stirnimann, B. Lorber, N. Terrier, R. Ferrigno, C. Sauter, *Cryst. Growth Des*. **2013**, DOI: 10.1021/cg301757g.

[12] a) J. Puigmartí-Luis, M. Rubio-Martínez, U. Hartfelder, I. Imaz, D. Maspoch, P. S. Dittrich, *J. Am. Chem. Soc*. **2011**, *133*, 4216-4219.

Supporting Information

Trapping the morphological transitions of a coordination polymer by microfluidics: from needles to frames to plate-like single crystals.

Marta Rubio-Martínez, Inhar Imaz, D.B. Amabilino, Neus Domingo, Josep Puigmartí-Luis,* Daniel Maspoch,*

Part S1. Materials and methods

The reagents $Cu(NO_3)_2 \cdot 3H_2O$ and 4,4'-bipyridil were obtained from Sigma-Aldrich Co. Hight purity EtOH was pursached from Teknokroma. Deionised Milipore Mili-Q water was used in all experiments. Infrared (IR) spectra were performed on a FTIR Tensor 27 InfraRed spectrophotometer (Bruker) equipped with a Bruker Golden Gate diamond ATR (Attenuated Total Reflection) cell. Scanning electron microscopy (SEM) images were collected on a scanning electron microscope (ZEISS EI MERLIN FE-SEM) at acceleration voltages of 0.2-30 kV. Aluminium was used as support. Transmission electron microscopy (TEM) images were obtained with a JEOL JEM 1400. The X-Ray EDX microanalysis was performed on an Oxford Instruments INCA energy SEM system. The measurements were performed at room temperature and a voltage of 120 kV. XRD measurements were performed with an X'Pert PRO MPD diffractometer (Panalytical) especially configured for in-plane diffraction. Elemental analysis was performed with CHNS Thermo Scientific Flash 2000 model.

Fabrication of the microfluidic device

The microfluidic channels employed in our experiments were moulded into polydimethylsiloxane (PDMS, SYLGARD® 184 Silicone Elastomer Kit) using an SU-8 (2015, Microchem) master form fabricated with standard photolithographic techniques. Before attaching the cured and structured PDMS mould to a patterned electrode surface, inlet holes connecting to the microfluidic channels were punched with a Biopsy puncher. Non-bonded chips were used, which enabled peeling of the PDMS mould before the thermal treatment processes were conducted on the localized superstructures. The dimensions of the microchannels were 50 μm ×50 μm for the four input microchannels, and 250μm × 50 μm for the main reactor channel. The total length of the main reactor channel was 9mm.

Preparation of 2D Cu(II)-4,4'-bipy single-crystals using interfacial polymerization synthesis

In a typical experiment, a solution in ethanol of 4,4'bipy (100 mM) and an aqueous solution of $Cu(NO_3)_2 \cdot 6H_2O$ (100 mM) were prepared. The solutions were transferred carefully to a test tube generating an interface of water/ethanol between the two layers. After 4 days, dark blue crystals start to form at the liquid-liquid interface. Anal. (%) Calcd. for C16H10CuN4O7 C, 33.19; H, 2.79; N, 15.49. Found: Cu, 17.57; C, 34.05; H, 2.59; N, 14.98.

Preparation of 2D Cu(II)-4,4'-bipy crystals using laminar flow

The experiments to synthetized Cu-4-4'bypi crystals are carried out in a planar microfluidic device that consists of four input channels and one outlet channel, imprinted in poly-dimethylsiloxane (PDMS) and covered by a glass plate. The solutions of reactants were injected via a syringe pump system at different flows rates. We define the flow rates (all μL/min) with the following abbreviations: flow (1), Q_1; flow (2), Q_2; flow (3), Q_3; and flow 4, Q_4. In a typical synthetic procedure, Cu-4-4'bypi crystals were initially prepared by injecting an aqueous solution of $Cu(NO_3)_2 \cdot 3H_2O$ (100mM) in Q_2 and an ethanolic solution of 4-4'bypi (100mM) in Q_3. Both were accomplished by an auxiliary flow with the corresponding solvents, Q_1 and Q_4 at the same flow rate of the reactants. The crystals growth in the main channel in the interface of Cu(II) and 4,4'-bipy solutions. The crystals were collected and analysed by Transmission Electron Microscopy (TEM). The TEM images show that the crystals have a special square shape but with a curious morphology. The frame shows a higher density on the TEM images than the centre of the square. This suggests that the centre of the square is thinner than the frame.

Single-Crystal: X-ray single-crystal diffraction data for Cu-4-4'bipy were collected on the BM16 Spanish line of ESRF synchrotron in Grenoble. The H atoms have been included in theoretical positions but not refined. The low max value is due to the data collections that have been performed in the BM16 line with only a phi scan. The structure was solved by direct methods using the program SHELXS-97. The refinement and all further calculations were carried out using SHELXL-97. Empirical absorption corrections were applied in both cases with SCALEPACK.

Part S2. Experimental section

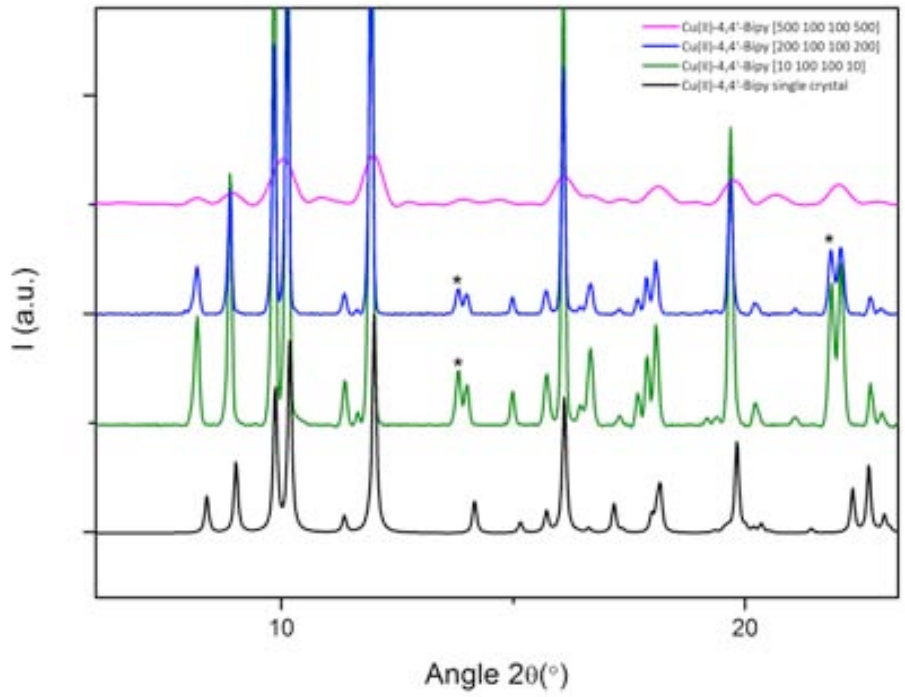

Figure S1. XRPD spectra of Cu(II)-4,4'-bipy crystals synthesized by interfacial polymerization approach (black) and microfluidics at [10;100;100;10], [200;100;100; 200] and [500;100; 100; 500] showing the same diffractogram. The peaks marked by stars correspond to 4,4'-bipy.

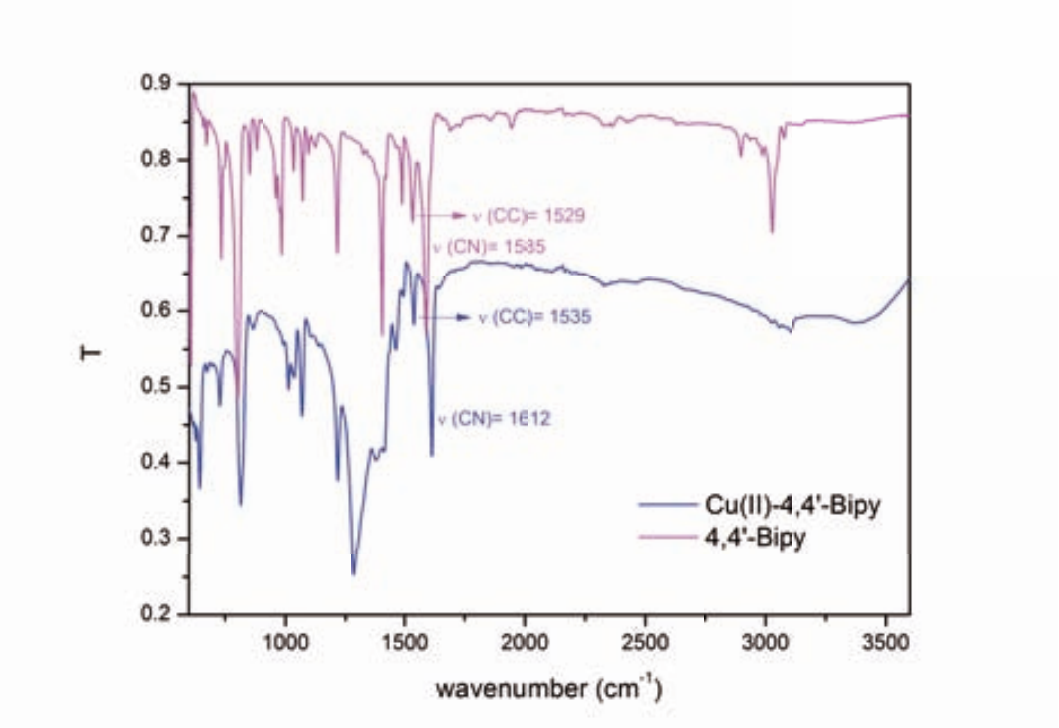

Figure S2. Infrared spectra of 4,4'-bipy (pink) and Cu(II)-4,4'-bipy crystals (blue).

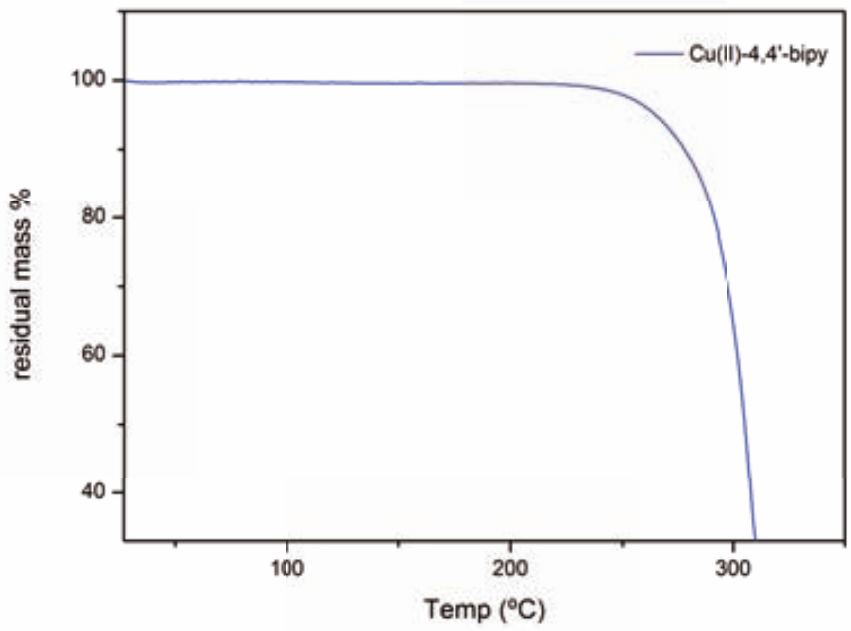

Figure S3. Thermogravimetric analysis of Cu(II)-4,4'-bipy crystals (heating rate: 0.5ºC /min).

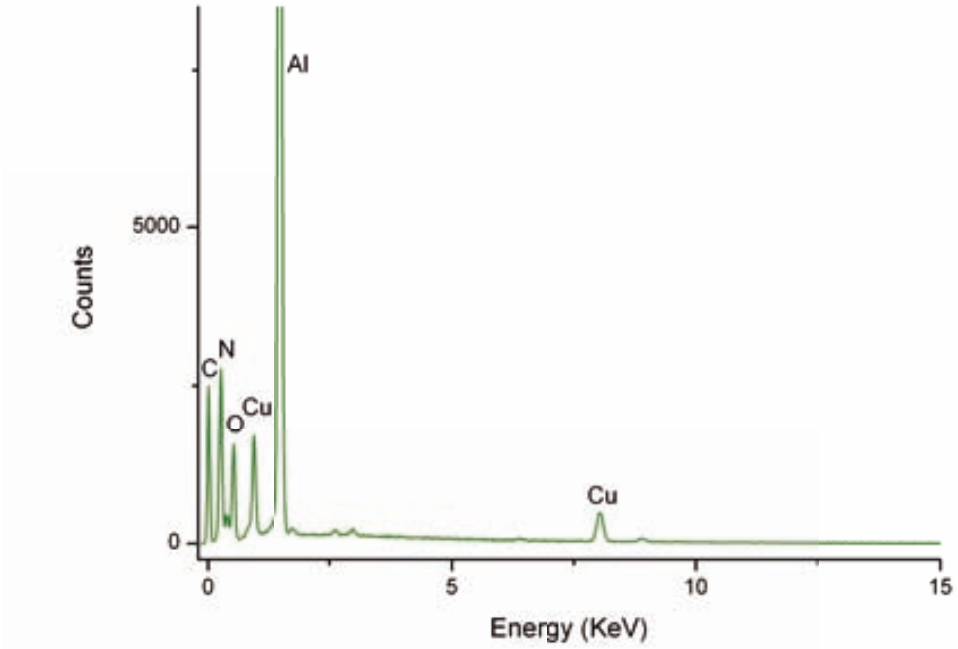

Figure S4. EDX spectrum of Cu(II)-4,4'-bipy crystals showing the presence of the copper and nitrogen. (The Aluminium peak corresponds to the SEM grid).

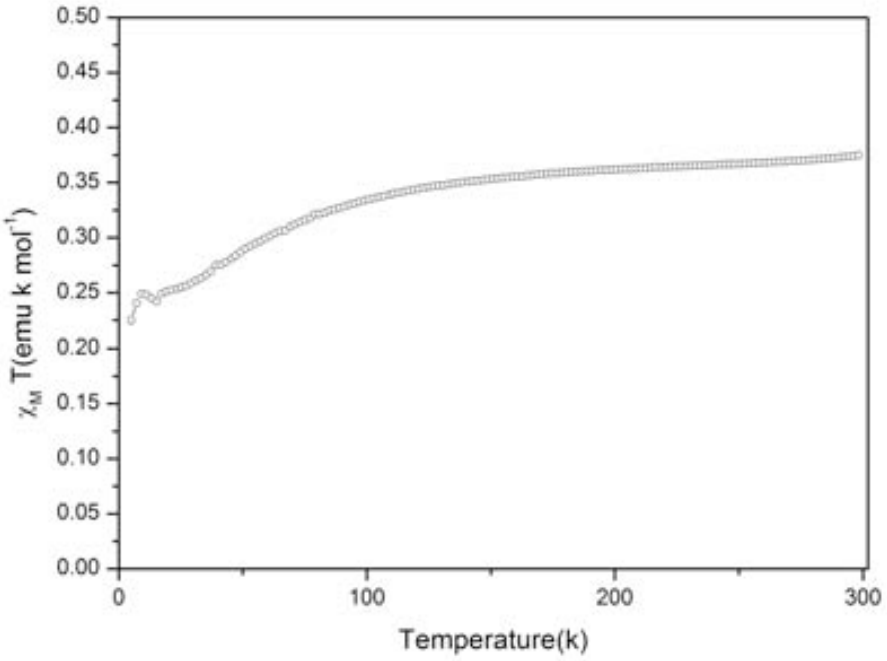

Figure S5. Magnetic susceptibility graph of Cu(II)-4,4'-bipy crystals